

Acceleration of heavy Ions to MeV/nucleon Energies by Ultrahigh-Intensity Lasers

*Dissertation der Fakultät für Physik
der Ludwig-Maximilians-Universität München*

vorgelegt von
Björn Manuel Hegelich
aus Herdecke

München, den 09.11.2002

1. Gutachter: *Prof. Dr. D. Habs*

2. Gutachter: *Prof. Dr. T. W. Hänsch*

Tag der mündlichen Prüfung: *12.12.2002*

...

There is a theory which states that if ever anyone discovers exactly what the Universe is for and why it is here, it will instantly disappear and be replaced by something even more bizarre and inexplicable.

There is another which states that this has already happened.

DNA [1]

...

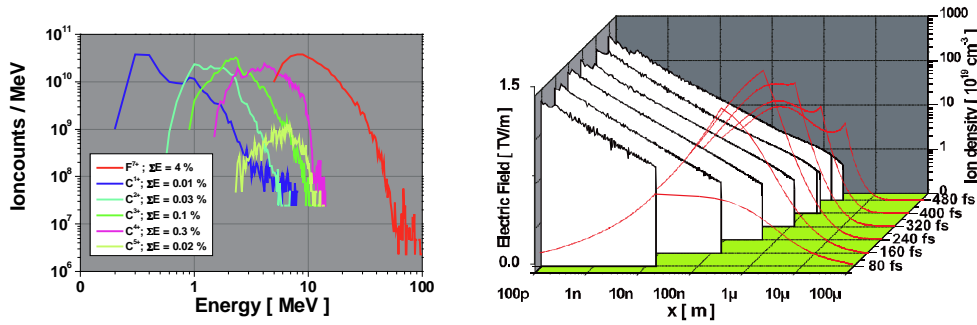
Abstract

The primary aim of this thesis was the acceleration of ions with a nuclear charge $Z > 1$ to multi-MeV energies by means of a laser pulse. While laser-induced proton acceleration in the MeV-range has recently been achieved by a number of groups, the laser acceleration of high quality, high energy beams of heavier particles has been demonstrated for the first time within the framework of this thesis. Furthermore, the obtained data could then subsequently be used to understand the dynamics of the acceleration physics, which was not accessible by the means of the previously performed experiments.

The particles were accelerated using a state-of-the-art ultrahigh-intensity laser, with a peak power in excess of 100 Terawatt (TW) and a focused intensity $I \sim 5 \times 10^{19} \text{ W/cm}^2$. These powers and intensities are achieved by compressing 30 Joule of energy in a laser pulse as short as 300 femtoseconds (fs) and focussing this pulse down to a spot with a radius $r \leq 8 \mu\text{m}$. When laser pulses with intensities of $\sim 10^{19} \text{ W/cm}^2$ interact with thin metal foils they ponderomotively accelerate electrons to energies of several MeV. Due to the relativistic nature of the interaction at these intensities the acceleration is mainly directed in forward direction and the electrons penetrate the target foil. Upon exiting they set up an ultrastrong space charge field of several TV/m. While the ions have a too high inertia to be significantly moved by the rapidly oscillating laser field, this quasistatic field at the target rear surface accelerates ions to multi-MeV energies. The ions are emitted in a narrow beam with a divergence decreasing with increasing energy and charge state. Without any special precautions this acceleration mechanism is only effective for protons, regardless of the target material. Due to the operating conditions of ultrahigh-intensity lasers an ultra-high vacuum environment is not possible and the target surfaces are always contaminated by a thin layer of hydrocarbons. Due to their higher charge-to-mass ratio protons are always more efficiently accelerated than any other ion and subsequently the protons outrun all other ion species and effectively screen the accelerating potential.

The way to accelerate other ion species therefore lies in getting rid of the protons. By heating the targets we succeeded in removing the contaminant layers of hydrocarbons. This is achieved by either resistive heating or laser heating. Once the hydrocarbons are removed, other ions are efficiently accelerated as can be seen in the spectrum shown below. Two Thomson-parabola ion spectrometers were designed and employed to obtain these high-resolution, absolutely calibrated ion energy spectra and charge state distributions. Carbon and fluorine ions were accelerated to energies of several MeV/nucleon, the highest achieved energy was measured for F^{7+} -ions with more than 100 MeV. A conversion efficiency of laser energy to heavy ion energy of $> 5 \%$ has been achieved for optimal heating parameters. This corresponds to roughly the same conversion efficiency that was otherwise measured for protons.

The measured spectra and charge state distributions contain information on the dynamics of



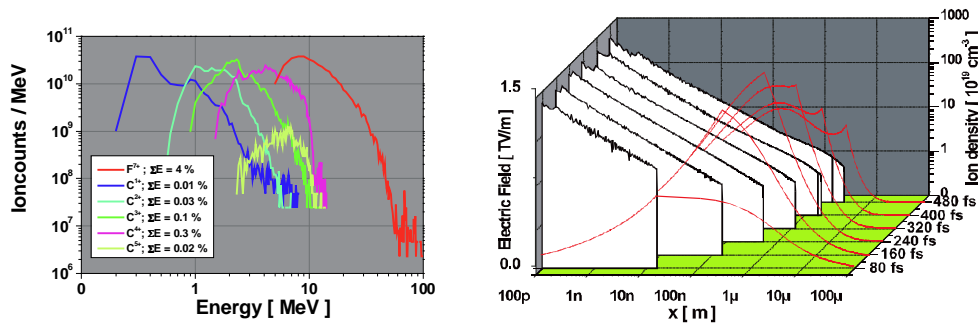
the ionization and acceleration processes. It is shown that the main ionization mechanism is Field Ionization by Barrier Suppression (FIBS) and that collisional ionization and recombination are of minor importance. The ionization happens sequentially as the ion moves away from the target surface, on a spatial scale of \sim nm and a temporal scale of \sim fs. The initial ion distribution during and shortly after the laser pulse is stratified - i.e. C^{1+} closest to the unperturbed surface, followed by C^{2+} , C^{3+} and finally C^{4+} extending and forming the forward edge of the expanding ion front. The accelerating field moves outwards into the vacuum as could be shown by simulations with a 1-dimensional kinetic code which was developed within the scope of this work. The interaction is highly dynamic and gets increasingly complex as the system cools down after the pulse. Having established FIBS as the responsible ionization mechanism, it is now possible to use the charge state distribution as a probe for the strength of the accelerating field. Since the individual charge states have different energy distributions this probe is automatically time-dependent and reveals information about the field dynamics. The highest fields are on the order of several TV/m and have a duration $\tau \sim 500$ fs, comparable to the laser pulse duration. The lower charge states, however, which only see fields of ~ 10 GV/m, are accelerated on a time scale of > 10 ps. This requires a mechanism that maintains the high electron temperature after the source (i.e. the laser pulse) has shut off. One possibility are oscillating or recirculating electrons, which undulate around the positive ion distribution.

Our measurements show that the accelerated ion beam is of high quality, showing a small divergence ($\leq 15^\circ$) and source size ($\sim 100 \mu\text{m}$). The transverse temperature of the beam is very low, allowing imaging on a sub-micron scale. Furthermore the ion pulse is initially short, i.e. of the same duration as the laser pulse, and carries a current of several MA. These characteristics cannot be obtained by any conventional accelerator and open the door for a multitude of potential applications, among them proton imaging, ion fast ignition and ion fusion drivers, advanced accelerator concepts and tools for fundamental physics studies, e.g. on transport and stopping of high current beams and isochoric heating of matter.

Zusammenfassung

Laser-induzierte Beschleunigung von Protonen auf MeV Energien konnte in den letzten zwei Jahren von mehreren Gruppen erreicht werden. Im Rahmen dieser Arbeit demonstrieren wir nun erstmalig die effiziente Beschleunigung von hochenergetischen leichten Ionen mit guter Strahlqualität durch einen Laserpuls. Die gewonnenen Daten liefern ausserdem einen entscheidenden Beitrag zum Verständnis der Dynamik des Beschleunigungsprozesses, die bisherigen Experimenten nicht zugänglich war.

Ein state-of-the-art Nd:Glass Höchstintensitätslaser lieferte die erforderlichen Lichtpulse mit einer Energie von 30 J und einer Dauer von 300 fs. Sie wurden mit einem Parabolspiegel auf einen Fleck mit einem Durchmesser von 8 μm fokussiert, was einer Intensität von 5×10^{19} W/cm² entspricht. Wird Materie einer solchen Bestrahlungsdichte ausgesetzt, verwandelt sie sich instantan in ein Plasma, dessen freie Elektronen der Gradient des Lichtdruckes auf Energien von einigen MeV in Laserstrahlrichtung beschleunigt. Targets von nur einigen 10 μm Dicke (dünne Folien) vermögen die Elektronen zu durchdringen und durch die Rückseite zu verlassen. Dadurch baut sich dort ein zeitlich nicht oszillierendes Raumladungsfeld mit Feldstärken von mehreren TV/m auf. Es ist in der Lage, Atome auf der Targetrückseite zu ionisieren und auf viele MeV zu beschleunigen. Die Ionen werden in einem engen Strahl emittiert und weisen eine mit zunehmender Energie und Ladungszustand abnehmende Divergenz auf. Ohne besondere Massnahmen hinsichtlich der Targetpräparation werden unabhängig vom Folienmaterial immer Protonen beschleunigt. Diese stammen aus Wasser- und Kohlenwasserstoffschichten, die auf Grund der Vakuumbedingungen in Hochintensitätslaser-Experimenten allen Oberflächen anhaften. Wegen ihres grösseren Ladung-zu-Masse-Verhältnisses werden Protonen immer effektiver beschleunigt als jede andere Ionenspezies. Die Protonen laufen daher vor den anderen Teilchen her und schirmen die beschleunigenden elektrischen Felder für diese ab. Um also Ionen mit $Z > 1$ auf hohe Energien zu beschleunigen, muss man zuerst die kontaminierenden Schichten entfernen. Dies geschieht durch Ohmsche Heizung des Targets. Die gemessenen Spektren bestätigen dann eindeutig, dass dominant schwerere Ionen effizient beschleunigt werden. Um die Spektren und Ladungszustandsverteilungen absolut kalibriert und hochaufgelöst messen zu können, wurden im Rahmen dieser Arbeit zwei Thomsonparabel-Spektrometer entwickelt und eingesetzt. Kohlenstoff- und Fluorionen wurden auf mehrere MeV/nucleon beschleunigt, wobei die höchste gemessene Energie von über 100 MeV mit F⁷⁺-Ionen erreicht wurde. Für ein optimal gereinigtes Target konnten Konversionseffizienzen von Laserenergie in Ionenenergie von mehr als 5% erreicht werden. Dieser Wert entspricht in etwa dem für Protonen gemessenen, d.h. man kann zu schwereren Teilchen übergehen ohne nennenswerte Effizienzeinbussen hinnehmen zu müssen. Die gemessenen Spektren enthalten Informationen über die Dynamik des Ionisations- und Beschleunigungsprozesses. Wir können zeigen, dass die primäre Ionisation mittels Feldionisation durch Potentialunterdrückung (Field Ionization by Barrier Suppression) geschieht



und dass Stossionisation und Rekombinationsprozesse von untergeordneter Bedeutung sind. Die Ionisation geschieht sequentiell, während sich das Ion von der Folienoberfläche fortbewegt, allerdings auf extrem kleinen räumlichen (nm) und zeitlichen (fs) Skalen. Die ursprüngliche Ionenverteilung direkt nach der Spitze des Laserpulses ist geschichtet - d.h. C¹⁺ am nächsten an der Folienrückseite, gefolgt von C²⁺, C³⁺ und schliesslich C⁴⁺ an der vorderen Kante der expandierenden Ionenfront eines Kohlenstofftargets. Das Maximum des beschleunigenden Feldes bewegt sich mit den Ionen mit, wie wir durch kinetische Simulationen zeigen konnten. Die Wechselwirkung ist gekennzeichnet durch ihre hohe Dynamik und wird zunehmend komplexer mit fortschreitender Abkühlung nach Ende des Laserpulses. Die Identifizierung von Feldionisation als primärer Ionisationsmechanismus ermöglicht es, die Ladungszustandsverteilung als Sonde für die auftretenden Feldstärken zu benutzen. Durch die unterschiedlichen Energieverteilungen der Ladungszustände ist diese Sonde inhärent zeitabhängig und ermöglicht so eine erste Messung der Felddynamik. Die höchsten Feldstärken erreichen mehrere TV/m und haben Lebensdauern im Bereich der Pulsdauer des Lasers. Die niedrigen Ladungszustände werden jedoch von Feldern von "nur" ~ 10 GV/m beschleunigt, das jedoch über eine Zeit von einigen 10 ps. Dies erfordert einen Mechanismus, der in der Lage ist, auch nach Abklingen des Laserpulses noch eine hohe Elektronentemperatur aufrecht zu erhalten. Dafür könnten rezirkulierende Elektronen, die im Potenzial der Ionen und des Targets oszillieren, in Frage kommen, wie es kürzlich von Y. Sentoku vorgeschlagen wurde.

Unsere Messungen zeigen einen Ionenstrahl von ausserordentlicher Qualität, mit einer kleinen Divergenz und sehr kleiner Quellgrösse. Weiterhin ist die transversale Temperatur des Strahls so extrem niedrig, dass sie sogar Abbildungen im Sub-Mikrometerbereich ermöglicht. Der Ionenpuls ist verglichen mit konventionell beschleunigten Pulsen sehr kurz, er hat ungefähr die gleiche Dauer wie der ihn auslösende Laserpuls, und enthält ausserdem einen Strom von vielen MA. Diese Eigenschaften, die konventionelle Beschleuniger nicht erreichen, ermöglichen neue Beschleunigerkonzepte sowie Anwendungen in der Isotopenproduktion für medizinische Zwecke, Laserfusion und Grundlagenforschung bezüglich isochorem Heizen von Materie auf Inner-Stern-Bedingungen.

Contents

1	Introduction	1
1.1	Motivation	1
1.2	Thesis Structure	3
1.3	Nature of the experiments	3
2	Laser-induced Ion Acceleration	7
2.1	Laser – plasma interaction	8
2.1.1	Interaction of ultra-intense light and a single electron	8
2.1.2	Interaction of an ultra-intense laser pulse with a plasma	11
2.2	Laser-electron acceleration	14
2.2.1	Laser-Wakefield-Acceleration	15
2.2.2	Direct Laser Acceleration	15
2.2.3	Ponderomotive acceleration in an ultra-strong laser field	15
2.3	Ion acceleration Mechanisms	16
2.3.1	Ion acceleration in gas targets	18
2.3.2	Ion acceleration from solid bulk targets	19
2.3.3	Ion acceleration from thin foil targets	20
2.3.4	Ion acceleration by long-pulse lasers	24
3	Ionization Mechanisms	27
3.1	Direct Laser Ionization	27
3.2	Field Ionization	28
3.2.1	FIBS-Model	29
3.2.2	Keldysh-Model	30
3.2.3	ADK-Model	31
3.3	Collisional Ionization	32
3.3.1	Collisional Ionization by the hot electron component: Analytical Estimate	33
3.3.2	Collisional Ionization by cold electrons in return currents : Analytical Estimate	33
3.4	Ionization Code FLY	34

3.5	Comparison of Ionization Mechanisms	35
4	The Experiment	39
4.1	LULI 100 TW Laser System	40
4.1.1	The Oscillator	40
4.1.2	The Mixed Glass Amplifiers	41
4.1.3	The Pulse Compressor	44
4.1.4	The Target Chamber	45
4.1.5	Laser Diagnostics	45
4.2	Experimental Setup	46
4.2.1	Interferometry	49
4.2.2	Neutron Detectors	50
4.2.3	Radiochromic Film and CR-39 stacks	50
4.2.4	Proton and Electron Spectrometer	51
4.3	Targets	52
5	Ion Diagnostics	53
5.1	The Thomson parabola spectrometer	53
5.2	Solid State Nuclear Track Detectors	56
5.2.1	Working principle of SSNTDs: Track formation mechanism	57
5.2.2	Track Etching	59
5.3	Automated Single Track Counting	61
5.3.1	Reflective and transmissive behavior of etched tracks	61
5.3.2	Automated Single Track Counting	62
6	General Measurements	65
6.1	Electron Measurements	65
6.2	Proton Acceleration	66
6.2.1	Proton Spectra	67
6.2.2	Divergence, Emittance and Source Size	68
6.3	Target Properties	71
6.3.1	Plasma density gradients	71
6.3.2	Front surface damage	72
6.3.3	Rear surface damage	73
6.3.4	Conductors and Insulators	73
6.3.5	Curved Targets	74

7	Ion Measurements	77
7.1	Removal of Hydrocarbon Contaminants	77
7.1.1	Cleaning Methods	78
7.2	Ion Spectra Measurements	79
7.2.1	Carbon Spectra	81
7.2.2	Fluorine Spectra	84
7.2.3	Divergence	86
7.2.4	Source Size	89
8	Interpretation and Theory	91
8.1	Acceleration Mechanism	91
8.1.1	Recombination	91
8.1.2	Ionization	92
8.1.3	Field Dynamics	92
8.1.4	Front- versus Rearside mechanism	95
8.2	Computer Simulations	96
8.2.1	1D-code	97
8.2.2	1D-PIC code with ionization	99
8.2.3	1D-PIC results: Influence of H ⁺ contamination	100
9	Summary and Perspective	103
9.1	Modified TNSA-Model	104
9.2	Future Experiments	105
9.2.1	Time-resolved measurement of the accelerating electric field	105
9.2.2	Spatial origin of low charge state ions	107
9.2.3	Truly heavy ion acceleration	107
9.2.4	MeV-Ion acceleration with table-top lasers	108
9.3	Scaling parameters for laser accelerated ions	109
9.4	Applications	112
	Literature	116
	Publications	127
1.5	M. Hegelich <i>et al.</i> , Phys. Rev. Lett. 89 , 085002 (2002)	129
1.6	M. Roth <i>et al.</i> , Phys. Rev. Spec. Top. - AB 5 , 061301 (2002)	135
1.7	M. Roth <i>et al.</i> , Plasm. Phys. Control. Fusion 44 , 1 (2002)	145
1.8	H. Baumhacker <i>et al.</i> , Opt. Lett. 27 , 1570 (2002)	157
1.9	M. Hegelich, Physik in unserer Zeit 6 , 252 (2002).	161

Danksagung

163

Chapter 1

Introduction

1.1 Motivation

When investigating laser-induced ion acceleration the first question has to be what happens when light of high intensity comes into contact with matter? The light wave couples to the electrons of the target, which start to oscillate in the electromagnetic field. Already at relatively moderate intensities ($10^{12}W/cm^2$) enough energy is transferred to ionize the surface layer of the target. The matter heats up and a plasma evolves and expands. The main part of the laser pulse now interacts with the plasma. The plasma is heated and modified and at the same time modifies the incident light. Very generally spoken, light energy is converted into particle motion, which means in most cases *unordered* motion, i.e. temperature. Under the internal pressure of this temperature the plasma will expand further which results in the acceleration of the plasma ions. These acceleration mechanisms have been studied almost as long as high energy pulse lasers exist. However while lasers with pulse energies in the hundreds of Joules and even kilojoule range exist for many years, the pulse durations achievable with these systems used to be in the nanosecond range. Consequently experiments with these Nd:glass and CO_2 lasers [2, 3, 4, 5, 6] were performed at intensities between 10^{14} and $10^{16}W/cm^2$ and the typical ion energies were in the keV or later 100-keV range. And due to the origin of the acceleration in unordered motion, the resulting ion acceleration is also unordered and the ions are emitted in a large cone ($> 45^\circ$) against the laser direction and exhibit high transverse temperatures. Due to their poor beam characteristics, these ions could never be put to any further use.

With the advent of Chirped-Pulse-Amplification (CPA) [7] a new aspect came into play. Achievable intensities jumped by many orders of magnitude to up to and beyond $10^{21} W/cm^2$. Intensities like this and the corresponding fields had never before been accessible within a laboratory. It turned out that at intensities beyond $\sim 10^{18}W/cm^2$ a fundamental threshold is crossed, and the laser-plasma interaction becomes relativistic.

More specific the quiver velocity of the electrons in the electromagnetic field of the lasers approaches the speed of light in a single oscillation period. As a consequence the magnetic component of the field is no longer negligible and the electron mass increases. The changes in single-particle interaction lead to collective effects in the plasma allowing a conversion of light energy into *ordered* motion.

The most intriguing possibility of this development is the acceleration of charged particles along very short distances (typically hundreds of microns) into well directed dense bunches with energies up to tens of MeVs. Using ultrahigh-intensity lasers electrons with energies up to 200 MeV have been demonstrated [8] and protons have been accelerated to ~ 60 MeV [9]. This work now demonstrates for the first time the acceleration of heavier ions by short pulse lasers to equivalently high energies, specifically accelerating fluorine ions to energies up to 100 MeV.

Describing these acceleration processes and indeed the interaction of ultra-high intensity laser pulses with matter is still work in progress, both theoretically and experimentally.

Although on a microscopic scale, the problem in principal reduces to the Maxwell equations and the relativistic equations of motion for the involved particles, it is not easy to extrapolate to the macroscopic scale of an experiment. Modern computer simulation codes try this approach very successfully for a limited problem, but even the biggest massively parallel computers have not enough computing power to simulate a 3-dimensional all-particle description of a dense plasma in a sufficiently large simulation area. Therefore, severe restrictions and simplifications must be made which require a profound pre-understanding of the effects involved. The other way is an analytic description of the plasma as a collective entity analogous to classic plasma physics, which yields tendencies, functional dependencies, and model pictures.

The basic model picture for the ion acceleration mechanism is easily sketched and explained in more detail in Chapter 2. The high-intensity electromagnetic fields in the laser focus accelerate electrons by various collective mechanisms to relativistic energies. In contrast to non-relativistic laser-plasma interaction, this acceleration can be directed. The displacement of a large number of electrons leads to the build up of space charge fields of the same order of magnitude than the laser fields. In contrast to the quickly oscillating laser fields ($T \sim 3$ fs) these space charge fields are stable on a time scale of up to picoseconds, which can be even longer than the total laser pulse duration. These "quasistatic" space charge fields can now accelerate ions which are too inert to follow the fast changing laser fields.

As simple as this model picture as complex are the details and dynamics of the acceleration process. They, and with them a way to control them, are largely not understood

yet and the topic of current research. Up to now neither an analytical model nor a computer simulation could be produced that describes the entire process. However, by the virtue of a number of ongoing experiments more pieces of the puzzle are found continually, such as this work was able to shed light in the topics of effectively selecting the ion species as well as the ionization and acceleration dynamics.

1.2 Thesis Structure

The thesis is divided into three major parts. The first part consists of Chapter 2 and Chapter 3 and explains the basic theoretical concepts. Chapter 2 explains the physics of laser acceleration, while Chapter 3 deals with the different ionization mechanisms. The topic of the second part is the technical aspect of this work. Chapter 4 describes the laser system, the experimental setup, and the different diagnostics. Chapter 5 explains in detail Thomson parabola -spectrometers which formed the main diagnostics, the detector physics and working principles of the CR-39 Solid State Nuclear Track Detectors (SSNTD) and the automated scanning microscope system used to analyze the CR-39.

The third and main part is dedicated to the experimental results of the thesis. Chapter 6 gives an introduction to the proton measurements and contains measurements on general beam parameters like divergence and source size. In Chapter 7 the results on carbon and fluorine ion acceleration are presented and the ion beam parameters are analyzed and compared to the proton measurements. Chapter 8 then carries on from there and uses the obtained data to illuminate the underlying physics. Information on recombination and ionization processes, the field dynamics and the acceleration mechanism is extracted from the data and further analyzed by means of kinetic and Particle-In-Cell computer simulations. Chapter 9 finally discusses future perspectives of laser accelerated ions both with respect to fundamental science and applications and tries to give a scaling of the effects to the new bigger laser systems currently under construction.

1.3 Nature of the experiments

In contrast to the table-top ATLAS system at the MPQ the high-energy lasers used within the scope of this work are fairly large facilities which are operated very much like large scale accelerators. That means that each user gets only a limited amount of beamtime and due to the low repetition rates of large high energy glass lasers the actual number of shots for an experiment is even more limited. Also the beamtime

is not scheduled to one user but to a group of users meaning that usually a number of different experiments are carried out at one beamtime which further decreases the number of laser shots available to a specific task.

The experiments described in this thesis were mainly part of a larger experimental campaign at the Laboratoire pour l'Utilisation des Lasers Intense (LULI) 100 TW Laser at the Ecole Polytechnique, Palaiseau, France. Our group consisted of J. Fuchs, P. Audebert and J.C. Gauthier from LULI, M. Roth, A. Blacevic, M. Geissel and E. Brambrink from GSI/TU Darmstadt, M. Allen and T. Cowan from General Atomics, San Diego and S. Karsch and myself from MPQ/LMU Munich.

The campaign consisted of four beamtimes of two weeks each and its aim was to investigate particle acceleration from thin foils by ultrahigh-intensity lasers. Within these campaigns especially measurements of the accelerated protons and their beam properties, i.e. yield, divergence, emittance, spectrum, etc. were performed. We also studied the dependence of the proton beam parameters on laser and target properties, such as laser energy, prepulse, target material, thickness, or surface quality. Moreover, the possibilities of neutron production by $d(d,n)^3\text{He}$ fusion and (p,n) -reactions using laser accelerated deuterons and protons have been investigated.

The primary part of these experimental campaigns that this thesis deals with is the acceleration and subsequent characterization of ions with $Z > 1$. Can these heavier ions be accelerated efficiently by ultrahigh-intensity lasers and what targets are suited best for that task? Moreover, what can be learned from the measured spectral and charge state distributions concerning the ionization and acceleration mechanism? In contrast to the protons the heavier ions exist in a multitude of charge states which have all different sensitivities towards the ionizing and accelerating mechanisms and thus inherently contain much more information regarding these physical processes than the proton signal.

An additional campaign was run recently at the new Trident Shortpulse Laser at the Los Alamos National Laboratory in cooperation with J. Cobble, S. Letzring, R. Johnson and J. Fernandez. The primary aim of this campaign was to commission the new laser facility and to validate its abilities for particle acceleration. Though the number of shots was very limited and no dedicated heavy ion targets could be shot due to lack of time and difficulties with the target insertion mechanism, the main goal of the campaign was met and some of the results on beam parameters presented in Chapter 6 were obtained at the Trident facility.

This thesis mainly describes the results of the ion acceleration experiments, however, to draw an as complete and conclusive picture of the underlying physics as presently possible, the results of the other experiments will frequently be used to complement the

ion measurements. For a detailed description the reader is referred to the respective publications as given in the text and the addendum, in particular the PhD-theses of M. Allen and S. Karsch [10, 11].

Chapter 2

High-Intensity Laser – Matter Interaction and Laser-induced Ion Acceleration

In laser-matter interactions plasma creation already starts at very moderate intensities of $I \sim 10^{12}$ W/cm². When a high-intensity laser pulse hits any target, already the onset of the pulse many orders of magnitude below peak intensity is strong enough to ionize the target atoms and start plasma creation. Therefore, all kind of matter will thus always be in the plasma state when it interacts with the main part of ultrahigh-intensity laser pulse. While laser-matter interaction has been treated thoroughly in the past, new effects come into play when ultra-short laser pulses are involved.

In the case of ultrashort and ultra-intense laser pulses the energy is deposited into a much smaller spatial area because the diffusion and equipartition processes happen on time scales much longer than the laser pulse. Furthermore the relativistic nature of the interaction changes the mechanism of laser coupling to single particles, which leads on the whole to collective motion and to the creation of large quasistatic fields. Another point is that the plasma is not only created and heated but also strongly modified in its properties when an ultra-intense laser pulse is present. The ion acceleration in the wake of such a laser-plasma interaction, at least for the high energetic ions which are the topic of this thesis, is not caused by the well-known expansion processes but takes place on much shorter time-scales. More important, charge neutrality is not maintained in the acceleration phase but on the contrary the acceleration is caused by a quasistatic field set up by charge separation.

In spite of these major differences all ion acceleration schemes have one thing in common. The ions are not accelerated by the laser itself but the interaction is mediated by the plasma electrons. To understand the different acceleration schemes it is therefore

important to understand the laser-electron interaction. The following section therefore discusses the laser-plasma interaction, starting with a single free electron before going over to a full plasma. The second section then discusses the different ion acceleration mechanisms possible with short-pulse lasers and compares those to the well-known long-pulse case.

2.1 The interaction of an ultrahigh-intensity laser pulse with a plasma

When a high-intensity laser pulse interacts with a plasma at intensities beyond $\sim 10^{18}$ W/cm² one enters a relativistic regime. While on the one hand the laser acts upon the plasma, simultaneously the plasma acts on the laser pulse, too. This interaction gives rise to several new effects which could not be observed before in conventional laser plasma interaction. But before discussing those collective plasma effects the interaction of a single charged particle with ultra-intense light is reviewed.

2.1.1 Interaction of ultra-intense light and a single electron

When light interacts with a charged particle, this particle moves in the electromagnetic field of the light wave. In SI units and in vacuum (with the relative permittivity and permeability $\varepsilon_r = \mu_r = 0$) and in the slowly varying envelope approximation (SVEA), a linearly polarized light field is given as

$$(2.1) \quad \begin{aligned} \vec{E}(\vec{r}, t) &= E_0(\vec{r}, t) \vec{e}_x e^{i(\omega t - kz)} \\ \vec{B}(\vec{r}, t) &= B_0(\vec{r}, t) \vec{e}_y e^{i(\omega t - kz)} \quad \text{with} \quad B_0 = \frac{E_0}{c}, \end{aligned}$$

where \vec{e}_x and \vec{e}_y are normal and normalized vectors, both normal to the propagation direction \vec{e}_z , and c is the speed of light. The corresponding intensity is defined as the energy flux density averaged over the fast oscillations

$$(2.2) \quad I(\vec{r}, t) = \left\langle \left| \vec{E} \times \frac{\vec{B}}{\mu_0} \right| \right\rangle = \frac{\varepsilon_0 c}{2} |E_0(\vec{r}, t)|^2,$$

and is usually given in [W/cm²]. Here ε_0 is the permittivity and μ_0 the permeability of free space. The force exerted on a charge Ze moving with a velocity $\vec{\beta} = \vec{v}/c$ is given by the Lorentz-law

$$(2.3) \quad \frac{d\vec{p}}{dt} = \frac{d(\gamma mc\vec{\beta})}{dt} = Ze \left(\vec{E} + c\vec{\beta} \times \vec{B} \right) = Ze \left(\vec{E} + \vec{\beta} \times (\vec{e}_z \times \vec{E}) \right),$$

where m is the particle mass and the usual relativistic γ .

The second term in (2.3) is negligible for non-relativistic particles with $\beta \ll 1$. Their motion is described by a harmonic oscillation in the electric field with a maximum amplitude and velocity in the order of

$$(2.4) \quad s_0 \approx \frac{|Ze| E_0}{m \omega^2} \quad \text{and} \quad |\vec{v}| \approx \frac{|Ze| E_0}{m \omega} .$$

As one can see the motion of an ion is by far weaker than that of an electron due to the ions higher mass m_i . Therefore, in the following the ions are assumed to be at rest.

A convenient quantity frequently used in relativistic laser plasma physics is the dimensionless light amplitude

$$(2.5) \quad a_0 = \frac{eE_0}{\omega m_e c} ,$$

where m_e denotes the electron mass. One can then rewrite the field equations

$$(2.6) \quad \begin{aligned} E_0 &= a_0 \frac{2\pi m_e c^2}{e\lambda} = \frac{a_0}{\lambda [\mu\text{m}]} 3.2 \times 10^{12} \text{ V/m} \\ B_0 &= a_0 \frac{2\pi m_e c}{e\lambda} = \frac{a_0}{\lambda [\mu\text{m}]} 1.07 \times 10^7 \text{ T} \\ I &= a_0^2 2\epsilon_0 c \left(\frac{\pi m_e c^2}{e\lambda} \right)^2 = \frac{a_0^2}{\lambda^2 [\mu\text{m}^2]} 1.37 \times 10^{18} \text{ W/cm}^2 . \end{aligned}$$

Describing the electron motion (2.4) in terms of the dimensionless light amplitude a_0 one obtains

$$(2.7) \quad s_0 \approx a_0 \frac{\lambda}{2\pi} \quad \text{and} \quad |\vec{v}| \approx a_0 c .$$

A relativistic description of the periodic electron motion becomes necessary when a_0 approaches unity. At a laser wavelength $\lambda \approx 1 \mu\text{m}$, this is the case at intensities around 10^{18} W/cm^2 , a threshold crossed by orders of magnitude with last-generation high-intensity lasers. By crossing this threshold one reaches the new regime of relativistic laser-matter interaction, where particle dynamics change due to several phenomena:

- **mass increase:** When an electron approaches the speed of light in every oscillation, its (average) mass increases.
- **anharmonic motion:** The electron oscillation in the electric field is no longer harmonic, but the relation (2.7) for the maximum transverse oscillation amplitude s_0 remains valid.

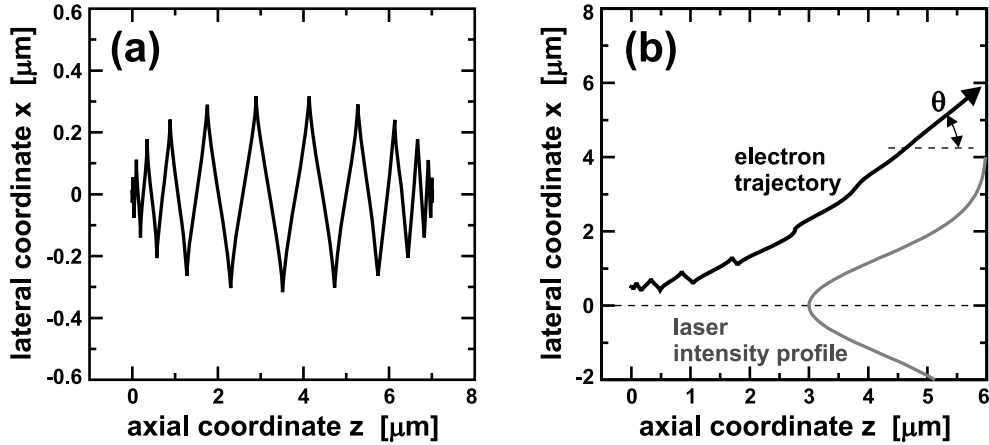


Figure 2.1: Electron trajectories in a strong laser field: (a) laser pulse of duration $\Delta\tau = 20$ fs, amplitude $a_0 = 2.5$ ($I = 1.3 \times 10^{19}$ W/cm² at $\lambda = 800$ nm), and large lateral beam size; (b) same laser pulse, but in a tight focus (diameter $d_{\text{FWHM}} = 3 \mu\text{m}$, the laser lateral intensity profile is also shown). An electron, initially at rest at a distance of $x_0 = 0.5 \mu\text{m}$ from the laser axis, is ejected under an angle of $\theta \approx 52^\circ$ to the axis with an energy of $E_{\text{kin}} = 0.64$ MeV.

- **forward drift:** The $\vec{v} \times \vec{B}$ term in the Lorentz force (2.3) is no longer negligible if $\beta \approx 1$, which results in more complex particle trajectories (see Fig. 2.1(a)).

The relativistic particle motion is described by a figure-of-8 shape in the frame of the average drift, as shown below. This average drift is caused by the magnetic field in combination with the electric field induced by transverse velocity. This drift is always directed in the light propagation direction with a velocity

$$(2.8) \quad \vec{v}_D = \frac{a_0^2}{4 + a_0^2} c \vec{e}_z .$$

It has to be noted, that in spite of the high *average* kinetic energy during the light pulse, the electron *does not gain net energy* by this process.

Up to now all considerations have been made for an electron in an infinitely extended plane wave. However, when the light is focused, a transverse intensity profile comes into play. The major effect of this transverse profile is, that an electron which is driven out of the focus in one half-cycle by the very high fields in the immediate focal region, feels a very much weaker force in the second half-cycle. It is therefore not as hard drawn back as it was pushed out and will eventually leave the focal region as shown in Fig. 2.1 (b). Thereby it will now effectively *gain energy*. For a realistic laser pulse with finite dimensions this constitutes an effective acceleration mechanism that allows electrons to be accelerated by the light wave.

However, this simple explanation, which is worked out numerically and analytically for

the relativistic case in [12], predicts electron ejection in the plane of polarization, while experimental evidence shows that electrons leaving the focus have an azimuthally symmetric distribution, even in the case of linearly polarized laser light. This discrepancy is due to the fact that the above explanation neglects that a spatially confined light field always has non-zero field components in the propagation direction [13, 14] to fulfill the Poissons equation. Usually these components are fairly small but for ultra-high intensities they become big enough to play a role. If one takes into account those terms (see e.g. [15, 16]) the electron trajectories in these modified fields are complex 3-dimensional patterns (see Fig. 2.2) and the electron ejection is radially symmetric, independent of the laser polarization direction. To get a first understanding without having to deal with the full 3-dimensional trajectory it is useful to consider the electrons final state. The final energy of the electron depends on its escape angle θ with the laser axis, (see Fig. 2.1(b)). For an electron initially at rest,

$$(2.9) \quad \cos \theta \approx \sqrt{\frac{\gamma - 1}{\gamma + 1}}$$

is a good approximation for $\gamma \leq 3$ and gives a lower estimate of θ for larger γ [16]. The exact relativistic solution can be found in [16] and describes the acceleration in terms of a so-called *ponderomotive force*:

$$(2.10) \quad \left\langle \frac{d\vec{p}}{dt} \right\rangle = \frac{1}{2m_e\bar{\gamma}} \nabla \langle |eA_{\perp}|^2 \rangle ,$$

where $\bar{\gamma}$ is the local relativistic γ -factor averaged over an oscillation period, e the electron charge and \mathbf{A}_{\perp} is the transverse component of the 4-vector of the electromagnetic potential ($\mathbf{A} = (e\Phi, \mathbf{A})$).

2.1.2 Interaction of an ultra-intense laser pulse with a plasma

Considering now the interaction of the laser pulse with a whole ensemble of charged particles instead of a single electron new collective effects come into play. Furthermore does not only act the laser on the plasma but also the plasma on the laser pulse, which of course immediately affects the way the laser acts on the plasma and so on. The interaction becomes recursive. The three most important effects are

- laser induced transparency
- relativistic self-focussing
- profile steepening at the pulse front

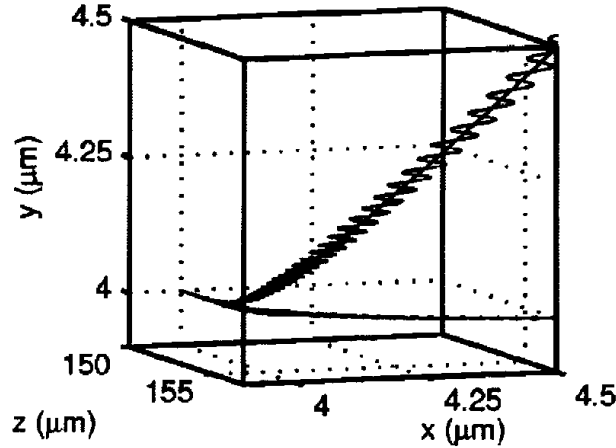


Figure 2.2: 3-dimensional trajectory of an electron accelerated and ejected by a high intensity laser pulse ($a_0 = 0.3$, $\tau_{Pulse} = 200$ fs). The calculations take into account the field components in laser direction arising from the focussing [16].

To understand these effects one has to bear in mind that the properties of a plasma are largely governed by its free electrons. Key quantities are the electron density n_e and the electron plasma frequency

$$(2.11) \quad \omega_p = \sqrt{\frac{e^2 n_e}{\varepsilon_0 \bar{\gamma} m_e}},$$

which is the resonance frequency of collective electron density oscillations against the ion background. With respect to laser frequency ω_L , a plasma is called overdense (or overcritical) when $\omega_p > \omega_L$. In this case, the collective electron motion is strong enough to cancel the light propagation. When the electron density n_e is below the so-called critical density

$$(2.12) \quad n_c = \frac{\omega_L^2 \varepsilon_0 \bar{\gamma} m_e}{e^2}$$

(for example, $n_c \approx 10^{21} \text{ cm}^{-3}$ for $\lambda = 1 \mu\text{m}$), the plasma is underdense with $\omega_p < \omega_L$, and light can propagate with phase and group velocities

$$(2.13) \quad v_p = \frac{c}{n_p} \quad \text{and} \quad v_g = c n_p, \quad \text{with} \quad n_p = \sqrt{1 - \left(\frac{\omega_p}{\omega_L}\right)^2},$$

where n_p is the refractive index of the plasma. For light intensity high enough to cross into the relativistic regime, i.e. $\bar{\gamma} \geq 1$, the plasma frequency gets smaller and the critical density moves to larger values. That means that the plasma at the place of the former critical density becomes transparent for the laser pulse and the pulse can

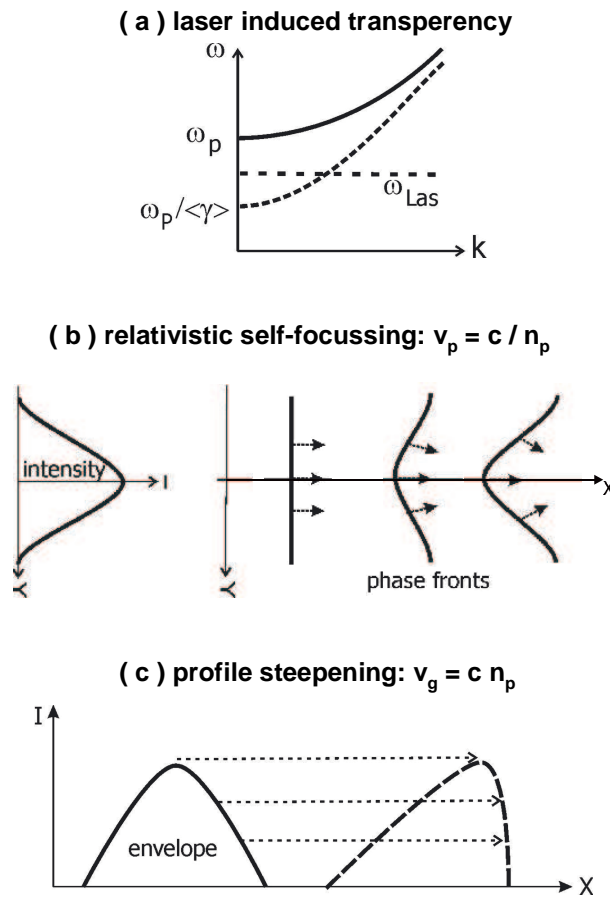


Figure 2.3: Effects of relativistic non-linear optics: **(a) Laser Induced Transparency:** High intensities producing $\gamma \gg 1$ reduce the plasma frequency ω_p . The plasma becomes transparent at its former plasma frequency. **(b) Relativistic Self-focussing:** A pulse with a transverse intensity profile increases the refractive index of the plasma strongly along its propagation axis, but not as much in the fringe region. The plasma acts as a positive lens. **(c) profile steepening:** The central pulse regions with higher intensities move with larger group velocity $v = n_p c$ than the head of the pulse, the profile steepens.

propagate to the new critical density, where the same effect happens all over again until the laser pulse loses too much energy and the intensity falls below the critical value. This effect is called **laser induced transparency** (see Fig. 2.3 (a)).

At ultra-high intensities the electrons also gain mass due to their relativistic motion [17, 18]:

$$(2.14) \quad \bar{\gamma} \approx \sqrt{1 + a_0^2 / 2} ,$$

and they are pushed out of the region of high light intensities by the ponderomotive force. In a plasma, this leads to an effective charge separation, since the ions remain

initially stationary, and thus to the creation of a quasistatic radial space charge field. These space charge fields reduce the electron acceleration compared to a free particle in vacuum, where $\gamma = 1 + a_0^2/2$, but as we will see below still huge energies are achieved. Electron depletion on the laser axis may continue up to the point where the created space charge distribution cancels the ponderomotive force. The electron density reduction on axis can be self-consistently estimated [19]

$$(2.15) \quad \frac{\Delta n_e}{n_e} \approx \left(\frac{c}{\omega_p w_0} \right)^2 \frac{a_0^2}{\sqrt{1 + a_0^2/2}},$$

(with the Gaussian focus width w_0), and can lead to a total depletion when the laser amplitude a_0 is sufficiently high.

Both of these effects again significantly decrease the plasma frequency ω_p (2.11) on the axis of laser propagation. From (2.13) it follows that the refractive index increases with decreasing ω_p . This leads to the build-up of a spatial refractive index profile results with a maximum on axis, which acts analogous to a positive lens, focussing the laser pulse (and thereby increasing its intensity even further). This effect is known as **relativistic self-focusing** and is schematically shown in Fig. 2.3 (b).

Profile steepening is caused by the finite temporal extension of the pulse. The central regions of the pulse with higher peak intensities move with larger group velocities as seen in (2.13) and Fig. 2.3 (c). Thus they catch up with the pulse front where the intensities and therefore the group velocity is lower and the pulse profile steepens.

2.2 Electron acceleration by laser - plasma interactions

The effects described above can now in turn give rise to various modes of electron acceleration, depending on the exact laser and plasma parameters. Very high electron energies on the order of many tens and recently even hundreds of MeV have been realized in strongly underdense plasmas using wakefield-acceleration [20] or in higher but still underdense plasmas using Direct Laser Acceleration [21]. In dense and overdense plasmas ponderomotive acceleration is the most important mechanism. The electrons are not as well collimated and have lower (but still relativistic) energies but the number of accelerated electrons is about two to three orders of magnitude higher. Since electrons are the mediator between the laser pulse and the ions that shall ultimately be accelerated in this work, their acceleration plays a crucial role. The following paragraphs give a brief overview over the different acceleration mechanisms, ordered by increasing plasma densities and importance for the ion acceleration process.

2.2.1 Laser-Wakefield-Acceleration

Laser-Wakefield acceleration (LWA) [22] works best in very underdense plasmas of $n_e \sim 10^{18} \text{ cm}^{-3}$. In this mechanism an ultra-high intensity pulse creates a plasma wave in its wake as it propagates through the medium. Due to its ponderomotive potential it expels electrons creating a density disturbance. This plasma wave or "wake" follows the pulse at almost the speed of light. Electrons can get trapped in this wake and "surf" the wave gaining very high energies. Recently 160 MeV electrons were reported by Malka et al. [8] from laser interaction with an underdense plasma at an intensity $I < 10^{18} \text{ W/cm}^2$.

2.2.2 Direct Laser Acceleration

When the plasma density is increased one enters the regime of **Direct Laser Acceleration (DLA)** [23]. At densities $n_e \sim 10^{20} \text{ cm}^{-3}$ strong relativistic self-focussing is a dominating effect and leads to the formation of a so-called "superchannel" [21]. The ponderomotive force drives a strong electron current within the channel which in turn induces a radial electric field and an azimuthal magnetic field. All the time electrons which are ponderomotively expelled from the channel are bent back in by the quasistatic fields. If the electrons have the right timing with respect to the phase of the laser pulse they can gain net energy on each pass. Energies of several tens of MeV can be achieved by this method but it still requires an underdense plasma of rather large scale length ($\sim 100 \mu\text{m}$) to give enough room for the channel formation.

2.2.3 Ponderomotive acceleration in an ultra-strong laser field

The most important mechanism with respect to ion acceleration is **ponderomotive acceleration (PA)**. The ion experiments discussed in this thesis were all carried out with solid state targets, which means that the main laser plasma interaction takes place in a dense to overdense plasma, namely exactly at the critical density surface. Under these conditions ponderomotive acceleration is the most effective mechanism even when onsets of channel-formation and subsequent DLA or LWA in the underdense preplasma might add a superhot tail to the electron spectrum. As an example the following paragraph reviews the ponderomotive effects caused by a ultrahigh-intensity laser -pulse of $\sim 10^{21} \text{ W/cm}^2$ [$5 \times 10^{19} \text{ W/cm}^2$] which represents the highest possible intensity today and in brackets [] a typical intensity for our experiments. The intensities correspond to a local field strengths E_{laser} of

$$(2.16) \quad E_{laser} = \sqrt{\frac{2I}{\epsilon_0 c}} \approx 10^{14} [2 \times 10^{13}] \text{ V/m},$$

in the focal region, with I being the intensity in W/m^2 . Using (2.5) we obtain for the dimensionless light amplitude a value of $a_0 \sim 30$ [6.3]. The laser-plasma interaction becomes relativistic at a value of $a \sim 1$, so we have to consider the relativistic factor γ :

$$(2.17) \quad \bar{\gamma} = \frac{1}{\sqrt{1 - \frac{\langle v^2 \rangle}{c^2}}} = \sqrt{1 + \frac{\langle p^2 \rangle}{(mc)^2}} = \sqrt{1 + \frac{a^2}{2}}.$$

Substituting a_0 yields $\bar{\gamma} \approx 21$ [4.5].

The electrons react on the ponderomotive potential and are pushed away from the high-intensity region. Thereby the potential energy Φ_{Pond} is converted into kinetic energy W_{kin} . The ponderomotive potential can be estimated as

$$(2.18) \quad \Phi_{pond} = W_{kin} = m_e c^2 (\bar{\gamma} - 1) = m_e c^2 \left(\sqrt{1 + \frac{a_0^2}{2}} - 1 \right) \approx 10 \text{ MeV} \quad [2 \text{ MeV}].$$

Thereby charges are separated and space charge fields are generated, but the electron depletion in the focus will continue until the ponderomotive potential is cancelled by the space charges. The accelerated electrons show a quasi-maxwellian distribution with a temperature $k_B T \cong \Phi_{Pond}$. For a more detailed and rigorous treating of electron behavior in laser fields see e.g. [24, 25].

2.3 Mechanisms for Laser-driven Ion Acceleration

The idea of ion acceleration with lasers has been around almost as long as the first laser itself. Experiments started already in the early seventies and succeeded in ionizing and accelerating ions to at first very moderate sub-keV energies. With the progressing laser technology high energy pulse lasers became available delivering ns-pulses and reaching ion energies in the 100keV/nucleon range ([26] and ref. therein). With the recent step to sub-ps high-energy lasers intensities of more than 10^{21} W/cm^2 and MeV-ion energies are possible. What mechanism is responsible for those vastly higher ion energies?

Traditional long-pulse laser system with pulse durations in the ns-range create a plasma at quasi-equilibrium. It can react fast enough to adapt to the slowly varying laser pulse shape. Plasma expansion, heat transport and the dissipation and equipartition of energy play important roles in describing this situation. Ion acceleration is primarily driven by the pressure gradient in the hot plasma and the surrounding vacuum which causes an quasineutral, isothermal expansion described by a self-similar solution [27].

With short pulse lasers these effects can largely be neglected with respect to the observed high energy ions. Heat transfer and dissipation, shock waves and plasma expansion act on timescales much longer than the laser pulse duration and cannot explain the

observed effects, especially since the key requirements for the long pulse acceleration model, quasineutrality and isothermal conditions, are specifically *not* fulfilled as will be shown below.

As was just demonstrated in the previous section modern short-pulse lasers create enormous potentials, driving electrons to many MeV. But while the electrons experience this huge ponderomotive potential, the ions because their larger inertia combined with the short laser period ($T \sim 2\pi/\omega \sim 3fs$) are not directly moved by those fields. Their ponderomotive potential is negligible due to their much higher mass. If we replace m_e by the proton mass m_p in eqs 2.5 and 2.18 we obtain a ponderomotive potential $\Phi_{pond} \sim 56$ keV for a laser intensity of 10^{21} W/cm². But the relativistic effects always lead to ponderomotive electron expulsion, which will continue until the space charge potential induced by the charge separation balances the ponderomotive potential. The electron distribution remains quasi stationary for the duration of the laser pulse. The ions now feel these space charge fields, whereas the counterbalancing laser fields do not create a substantial ponderomotive potential for the ions, which therefore will be accelerated in a quasistatic electric field as long as the laser fields maintain the charge separation. The plasma is the key element of this acceleration scenario. Whereas in vacuum laser-irradiated ions remain essentially at rest, the plasma can store the laser energy and transfer it first to the electrons which then can hand it on to the ions. The ions can thereby be accelerated to energies of the order of the *electron* ponderomotive potential (2.18) and even above. The charge state and energy distribution, directionality, emittance, etc. depend on the actual geometry and parameters of the charge separation. Several different variations of this main theme with different target and laser conditions have demonstrated to accelerate ions to high energies and are briefly discussed below. Four different approaches have been reported so far:

1. Ions in clusters are stripped to high charge states by intense laser radiation and explode due to several mechanisms, e.g. [28, 29], leading to an isotropic ion distribution.
2. In an underdense plasma, self-focusing and channel formation take place and increase both the ponderomotive potential and the high-intensity interaction length. Ions are ejected radially outwards from such a plasma channel in the electron depletion space charge fields in kind of a radial Coulomb explosion, as observed in several experiments [30, 31, 32].
3. When laser pulses are focused on solid surfaces, suprathermal ions are ejected along the target normal, as observed in the 1980s already [26]. With today's

lasers, this effect is enhanced, leading to huge numbers of multi-MeV protons and highly charged ions [33] with broad angular (typically 40°) and Boltzmann-like energy distributions.

4. Collimated high-energy proton beams in laser direction are observed when focussing ultrahigh-intensity laser pulses on thin foils targets ($\sim 50 \mu\text{m}$) at intensities of $> 10^{19} \text{ W/cm}^2$ [9].

2.3.1 Ion acceleration in gas targets

Two different type of experiments have been reported which observe ion acceleration in underdense plasmas: laser-cluster interactions and laser channeling experiments. Both methods employ gas nozzles to generate the interaction target for the laser pulse.

Clusters: In cluster experiments the gas nozzle is set up in such a way that the gas atoms (e.g. Deuterium) do not come out in a homogenous flow but form large clusters of typically $10^2 - 10^5$ atoms. When these clustered are irradiated by a high intensity laser pulse, the atoms quasi instantaneously stripped to very high charge states [34]. The coupling of laser energy into cluster electrons is extremely efficient and leads to strong intra-cluster space charge fields which in turn ionize the cluster atoms and subsequently lead to a Coulomb explosion. The ions are accelerated by this explosion to energies up and beyond 1MeV [29]. Relatively modest intensities even below 10^{16} W/cm^2 are sufficient to cause this result which makes it possible to use a large focal spot and thereby have a great number of clusters in the interaction region. Several models have been developed to explain these findings (see review in [28]). The nanoplasma model [35] predicts an optimum cluster size for a given pulse duration, and experiments support this assumption [36, 28]. However it cannot explain all measured ion spectra and seems to be inadequate to model the cluster expansion after heating. Ditmire et al. [37] found e.g. for a 2500 atom Xe cluster that its spectrum is reproduced by the self-similar solution of the ion fluid equations for an isotropic, radial expansion for a Xe plasma with a mean charge of 20+ and an electron temperature of 2.5 keV, suggesting that the expansion is driven largely by hydrodynamic pressure. The spatial ion distribution is mainly spherical isotropic since it consists of a great number of point explosion centers. However a moderate anisotropy in the laser polarization direction was reported in [28]. This spatial characteristic does not make this mechanism attractive as an injector for accelerators or similar applications requiring a directed beam. However by using Deuterium clusters the production of fusion neutrons has been demonstrated and an application as neutron point source might seem feasible.

Plasma channel: In an underdense plasma produced in a gas jet or by substantial prepulses on solid targets, relativistic self-focusing and subsequent channel formation take place [38, 21, 24]. This channel provides a larger high-intensity interaction length and electrons can be accelerated by various plasma mechanisms like "Self-modulated Wake Field Acceleration" (SMWFA) or "Direct Laser Acceleration" (DLA) which further depletes the electron density in the channel and increases the quasistatic potential set up by the ponderomotive pressure. This potential will finally cause the channel to undergo a radial Coulomb explosion in which ions are ejected radially outwards from the plasma channel. This radial ion ejection was observed in a couple of experiments which agree well with theoretical predictions from PIC-codes, which estimate for a 1.5-TW pulse in a 30 μm scale length deuterium preplasma, $\sim 4 \times 10^{10}$ ion energies up to 500 keV [30]. Sarkisov et al. [31] observed He-ions up to 500 keV with a 4-TW laser, and Krushelnick et al. [32], using laser intensities of up to $5 \times 10^{19} \text{W}/\text{cm}^2$, measured multi-MeV He-ions.

2.3.2 Ion acceleration from solid bulk targets

Ultra-high intensity laser interaction with solid target does almost never really happen. Even for a good intensity contrast ratio of typically 10^7 a couple of nanoseconds before the main pulse, the focussed prepulse intensity from a main pulse of $10^{19} \text{W}/\text{cm}^2$ still exceeds $10^{12} \text{W}/\text{cm}^2$. When laser pulses are focused on solid surfaces, ions are accelerated to suprathermal velocities in the blow-off plasma at the front side. This effect has been observed with CO_2 lasers in the 1980s already, with ion energies up to 2 MeV/nucleon [26]. Using modern ultrahigh-intensity lasers increases this effect drastically, and huge numbers of multi-MeV protons and highly charged ions have been observed recently [33], namely a few times 10^{11} protons per sr with energies above 4 MeV, which was sufficient for demonstrating the production of various radioactive isotopes in secondary p, n -reactions [20]. The protons and ions produced in this way have a broad angular distribution (typically about 45°) and their spectra exhibit rather complex substructures under a Boltzmann distribution [33]. Additionally ions are accelerated more or less isotropic out of the focal region of the laser pulse where ponderomotive charge separation occurs. Half of these ions stream off ahead of the blow-off plasma, while the other half is accelerated into the bulk of the target where they are stopped. Those ions have been measured using nuclear reactions like $d(d,n)^3\text{He}$ fusion [11].

2.3.3 Ion acceleration from thin foil targets

The most promising way for creating well-collimated high-energy ion beams has been found in the interaction with thin foil targets: When focussing ultrahigh-intensity laser pulses on thin foils high energetic proton beams are observed which exhibit new features [9, 39, 40]:

- (i) $10^{11} - 10^{13}$ well collimated ($\leq 15^\circ$) protons with 5 to 60 MeV are generated,
- (ii) they come from the *rear surface* and move in laser direction,
- (iii) they form a dense, charge-neutralized bunch of ~ 1 ps duration,
- (iv) up to 12% of the laser energy was converted to protons with energies $E > 10$ MeV and up to 30% to energies > 2 MeV [9].

To explain these experimental observations, Hatchett introduced a mechanism called target normal sheath acceleration (TNSA) in [41] which will be explained in detail in the next paragraph. The TNSA-mechanism is the most widely accepted theory to explain the observed high energetic proton acceleration from the backside of a thin foil. It also forms the basis for understanding the ion acceleration observed in the scope of this work.

Target Normal Sheath Acceleration: Target Normal Sheath Acceleration works on the same principal as an ion diode: A cloud of relativistic electrons is expelled by the enormous ponderomotive force of the laser penetrates the target and extends past the rear surface, inducing an ultra-strong space charge field. This field is of the same order of magnitude as the laser fields, i.e. TV/m. Atoms at this surface are ionized and accelerated, but the energetic part of electrons will always leak further out into vacuum and maintain the accelerating gradient as long as the electron temperature is high. At a conversion efficiency of 30 - 40 % [9] and typical temperatures in the order of 2 MeV as (see Sect. 2.2.3) the number of electrons created by a 30 J laser pulse is roughly $N_e \sim 4 \times 10^{13}$. Only the most energetic electrons can escape into the vacuum before the rest is trapped by the resulting Coulomb potential. The electrons penetrate the target with a wide angle of $\sim 45^\circ$, as seen in bremsstrahlung data [41], exit the target rear surface and are turned around. There is recent evidence from [42] and also from this work [43], suggesting that the electrons are turned around again at the front surface and start oscillating, but this is not within the scope of this basic model and is discussed later (see Chapter 8). At a cone angle of 45° the radius of the electron spot at the target rear surface is approximately equal to the target thickness $d \sim 50 \mu\text{m}$.

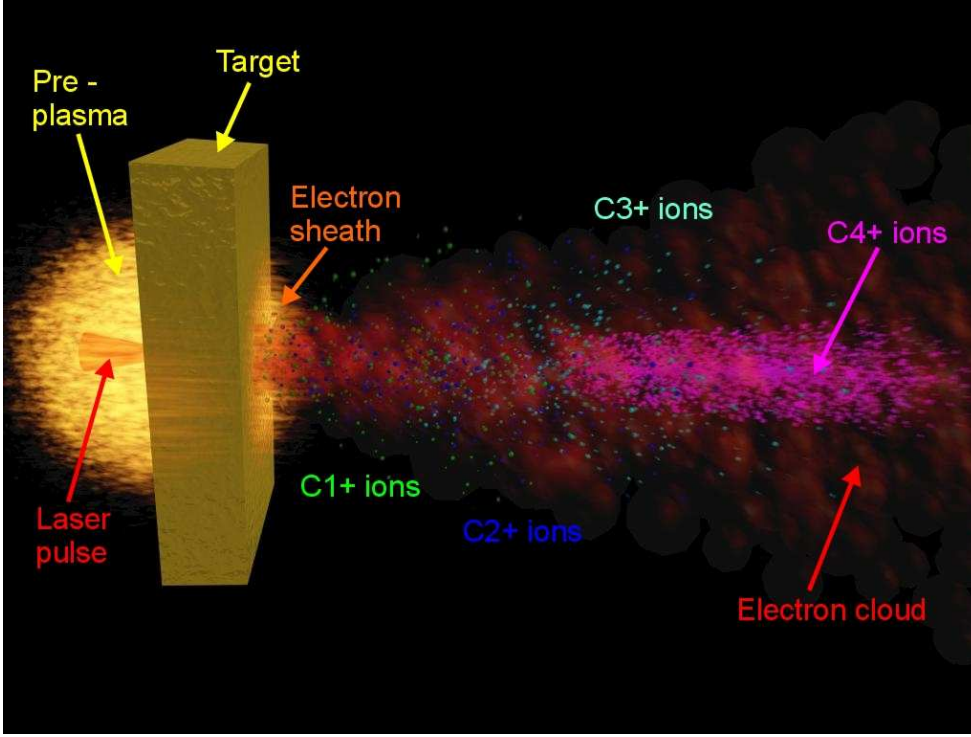


Figure 2.4: Ion acceleration from thin foil targets.

At a pulse duration of $\tau_p \sim 300$ fs the electron density at the back of the target can then be estimated to be

$$(2.19) \quad n_e \approx \frac{N_e}{c\tau_p\pi d^2} \approx 5 \times 10^{19} \text{cm}^{-3}.$$

The TNSA-model assumes the hot electrons to relax to Boltzmann equilibrium, i.e.

$$(2.20) \quad N_e^{hot} \sim \exp\left(\frac{-e\Phi}{kT_e^{hot}}\right).$$

This electron population will set up a sheath at the target rear surface whose scale length l_0 will be given by the Debye length of the hot electrons λ_D . The Debye length of a plasma is defined as the length needed to totally shield an internal electric field [44]. We therefore obtain for the scalelength

$$(2.21) \quad l_0 \equiv \lambda_D = \sqrt{\frac{\epsilon_0 k_B T_e}{e^2 n_e}}.$$

for the parameters used above this expressions evaluates to $l_0 \sim 1.5 \mu\text{m}$. This combination of a high electron density and a relativistic temperature over an extremely short scale length will establish a very strong ambipolar electric sheath field

$$(2.22) \quad E \approx \frac{k_B T_e^{hot}}{e\lambda_D}$$

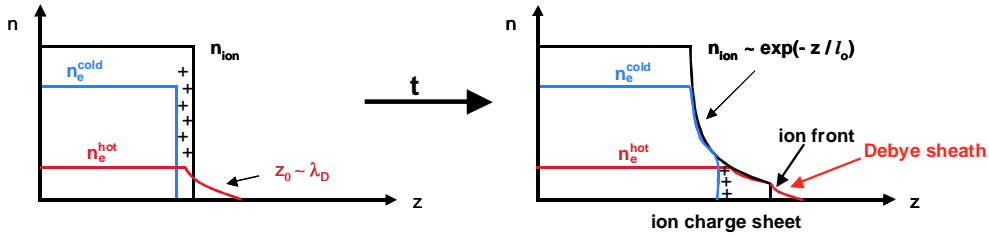


Figure 2.5: Schematics of the TNSA-mechanism

Again substituting the values for our experimental conditions we can expect an accelerating Field E of roughly $E = 1.5$ TV/m. This field is by far larger than the field created by the initially escaping electrons for which the scale length is of the order of the target thickness.

The new feature making this mechanism possible is that the hot electrons are created basically in a delta-function pulse with respect to the plasma expansion time and that the electron ranges are high enough to penetrate the target. Furthermore this mechanism works only at the rear surface. The electron cloud lasts only for a finite and very brief time. The accelerating field scales with the plasma scale length which at the front side is on the order of 100 microns due to the plasma creation by the foot of the laser pulse (prepulse). Therefore while the potential is basically the same at the front and rear surface the fields at the front are substantially lower. This would not matter if the life time of the field was arbitrarily long and the ions had time to fall through the whole potential. Due to the finite duration of the hot electron pulse however the potential changes and decreases by cooling effects before the front side protons are able to reach high energies [45].

Once created the field will ionize and accelerate the protons on the surface. The ions start moving outwards while the cold electron population is pushed back into the target at ion densities lower than the hot electron density as shown in Fig. 2.5. Further out the hot electron density will fall with the ion density maintaining a local quasineutrality that is also observed in PIC-code simulations (see Chapter 9). According to the TNSA-model quasineutrality is maintained until the *local* hot electron Debye length becomes greater than the local ion scale length. There, an electron sheath is retained whose charge is balanced by a positive charge sheet which forms where the cold electrons have been excluded. Between the sheath and the positive charge sheet a region of roughly constant E -field persists for a few times the laser pulse duration.

Ion acceleration: The TNSA-model was developed to explain the observed high proton energies and does not take into account other ions with multiple charge states.

However this turns out to be important not only for the consideration of ion acceleration but for the model as a whole. Because what happens as soon as multiple charge states and masses are present, is that the ions with the highest charge-to-mass ratio will out-accelerate the other ions and screen the accelerating fields for everything behind them. This effect is strong enough to positively inhibit the acceleration of all other ion species as soon as protons are present. To accelerate heavier ions it was therefore important to find a way to experiment with a proton free target. As is discussed in Chapter 7 that can not be achieved by simply choosing the right target material but requires a dedicated cleaning procedure. The same screening effects of course hold true for every other ion population as well leading to a field that is much less quasistatic and constant than assumed in TNSA. While it is still quasistatic with respect to the laser frequency it nevertheless displays a highly dynamic behavior, with the region of highest field strength moving outwards in vacuum during the course of the acceleration, as we are able to show by our data analysis presented in Chapter 8. Furthermore the field at the target surface never reaches the maximum field strength since it is pinned at a value defined by the field ionization value of the first charge state. The field ramps up to that first ionization value. When now an additional fast electron joins the population setting up the field the threshold is crossed and an atom is ionized. The freed electron is pushed into the target by field, leaving the positive ion charge to balance the new electron that caused the ionization. At the surface where there is an infinite supply of ions the field can therefore never substantially exceed that first ionization threshold. However, as soon as one moves outwards this condition does not hold anymore and the field increases. As our simulations show this increase happens on very small spatial and temporal scales (nm and fs), i.e. very small compared to relevant scales for TNSA. Therefore these effects can be neglected in first order and the TNSA-model is well suited to predict the limits of the acceleration process, i.e. the parameters responsible for the high energies of the particles with the highest charge-to-mass ratio .

Front-surface Mechanism: Another mechanism was proposed by Maksimchuk in [46] and Krushelnick in [39, 47] to explain the acceleration of high energetic protons and deuterons from thin foils. This mechanism assumes acceleration on the target front side by the space charge fields generated when hot electrons disappear from the dense plasma into the solid material. In this mechanism the ions are pushed through the target, much as the relativistic electrons in TNSA. Measurements of the ring structures in the proton beam are explained by proton deflection by magnetic fields inside the target. While there is no doubt that indeed both a front and a rear surface mechanism exists there is an ongoing discussion which of the two is responsible for the really high energies beyond ~ 10 MeV. Most experimental evidence suggests that it is the rear

surface mechanism. It has e.g. been shown that the accelerated protons are influenced by a structure *on* the rear surface but not by one very close *behind* it. Also simulations [48] show that the ion population from the front shows much lower energies (< 5 MeV) and are less collimated. The presented work shows by demonstrating ion acceleration out of well defined source layers on the *rear surface* that an effective rear surface mechanism exists that produces well collimated high energy ion beams.

2.3.4 Ion acceleration by long-pulse lasers

For completeness and better distinction the traditional laser ion acceleration mechanism is briefly summarized. For over 25 years now, energetic protons and heavier ions have been generated by focusing \sim ns-pulses from large CO_2 and Nd:glass lasers, on solid targets at intensities of $10^{14} - 10^{16} \text{W/cm}^2$. The accelerated ions showed a very broad distribution in energy as well as a large emittance and could therefore not be put to any further use. In those experiments one focusses a high-energy ns-pulse on a target, e.g. a foil, bulk material or glass micro-balloon targets for fusion studies. Thereby a hot coronal plasma is created, which expands into the vacuum. The expansion proceeds radially outward in an isothermal, self-similar fashion,

$$(2.23) \quad n_{ion} \sim \exp(-r/c_s t)$$

with ions being fed into the expanding corona by a rarefaction wave propagating at the sound speed, c_s , into the bulk plasma. The ions are accelerated by the electric field present in the quasi-neutral expanding plasma,

$$(2.24) \quad E \sim -\frac{kT_{hot}}{e} \frac{\partial n_{ion}}{\partial r},$$

where r is the distance from the laser focus center. In these experiments ions, mostly originating from the target front, moved against the laser direction and showed a very large dispersion ($\sim 90^\circ$). Typical energies were ~ 100 keV/nucleon for sub-kJ lasers and up to 2MeV for protons from kJ-systems. Ion acceleration from the rear surface in laser direction was a minor effect only. Begay et al. [5] reported ion acceleration from the rear surface in laser direction from wire targets, but the signal vanished almost completely when the contaminating hydrocarbons were removed. In another experiment on the Asterix iodine laser at MPQ¹ Tsakiris et al. [4] observed ions in laser direction from thin foil targets but only for foil thicknesses beyond a few μm , i.e. the foil is thin enough that the whole foil is heated at once and the expansion can

¹Asterix was decommissioned at MPQ in 1996 and is currently set up again as PALS (Prague Asterix Laser System) in Prague.

proceed spherically in all directions. When using thicker foils on the other hand the still cold bulk of the foil hinders the expansion in that directions and the ions are not energetic enough to penetrate the foil.

The main difference to present experiments lies in the timescales. In ns-laser experiments the acceleration occurs simultaneously with the laser-plasma interaction. Both processes are necessarily coupled meaning that the stochastic and chaotic plasma behavior imprints itself on the ion signal. Using short-pulse lasers, it appears that ion acceleration can be largely decoupled from the details of the laser-plasma interactions at the front of the target over a broad range of conditions. Though of course at later times a isothermal expansion occurs, the conditions at the ion front are *not* isothermal and quasineutral and therefore the self-similar model (e.g. [49]) cannot be applied to explain the high ion energies. The same is true for the charge state distribution. In long-pulse laser interactions the atoms are ionized due to target heating, i.e. collisionally, and the temperature is maintained over a long time, leading to an almost complete ionization in the highest charge state (e.g. C^{6+}). The measured charge state distribution is than created by recombination processes and consequently all charge states show the same cutoff energy, as can be seen in Fig. 2.6.

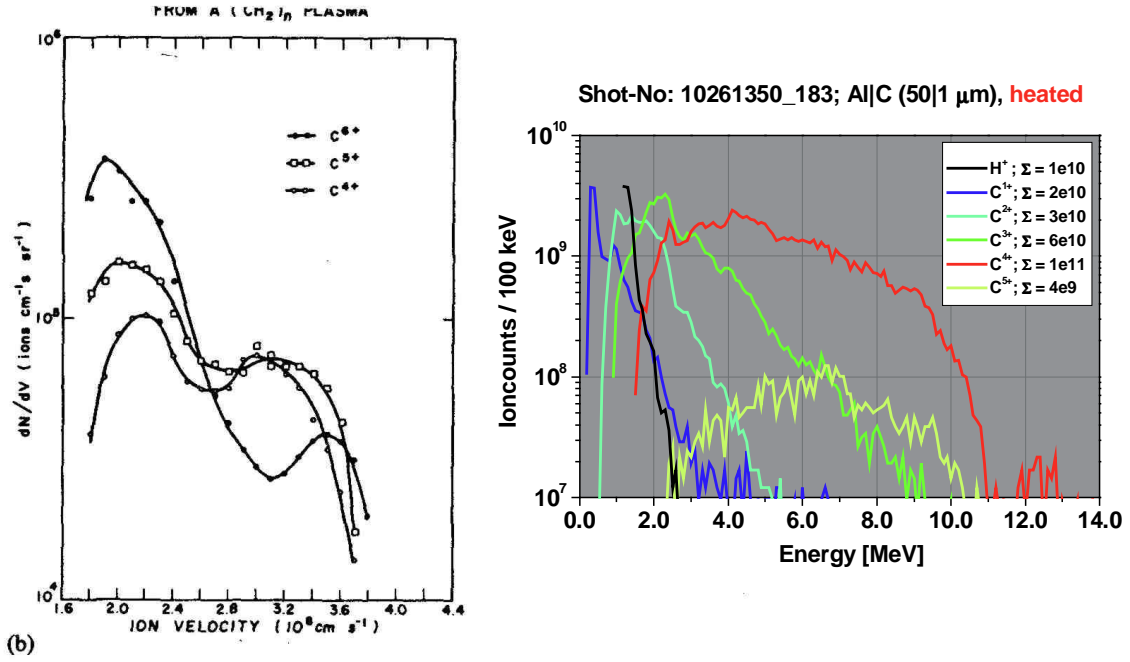


FIG. 1. (a) The energy distributions of ionic species from a polyethylene plasma and (b) the corresponding velocity distributions of the carbon ions.

Figure 2.6: Comparison of charge state distributions for laser accelerated ions from long-pulse experiments (left) [3] and short-pulse experiments (right) [43]: In the long-pulse case all carbon charge states have the same cutoff velocity, suggesting collisional ionization to the highest charge state followed by recombination after the acceleration process. In the short-pulse case the cutoff energy increases with charge state suggesting field ionization and freezing of the charge state distribution by rapid expansion. The expansion velocity of the ion front is a factor 5 faster than in the long pulse case.

Chapter 3

Ionization Mechanisms and Recombination at the target rear-surface

The topic of this work is the acceleration of ions by means of laser pulses. But the laser is fired not at a plasma of ionized atoms but at a solid target, so an important question in understanding the complete process is "How are the ions created in the first place?". Which ionization mechanisms play a role and in how far is the time integrated charge state distribution measured in the spectrometer representative for the charge state distribution during the acceleration stage.

Therefore this chapter looks at the basic ionization and recombination processes which might play a role at the experimental conditions present in our experiment. The important ionization processes are "Field Ionization by Barrier Suppression" (FIBS) and "Collisional Ionization" (CI) by the ambient electron populations. Another process to bear in mind is recombination and charge exchange of ions on their way to the spectrometer, to be able to judge in how far the measured charge state distributions may have changed since their respective birth. The contributions of all three processes are analyzed by analytical estimates as well as by using a numerical model, the FLY-code.

3.1 Direct Ionization of rear surface atoms by the Laser Pulse

One possible source of ionization is of course the laser pulse itself. The fields in the focal region reach many times the strength necessary to ionize the target atoms. However,

with regard to the ion signal the region of interest is the rear surface of the target, while the laser is interacting with the front surface. By employing an interferometric diagnostic described in Sect. 4.2.1, we can directly observe the laser interaction and the plasma conditions on both sides of the target. The target's thickness in the experiment was chosen such that the laser pulse is completely absorbed in the preplasma and prevents shock-breakout until well after the interaction time (10ns).

We can therefore rule out ionization by the laser pulse or by a shock front, which leaves us with field ionization by the strong quasistatic fields and collisional ionization due to the ambient electrons as possible ionization sources. These mechanisms are discussed in the following paragraphs.

3.2 Field Ionization by Barrier Suppression by ultra-strong Electric Fields

As was shown in Chapter 2, the electric fields in the laser focus are by far stronger than the atomic field in a hydrogen atom. Furthermore, the fields on the backside of the target predicted by the TNSA-model are of the same order of magnitude. The fact that TV/m fields, capable of field ionization, are present has been shown in several publications in the last years experimentally [50, 51, 52], with simulations [45, 48] and analytical estimates [41, 53, 54]. Given the laser parameters, electron acceleration by ponderomotive force as well as plasma acceleration mechanisms yield typical values of $k_B T_e \sim 2MeV$ and $n_e \sim 10^{19}cm^{-3}$. The maximum amplitude of the resulting electric fields can be easily estimated from that charge distribution e.g. by the TNSA equation or in more detail by solving Poisson's equation for different time steps as in our 1D-kinetic model described in Chapter 8. The results from the 1D-PIC-code presented in the same chapter even include electric fields within the target, especially at interfaces. The duration of the maximal field at the rear surface is on the order of the laser pulse length, i.e. as long as hot electrons are supplied. In order to describe the ionization by a strong external field, a number of models has been developed in the past. However, all these models assume fields of approximately the same strength as the binding atomic field of the electron in question, while the fields in our experiments are one to two orders of magnitude stronger. That means that the predictions made by those models compose a very conservative estimation and a lower threshold, while the real contributions of field ionization may be considerably higher.

Different models for field ionization exist, having their origin in the different possibilities in describing the ionization in strong external fields. The most direct way to do this lies in solving the time-dependent Schrödinger Equation numerically, as done by Bauer

and described in [55]. This method as well as the "Density-Functional Theory" [56, 57] and the "time-dependent Hartree-Fock theory" [58] require a large numerical effort. A different approach was chosen by Keldysh [59], Faisal [60] and Reiss [61], who describe the amplitude of the transition probability of the original Coulomb-state in a Volkov-state [62]. From this model as well as from the quantum mechanical model from Ammosov, Delone, and Krainov (ADK-model) [63], and the classical model from Posthumus [64], analytical rate equations can be obtained. In the following these rate equations are used to get an estimation of the contribution of field ionization in our experiments. Furthermore, the results are compared to the much more detailed numerical solutions obtained by Bauer [55] and found to be in good agreement for our parameters.

As an example the two models used by the codes presented in later chapters are described in more detail. This is first the Barrier Suppression Ionization (BSI) model which is used in our 1D-kinetic code and then the ADK-model which is used to get an analytical estimate and also in the 1D-PIC code by Pfund and Kemp [65] which was used to model different subsets of the interaction process (see Chapter 8).

3.2.1 FIBS-Model

Field Ionization by Barrier Suppression (FIBS) is the most simple model to be considered. The basic idea is that an external electric field deforms the Coulomb potential of the atom as shown in Fig. 3.1. As soon as the external field exceeds a certain threshold, defined by the binding energy of the electron, the barrier is lowered below the electron state and this electron finds itself in the continuum and is thus instantly ionized. To calculate the threshold value one starts considering the effective potential that acts on the electron. In the case of a Coulomb potential it is of the form

$$(3.1) \quad U(x, t) = -\frac{eZ}{4\pi\epsilon_0 x} + x E(t).$$

Here E is the time-dependent external electric field and the x-axis is lying in the direction of that field. For the maximal field E_{max} at $t = t_{max}$, the maximum of the potential is defined by

$$(3.2) \quad \frac{dU(x)}{dx} = \frac{eZ}{4\pi\epsilon_0 x^2} + E_{max} = 0, \implies x = \pm \sqrt{\frac{eZ}{4\pi\epsilon_0 E_{max}}}.$$

Substituting the result of (3.2) in (3.1) we obtain

$$(3.3) \quad U = 2\sqrt{\frac{eZE}{4\pi\epsilon_0}},$$

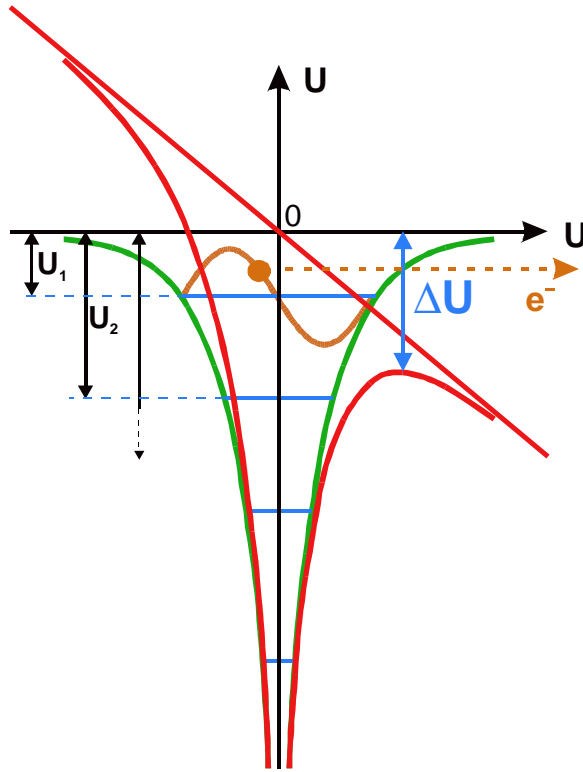


Figure 3.1: Field Ionization by Barrier Suppression: An external electric field disturbs and suppresses the Coulomb barrier of an atom. An electron at the potential U_1 is bound in the unperturbed potential (green). The external field depresses the barrier by the amount ΔU so that the electron suddenly finds itself at an energy higher than the new disturbed potential (red).

With U_k as the binding energy of the k -th charge state we then obtain the threshold condition for the external electric field as:

$$(3.4) \quad E_k = \frac{U_k^2 \epsilon_0 \pi}{eZ} .$$

For the C^{4+} charge state for example, which has a binding energy of 64.5 eV the threshold for the electric field is at ~ 0.2 TV/m. Since the fields predicted by the TNSA-model are of the order of 2 TV/m, i.e. one order of magnitude higher, one can expect a very rapid field ionization of C^{4+} .

3.2.2 Keldysh-Model

As explained above, Keldysh perturbatively calculated the transition rate from a bound electron to a free electron oscillating in a laser field, which is called a nonperturbative Volkov state. Using the Keldysh formula as given in [54] we obtain for the ionization

rate

$$(3.5) \quad W_K = 4\omega_a \left(\frac{U_k}{U_H} \right)^{1/2} \frac{E_a}{E} \exp \left[-\frac{2}{3} \left(\frac{U_k}{U_H} \right)^{3/2} \frac{E_a}{E} \right],$$

where $E = 2\text{TV/m}$ (from (2.22)) is the ionizing field, $E_{at} = \frac{e}{4\pi\epsilon_0 a_b^2} = 0.51 \text{ TV/m}$ is the atomic electric field and U_H and U_k are the ionization potentials of hydrogen and the ionized electron, respectively. An important feature of the Keldysh theory is that the ionization rate is determined more by the properties of the outgoing electron than by the details of the atomic structure [66]. The Keldysh theory does not include any species dependence into the rate equation.

3.2.3 ADK-Model

A different treatment of the problem can already be found in the book by Landau [67]. There the ionization rate for a hydrogen atom in a static electric field E is deduced as

$$(3.6) \quad W_L = 4 \left(\frac{U_k}{U_H} \right)^{5/2} \frac{E_a}{E} \exp \left[-\frac{2}{3} \left(\frac{U_k}{U_H} \right)^{3/2} \frac{E_a}{E} \right].$$

This rate follows from the tunneling probability of the electron through the Coulomb-barrier (reduced by the electric field). Ammosov, Delone, and Krainov extended this theory for larger atoms with a higher number of charge states. The resulting field ionization rate due to the ADK-model [63] is then given by:

$$(3.7) \quad W_{ADK} = C_{n^*l}^2 \left(\frac{3}{\pi} \frac{E}{E_a} \left(\frac{U_H}{U_k} \right)^{3/2} \right)^{1/2} U f(l, m) \times \left(\frac{2E_a}{E} \left(\frac{U_k}{U_H} \right)^{3/2} \right)^{2n^* - |m| - 1} \exp \left(-\frac{2}{3} \left(\frac{U_k}{U_H} \right)^{3/2} \frac{E_a}{E} \right),$$

with

$$(3.8) \quad C_{n^*l} = \left(\frac{2e}{n^*} \right)^{n^*} \frac{1}{(2\pi n^*)^{1/2}}, \quad f(l, m) = \frac{(2l+1)(l+|m|)!}{2^{|m|} |m|! (l-|m|)!},$$

n^* is an effective quantum number, l and m are angular and magnetic quantum numbers and e in the coefficient C_{n^*l} is Euler's number 2.71828... . The ADK-model does include atomic structure via terms $f(l, m)$ and C_{n^*l} . For a more detailed description of the model see [63, 66]. Incorporating Krainov's extension to incorporate FIBS [68] and using the implementation of Penetrante and Bardsley [69], the ionization rate can be written as:

$$\begin{aligned}
(3.9) \quad W_{ADK} &\approx 6.6 \times 10^{16} \frac{Z^2}{n_{ef}^{4.5}} \left(10.87 \frac{Z^3}{n_{ef}^4} \left(\frac{E_a}{E} \right)^{1/2} \right)^{2n_{ef}-1.5} \\
&\times \exp \left[-\frac{2Z^3}{3n_{ef}^3} \left(\frac{E_a}{E} \right)^{1/2} \right] t ,
\end{aligned}$$

where Z is the charge of the created ion, t is the time, and $n_{ef} = Z/\sqrt{U_k/U_H}$.

3.3 Collisional Ionization

Theoretical Estimates on the Collisional Ionization Rates

By the laser plasma interaction on the front side, large amounts of hot electrons are accelerated which penetrate through the target and reach the back surface. The hot electrons exit the target rear surface and only the most energetic escape the target completely, while the majority will be drawn back by space charge effects and hit the target rear surface again. Recent experiments by Mackinnon et al. [42] even suggest extensive oscillations in the target. Furthermore these electrons draw colder return currents in the opposite direction. All these electrons can and will ionize atoms they encounter, however mostly within the target. To analyze the ion spectra it is important to know the contribution of collisional ionization to the back surface ions, since only those are accelerated. The ionization within the target is a more complex problem which is difficult to address experimentally but is part of the studies performed by PIC-codes.

Electron-atom collisions can be divided into soft or distant collisions with a large impact parameter and hard or close collisions with small impact parameter. The Mott theory [70] accounts for hard collisions as between two electrons but not for soft collisions [71]. As was shown by Bethe, soft collisions essentially take place by dipole interaction between the incident electron and the target electron [72]. A combined model valid for energies from ionization the ionization threshold to the keV range was developed by Kim in [73] and extended to the high energy MeV-range by Tikhonchuk in [54]. This model is used to estimate the amount of collisional ionization for the relevant range of parameters.

3.3.1 Collisional Ionization by the hot electron component: Analytical Estimate

From the TNSA-model of Chapter 2 we know that we have to expect a hot electron component with a temperature of ~ 2 MeV at a density of $\sim 10^{19}$ cm $^{-3}$. The cross sections for ionization by electron impact are well known. An estimate of the contribution of this electron component to the overall ionization balance can be obtained from [54]:

$$(3.10) \quad W_{col} \approx 4\pi a_b^2 n_e v_e t \frac{U_H^2}{U_k k_B T_e} \ln \left(\frac{k_B T_e}{U_k} \right).$$

where a_b is the Bohr radius, v_e is the electron velocity and U_k and U_H are the ionization potentials of the ionized species and hydrogen, respectively. The results are collected in Sect. 3.5 where they are compared to the field ionization contributions as well as to the numerical results calculated by the FLY-code.

3.3.2 Collisional Ionization by cold electrons in return currents : Analytical Estimate

The hot electron component drives return currents in the target in order to stay below the Alfvén-limit. Measurements by Gremillet et al. [74] and simulations by Ruhl [75] suggest temperatures on the order of tens of eV for those return currents. The contribution to the ionization balance return current heating can easily be estimated. The return current with a temperature $k_B T_e^{ret} \sim 50$ eV, which must balance the hot electron flow, i.e.

$$(3.11) \quad n_e^{ret} v_e^{ret} \simeq n_e^{hot} v_e^{hot} \Rightarrow n_e^{ret} \sim \frac{n_e^{hot} v_e^{hot}}{v_e^{ret}} \sim n_e^{hot} \sqrt{\frac{T_e^{hot}}{T_e^{ret}}}.$$

While the ionization rates due to a 50 eV electron component at 100 times higher density are clearly much higher than those due to the hot component, one has to take into account the interaction times as well. The hot component can ionize the surface atoms on the rear for as long as hot electrons are supplied from the laser interaction region, i.e. for the duration of the laser pulse. The cold electrons however are pushed into the target by the quasistatic electric field on the back surface as soon as it gains some strength. When this field is strong enough to start ionizing carbon it is on the order of several GV/m, which is still more than three orders of magnitude below its maximum. While the cold electrons will be pushed back into the target, the surface ions will be accelerated outwards. The resulting overlap time of a 50eV electron and a

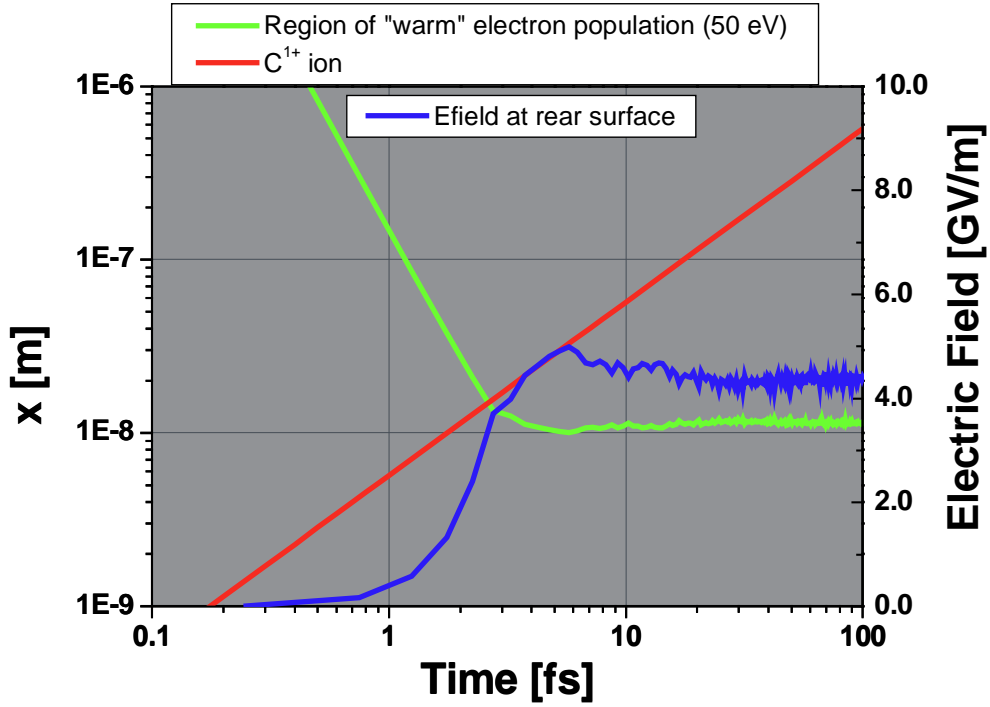


Figure 3.2: In the presence of a comparatively weak field of $\sim 10^9\text{V/m}$, a cold electron component is pushed back into the target, while C^{1+} -ions on the surface are accelerated outward. The mutual overlap time is less than 2 fs. The field is calculated by selfconsistently solving Poisson's equation using our 1D-kinetic code (Chapter 8).

C^{1+} -ion both initially at rest in presence of this comparatively low field of $\sim 10^9\text{V/m}$ is less than 2fs as can be seen in Fig. 3.2. A higher collisional ionization frequency due to lower temperatures is therefore immediately compensated for by a decreasing interaction time.

3.4 Numerical Model of Collisional Ionization and Recombination Processes using the FLY-code

In addition to the simple analytical estimates the numerical FLY-code [76] can be used to simulate collisional ionization and recombination with time-dependent electron density $n_e(t)$, and ion density $n_i(t)$, and an equally time-dependent electron temperature $T_{hot}(t)$.

For a model case of a typically measured C^{4+} -spectrum there is no significant transfer to other charge states due to collisional ionization or recombination. The simulation starts with solid state density at the target rear surface, n_i in the adjacent half space

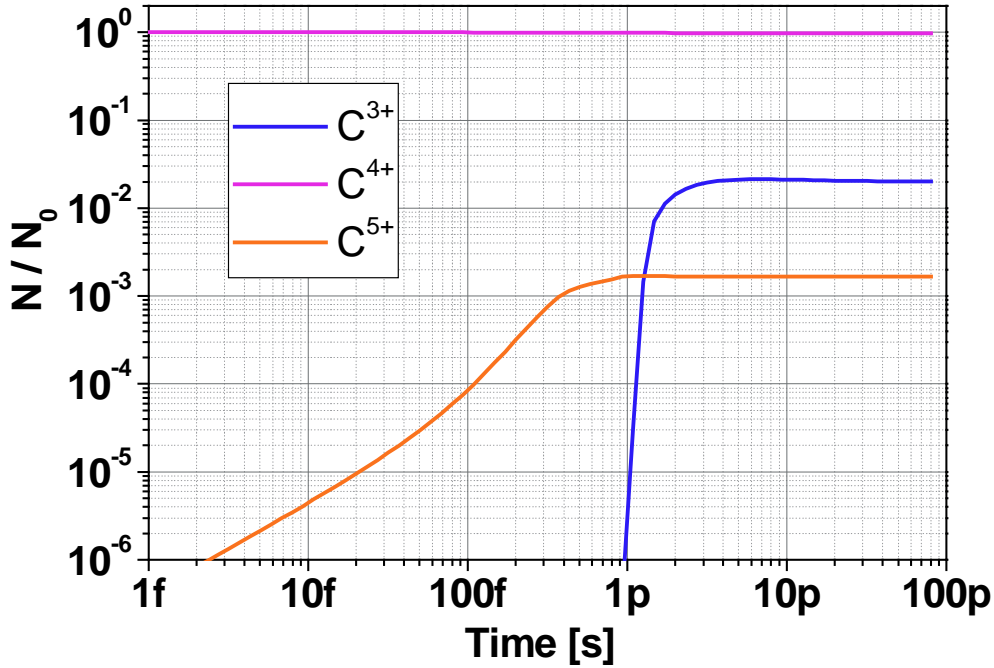


Figure 3.3: Charge transfer due to electrons in a laser accelerated C^{4+} -ion cloud from the time it leaves the target till it reaches the Thomson parabola-spectrometer. The transfer rates are calculated by the FLY-code. Electron and ion densities and temperatures are fully time-dependent.

follows from velocity dispersion and angular divergence; n_e is assumed to rise with the laser pulse up to $2.5 \times 10^{19} \text{ cm}^{-3}$ and fall again to $\bar{q}n_i$, where \bar{q} is the local average ion charge, to finally assure quasi-neutrality of the plasma cloud. T_{hot} is estimated from the modelled acceleration fields via (2.22). The total recombination and collisional ionization rates, integrated along the path to the detector are in the range of 1% and 0.1%, respectively, as can be seen in Fig. 3.3. For the hot electron component this small level of collisional ionization is to be expected.

3.5 Efficiencies of Field Ionization and Collisional Ionization in ultrahigh-intensity laser ion acceleration

Having discussed the different possible mechanisms one can now evaluate each mechanisms contribution to the observed charge state distribution. First one has to bear in mind that the region of interest is the backside of the target foil, there is the origin of

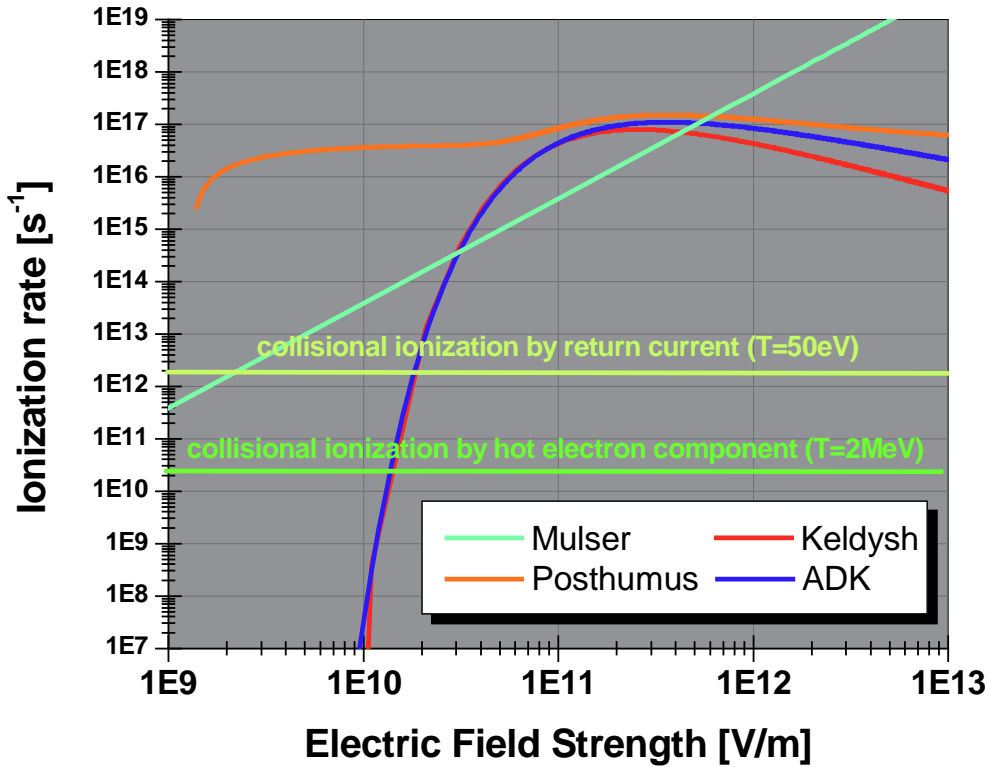


Figure 3.4: Ionization rates for C^{1+} in a strong external electric field according to the numerical model of Mulser (cyan) and the analytical models by Keldysh (red), Posthumus (orange), and ADK (blue). The horizontal lines show the ionization rates due to collisional ionization by the hot (2 MeV) electron component (green) and the cold (50 eV) return current (yellow).

the observed ion signal.

Direct ionization by the laser can be ruled out as explained in Sect. 3.1. Models for both collisional ionization and field ionization are explained above and Fig. 3.4 shows the respective ionization rates for C^{1+} in an external electric field due to the analytical Keldysh, Posthumus and ADK models as well as for the numerical model developed by Mulser and Bauer [55]. Also shown are the collisional rates due to a hot electron population of ~ 2 MeV as predicted by the TNSA-model with a density of 10^{19} cm^{-3} and the due to the return current necessary to compensate that current. The return current is assumed to have a temperature of 50 eV and with (3.11) follows a density of $\sim 2 \times 10^{21} \text{ cm}^{-3}$.

It is obvious, that no matter which of the field ionization models is used, at the relevant electric field strength FIBS is by many orders of magnitude more effective than collisional ionization by the electrons. One also has to remember that the field ionization rates are just lower boundary estimates since the fields are still higher than normally considered in most of the theories which account for example for effects as tunneling

Table 3.1: Calculated field and ionization parameters for carbon. Q denotes the charge state, U_k is the ionization potential of the k^{th} ionic charge state and E_k is the corresponding field strength (3.4). E_k^{max} is the maximal E-field, t_k^{min} is the minimal field duration and l_k^{min} is the minimal acceleration length for given k . W are the ionization rates due to the hot electrons ($k_B T_e^{hot} \sim 2\text{MeV}$, $n_e^{hot} \sim 2.5 \times 10^{19} \text{cm}^{-3}$), the return current ($k_B T_e^{ret} \sim 50 \text{eV}$, $n_e^{ret} \sim 2.5 \times 10^{21} \text{cm}^{-3}$) and the field ionization ($E_f = 2\text{TV/m}$).

Q	U_k [eV]	$W_{col,hot}$ /ps	$W_{col,ret}$ /ps	W_{ADK} /ps
1	11.16	$2.53 \cdot 10^{-2}$	2.13	$5.93 \cdot 10^4$
2	24.38	$1.1 \cdot 10^{-2}$	0.68	$2.65 \cdot 10^5$
3	47.89	$5.29 \cdot 10^{-3}$	0.21	$1.46 \cdot 10^6$
4	64.5	$3.28 \cdot 10^{-3}$	0.11	$4.62 \cdot 10^6$
5	392.09	$5.29 \cdot 10^{-4}$	–	$8.5 \cdot 10^{-5}$
6	490.00	$4.14 \cdot 10^{-4}$	–	$7.03 \cdot 10^{-9}$

through the Coulomb barrier. However at the field strength present the potential barrier is lowered by such a large amount that the electrons are above the barrier anyway and tunneling is not necessary. The numerical model of Bauer accounts for that and as one can see at high field strength on the order of TV/m the respective curve (cyan) lies again considerably higher than the analytical predictions.

While the curves shown in Fig. 3.4 are computed just for the C^{1+} charge state, Tab. 3.1 lists the ionization rates for all carbon charge states due to field ionization (using the ADK-model), collisional ionization by hot electrons and by the return current. The calculations show that field ionization is orders of magnitude more effective than collisional ionization with ionization frequencies of $\sim 10^6 \text{ps}^{-1}$. The collisional ionization frequencies are more than six orders of magnitude lower, meaning that every ion which experiences a field is more or less instantly ionized by it. For the C^{5+} -case however the collisional ionization frequency is about an order of magnitude higher than the field ionization frequency. The number of collisionally ionized C^{5+} is given by $N_{5+} = \nu_{col}^{5+} \tau_e N_e$, with $\nu_{col}^{5+} = 5.3 \cdot 10^{-4} \text{ps}^{-1}$, $\tau_e \sim \tau_{laser} = 350 \text{fs}$, and $N_e = n_e V = n_e \pi r^2 \tau_e v_e$, with radius $r \sim 50 \mu\text{m}$, $n_e \sim 2 \times 10^{19} \text{cm}^{-3}$, $v_e \sim c$. This yields a $N_{5+} \sim 4 \times 10^9$ and is in good agreement with the measured number of $\sim 4.5 \times 10^9$.

In the limit that only FIBS takes place, our model so far predicts sharp low-energy cutoffs for each species. Note that this is qualitatively different from previous work with long-pulse, isothermal expansion, for which ion spectra are continuous and rising towards zero energy. In some shots such cutoffs are seen while for others the low-energy cutoff is determined by detector properties. In the presented carbon measurement we

observe a rolloff of the C^{4+} and C^{5+} charge states at low energies and for C^{5+} we observe a high-energy cutoff that seems not to scale with q . This does not fit into the basic picture of TNSA but is reasonable due to a small degree of collisional ionization.

In conclusion the analytical as well as numerical models show that collisional ionization is far less effective than field ionization. The collisional ionization frequencies are more than six orders of magnitude lower ($W_{col} \sim ps^{-1} 10^{-3} - 10^0 ps^{-1}$), meaning that every ion, once exposed to the space-charge field is quasi instantly ionized. For C^{5+} or other hydrogen-like charge states however, the collisional ionization frequency is about an order of magnitude higher than the field ionization frequency. The C^{5+} distribution could thereby be created to a significant part by field ionization, though short spikes and fluctuations in the field as seen in some PIC-simulations may also play a role.

Its decay is not completely understood yet and takes possibly much longer. The main question for determining the dominant ionization mechanism therefore has to be which possible mechanism is the most effective for the given conditions. To that purpose in the first version of the paper we presented a FLY-simulation, showing that for a population of C^{4+} ions there is no significant transfer to other charge states due to collisional ionization and recombination.

Chapter 4

Experimental Realization of Laser-induced Ion Acceleration

The experiments this work is based upon were carried out at the 100-TW laser at the Laboratoire pour l'Utilisation des Lasers Intenses (LULI). They were part of three experimental campaigns of two weeks each in October 2000, May 2001, and August 2001. A fourth campaign January 2002 as well as a two weeks beamtime at the Trident facility at the Los Alamos National Laboratory did not include heavy ion experiments but yielded some data on the ion origin as well as general beam characteristics. The LULI 100 TW laser is a single-shot high energy glass laser and delivers pulses of $W_p \sim 30$ J with a pulse length $\tau_p \sim 300$ fs at a wavelength $\lambda_p = 1.057 \mu m$. These pulses are focused at normal incidence on thin foil targets to an intensity of up to 5×10^{19} W/cm². The contrast, i.e. the peak-to-pedestal intensity ratio, amounts to $\sim 10^7$ at 1.5 ns before the main pulse. This corresponds to an energy contrast of $\sim 10^{-4}$. The complete laser system, and the exact experimental setup including the used diagnostics and targets are described in the following paragraphs. The Trident shortpulse system is of similar design, and all its working principles and basic setup are analogous to the LULI system, therefore no extra section describing the Trident laser is included. The main differences are a slightly longer pulse duration (~ 600 fs) and slightly higher pulse energy (up to 40 J) at Trident. Due to the fact that the pulse compression is done in air the focussability of the pulse is limited to about three times the diffraction limit. This combined with the longer pulse length leads to slightly lower intensities on target of $\sim 10^{19}$ W/cm².

4.1 Ultra-high-intensity lasers for ion acceleration: The LULI 100 TW Laser System

With advent of high-intensity lasers based on "chirped pulse amplification" (CPA)[7] a new class of lasers became available. These lasers deliver pulse energies of 1 to 1000 J in pulses between 30 and 500 fs, thus achieving intensities of well above 10^{19} W/cm². Today two basic types of high-intensity lasers exist: The Ti:Sapphire type lasers, like ATLAS at the MPQ, with typical pulse durations of tens of fs and pulse energies in the 1-Joule range. These lasers have the advantage of high repetition rates of usually 10 Hz. Ti:Sapphire lasers can today achieve powers of up to 100 TW (3 J in 30 fs) which can be focussed to intensities of up to 10^{20} W/cm². The second type are huge Nd:Glass lasers, capable of delivering up to 1 kJ in pulses of typically half a picosecond. The higher energy as well as the longer pulse duration are both due to the amplifier material. Glass amplifiers can be build big enough to extract huge amounts of energy but the reduced bandwidth in the gain curve limits the pulse duration of pure Nd:glass systems to about half a picosecond. Furthermore, these systems are single-shot lasers, with repetition rate usually not above 1 shot/hour. So far, the now dismantled Livermore Petawatt-laser holds the record in power (as the name says 1 PW: 500 J in 500 fs) as well as in intensity ($>10^{21}$ W/cm²), though systems of up to 5 kJ are currently under construction.

Though some experiments were performed on the MPQ's Ti:Sapphire system ATLAS, which is described in detail in [77] the bulk of the experiments were performed with the 100-TW laser at the Laboratoire pour l'Utilisation des Lasers Intenses (LULI) [78] which is described in the following paragraphs. The LULI 100 TW laser is a kind of a hybrid laser of the two types discussed above, though leaning more towards the glass-lasers. By using a Ti:Sapphire oscillator together with mixed-glass amplifiers, pulses down to 300fs with energies of up to 30 J on target (100 TW) can be achieved. The laser can theoretically be fired every 20 minutes though to obtain a good quality beam a 40 minute interval is more realistic.

4.1.1 The Oscillator

The LULI 100-TW laser utilizes a commercial Ti:Sapphire oscillator with Kerr-lens mode-locking [79, 80]. This oscillator delivers an 80 MHz train of pulses with a duration $\Delta\tau = 80$ fs at $\lambda = 1057$ nm. For Gaussian laser pulses the relation between the pulse duration $\Delta\tau$ and the spectral width $\Delta\lambda$ at FWHM is defined by

$$(4.1) \quad \Delta\tau\Delta\lambda \geq \frac{2\ln 2}{\pi} \frac{\lambda^2}{c}$$

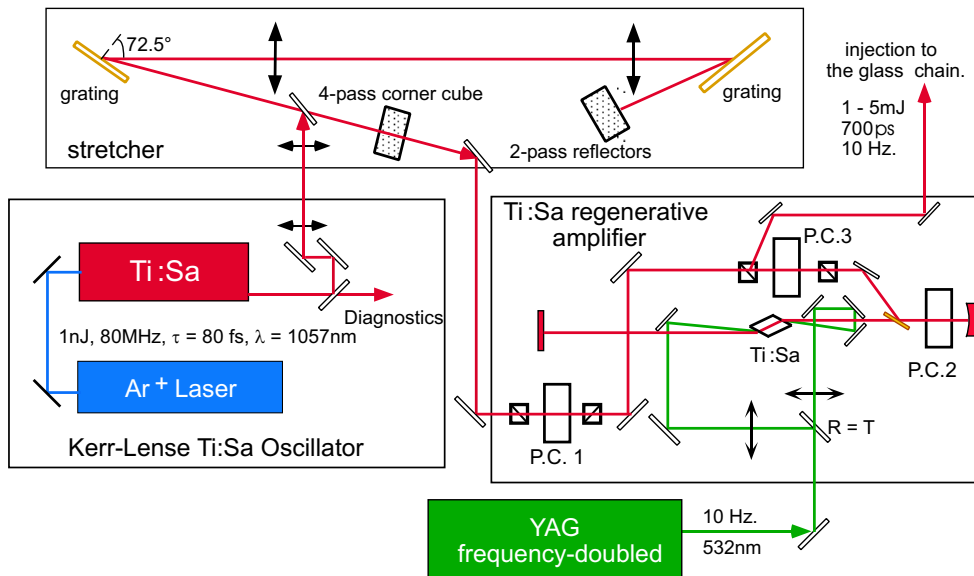


Figure 4.1: The frontend of the LULI 100 TW laser produces 80fs laser pulses. First the pulses are created in a Ti:Sapphire oscillator pumped by an Ar^+ -laser. These pulses are then stretched to 700 ps by a grating stretcher and amplified in a Nd:YAG pumped Ti:Sapphire regenerative amplifier to a level of ~ 5 mJ.

[81], with λ being the central laser wavelength and c the vacuum speed of light. The pulses are then stretched to up to 1.3ns in a 4-pass grating stretcher with a spectral bandwidth $\Delta\lambda > 16$ nm. A Pockels-cell extracts a single pulse which is amplified in a regenerative amplifier (Ti:Sapphire, TEM₀₀) pumped by a frequency-doubled Nd:YAG laser. This regenerative amplifier delivers 10 mJ pulses at 10Hz repetition rate with a bandwidth of $\Delta\lambda > 9$ nm, i.e. $\Delta\tau > 180$ fs. The shot-to-shot energy fluctuation is about $\pm 8\%$. The setup of the oscillator, stretcher and regenerative amplifier is depicted in Fig.4.1.

4.1.2 The Mixed Glass Amplifiers

The pulses from the regenerative amplifier then pass through a chain of consecutive glass amplifiers. As shown in Fig.4.2 the amplifier chain consists of 3 rod amplifiers stages with increasing diameters (16, 25, 45mm) and the final 108mm disc amplifier. Each rod amplifier stage consists of a rod of LHG-8 phosphate glass and one of LSG91-H silicate glass in series to generate a broader gain curve (see Fig.4.3). The 108mm phosphate glass disc amplifiers is custom made at the Rutherford Appleton Laboratory in the UK and is operated in a double pass configuration. The 6 glass discs sit at Brewster angle and are pumped by an array of flashlamps. The complete amplifier

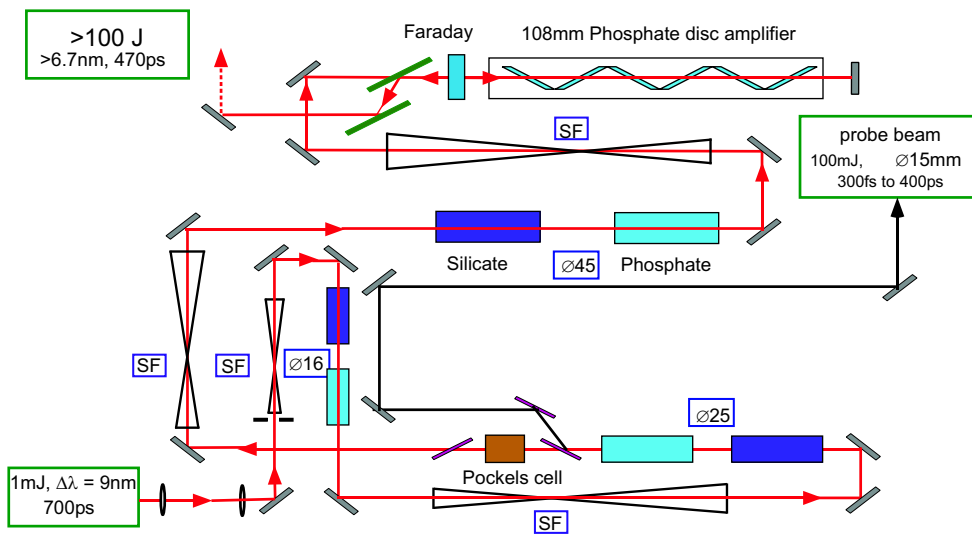


Figure 4.2: The pulses from the front end are amplified in two 16, 25 and 45 mm diameter glass amplifiers, respectively. The rods consist of different glass sorts to widen the gain curve. The final amplification is done in a 108 mm disc amplifier. Between the single amplifier stages are spatial filters (SF) to clean the beam profile.

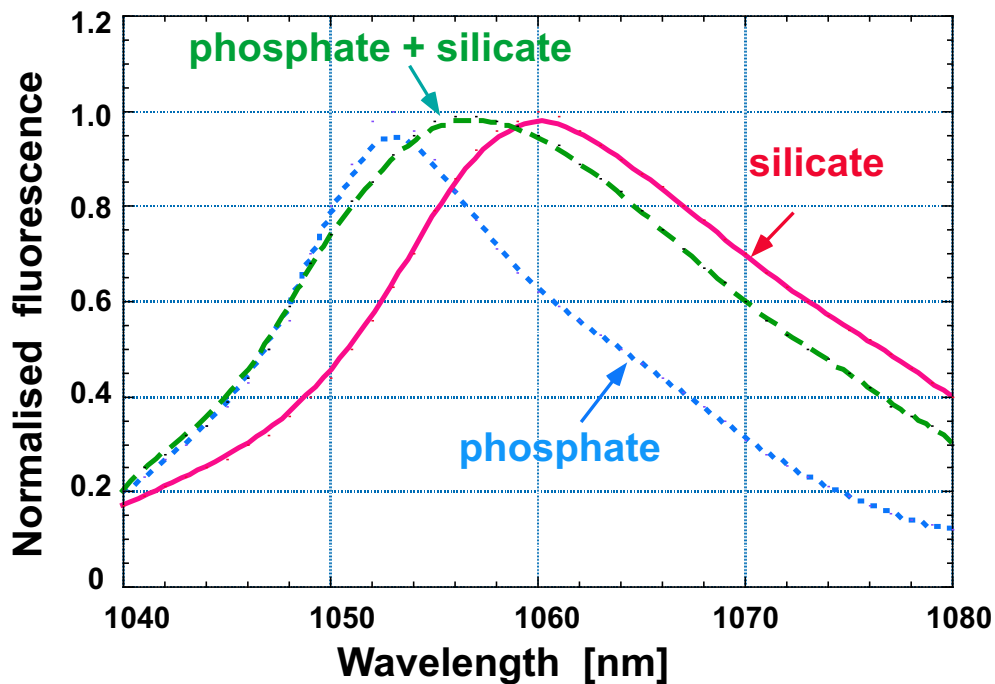


Figure 4.3: Different glass sorts show different gain characteristics. By combining two glass sorts in the amplifier setup the overall gain can be broadened and thus gain narrowing can be reduced.

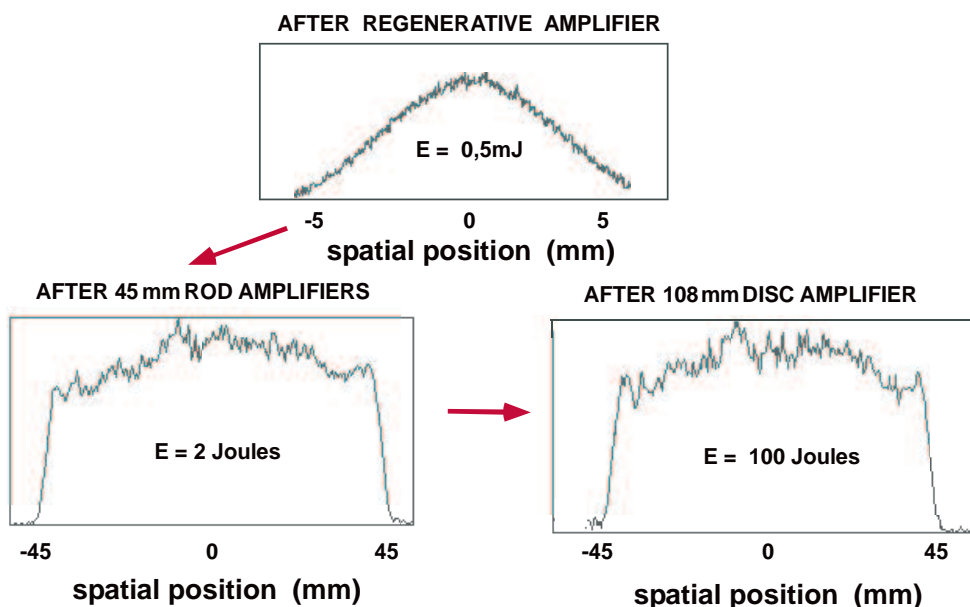


Figure 4.4: The beam profiles evolves gradually in a flat-top profile while passing the different amplifier stages. This reduces the peak intensities on the compressor gratings.

chain has an accumulated B-integral of ~ 1.5 and is able to deliver chirped pulses of up to 150J. (The B-integral is defined as

$$(4.2) \quad B = \frac{2\pi}{\lambda} \int \frac{\Delta n(I)}{n_0} dl$$

and describes the nonlinear effects on the pulse due to the intensity dependent second order of the refraction index). By taking advantage of the radial gain of the rod amplifiers, it is possible to set up the amplifier in a way which causes the Gaussian pulse profile at the beginning of the amplifier chain to gradually evolve into a flat-top profile at the end of the chain as illustrated in Fig.4.4. This is of great advantage for the following compressor stage, since the total energy in a pulse is limited by the damage threshold of the gratings, which in turn depends on the peak intensity on any one given point of the beam profile. Thus it is clear, that with a flat-top pulse with the same peak intensity a significantly higher total energy can be transported over the gratings than with a Gaussian shaped pulse.

The whole laser system is set up on several tables in two rooms. Fig. 4.5 shows the actual setup of the frontend, the rod amplifiers and the disc amplifier. The space in the laboratory is very confined, therefore the disc amplifier had to be installed in a second plane above the rest of the setup. The compressor chamber and the target chamber are installed in a separate room to ensure a disturbance free laser operation and a reduced laser hazard in the experimental area.

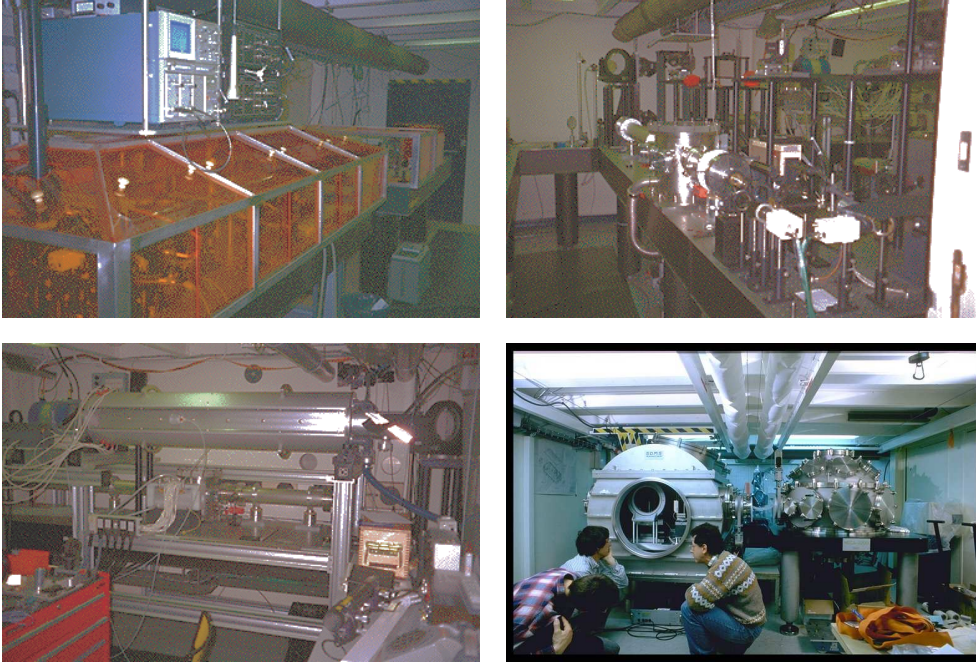
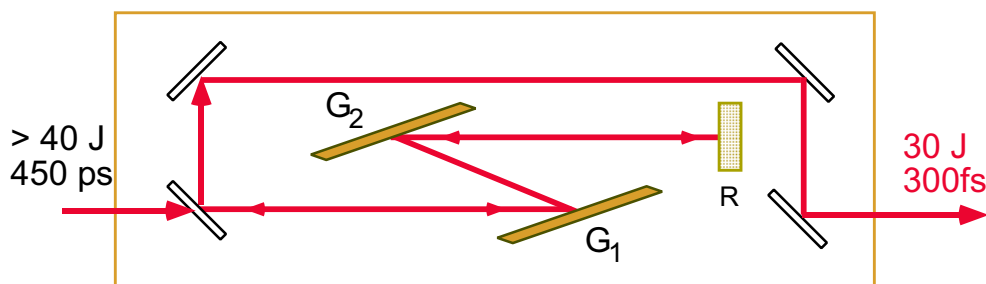


Figure 4.5: Photographs of the LULI laser system: top left: front end, top right: rod amplifier and beam diagnostics, bottom left: disc amplifier, bottom right: compressor and target chamber.

4.1.3 The Pulse Compressor

After passing through the glass-amplifier chain the pulse is split into two. One part (containing typically ~ 60 J) stays long and can for example be used for plasma creation. The second part with typically ~ 40 J is sent through a grating compressor to reduce the pulse duration to ~ 300 fs. The compressor and the attached interaction chamber form a connected vacuum system with an operating pressure of $\sim 10^{-5}$ mbar.

As illustrated in Fig.4.6, the compressor consists of two gold-coated diffraction gratings of 42×21 cm. The pulse makes a double pass in the compressor and the maximum pulse energy is limited by the fluence at the second pass on G1, when the pulse is already short. Holographic gold-gratings have a damage threshold of ~ 0.35 J/cm² for a pulse of ~ 200 fs [77], limiting the maximum pulse energy to 30-40 J. With an overall compression system efficiency measured to be $\sim 70\%$ this yields about 20-30 J on target. This is only a small part of the energy delivered by the amplifiers. Currently developed dielectric gratings promise higher damage thresholds, resulting in higher throughput energies for the compressor system once they become available.



- Cylinder (diameter : 1.3 m, length : 2.6 m)
- G_1, G_2 : 42 x 21cm, 1740 lines / mm,
holographic gold coating gratings separated by 70 cm
- R : reflector used for realising 2-pass compression
- Overall compression efficiency : > 68%

Figure 4.6: LULI double-pass compressor with holographic gold gratings

4.1.4 The Target Chamber

After entering the compressor all pulse transport is done in vacuum to prevent beam breakup. The pressure inside the pumped-down target chamber is typically of the order of $\sim 10^{-5}$ mbar. Due to the short pulse duration and the resulting high intensities nonlinear effects like small-scale self-focussing can cause serious distortions to the wavefront and thus prevent a good focussing when the beam is transported in air. Therefore the interaction chamber is attached to the compressor chamber as can be seen in Fig.4.7 and forms a closed vacuum system.

The target chamber itself is of roughly spherical shape with a diameter of 1.2 m. Various ports allow to connect different detectors and diagnostics for beam characterization and of course the experiment. The photograph in Fig. 4.7 shows Thomson parabola spectrometers in the foreground and the transport setup for a probe/heater pulse on the right.

4.1.5 Laser Diagnostics

The beam is transported by dielectric mirrors and focussed by an off-axis parabola down to intensities of $\sim 5 \cdot 10^{19}$ W/cm². The critical alignments of the system, such as pulse compression and focussing are done with an injected 10 Hz-beam from the regenerative amplifier. The focal spot is measured by a far field camera system which shows it to be roughly 2 times diffraction limited. A typical focus measurement is

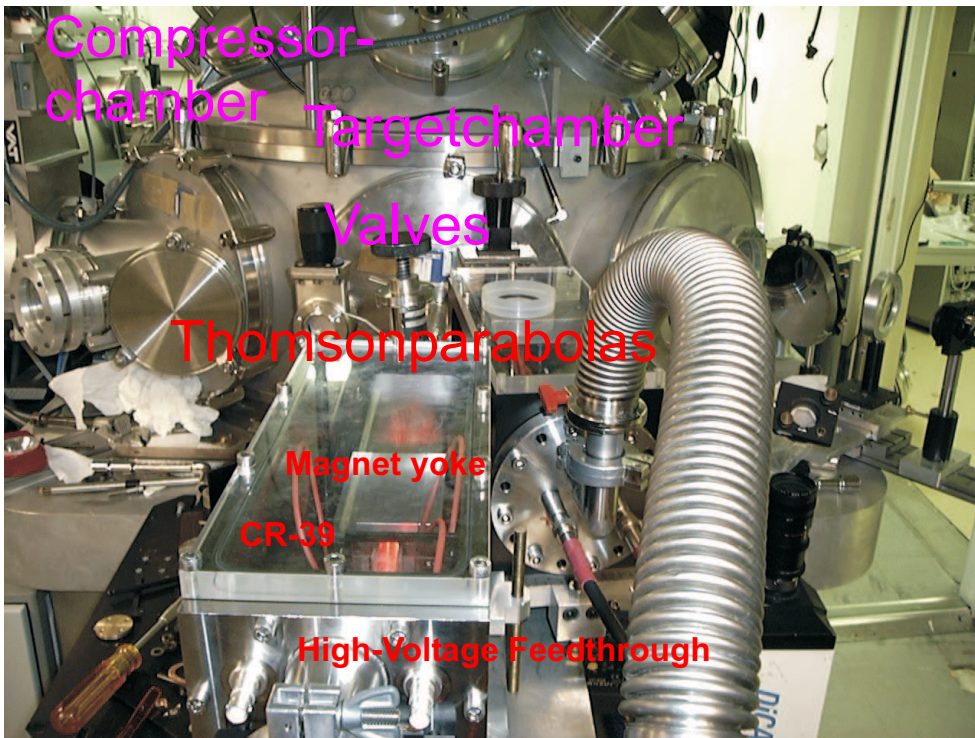


Figure 4.7: The LULI targetchamber has 1.2 m diameter. In the foreground the two Thomson parabolas can be seen which are attached to the chamber via valves to have independent access without breaking the vacuum. In the upper left corner a part of the compressor chamber can be seen.

shown in Fig. 4.8. For the pulse duration measurement a single-shot autocorrelator is used which showed typical pulse durations between 300 and 350fs.

4.2 Experimental Setup and Diagnostics

As targets mostly thin metal foils were used with thicknesses ranging from 5 to 200 μm . The foils were mounted free standing on washers as shown in Fig. 4.9 to provide access for the laser pulse, the different spectrometers and other particle diagnostics and the simultaneous target interferometry, as illustrated by the green laser beam in Fig. 4.9. At ~ 5 cm distance behind the target a stack of Radiochromic film (RCF) was mounted to catch an imprint of the proton signal. Usually the stack was fitted with a slit to provide free line of sight for the spectrometers. One special targetmount had the option of resistively heating the targets by running a ~ 10 A current through it. While the non-heated targets were simply glued to the washers this what not possible for heated targets. In order to maintain contact and stay in place also at temperatures

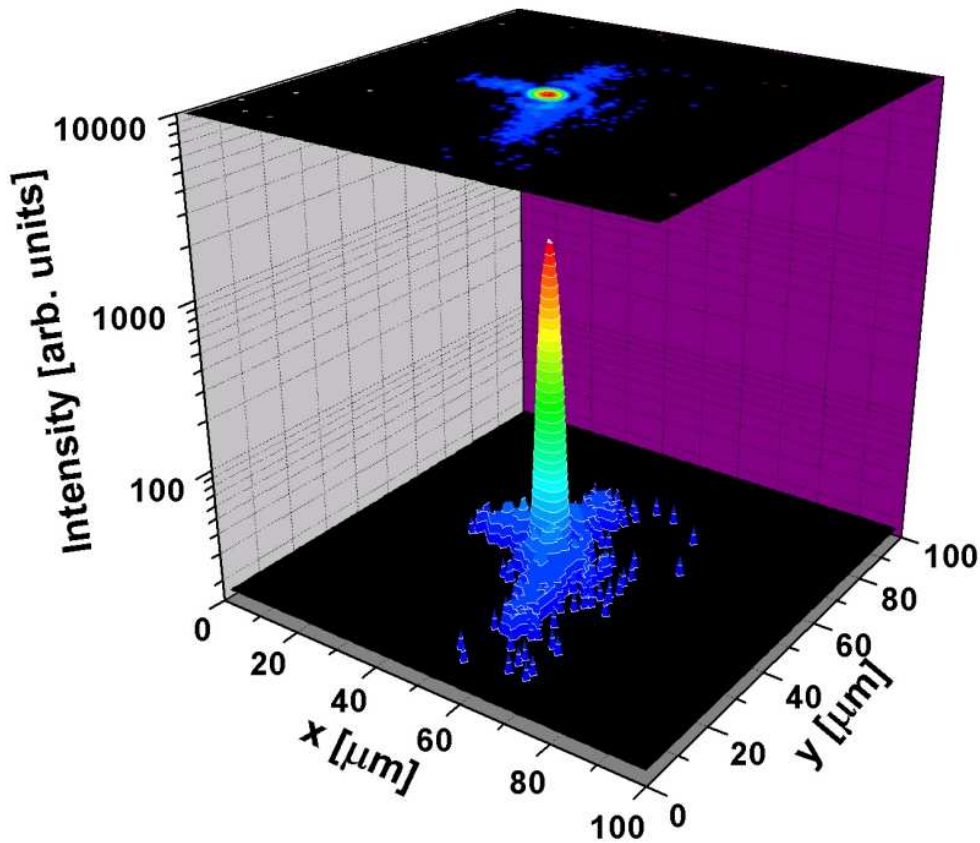


Figure 4.8: Typical focal spot for a LULI laser shot with an energy of ~ 15 J. The plot shows the intensity over the spatial extension of the focus.

~ 1000 °C, these targets were clamped down on an insulating mount. Attached to this mount were the wires carrying the heating current.

The setup for most experiments is depicted in Fig. 4.10. The main interaction beam (red) is focussed by an off-axis parabola, hitting the target under an angle of 0° with respect to the target normal. Perpendicular a frequency doubled probe beam (green) was used to obtain an interferometric image of the plasma conditions at the target surfaces.

The accelerated particles were investigated by four complementary diagnostics:

- (a) a stack of radiochromic films (RCF) 5cm behind the target to record the angular distribution of the emitted proton beam [41, 33];
- (b) two combined magnetic proton/electron spectrometer [82] with a Kodak DEF X-ray film to measure the proton energy spectra;
- (c) a cluster of neutron detectors to measure the neutrons produced by second order

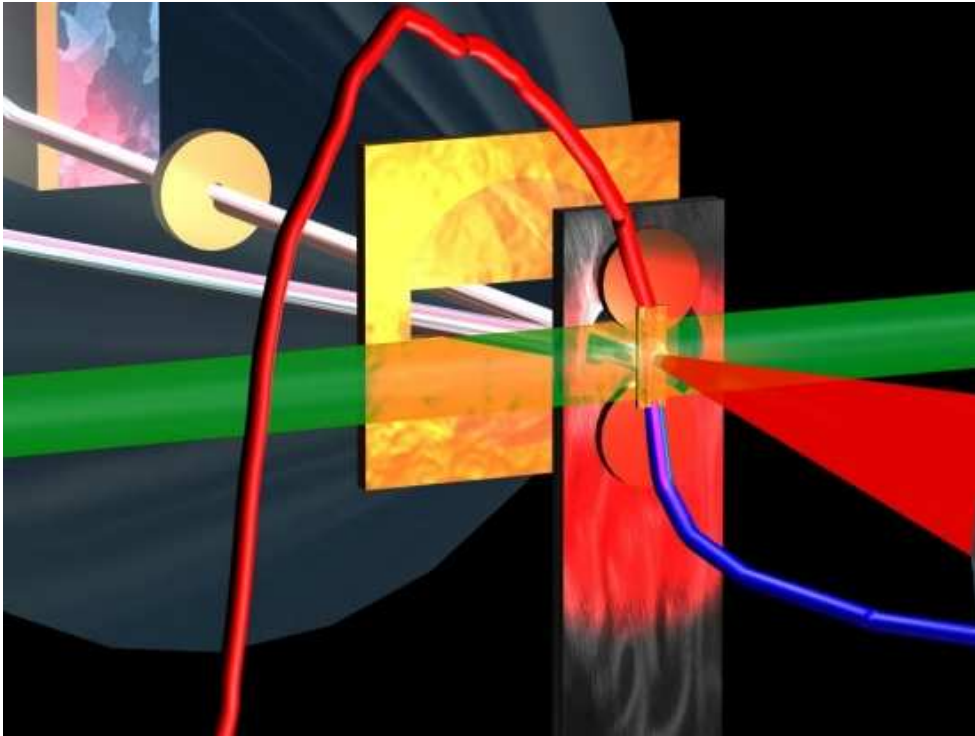


Figure 4.9: The target is mounted with free access from the front, rear and the sides. The laser is impinging on the front the ions are accelerated from the rear in laser direction where most of them hit the stack of RCF. Some pass through the slit to the spectrometers. Attached to the targets are the current-carrying wires for resistive heating.

(p,n), (γ ,n) and fusion reactions [11], these detectors are not shown in Fig. 4.10;

- (d) the main diagnostic for the ion experiments (see Chap.5): two Thomson parabola spectrometers ($B = 0.65$ T, $E = 1.3$ MV/m, solid angle $\sim 5 \cdot 10^{-8}$ sr) with CR-39 track detectors to obtain the ion energy spectra.

The Thomson parabolas as well as the proton spectrometers are attached to the outside of the target chamber at at -6.5° , 0° , or 13° to the target normal at a distance of about 1 m as is shown on the photograph in Fig. 4.7. Three spectrometers could be used simultaneously. While the proton spectrometers use standard X-ray film as a detector, this is not possible for the detection of heavier particles which would be stopped in the protective layer. The Thomson parabolas work instead with a Solid State Nuclear Track Detector (SSNTD) called "CR-39". CR-39 is sensitive to single ion events but insensitive to electromagnetic radiation and electrons. An ion striking a CR-39 plate destroys the polymer matrix along its path and causes nm-scale damage sites. These damage trails are transformed into cone- or bowl-shaped craters when

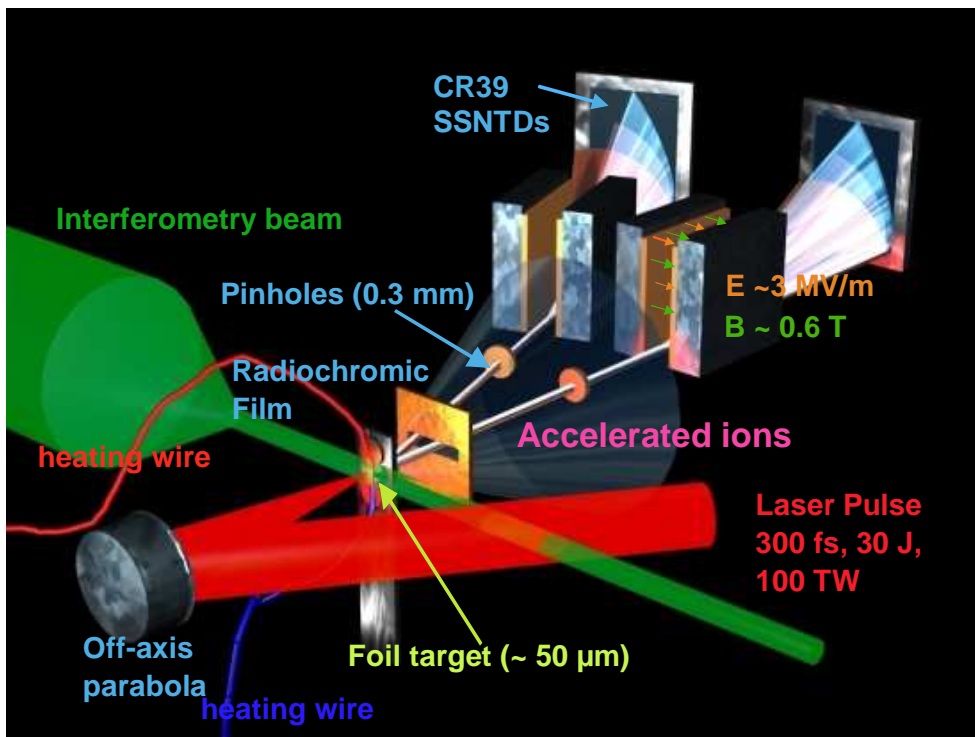


Figure 4.10: Experimental Setup: the target is mounted free standing and can be resistively heated via the two wires, the main laser pulse (red) is focused optics by an off-axis parabola. The interferometry beam (green) is expanded after the target to obtain a magnified image. Behind the target is the RCF-stack diagnostics and two Thomson parabola-spectrometers with CR-39 detector plates.

the CR-39 is etched in NaOH solution. Each individual track is analyzed by optical microscopy with custom pattern recognition software [83] yielding position and track size parameters. The absolute energy spectra for each ion species are then obtained from the distribution of pits along the distinct traces. Only this "single-track counting method" yields correct results for the areal ion density. Optically scanning an etched CR-39 plate as often done may lead to erroneous results because the optical density is not simply proportional to the number of pits. While the next sections describe the general diagnostics (a) - (c) as well as the target interferometry, the main ion diagnostics, i.e. the Thomson parabolas, the CR-39 detectors and the automated track counting system is discussed in Chapter 5.

4.2.1 Interferometry

The free standing target was probed by a frequency doubled laser beam parallel to the surface to determine the plasma conditions on the front and rear surface. The

interferometric setup yielded information on plasma formation on the target surfaces. The interferometric setup makes it in principal possible to obtain the exact electron densities. This data is however not part of this work and will be published elsewhere. The important aspect for the acceleration of fast ions is to have unperturbed target rear surface at the time of the interaction. The timing of the probe beam could be varied by a delay line to adjust the prepulse in a way to give a large enough preplasma for effective electron acceleration but to be close enough to the main pulse so that the prepulse-launched shock wave does not destroy the back surface.

4.2.2 Neutron Detectors

In addition to the ion and laser beam detectors, a silver activation neutron detector [84] was placed close to the target chamber determining the neutron yield for the different experiments. The silver is activated by neutron capture and β -decay with a half life of 28 seconds, which is detected in a scintillator and recorded by a photo multiplier tube (PMT). This detector measures the neutron emission caused by (γ, n) and (p, n) reactions from the target. On typical shots, the neutrons are generated by (γ, n) reactions within the target (caused by the bremsstrahlungs photons from the relativistic electrons) and by (p, n) reactions of our proton beam impacting on the RCF screen. We also used a target of deuterized plastic (CD_2), which was laser-heated to produce a beam of deuterons. Placing a CD_2 catcher behind the target we observed the yield of neutrons from (d, d) fusion reactions. We detected a total yield of 2.8×10^7 neutrons in this experiment, which was at least an order of magnitude above the yield on average shots. The details of this experiment which also used time-of-flight neutron detectors to measure a neutron spectrum can be found in [11].

4.2.3 Radiochromic Film and CR-39 stacks

As is shown in Fig. 4.9, a stack of radiochromic film (RCF) was mounted ~ 5 cm behind the target to record the angular distribution and spatial beam profile of the emitted proton beam [40]. Due to ion Bragg-peak, i.e. the pronounced energy loss of ions at the end of their range, different layers of the RC film pack allow the imaging of the proton beam at different energies. The RCF changes through polymerization of a diacetylene active layer, from transparent to dark blue in proportion to the absorbed dose (in rads) of ionizing radiation ($1 \text{ rad} = 100 \text{ erg/g}$). The response of the RC film package was modelled with the SRIM Monte Carlo ion transport code, and obtained response functions for the layers of RCF similar to the ones presented in [32]. Furthermore the RCF was specially calibrated for protons at a proton accelerator facility. The resulting

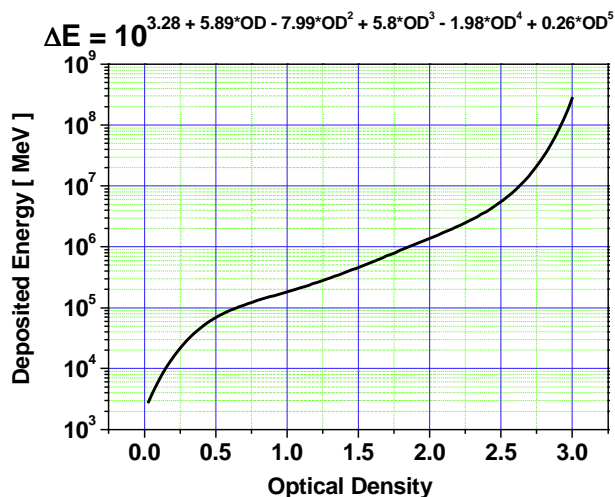


Figure 4.11: Calibration curve for proton energy deposition in RCF (courtesy of A. Blazevic).

calibration curve is given in Fig. 4.11.

4.2.4 Proton and Electron Spectrometer

The two magnetic spectrometers were mounted at a distance of about 1 m from the target covering a solid angle of $\sim 5 \times 10^{-6}$ sr. The spectrometer design allows to simultaneously record a proton spectrum as well as an electron and a positron spectrum. The layout of the spectrometers is shown in Fig. 4.12 and a detailed description of its properties can be found in [82]. Electrons and protons were recorded in nuclear emulsion track detectors which allow single particle detection without being overwhelmed by the blinding X-ray flash from the laser plasma. The use of an additional X-ray film layer extended the dynamic range to higher particle fluxes. A protective light tight paper in front of the emulsion and X-ray film stopped protons below ~ 2 MeV.

The upper energy limit for protons is around 100 MeV. The instrumental energy range for electrons is between 0.2 and 140 MeV and for positrons between 0.2 and 40 MeV. The spectrometers were supplied by our coworkers from General Atomics and the detailed data obtained by them will be presented in [10].

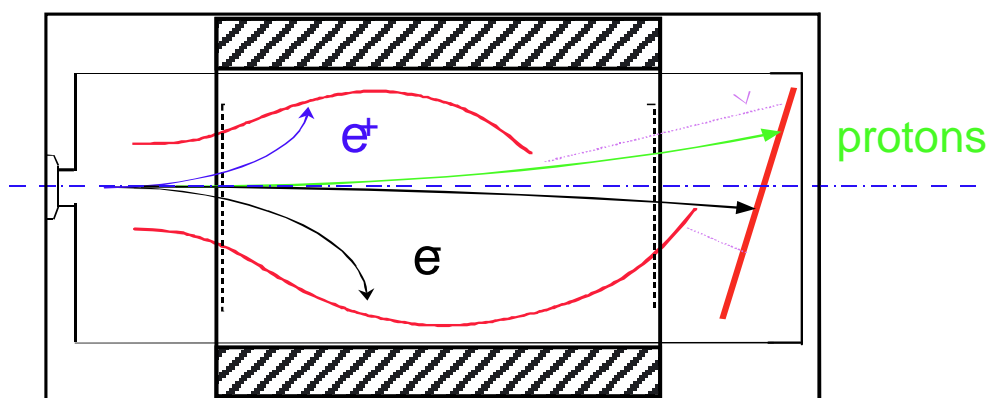


Figure 4.12: Magnetic spectrometers to record proton electron and positron spectra.

4.3 Thin Foil Targets for Ion acceleration: material choice and properties

A wide range of different target materials was tried within the experimental campaign, including insulators as well as conductors. The typical targets for proton production were Au- and Al-foils, sometimes with additional CH layers on the back to boost the proton yield. The thickness ranged from 5 to 200 μm , with $\sim 10 \mu\text{m}$ targets giving the highest yields and energies. For dedicated ion experiments Al-foils with a 1 μm carbon coating were used in the beginning. Due to the low melting point of aluminum the substrate was later changed to tungsten. The coating was changed from carbon, which has too much hydrogen embedded in its matrix, to CaF_2 or UF_4 . 10 to 50 μm thick targets were used, with coatings in the 100 nm range.

Chapter 5

Diagnostics for laser-accelerated heavy Ions

After high-energy protons had been measured in a number of experiments [41, 39, 52], the next logical step was to search for heavier elements, which might also be accelerated by the same mechanism. Since a basic magnetic spectrometer like the one used to detect the protons is not able to distinguish different ion species and charge states a new detector had to be deployed. Two Thomson parabola spectrometers were designed, the parameters like electric and magnetic fields, but also outer dimensions, vacuum capability, etc. were chosen to match the expected experimental conditions. These detectors consists of two parts: (i) the real spectrometer, which uses parallel electric and magnetic fields to separate the entering ions by charge-to-mass ratio and energy and (ii) a CR-39 detector plate normal to the flight path to record the impinging ions. The following sections give an overview over those detectors.

5.1 Design of the Thomson parabola spectrometer

A Thomson parabola -spectrometer is an established detector, invented 1912 by Joseph John Thomson, the discoverer the electron, to investigate "*Kanalrays*" or positive rays. It basically consists of parallel electric and magnetic fields which are arranged with there field lines perpendicular to the flight path of the particles to be measured. If now a charged particle passes through the fields it is deflected parallel to the electric and perpendicular to the magnetic field. Using this arrangement, Thomson first identified the isotope ^{22}Ne . For an ideal Thomson parabola , neglecting any fringe fields the amount of the deflection is given by

$$(5.1) \quad x \simeq \frac{qElD}{mv^2} = \frac{qElD}{2E_{kin}}$$

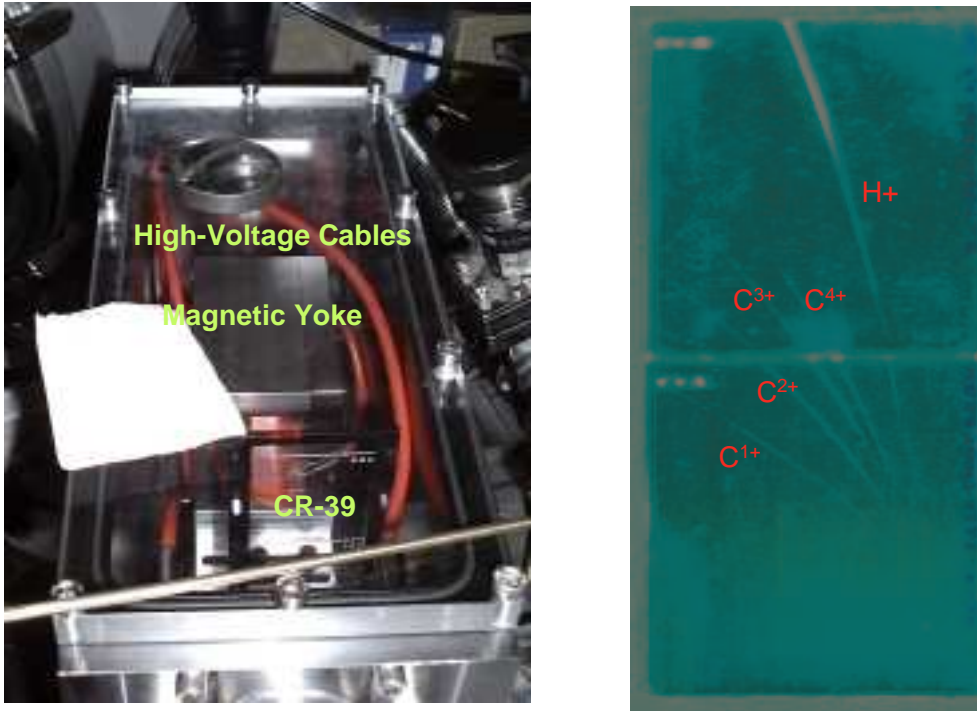


Figure 5.1: eft: Thomsonparabola spectrometer and right: etched CR-39 detector, showing H^+ and C^{1+} – C^{4+} parabolic ion traces.

and

$$(5.2) \quad y \simeq \frac{qBlD}{mv} = \frac{qBlD}{\sqrt{2mE_{kin}}},$$

where E, B are the electric and magnetic fields, l is the length of those fields, D the distance from the middle of the fields to the detector plane and m, q, v , and E_{kin} the particles mass, charge, velocity and kinetic energy. Combining (5.1) and (5.2) now yields

$$(5.3) \quad y = \frac{mE}{qlDB^2}x^2 = \frac{q}{m} \frac{E}{lDB^2}x^2,$$

a parabolic equation with the charge-to-mass ratio as a parameter. From (5.3) it is easy to see that particles with the same charge-to-mass ratio but different energies are deflected on a parabolic trace in the detector plane, while particles with different charge-to-mass ratio lie on different parabolas, as can be seen in Fig. 5.1.

The Thomson parabolas used in our experiments were housed in their own vacuum casing which was attached to the targetchamber with a valve to allow separate pumping. This was important to be able to change the CR-39 detector in the Thomson parabola between two shots without having to open the whole targetchamber. The fields were

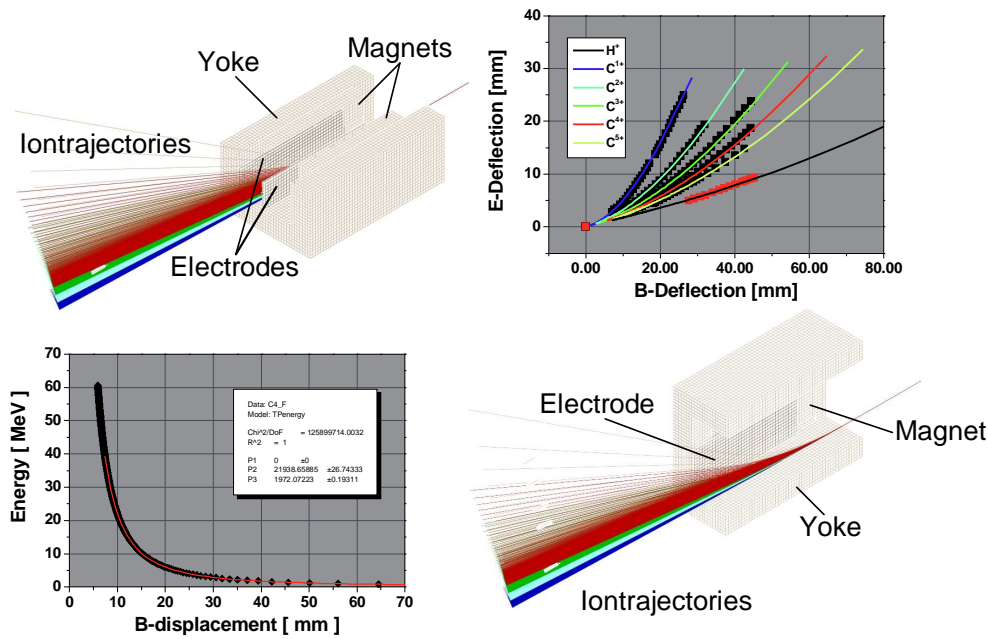


Figure 5.2: Thomson parabola calibration: top left and bottom right: a 3D computer model was needed to treat the fringe fields correctly. Top right: the simulated traces are overlaid with the measured data to identify the charge states. Bottom left: from the simulation an energy dispersion relation for the Thomson parabola can be obtained.

supplied by permanent magnets and copper electrodes, respectively. The magnetic fields have a strength of ~ 0.65 T, the high voltage fields can be continually adjusted up to 16 kV for one of the Thomson parabolas and up to 30 kV for the other, yielding electric fields of up to 1.3 MV/m. These fields cause a dispersion strong enough to separate charge-to-mass ratio -differences < 0.1 at MeV/nucleon energies by more than $500\mu\text{m}$. The Thomson parabolas can be fitted with pinholes of varying size to adjust for target distance and ion yield. A typical pinhole size is $300\mu\text{m}$, resulting in a solid angle for the spectrometer of $\sim 5 \cdot 10^{-8}$ sr.

Due to the compact design and the very strong magnets and high voltages the Thomson parabolas cannot be described by (5.3) with sufficient accuracy. Strong fringe fields, a design-based geometric shift between the electric and magnetic fields and a variable entrance point for the ions lead to an additional linear term in the equation. In order to obtain an exact calibration it is necessary to do a full 3D tracing routine for ions crossing the deflecting fields. This was done using the ion optics code SimIon¹. Fig. 5.2 shows cutaway views of the 3D-Thomson parabola simulation with computed ion traces for Hydrogen and Carbon. The simulated traces were then overlaid with the measured

¹Idaho National Engineering and Environmental Laboratory, Bechtel 1999

data in order to identify the correct species and charge-to-mass ratio (Fig. 5.2 top right). To obtain a dispersion relation the simulated data was then fitted with a second order polynomial:

$$(5.4) \quad E_{kin} = P_1 + \frac{P_2}{x} + \frac{P_3}{x^2}$$

A typical fit for a C^{4+} trace is shown in the bottom left picture of Fig. 5.2. Using this dispersion relation the energy of for each point on a specific ion track can be obtained. CR-39 is sensitive to single ion events but very insensitive to electromagnetic radiation and electrons. An ion striking a CR-39 plate destroys the polymer matrix along its path and causes nm-scale damage sites. These are transformed into cone- or bowl-shaped craters when the CR-39 is etched in NaOH solution. Each individual track is analyzed by optical microscopy with custom pattern recognition software [83] yielding position and track size parameters. The absolute energy spectra for each ion species are then obtained from the distribution of pits along the distinct traces. Only this "single-track counting method" yields correct results for the areal ion density. Optically scanning an etched CR-39 plate may lead to erroneous results because the optical density is not simply proportional to the number of pits.

5.2 Solid State Nuclear Track Detectors

CR-39 characteristics and functional principle

To record the ion traces Solid State Nuclear Track Detectors (SSNTD) were used. (SSNTD) are used for more than 40 years to detect ionizing particles in a wide range of experiments and applications, including dosimetry, medicine and biology, space physics, nuclear physics, fusion physics, and recently also in the new field of ultrahigh-intensity laser-plasma physics². SSNTDs can be made of various materials, as e.g. crystals like LiF, or different sorts of plastic. They are robust and easy to handle and sensitive to single particle interaction. The track forming mechanism only works for heavily ionizing particles which makes SSNTDs insensitive for light, X-rays and even electrons. In the scope of ultrahigh-intensity laser experiments where one wants to detect ions within a strong background of virtually every other radiation possible this comprises a significant advantage over nuclear emulsions or films. The material used in the scope of this work, "TASTRAK CR-39" is a plastic solid state nuclear track detector, produced by TASL³ in Bristol, UK.

²For an extensive review on the applications of SSNTDs see [85].

³Track Analysis Systems Limited, H H Wills Physics Laboratory, Bristol. "CR" in CR-39 stands for "Columbia Resin".

5.2.1 Working principle of SSNTDs: Track formation mechanism

The working principle of a plastic SSNTD is fairly straight forward: a particle passing through the detector loses energy along its path which is transferred to the surrounding medium. If the differential energy loss of the particle is high enough and exceeds a material dependent threshold, molecules are excited or ionized and the polymer chains of the material break. The fact that a material dependent threshold has to be overcome to break the polymer chains is the reason that CR-39 is fairly insensitive for UV, X-ray, γ - or even electron radiation unless exposed to very high doses over a longer time. Heavy particles on the other hand leave a trail of damage in the material which can be detected and which contains information about the particle that caused it. Since the size of a damage track is on the order of $\sim 3\text{-}10\mu\text{m}$, detecting it is simple. Though there is recent work of direct track detection by atomic force microscopy [86], usual method is to enlarge the tracks by the use of a chemical reagent (etchant). These etchants (e.g. NaOH) dissolve the damaged regions at a higher rate than the bulk of the material thus first gouging out the damage trail and then enlarging it in all directions [87] until it becomes visible under an optical microscope.

Since the etch rate along a track depends on the differential energy loss of the particle let us now briefly consider the damage causing mechanism in a bit more detail: A charged particle passing through matter can lose energy due to radiation losses (Bremsstrahlung, Cerenkov-radiation), through electromagnetic interaction and by internuclear scattering. For ions in the MeV-range the electromagnetic interaction is the dominating energy loss mechanism and is described by the Bethe-Bloch-Formula [72]:

$$(5.5) \quad -\frac{dW}{dx} = 4\pi\alpha^2 \frac{(\hbar c)^2}{m_e c^2} n_e \frac{Z^{*2}}{\beta^2} \left[\ln \left(\frac{2m_e c^2 \beta^2}{(1-\beta^2)I} \right) - \beta^2 - \frac{\delta}{2} \right].$$

Here, α is the fine-structure constant, m_e the electron mass, n_e the electron density within the material, c the velocity of light and the usual relativistic $\beta = v/c$. The velocity of the impacting particle is denoted by v and its initial charge state by Z , $Z^* = Z(1 - \exp(-130\beta/Z^{2/3}))$ [85] being the effective charge state at a specific time caused by the interaction with the target material. $I \approx 16Z_M^{0.9} \text{eV}$ describes an average ionization potential of the target material and $\delta/2$ is a correction for density effects to the standard Bethe-Bloch-Formula described e.g. in [88]. The differential energy loss of the particle thus depends on its kinetic energy and its range R in the detector

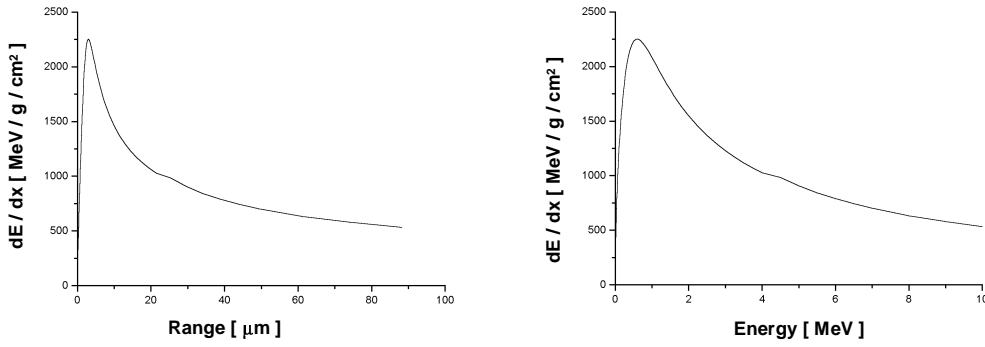


Figure 5.3: Energy loss dE/dx for alpha-particles in CR-39. The highest energy loss occurs at the end of the range at low energies, shortly before the particle is stopped.

material is determined by:

$$(5.6) \quad R = \int_{W_{max}}^0 dx = \int_{W_{max}}^0 \frac{1}{dW/dx} dW.$$

Due to the energy losses by electromagnetic interaction target electrons can be excited to higher energy level which can break the polymer chains. The electrons can also be totally ejected (δ -electrons) and cause further excitation and ionization (secondary electrons) which can also break the polymer chains. As can be seen in Fig.5.3, the highest energy loss occurs at low energies at the Bragg-peak, i.e. at the end of the particle range. In the next section, where the etching behavior is discussed, it will become clear that this means that particles stopping in the material will leave the most visible tracks and that it is possible to infer information on particle species and energy from the observed tracks. To determine if a given energy loss is sufficient to create an etchable track, several different criteria exist. The most obvious one is a threshold behavior in the total electromagnetic energy loss dW/dx : if dW/dx exceeds a material dependent threshold the particle leaves an etchable track. Unfortunately this is not confirmed by experiments which show that the threshold depends on the atomic number Z of the ion [85]. The criteria used in the scope of this work is the Restricted Energy Loss (REL), which is the part of the energy loss which produces δ -electrons below a maximum energy W_0 . Electrons with energies above W_0 deposit their energy too far away from the ion path to contribute to the track formation. With a correct (material dependent) choice of W_0 a Z -independent threshold for etchable tracks can be found [89]. A more extensive discussion of track formation criteria can be found e.g. in [87].

5.2.2 Track Etching

The most common method to render the individual tracks visible is chemical etching. The etching process in the track region proceeds with the velocity v_t which is larger than the bulk etch velocity v_B in the undamaged material. This means that along the ion path a narrow channel is etched until the stopping point is reached. Within the channel the etching process continues with v_B , so that pits or craters are formed. The exact form of these pits depends on the etching conditions and on the track etch rate v_t which in turn is a function of the energy loss. For ions with normal incidents a cone shaped crater with a circular opening and radius r forms, which becomes elliptic with increasing angles of incidents. The opening angle β of the cone depends on the ion range, i.e. the energy. The process is schematically depicted in Fig. 5.4. The new surface after etching the detector for a time t_e can be obtained by drawing a semicircle with radius $v_B t_e$ from every point of the original surface. The new surface is then determined by the envelope of these semicircles. Along the track the etch rate is $v_T > v_B$. While the track is etched the length $l = v_T t_e$, the surface is only etched by the distance $h = v_B t_e$. At each point along the track a circle with radius $r_T = v_B(t_e - t)$ can be drawn leading to the conical shape shown in Fig. 5.4 (a), if $R \geq L$ is fulfilled, with R being the ion's range. If the etching is continued beyond the stopping point the cone will develop a rounded end section and finally assume an increasingly flat bowl shape as illustrated in Fig. 5.4 (b). The dimensions of the track opening can be easily calculated. The opening angle β is given by:

$$(5.7) \quad \sin(\beta) = \frac{v_B t_e}{L} = \frac{v_B t_e}{v_T t_e} = \frac{v_B}{v_T}.$$

Also

$$(5.8) \quad \tan(\beta) = \frac{r}{L_e} \stackrel{(5.7)}{=} \frac{v_B}{\sqrt{v_T^2 - v_B^2}},$$

so that for the observed track radius follows:

$$(5.9) \quad r = \frac{v_B L_e}{L} = \frac{v_B t_e}{\sqrt{v_T^2 - v_B^2}} = v_B t_e \sqrt{\frac{v_T - v_B}{v_T + v_B}}.$$

Furthermore, for oblique tracks the angle of incidents can be determined by measuring the ellipticity. That means that by measuring the bulk etch rate v_B and the track radius r it is possible to determine the track etch rate v_t , from which in turn the energy loss and in the end the track causing particle can be inferred.

In the experiments presented in this work six-molar NaOH at 80°C was used as an etchant. Etching times were usually ~ 40 minutes for ion analysis and multiples of this to specifically etch for protons. To achieve reliable results it is important to hold the

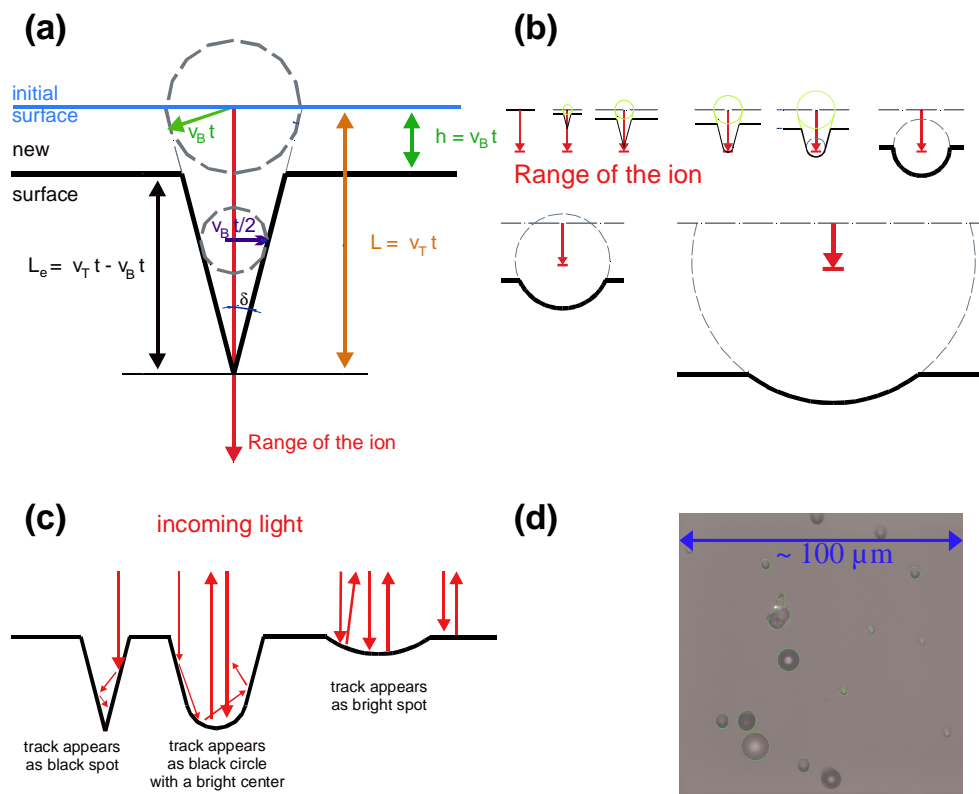


Figure 5.4: Iontracks in CR-39: (a) schematic diagram of track formation. h : thickness of removed surface, L : length of the etched track at time t , v_B : bulk etch velocity, v_T : track etch velocity. (b) development of the track during the etch process. First a cone is etched up until the end of the ion range is reached. Further etching produces a sphere at the end of the cone that gets bigger and finally develops into a bowl shape. (c) different track shapes show different appearances depending on how they reflect the light. (d) microscope image showing exemplary tracks.

temperature and the concentration constant during the etching process and also for different etching runs in order to compare different sets of CR-39 plates. To achieve this the etching apparatus is equipped with a temperature stabilization ($\pm 0.1^\circ$), the etchant is circulated and the CR-39 plates are constantly moved during the etching process to inhibit the build up of concentration gradients and to remove the etched material from the surface.

5.3 Analysis of the CR-39 plates using the Siegen Automated Scanning Microscope with pattern recognition system

Analyzing an etched CR-39 plate is usually done by optical means. Normally the individual tracks are counted under a microscope, either by hand or by an automated system. Especially in laser-ion experiments, the track density is usually high enough to cause a change in the mean optical density of the plate. Several groups tried to analyze CR-39 plates by using the optical density as obtained e.g. by a scanner, as a measure for the particle density. As it is shown below there are serious problems with this method, since the optical density is not only dependent on the number of particles but also on the track geometry. This in turn depends on the particle species, its energy, angle of incidence and the etching parameters.

5.3.1 Reflective and transmissive behavior of etched tracks

The reflective and transmissive behavior of an etched CR-39 plate determines its optical density. An undamaged CR-39 plate without any etched ion tracks is transparent, like plexiglass. Each surface damage, like an ion track but also like scratches, dust, dirt, material inhomogeneities, etc, acts as a scattering center which absorbs, reflects and scatters any incident light. Especially how the light is scattered at a single etch crater depends strongly on the form of the crater as is explained for a simple example in Fig. 5.4 (c). Cone-shaped tracks will appear almost black since the light is not scattered back to source, while with bowl-shaped ends will develop a very bright spot in the middle which gets bigger with increasing bowl-diameter. Tracks which have no cone walls left and consist entirely of a rounded bowl will appear light and with a weak contrast to an unperturbed surface. When one now relies on measurement of mean optical densities for analyzing the CR-39 as one does by using a flatbed scanner or photograph it is clear that this method is prone to error. The mean optical density depends strongly on the method of illumination, i.e. which angle, parallel or divergent light, etc. as one sees in Fig. 5.5. Using a mixed nuclid source (^{241}Am , ^{239}Pu), two alpha-particle spots were created on a CR-39 plate. One has a particle density typical for laser acceleration experiments, the other is a factor 10 less dense. The CR-39 plate was then scanned by an optical scanner. The top row in Fig. 5.5 shows two scans at different illumination angles, with superimposed optical density lineouts from a 5 x 100 mm wide area out of the middle of each plate. The bottom row shows a false color representation of the entire surface. Not only is it impossible to determine which of the

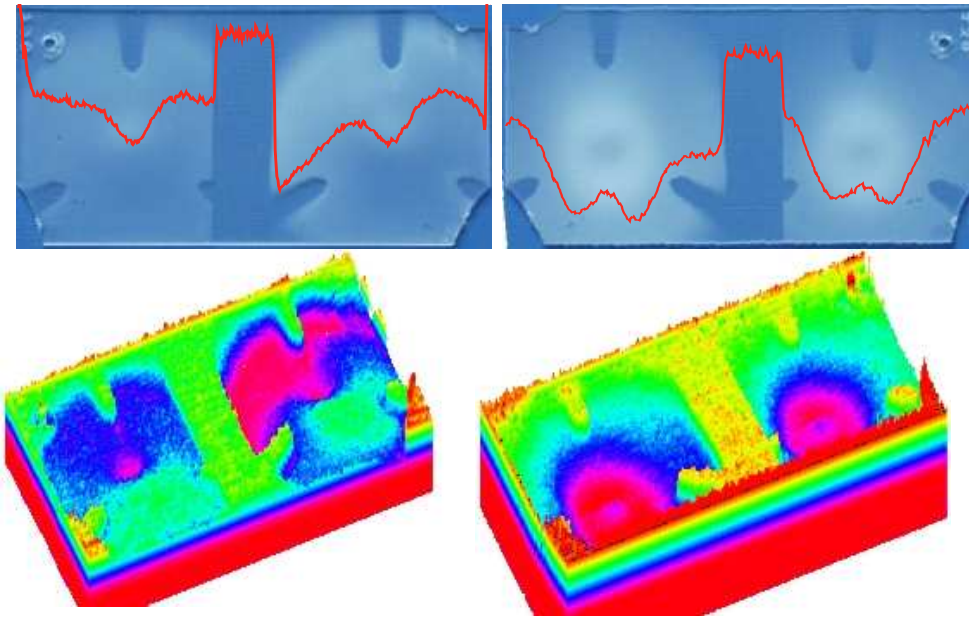


Figure 5.5: A CR-39 plate irradiated at two spots with an alpha source. After etching the plate was scanned at different angles. The change of the angle caused a drastic change in the signal. Top: scanned images, the left shows a bright center of the irradiated spots, the right shows ring structures. The red lines are horizontal line-outs from the middle of the plates. Bottom: False color image of the scanned pictures, the colors represent different brightness values.

two spots is of higher density, the profiles also change drastically with the illumination. It follows that analysis of CR-39 by mean optical densities as done e.g. in [39, 90] is not a reliable technique. Therefore this approach was discarded in the scope of this thesis and the analysis was done by single track counting.

5.3.2 Automated Single Track Counting

One CR-39 plate from a Thomson parabola detector typically holds $\sim 10^6$ tracks, ruling out a manual track counting procedure. Instead an Automated Track Counting System at the University of Siegen was used [91, 83]. This system consists of a high-precision microscope equipped with an autofocus, a positioning stage and a CCD-camera. The camera and the positioning stage are coupled to a computer with a specialized pattern recognition software. An updated version of the system was recently purchased by our group and is shown in Fig. 5.6.

The Samaica pattern recognition software analysis the video image and searches for ion tracks. To each recognized track it fits an ellipse (see Fig. 5.7) and stores a number of



Figure 5.6: Automated scanning and particle counting station: The CR-39 detectors are placed under a computer controlled microscope. A CCD-camera relays the image to the computer where a special pattern recognition software searches for particle tracks. The tracks are counted and analyzed. From the stored data the complete image on the CR-39 can be reconstructed, displayed and further processed.

parameters like position, semi-axis, angle, enclosed area, brightness, etc. . Afterwards the program moves the microscope stage by one image and the process is repeated until the whole CR-39 plate is scanned. For a 10 x 5 cm plate this typically took 20 to 30 hours at a 50x magnification, due to the fact that with the old system only rectangular scanning areas were possible. Due to this experience the new Munich system is fitted with a larger CCD-chip and can process up to 5 arbitrary shaped scanning areas for faster processing. The Samaica pattern recognition software was specially developed for the analysis of ion traces in CR-39 SSNTDs and has a wide range of options to tune the recognition process and discriminate against dirt effects. For more details on the system see references above and [92].

After a scan is completed the raw data is analyzed further. To postprocess the scanning data the Software Package PlotIt was developed. With this program the Thomson parabola images can be reconstructed, the individual parabolic traces identified and

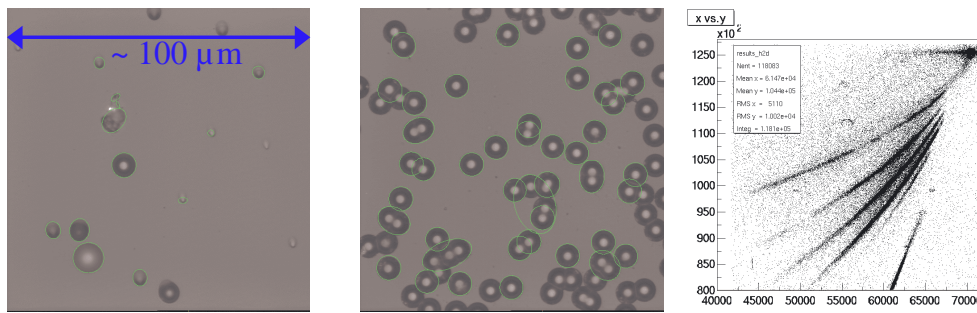


Figure 5.7: The automated scanning microscope takes a video picture and searches for tracks. Recognized tracks are fitted with ellipses and their parameters are stored. After further analysis a scatter plot reconstructs the Thomson parabola image.

the energy spectra extracted.

Chapter 6

Proton Acceleration and general Beam characteristics: Experimental Results

While the main topic of this work is to effectively accelerate ions which are heavier than protons and use the results to obtain a better understanding of the acceleration process, a number of other quantities are important to form a complete picture. In the scope of our experimental campaign we also measured the electron spectra, the proton energy spectra and beam divergence, the ion source size and the dependence of the acceleration process on a number of target conditions.

6.1 Electron Measurements

The magnetic spectrometers used to measure the proton spectra could be equipped with a second film to simultaneously record an electron spectra as shown in Fig. 4.12. Figure Fig. 6.1 shows a typical electron spectra measured for a gold target. Electron energies from ~ 200 keV up to 50 MeV, i.e. the high energy tail of the electron population were measured. The spectra can be fitted with a 2 temperature fit, the temperatures agreeing reasonably well with both the TNSA-model and more elaborate PIC-simulations. A detailed analysis and interpretation of the electron spectra is difficult, since the spectrum measured is not the original electron spectrum created by the laser pulse. It is influenced and deformed by the transport through the target as well as the space charge fields and the ion's charge fields on the back of the target. Furthermore only the high energy part which escape from the target is measured in the spectrometer, while all low energy electrons do not escape the vicinity of the target but are drawn back by the strong space charge fields. Baton et al. [93], using the same

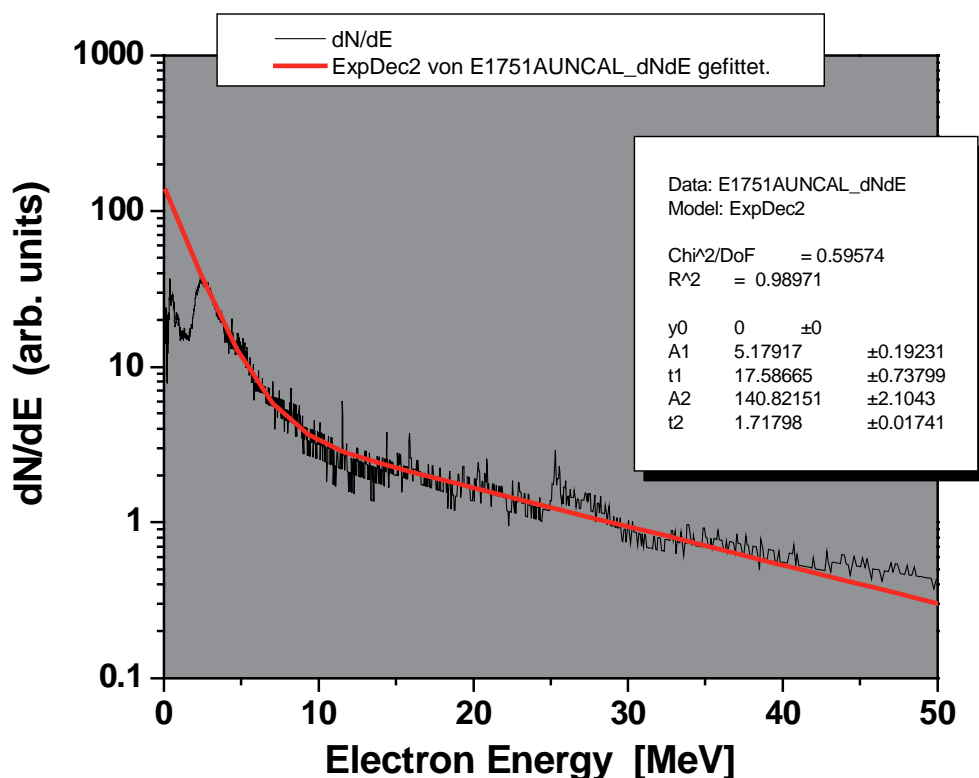


Figure 6.1: Electron spectra for a typical Au-target shot with 24J.

laser facility, were able to measure a part of that colder electron component exiting the rear surface of aluminum targets, employing optical transition radiation.

6.2 Proton acceleration from thin foil targets

As will be shown below by shooting a ultrahigh-intensity laser at any foil target, one will always accelerate protons, no matter what the target material. While heavier ions are a much better suited tool to probe the accelerating fields, some properties such as beam divergence for different energies, beam emittance and source size is much more readily measured by protons. Due to their higher range the protons penetrate several layers of stacked Radiochromic Film Detectors while the heavier ions are normally already stopped in the first protective layer of nylon and never reach even the first dye layer.

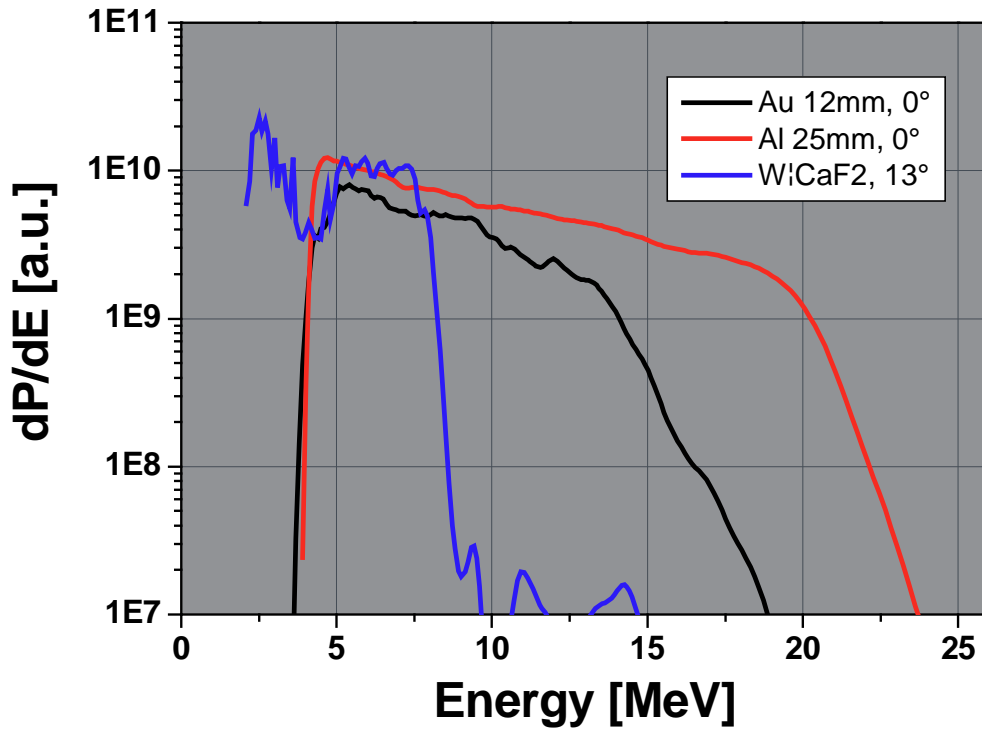


Figure 6.2: Proton spectra for an aluminum target (black), a gold target (red) and a coated tungsten target (blue). The spectra from gold and aluminum were measured at 0° , the one from the tungsten target at 13° , explaining the lower cutoff energy.

6.2.1 Proton Spectra

The spectral shape of each proton energy distribution is generally continuous up to the cut-off energy, in agreement with the electrostatic sheath acceleration mechanism and as well as observations in similar experiments [9, 39, 40]. Fig. 6.2 shows proton spectra from three different targets, namely from an Al-target, a Au-target, and a coated W-target. All these different target materials, as well as Teflon and other plastic targets, show strong proton spectra, dominating all other species and charge states. This is a known phenomena already observed with long pulse lasers, e.g. in [26]. The explanation lies in the typical vacuum conditions in laser experiments. All targets are coated with layers of hydrocarbons and the protons stem from those contaminants. It is shown that proton energies up to 25 MeV are typically achievable with the LULI 100 TW laser.

Taking into account the respective laser pulse energy in these experiments, we obtained an conversion efficiency of laser energy into protons on the order of a few percent, depending on actual shot parameters such as pulselength, prepulse level or target thickness. At a given maximum laser energy of 30 J and a conversion efficiency of $\sim 5\%$, a layer thickness in the nanometer range is sufficient to provide enough protons to be

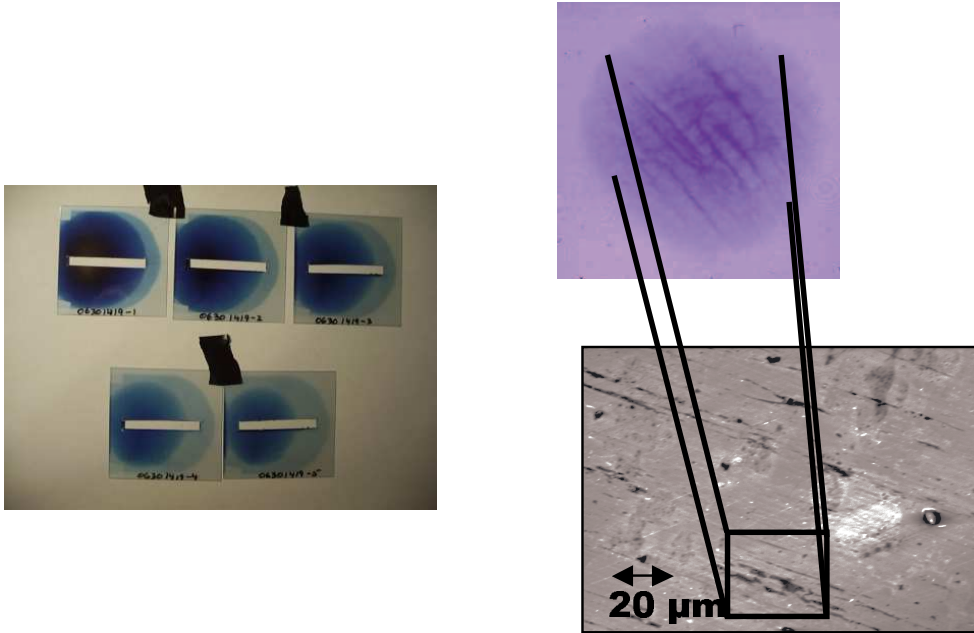


Figure 6.3: For an electroplated Au-target with smooth surface the signal is homogenous through all layers of RCF. For a target made from rolled gold structures appear in the proton signal which correspond to surface structures visible under an electron microscope.

accelerated. This observed conversion efficiency agrees well with experiments at similar facilities. At the Vulcan Laser at Rutherford Appleton Laboratory (100 J , $5 \times 10^{19} \text{ W/cm}^2$), conversion efficiencies of a also a few percent have been determined. From the Petawatt laser with both higher pulse energy and intensity up to 13% energy conversion is reported [9]. Another striking feature of the observed spectra is that the cutoff energy drops sharply at larger angles, as can be seen for the W-target in Fig. 6.2. This is the first indication for a really beamed ion emission with a rather small divergence. These feature is discussed in more detail in Sect. 6.2.2, but further details about the proton signal are not port of the scope of this work and will be published in [10].

6.2.2 Divergence, Emittance and Source Size

The angular dependence of the energy distribution of the proton beam was measured in two independent ways. The two ion spectrometers were positioned at different angles (0° , 6.5° , and 13°) as already explained in the previous section. The measured spatial distributions of protons on the dispersion plane were deconvoluted (with respect to the entrance aperture shape) and corrected for the spectrometer dispersion. The energy of the protons emitted normal to the target rear surface at 0° extended up to 25 MeV. The maximum energy of the protons dropped to about 10 MeV at an angle of 13° , as

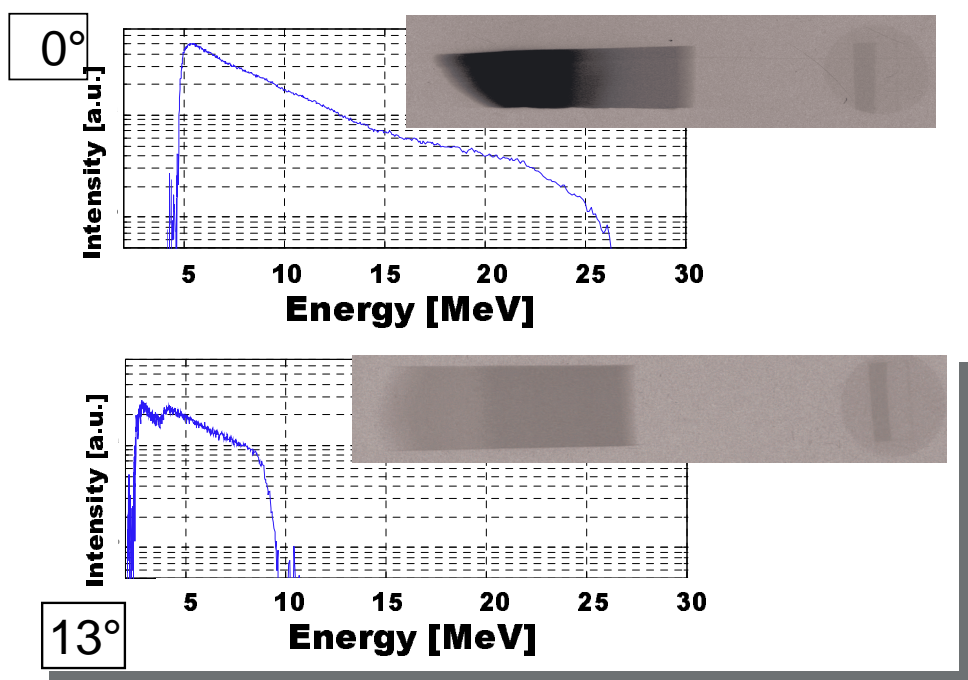


Figure 6.4: Proton spectra at 0° and 13° for a typical Au-target. The high-energy cutoff is strongly reduced at larger angles.

shown in Fig. 6.4 and consistent with a 2-D model of the sheath acceleration process. The other measurement is performed with the RCF stack detectors which record the ion beam crosssection for different energies as shown in Fig. 6.3. Both measurements yield an approximately 15° half-angle for the MeV-protons and a considerably smaller divergence for the high energy part of the spectrum [40].

An excellent way to measure the proton beam divergence as well as the actual source size as a function of proton energy was discovered accidentally in our experiments: in some of the beam imprints recorded in RCF, structures and lines were discovered whereas other shots from the same type of targets (e.g. $50\ \mu\text{m}$ Au-targets) produced a nice homogenous proton signal as is shown in Fig. 6.3. Upon closer investigation it turned out that a number of the targets were electroplated gold foils with a very smooth surface, while others were made from rolled gold and their surface is heavily structured as can be seen on the electron microscope pictures in Fig. 6.3. This effect can be put to use by shooting a target with a defined and well known structure on the back surface. The RCF in Fig. 6.5 was recorded with a $18\ \mu\text{m}$ thin Al-target with a one dimensional grid structure on the back surface. The grid was $0.2\ \mu\text{m}$ deep and had a spacing of $3\ \mu\text{m}$. From the number of visible grid lines one can now instantly deduce the source size. The overall beam divergence can be determined from the diameter of

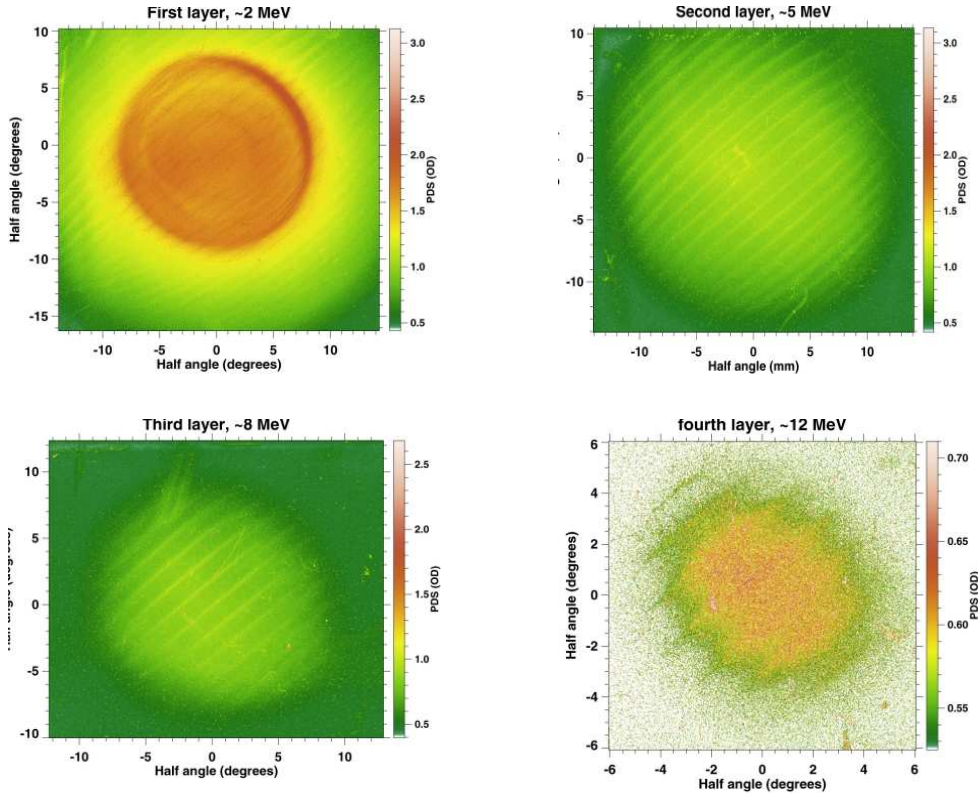


Figure 6.5: Proton signal in RCF from an $18\ \mu\text{m}$ Al-target with a $0.2\ \mu\text{m}$ deep and $3\ \mu\text{m}$ wide grid structure. The laser shot was fired at LANL’s Trident Short Pulse Laser and contained 26 J in a $\sim 20\ \mu\text{m}$ diameter focus. The pulse length was about 1.2 ps, making for an Intensity of $\sim 7 \times 10^{18}\ \text{W}/\text{cm}^2$ on target.

the beam imprint. A systematic analysis of the source size and beam divergence is displayed in Fig. 6.6 and published in [94].

For most of the future applications of laser generated ion beams the beam quality is the most important characteristic. Especially for the use as an ion source or the application as an inertial confinement fusion (ICF) ignitor beam, the ion beam emittance is crucial with respect to the accelerator structure acceptance or the achievable focus spot size. As is apparent from the radiochromic film data, the angular divergence of the proton jet is rather well defined and decreases with increasing proton energy. This suggests that protons or other light ions accelerated by this mechanism may have a usefully small emittance in the sense of an actual ion beam. To precisely estimate the emittance, penumbral imaging of edges at different distances from the target was used, to directly measure the core emittance of the proton beam. This technique is closely related to the conventional slit-emittance measurements made with apertures and screens at conventional accelerators. The normalized emittance of protons from flat gold foils is

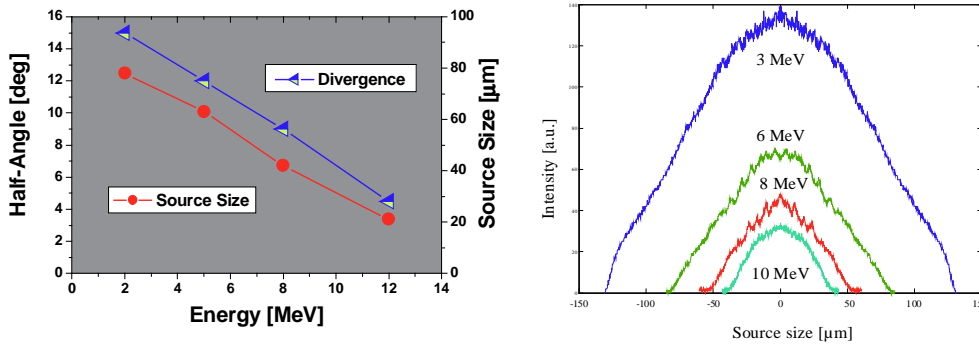


Figure 6.6: Real source size of laser accelerated protons in dependence of their energy. The spot size at the rear surface decreases from 260 μm diameter for 3 MeV protons to 80 μm diameter for 10 MeV.

determined to be of the order of 0.2 pi mm-mrad. The results of this analysis and subsequent modeling, developing a 2-D extension of the model in [45], suggest that we observe a rather cold proton beam, which is smoothly diverging and highly laminar. The phase space of the highest energy protons exhibits a tilted ellipse, whose width ultimately is the characteristic of the ion temperature. From these data, we deduce that the transverse proton temperature is less than ~ 1 keV. From simple electron-ion collisional heating during the expansion, one may expect the ion temperature to be even lower, on the order of ~ 100 eV.

6.3 Influence of target and surface properties on the ion acceleration.

6.3.1 Plasma density gradients

The determining parameter for the electron acceleration on the target front side, apart from laser energy and intensity, is the density gradient of the preplasma. This in turn is determined by the contrast ratio of the laser pulse, or the pre-pulse level. At a focal intensity of $10^{19}\text{W}/\text{cm}^2$ even with a contrast ratio of 10^{-7} at a few ns before the main pulse, this prepulse is strong enough to create a plasma. For the electron acceleration a large preplasma is beneficial, the drawback however is, that the prepulse also launches a shockwave through the target.

When we applied a prepulse at a contrast ratio of 10^{-7} of the main pulse 10 ns before the main pulse the maximum energy of the protons dropped to 2 MeV from the typical 10-20 MeV range typical of low-prepulse shots [40]. This is in good agreement with

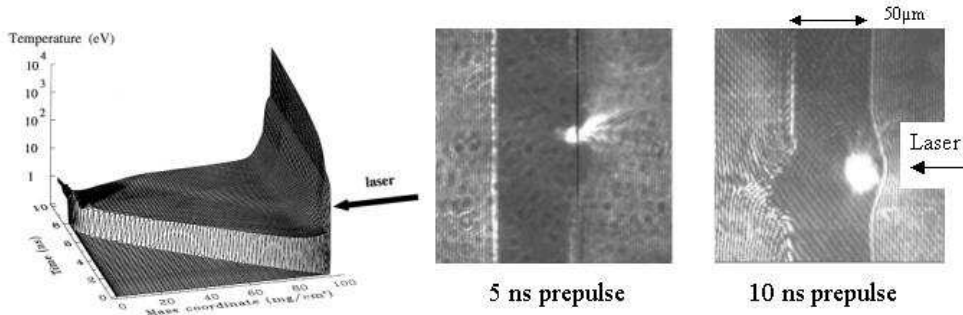


Figure 6.7: left: simulation of the shock wave launched by the prepulse. The shock wave reaches the rear surface at about 7 ns. middle: Interferometric image of the plasma conditions on the front and rear target surface at normal prepulse level at 5ns before the main pulse. No shock breakout occurred yet, the rear surface is unperturbed. right: The prepulse at 10 ns before the main pulse causes perturbation of the rear surface due to shock wave breakout. No protons were detected.

the MULTI calculations, which indicate that in 10 ns a shock wave launched by the prepulse penetrates the target and causes a rarefaction wave that diminishes the density gradient on the back and therefore drastically reduces the accelerating field. The inward moving shock wave also alters the initial conditions of the target material due to shock wave heating and therefore changes, e.g., the target density and conductivity. Because of its relevance to the electron transport, we chose the target thickness such that a considerable fraction of the target was still in its unperturbed, initial conditions. Fig. 6.7 also shows interferometric measurements of the target surface with and without the additionally applied prepulse. The interferometry detects the plasma density conditions on the front and rear surface simultaneously. In the figure, the laser is incident from the right (note that the bright spot is 2ω emission from the laser plasma during the pulse). As shown in Fig. 6.7, the front surface always shows the blowoff plasma caused by the ASE. In absence of a prepulse (left image) the rear surface is unperturbed and a high-energy proton signal could be detected on the RCF. When we observed the presence of an extended plasma at the rear surface due to the applied pre-pulse, no protons above the detection threshold of our RCF (~ 2 MeV) were measured. This result is also in excellent agreement with experiments using a second laser to generate a plasma at the rear target surface .

6.3.2 Front surface damage

Another somewhat accidental discovery in our campaign was the influence of any front surface damage structure on ion signal. While it stands to reason that a damaged front

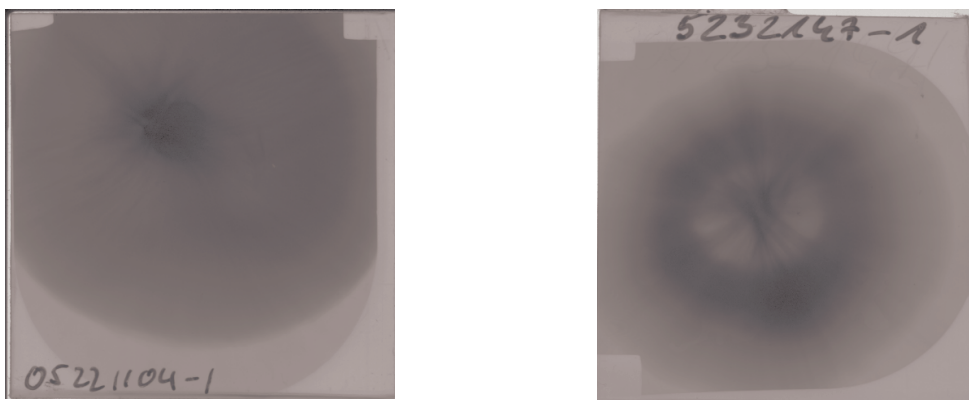


Figure 6.8: Beam imprint for an undamaged (left) and a damaged (right) target front side. A small crater on the front side caused a ring structure in the proton signal.

surface is not necessarily beneficial to the ion signal we did not plan dedicating any shots towards that problem. However at one time we had to use the 10Hz seed pulse to align the target instead of the usual HeNe-alignment laser. It turned out that the weak seed pulse was strong enough to dig a little pit in the target surface and instead of the usual smooth disk-like ion beam cross section we detected a ring structure as shown in Fig. 6.8.

Such ring-like structure keep appearing in experiments (e.g. [39]) and while a front surface damage is not the only possible explanation for such a signal it is worth keeping in mind the possibility.

6.3.3 Rear surface damage

As already shown above in Sect. 6.2.2 any structure on the back surface is mapped onto the ion signal. If the surface becomes too rough the beam even filaments and loses a considerable amount of energy. If the scale of the damage becomes large compared to the Debye length, which for our parameters is on the order of a few microns, the proton signal vanishes completely.

6.3.4 Conductors and Insulators

While most of our targets were metal targets, i.e. conductors, we also shot a variety of different plastic and even glass targets which are insulators. Though insulators also produce an ion signal of about the same strength and energy, the beam cross section is not homogenous as with conductors but strongly filamented. The similar beam patterns obtained from plastic and glass targets exclude the origin (surface or

bulk) of the protons to be the reason for the onset of the filamentary structures. In contrast, due to the strong coupling of the ion acceleration mechanism to the electron distribution at the rear surface of the target the smooth, laminar beam quality from metal, i.e. conductor targets, indicates a rather homogenous electron transport through the target. Insulating material seem to disrupt the electron transport, which causes filamentation of the electron distribution and therefore also a non-homogenous ion acceleration. The dependence of the electron transport on target conductivity has been observed by other research groups as well. As mentioned above the preceding ASE leads to a shockwave that preheats the target, thereby changing the conductivity of the insulating targets. However, in our experiments the target thickness has been chosen such, that a considerable fraction of the target material was still in the cold, solid state by the time of arrival of the main pulse.

6.3.5 Curved Targets

An important question to be addressed for any future application of laser-accelerated protons and ions is the possibility of tailoring the proton beam, either collimating or focusing it, by changing the geometry of the target surface. Ballistic focusing of the laser accelerated protons is expected to be rather difficult because of the inherent divergence associated with the spatial density dependence of the hot electron sheath, which drives the acceleration. Accordingly, we first attempted to defocus the beam in one dimension, by using a convex target. Using a 60 μm diameter Au wire as a target basically constituted such a one-dimensional de-focusing lens, and we observed a line as shown in Fig. 6.9. Tilting the wire also changed the orientation of the line, which results from the radial, fan-shaped expansion of the protons normal to the wire.

If one wants to focus the ions, there is an energy dependent angle of divergence that has to be compensated for. Therefore the effective focal length of a curved target rear surface is dependent on the ion energy. First results, that will be published in [95], show a strong reduction in the divergence of the central core of the proton beam representing ballistic collimating of laser produced proton beams.

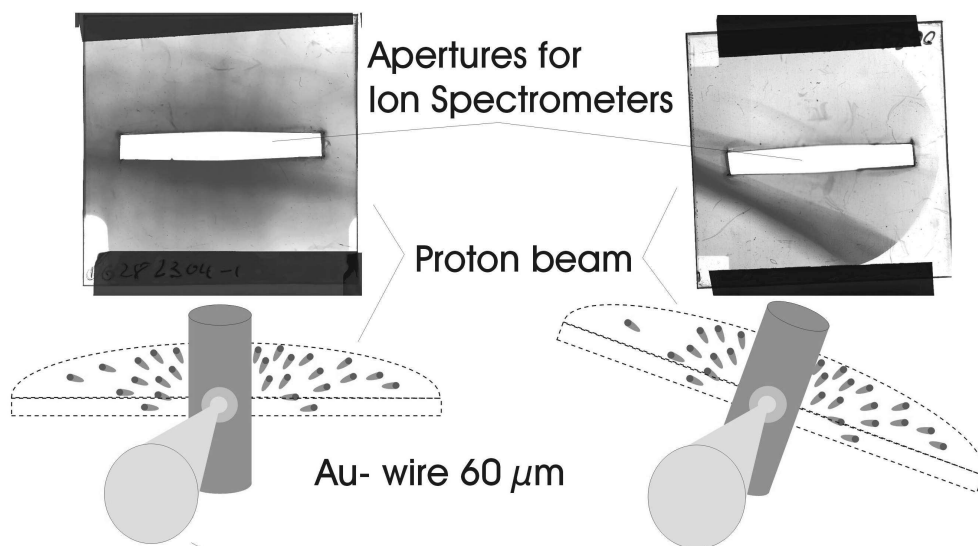


Figure 6.9: Experimental setup and RCF images of experiments with $60 \mu\text{m}$ gold wires. The convex rear surface constitutes a de-collimating cylinder-lens. Accordingly the proton beam was formed into a line.

Chapter 7

Acceleration of light Ions by short-pulse Lasers: Experimental Results

In this chapter, the first experimental study is presented, demonstrating that besides protons, also high-brightness, high-energy (\sim MeV/nucleon) ion beams can be accelerated from the *rear surface* of thin foils. As was shown in the last chapter and also observed by other groups experiments, no matter what target material is chosen, one always excites predominantly protons. These protons stem from hydrogenous impurities, such as water vapor and pump oil, adhered to the target surface. Due to their larger charge-to-mass ratio, the protons are accelerated more efficiently and outrun the other ion species thereby screening the accelerating fields for the latter. By removing the hydrogenous surface contaminants one can therefore increase the field coupling to heavier ions and accelerate them efficiently. Using the Thomson-parabola detector described in Chapter 5 high-resolution, absolutely calibrated energy spectra of different ion species and charge states could be obtained. From these spectra additional information, not contained in the proton signal, about the spatio-temporal evolution of the accelerating field and the origin of the observed ions could be extracted.

7.1 Removal of Hydrocarbon Contaminants by Target heating

As was shown in Chapter 6, no matter what target material one chooses, one always accelerates protons. This is due to the fact, that because of the technical setup and experimenting procedures at high-power lasers the vacuum in the target chamber is

on the order of 10^5 mbar. At this pressure levels all surfaces are coated by films of water- and oil-vapor even when using theoretically oil free components. That means that all targets will have protons present at their surfaces, which due to their at least twice as big charge-to-mass ratio, will always be more effectively accelerated than any other ion species and charge state. Thereby the protons take up the major part of the available energy and screen the accelerating potentials. To efficiently accelerate other ion species one therefore has to use targets which do not contain any protons. To do this the target has to be cleaned in situ and since typical desorption times are on the order of milliseconds, as close to the firing of the laser as possible or preferably even during the laser shot.

7.1.1 Cleaning Methods

The way to clean the target is to transfer enough energy to the contaminants to overcome the adhesion forces acting at the surface, i.e. heating the target or at least the target surface. Three different approaches were tried, depending on the target properties and other experimental parameters:

1. radiative heating
2. laser heating
3. resistive-heating as used in [96, 5].

While radiative heating with a strong lamp did not produce high enough temperatures to have the desired effect, the other two methods worked with resistive heating being the most effective if used in conjunction with a suitable target material. For resistive heating a ~ 10 A current at ~ 12 V was run through the target, which required fairly thick and therefore inflexible wires attached to the target mount as shown in Fig. 4.9. This reduced the number of targets on the mount from four to three and also constricted the movement of the setup, complicating the alignment. Some targets as the deuterated targets used for the neutron experiments [11] could not be heated to high temperatures without destroying them but required nonetheless the removal of protons. A nanosecond-pulse Nd:YAG-laser slaved to the main trigger roughly 100 μ s before the main pulse was used to ablate the outermost surface layer of the target, thereby taking with it part of the hydrocarbons.

The first series of dedicated ion experiments used aluminum targets coated with a carbon layer on the back surface. The targets were heated to just below the melting point of aluminum at 933 K. The current had to be carefully ramped up to just below the melting point, the correct parameters were determined by trial and error and a

number of targets burned through prior to the laser shot. Once the right parameters were established it was crucial to fire the laser as quickly as possible before burnthrough occurred. Subsets (a) and (b) of Fig. 7.1 show the measured Thomson parabola signals of unheated and heated aluminum targets coated with 1 μm carbon. From the unheated target basically only protons were accelerated, the ion number being more than two orders of magnitude lower and hard to spot in the scatterplot without an in detail analysis (comp. Fig. 7.3). In the case of the heated target the ion signal becomes clearly visible, even dominating the proton signal which is however still present, though reduced by more than an order of magnitude. In combination with the aluminum targets the resistive heating cleaning procedure showed its potential by removing a big enough percentage of hydrocarbons to enhance ion acceleration in overall ion numbers as well as in ion energy and conversion efficiency of laser energy to ions. However it became clear that higher temperatures are required to get rid of all hydrocarbons and this could not be achieved using aluminum substrates. Therefore tungsten target substrates were used in the later runs which were heated until they were white hot glowing, i.e. well above 1300 K. As shown in subset (c) of Fig. 7.1 the procedure worked perfect for tungsten targets and no protons were left on the target surfaces at the time of the laser interaction. The ion energy was increased further and also the energy conversion efficiency as discussed later in this chapter in more detail. Subset (d) finally shows the results of the laser cleaning process. The respective ion and proton fractions compare to the resistive heating case for aluminum targets, i.e. enough protons are removed to make a difference to the unheated case but the conditions are still far from optimal.

7.2 Energy Spectra, Yield and Divergence of the ion bunches

Using the two Thomson parabola detectors in conjunction with the automated scanning microscope and the custom made pattern recognition and analyzing software described in Chapter 5 it was possible to obtain absolutely calibrated, high resolution energy spectra for different ion species and charge states. Apart from demonstrating the ability to accelerate except from protons also heavier ions at various charge states these spectra contain information on the underlying physical processes not available in the proton signal. The charge state distribution and the cutoff energies of the individual charge states are a tell tale sign of the dominant ionization and recombination processes. Also they yield information on the field strength and the spatial and temporal extensions of the acceleration process. The highest ion energies were achieved with

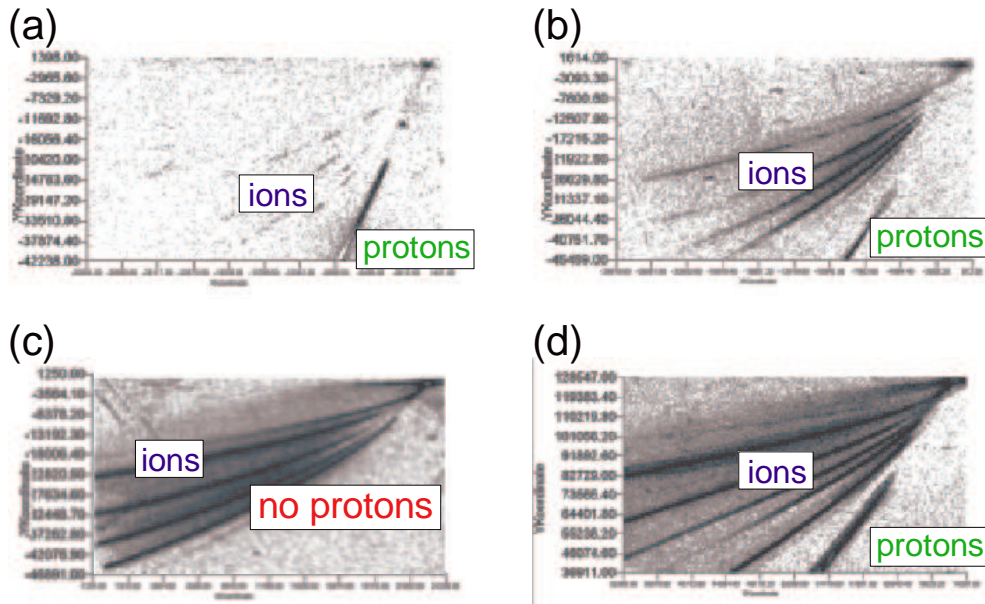


Figure 7.1: (a) Ion traces from an unheated Al|C-target on CR39. A strong proton line which is even too dense for counting at its onset is clearly visible while the ion signal is extraordinarily faint. (b) An Al|C-target resistively heated to ~ 800 K shows a strong increase in the ion signal and energy while the proton signal is reduced. (c) By heating W-targets to ~ 1300 K all protons can be removed. The ion signal and energy is strongly enhanced by orders of magnitude. (d) Al| D_2 -target cleaned by laser ablation with a mJ-ns Nd:YAG pulse some $100 \mu\text{s}$ before the main pulse. The result is similar to the resistive heating for Al-targets: The ion signal is enhanced but a substantial proton fraction remains.

tungsten targets coated with Calcium Fluoride (CaF_2), however due to the multitude of charge states with similar charge-to-mass ratio the detailed analysis proved to be difficult. From the CaF_2 -targets fluorine ions, calcium ions and residual carbon ions are accelerated and the individual traces overlap. Fig. 7.5 shows an example of a deuterated aluminum target where it is just possible to recover most of the traces and obtain spectra. But even in this case one Al-trace is missing while one other trace cannot be identified unambiguously. Much better results could be obtained by using a simpler carbon system with only 6 potential (and 5 observed) charge states. The modelling and interpretation of the acceleration mechanism is therefore done using the carbon spectra. The drawback of the Al|C-targets which could not be heated enough to drive out all the hydrogen imbedded in the carbon matrix, turned eventually out to be an advantage: It allows a much more detailed analysis of the influence of the hydrogen on the obtained spectral shapes, since now a series of different fractions of hydrogen contamination (dominantly hydrogen, approx. equal hydrogen and ion fractions, and

no hydrogen) could be studied in experiment and compared to simulations as is done in Chapter 8. Finally, also Deuterium spectra were obtained to supplement the measurements by S. Karsch ([11]) on fusion neutron generation and ion acceleration within the laser focus region.

7.2.1 Carbon Spectra

While the main in energy in the case of unheated targets is transferred to protons, other target ions are accelerated, too. For all unheated targets however the main part of the accelerated ions stems out of the contaminating hydrocarbon layers, resulting in acceleration of carbon ions independently of the target material. Thus, carbon spectra were obtained from a variety of different targets, and could indeed also be obtained on shots dedicated to other experiments. Consequently, carbon spectra form the majority of measured spectra, making carbon the best candidate for all comparisons and systematic studies. Figure 7.2 shows a typical result for a parasitic measurement performed on planar Au and Al targets set up to study the proton beam quality. The picture shows the Thomson parabola raw data and the corresponding carbon spectra for both targets. As noted in Chapter 5 there are three major difficulties in obtaining a proton spectra from the Thomsonparabolas: The crater size in the CR-39 depends on the energy loss of the particle and is substantially lower for protons than for other ions. Consequently proton tracks will be much smaller and reach the resolution of the used scanning microscope at about 3 MeV. To circumvent this problem one has to use longer etch times, thereby enlarging the tracks. However, due to the enormous particle numbers in the experiments and the resulting high track densities on the CR-39 this would cause the tracks to overlap significantly and again prevent a detailed counting. Since the main goal is to analyze heavier ions the choice of pinholes, detector stand-off distance, and etch conditions were optimized towards that purpose. This means that the high energy part of the proton signal above ~ 3 MeV could not be counted and the low energy part is frequently too dense to give a very accurate counting either. The proton signals as obtained from the Thomsonparabolas have therefore to be judged as a mere lower threshold while the real spectrum shows substantially higher energies. This choice of experimental parameters was further motivated by the fact that an independent proton spectrometer was operated on the experiment. The data obtained from that diagnostics will be presented in [10].

Both targets were irradiated with approximately the same laser energy, ~ 11 J, and for both targets the high energy cutoff for the helium-like carbon charge state is at slightly above 0.5 MeV/nucleon. This is a fairly typical cutoff energy for all unheated targets. When one looks in detail however, the Au-target shows slightly higher energies and ion

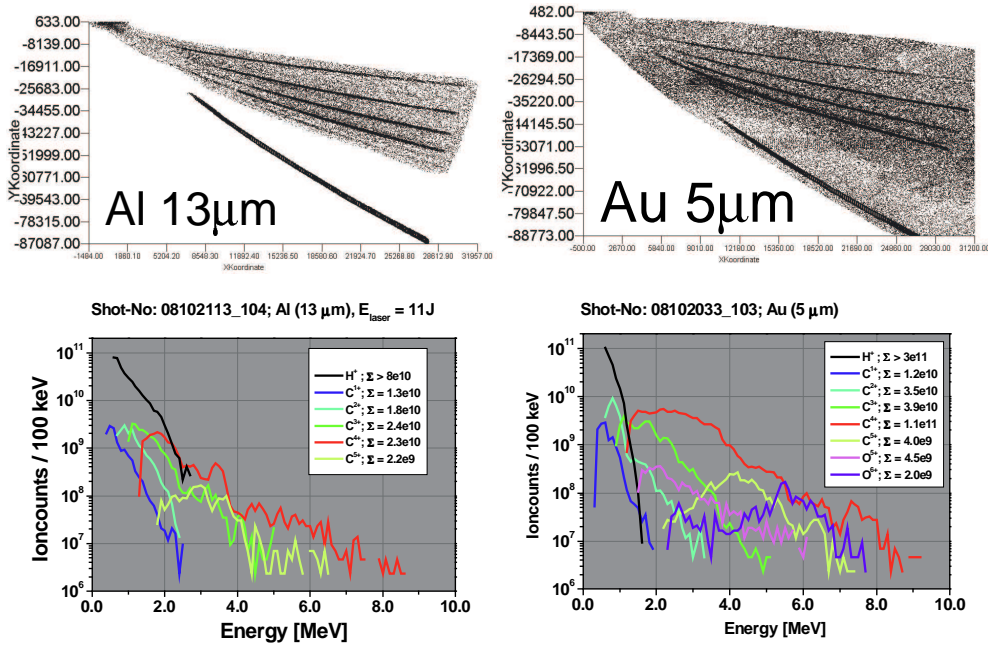


Figure 7.2: Typical Thomsonparabola raw data and spectra for unheated targets. Left: 13 μm Al-target, 11.2 J laser energy, right: 5 μm Au-target, 12 J laser energy. Both cases show strong carbon spectra, however in the case of the thin gold other traces, probably Oxygen, are also present, albeit very weak.

numbers and also some weak oxygen charge states. This is due to the smaller target thickness. As was shown in Chapter 6 thinner targets, as long as they do not suffer plasma breakthrough, tend to exhibit stronger fields caused by higher local electron densities. A thick Au-target as shown in Fig. 7.3 (a) shows a much weaker signal although the laser energy was more than 50% higher.

To examine the possibilities of target cleaning and enhancing the heavy ion yield we started with carbon coated Al-targets, which were easy to fabricate and the expected carbon spectra can be readily compared with those of other targets. We first shot a unheated aluminum substrate of 50 μm thickness coated on the backside with 1 μm of carbon. When not heated however the carbon signal is fairly weak and dominated by protons. The resulting spectra is shown in Fig. 7.3 (b), and again the He-like cutoff energy is around 0.5 MeV/nucleon.

If one now heats the target close to its melting point prior to the shot, a major fraction of the contaminants boils off from the surface into the vacuum. The number of accelerated protons is strongly reduced and the energy is instead transferred to heavier ion species. Already the partial removal of hydrocarbons strongly enhanced the acceleration of carbon ions, as shown in Fig. 7.1 and in the spectra in Fig. 7.3 (c). The proton

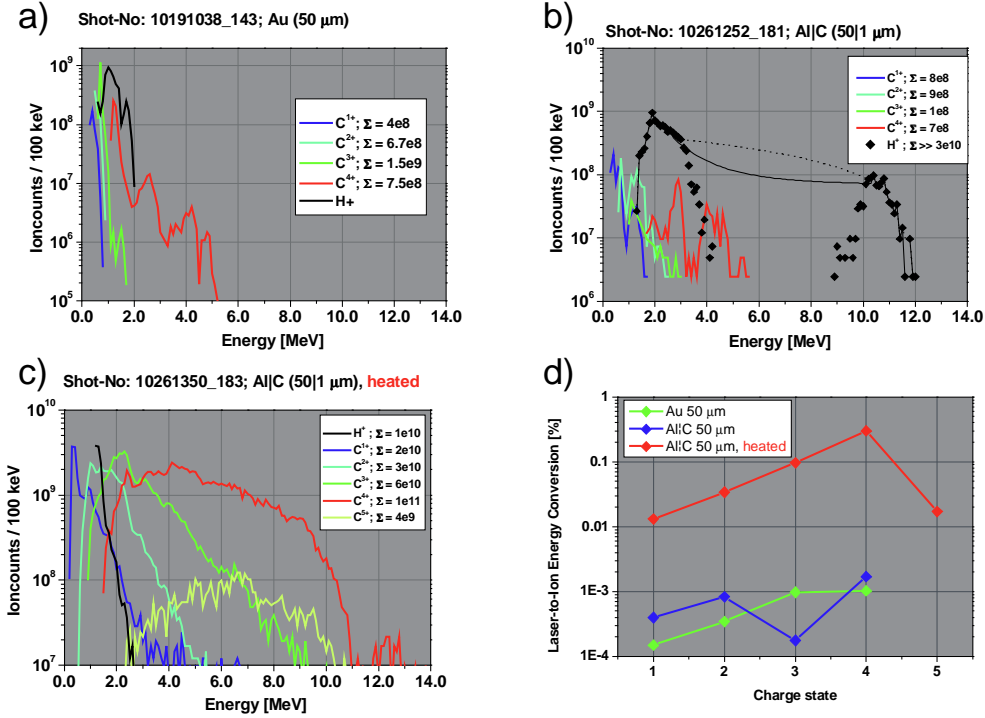


Figure 7.3: (a) Carbon spectra for an unheated 50 μm Au-target: the ion yield is very weak, the high energy cutoff for the highest charge state is around 0.5 MeV/nucleon. (b) Carbon spectra for an unheated Al|C-target (50 μm): the proton signal shows a gap due to detector properties which is optimized for heavier particles. The lines show two fits to bridge the detector gap H^+ -spectra, but the real spectra has still a high energetic tail which cannot be accounted for from the Thomson parabola -signal. (c) Carbon spectra for a heated Al|C-target (50 μm): The ion signals are strongly enhanced and the high energy cutoff is at higher energies. (d) Conversion efficiencies of laser energy to ions for all three targets: The unheated targets show a similar behavior. The heating increased the energy in the heavy ion signal by two orders of magnitude.

spectrometer yielded typically $\sim 10^{12}$ protons of up to 25 MeV, for unheated targets. For heated Al-targets, the number of protons is reduced to $\sim 10^{10}$ with energies of up to 3MeV as confirmed by the RCF-stack. The high-energy cutoff of the carbon ions rises by a factor of ~ 2 and the number by two orders of magnitude to $\sim 2 \times 10^{11}$. A detailed comparison between the heated and unheated targets as well as a standard 50 μm Au-target can be found in Tab. 7.1: The conversion efficiency from laser energy into heavy ion energy increases by more than two orders of magnitude from 0.002% to 0.5% (see Fig. 7.3 (d)). As one can see in Fig. 7.4, the acceleration is most efficient for C^{4+} -ions, with a spectral cutoff at ~ 1 MeV/nucleon at the high-energy-end. The other cutoff energies and overall ion numbers fall with the charge state number, the

Table 7.1: Conversion efficiency of laser energy into carbon ions for an unheated (u/h) Au-target, an unheated (u/h) Al|C-target and a heated (h) Al|C-target (reduced proton contamination). All targets were 50 μm thick. The ion charge states are denoted by Q.

Q	u/h Au			u/h Al C			h Al C		
	Ion No.	E_{abs} [J]	Conv. [%]	Ion No.	E_{abs} [J]	Conv. [%]	Ion No.	E_{abs} [J]	Conv. [%]
1	$4 \cdot 10^8$	$2.7 \cdot 10^{-5}$	$1.5 \cdot 10^{-4}$	$7.9 \cdot 10^8$	$7.9 \cdot 10^{-5}$	$4 \cdot 10^{-4}$	$2 \cdot 10^{10}$	0.004	0.013
2	$6.7 \cdot 10^8$	$6.2 \cdot 10^{-5}$	$3.4 \cdot 10^{-4}$	$8.8 \cdot 10^8$	$1.7 \cdot 10^{-4}$	$8.3 \cdot 10^{-4}$	$3.3 \cdot 10^{10}$	0.009	0.034
3	$1.5 \cdot 10^9$	$1.7 \cdot 10^{-4}$	$9.7 \cdot 10^{-4}$	$1.3 \cdot 10^8$	$3.5 \cdot 10^{-5}$	$1.8 \cdot 10^{-4}$	$5.7 \cdot 10^{10}$	0.026	0.096
4	$7.5 \cdot 10^8$	$1.8 \cdot 10^{-4}$	0.001	$6.5 \cdot 10^8$	$3.4 \cdot 10^{-4}$	0.002	$9.9 \cdot 10^{10}$	0.081	0.3
5	–	–	–	–	–	–	$4.5 \cdot 10^9$	0.005	0.017
Σ	$3.3 \cdot 10^9$	$4.5 \cdot 10^{-4}$	0.002	$2.5 \cdot 10^9$	$6.2 \cdot 10^{-4}$	0.003	$2.1 \cdot 10^{11}$	0.12	0.5

main acceleration and energy transfer processes happen during the time of highest field strength, on a timescale comparable to the duration of the laser pulse. The C^{5+} charge state alone shows lower energies and much lower numbers than its predecessor, suggesting a different ionization mechanism than for the other charge states. While C^{1+} to C^{4+} are created almost instantaneously in large numbers by field ionization as soon as the field reaches the ionization threshold (comp. Chapter 3), C^{5+} ions seem to be created by collisional ionization during the whole process. As will be explained in more detail in Sect. 8.1.2, the low cross section of the high energy electrons and the rather delocalized spatial and temporal origin lead to the lower numbers and energies.

The highest carbon energies were obtained on a shot dedicated to neutron production with a Al-target coated with CD_2 . Resistive heating was not possible because the Deuterons would be removed as well, so laser cleaning with a ns-pulse laser a few milliseconds before the main shot was tried. While this method was employed on a number of occasions and usually produced the same results as resistive heating of aluminum targets, i.e. ~ 1 MeV/nucleon ion energies, in this particular case the timing and focal conditions of the cleaning laser seemed to be better suited for the task and a greater fraction of Hydrocarbons were removed. This resulted in higher numbers of heavier ions and helium-like carbon and aluminum ions with energies of ~ 2.5 MeV/nucleon as can be seen in Fig. 7.5.

7.2.2 Fluorine Spectra

Even better results were obtained using tungsten as a target substrate. 50 μm tungsten substrates coated with a 300 nm thin layer of CaF_2 were used as targets both heated and unheated. The higher heating temperatures resulted in an almost complete removal

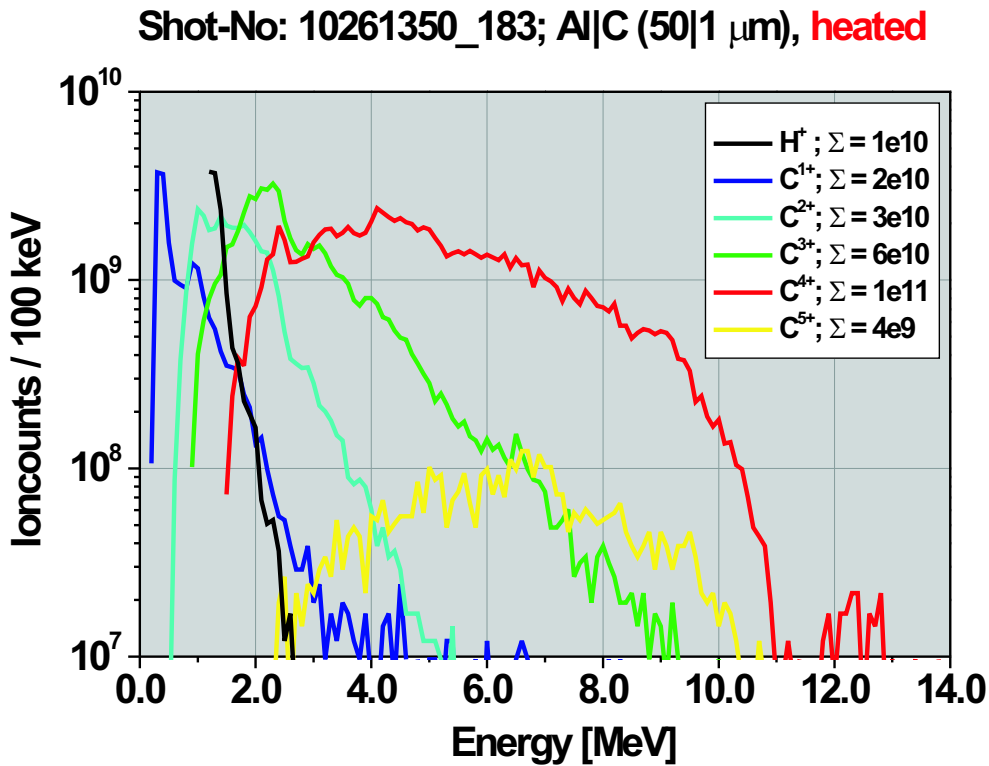


Figure 7.4: Carbon spectra for a heated Al|C-target (50 μm): The ion signals are strongly enhanced and the high energy cutoff occurs at higher energies. The cutoff energies and ion numbers increase with increasing charge state.

of hydrocarbons. As shown in Fig. 7.7 the proton spectrometer did not show any protons, while for an identical unheated target a typical proton spectrum for this target thickness was measured (see Fig. 7.7). The proton spectrometers lower energy cutoff is at ~ 2 MeV, while the Thomson parabola detects protons between 200 keV and 3 MeV. Since the CR-39 also showed no protons for the heated target we can rule out any significant amount of high energetic protons. The energy transferred instead mainly to the fluorine ions, especially the helium-like charge state. As shown in Fig. 7.6, energies up to 100 MeV were achieved for fluorine 7+ ions. This corresponds to more than 5 MeV per nucleon, the highest energy so far achieved for laser accelerated heavy ions. This finding is confirmed by the RCF data, shown in Fig. 7.7. A narrow spot appears in the first layer, which, in the absence of protons, indicates fluorine ions of energies of more than 4 MeV/nucleon. This is also the first measurement of a heavier ion beam profile and agrees well with the observed proton signals, as will be discussed in Sect. 7.2.3. The conversion efficiency of laser energy to ions was again increased by one order of magnitude. The F^{7+} ions alone hold more than 4% of the laser energy. The lower charge states however could not be distinguished as well as in the carbon

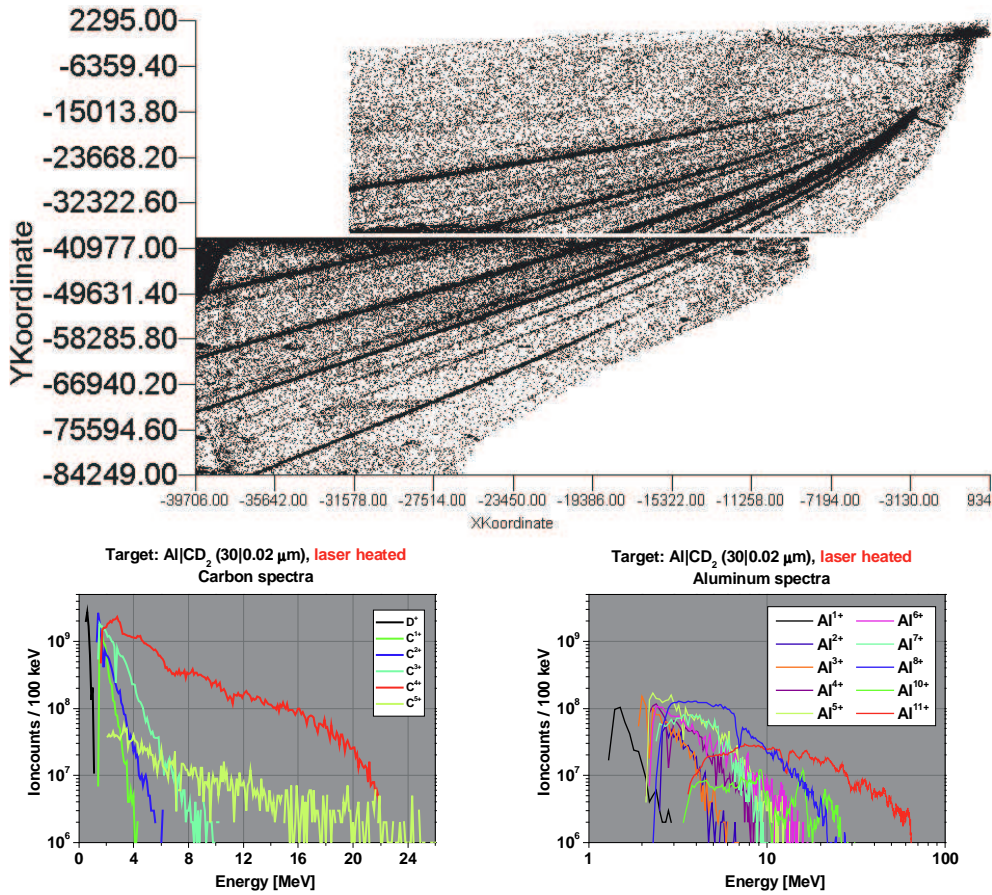


Figure 7.5: Carbon and aluminum spectra for a laser-heated Al|CD₂-target: The ion signals are strongly enhanced and the high energy cutoff occurs at even higher energies as before. Spectra for all carbon charge states up to C⁵⁺ could be identified and nearly all charge states of Al up to 11+. The Al₉₊ charge state cannot be identified since it coincides with the C⁴⁺ charge state. Between Al₃ and Al₄₊ is a track that could not be identified.

cases, due to a multitude of different charge states and species with sometimes close to identical charge-to-mass ratios .

Furthermore since only the target rear surface was coated with CaF₂, the fluorine ions found in our experiment originate unambiguously from the *rear surface* of the targets, proving once and for all the existence of an effective rear surface acceleration mechanism.

7.2.3 Divergence

For most of the future applications of laser generated ion beams the beam quality is the most important characteristic. Especially for the use as an ion source or an inertial

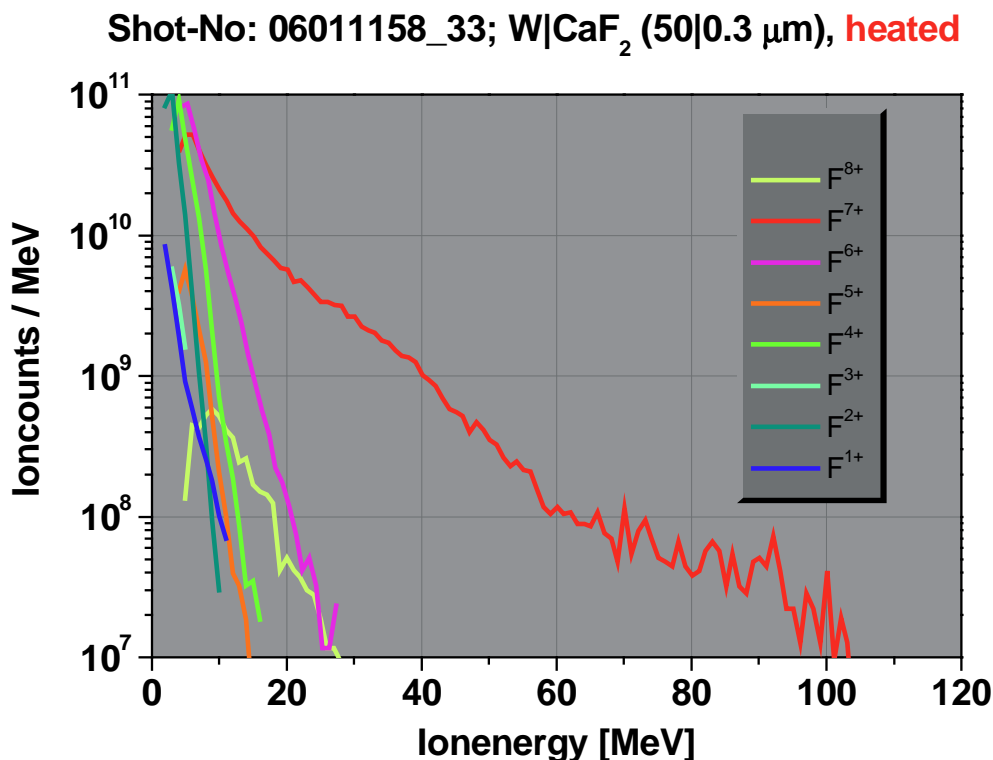


Figure 7.6: Resistively heated W/CaF₂-target: All protons were removed and F⁷⁺-spectra is now dominantly accelerated: More than 100 MeV (5 MeV/nucleon) energy and more than 4% conversion efficiency are achieved for F⁷⁺/ions.

confinement fusion (ICF) ignitor beam, the ion beam emittance is crucial with respect to the accelerator structure acceptance or the achievable focal spot size. As is apparent from the radiochromic film data, the angular divergence of the proton jet is rather well defined and decreases with increasing proton energy. This suggests that protons or other light ions accelerated by this mechanism may have a usefully small emittance in the sense of an actual ion beam. In contrast to the proton beam profile and divergence, which can be measured quite easily with stacks of radiochromic film, this is not possible in the case of heavier particles. Due to the higher stopping power all but the most energetic ions are stopped in the $\sim 60 \mu\text{m}$ thick protective Nylon layer covering the first dye layer of RCF. Only when one gets rid of all the protons and achieves optimal laser conditions for a shot, i.e. a high energy on target, a short pulse, and a small regular focal spot, the heavier ions gain enough energy to penetrate at least that first layer as can be seen in Fig. 7.7. Furthermore this gives only one signal for the highest energy and not, as with protons, different signals for a whole energy range. However this one signal agrees well with the measurements for proton signals, allowing the conclusion that the overall behavior with respect to beam divergence is similar.

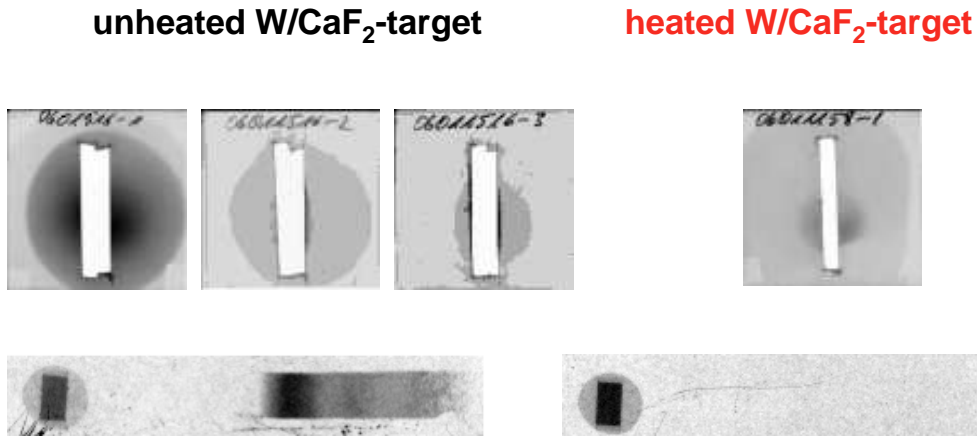


Figure 7.7: RCF and proton spectrometer raw data for shots on cold and heated W|CaF₂-targets. For non-heated targets the typical proton spectra was measured and the RCF detectors showed the usual beam profile. For the heated targets the proton signal completely vanishes, disproving the existence of high energy protons. The first layer of RCF shows a narrow spot, similar to the deeper layers, i.e. the high energy tail, of measured proton spectra. In the absence of protons this spot has to be caused by heavier ions and corresponds to fluorine ions >4 MeV/nucleon.

Another data point, this time for the low energy component could be obtained by replacing the RCF stack with a CR-39 plate. This will record ions of all energies i.e. especially all the low energetic particles. Due to the high flux, the CR-39 detectors are completely saturated with overlapping pits, making particle counting or any other quantitative analysis impossible, the overall transversal size of the ion beam however can be distinguished clearly. Again the ion beam divergence for low energies agrees with the proton data.

A more detailed measurement over the whole energy range was measured by employing two Thomson parabolas under different angles. The target chamber setup allowed for angles of -6.5° , 0° , and 13° , although only two angles could be occupied simultaneously. From our detectors we obtain absolute ion numbers for the small spatial angle of the spectrometers of $\sim 10^8$ sr. Fig. 7.8 shows that the ion spectrum is fairly constant over an angle of $\sim 7^\circ$ but drops steeply at 13° . This is true both for a moderately heated case where still a sizeable fraction of protons is left as in subset (a), as well as for the pure ion case shown in subset (b). Fig. 7.8 (a) shows C⁴⁺ spectra from resistively heated targets measured at three different angles, 0° , 6.5° , and 13° . The 0° and 6.5° spectra were obtained at the same shot, while the 13° spectra was obtained on a different shot. As can clearly be seen, the first two spectra are almost identical, a behavior observed on almost any other shots for 0 and 6° . For larger angles however the spectrum drops

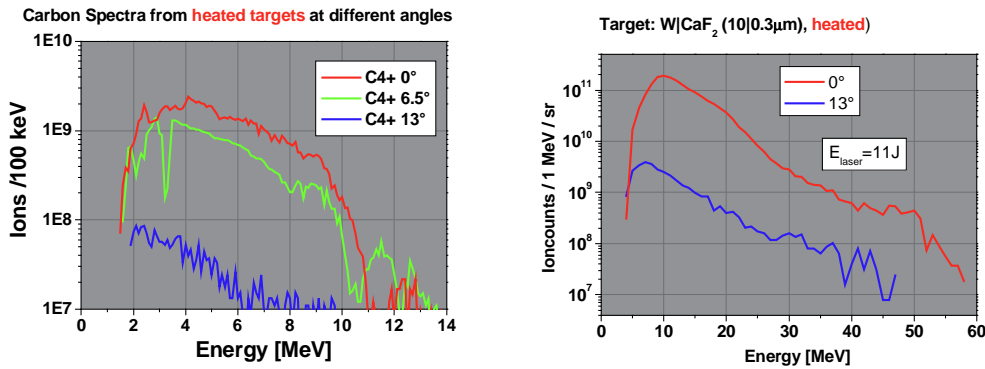


Figure 7.8: (a) C^{4+} spectra at 0, 6.5, and 13° from heated targets. The spectra at 0° and 6.5° were measured on the same shot. Due to the substrate a major proton fraction was still present but the ion acceleration was enhanced. (b) F^{7+} spectra at 0° and 13° from the same shot. The targets were resistively heated and most of the protons could be cleaned of. In both cases the 13° spectra are strongly decreased.

dramatically. The difference between the first two and the 13° spectrum in subset (a) might theoretically be accounted for in part by the difference in laser parameters between the two shots. The two F^{7+} spectra in subset (b) for 0° and 13° however were obtained on a single shot and show the characteristics. It is therefore safe to conclude and furthermore in agreement with the data discussed above, that the ions are emitted in a tight beam with a opening angle of $\sim 13^\circ$ as observed for the proton acceleration. Furthermore the measurements show that this behavior holds true over the whole spectral range of accelerated particles.

7.2.4 Source Size

A direct measurement of the source size as done in the proton case was not possible for heavy ions. RCF-detectors do not work due to the diminished range of heavier particles. CR-39 does not work either for this special measurement due to the extremely high current and particle densities which saturate the CR-39 and the possible detector distances and render a qualitative analysis using track counting impossible. Since however the performed divergence measurements reproduce exactly the proton properties it seems reasonably safe to assume the same features in source size.

Chapter 8

Analysis and Interpretation of the experimental Results

8.1 Analysis and Interpretation of the experimental data with respect to the underlying physics of the acceleration mechanism

To gain a better understanding of the acceleration mechanism from the measured ion data it is important to know how the charge state distributions were created. Therefore the following paragraphs first discuss recombination and ionization effects, drawing on the theory explained in Chapter 3. Then follows a detailed analysis of the measured spectra and charge state distributions with respect to the field dynamics. It turns out that the ion spectra contain new information not incorporated in any other experiment so far.

8.1.1 Recombination

As was already shown in the FLY-simulations in Chapter 3, recombination does not play a major role. This assumption is confirmed by the experimental data shown in Chapter 7. All spectra show a dependence of the high-energy cutoff on the charge state, which rules out recombination as a dominant effect in our experiments. If a major fraction of ions were to recombine on their way to the detector a high energy low charge state signal would be observable. The absence of this signal is the first experimental proof of a low recombination rate. Fig. 7.4 shows a roughly constant tail in the C^{1+} -distribution at a level of $\sim 10^{-3}$ compared to the higher charge state populations which likely originates from recombination and collisional ionization since

the neutral atoms are not accelerated and therefore have a much longer overlap time with the warm return current.

This finding is confirmed by a direct measurement. On all CR-39 track detectors from the Thomson parabolas an image of the pinhole can be seen. This must be formed by the low fraction of ions that actually recombine and are neutral upon entering the Thomson parabola. The number of ions in this zero-order image can be counted by the automated scanning microscope and for all analyzed shots it turns out to be between 0.1 and 1%. This is in good agreement with the spectra as well as the FLY-simulations. This behavior is fundamentally different from that observed in the carbon spectra in long-pulse experiments [3], where recombination played a major role and all charge states were found to have the same cutoff energy.

8.1.2 Ionization

Earlier work with ns-laser-produced C and CH plasmas demonstrated that the ion spectra can be used to infer the hot electron temperature. As noted previously, the ionization in those experiments was thermal from the direct laser heating, and $T_{e,hot}$ was nearly constant throughout the expansion ([3, 26] and ref. therein). For hot plasmas, only C^{6+} was present, and the other charge states were populated by recombination during the drift phase after the acceleration, leading to very similar energy spectra for each ionization state. From the ion spectra and their charge state independence an isothermal expansion with $T_{e,hot} \sim 10 - 100$ keV could be identified as the dominant mechanisms ([3, 26] and the acceleration could be described by a self-similar solution (see [97], Sect. 2.3.4).

As was shown in Chapter 3 field ionization dominates by orders of magnitude over collisional processes for our set of parameters and for charge states up to He-like. For C^{5+} , W_{col}^{hot} is stronger than W_{ADK} , which explains the different spectral shape and lower numbers for this charge state. Due to the short timescales (\sim fs) and high electron temperatures (\sim MeV) involved in short pulse experiments, Field Ionization by Barrier Suppression (FIBS) in the strong transient electric field dominates, leading to charge state distribution depending on the temporal shape and cooling behavior of the laser-induced electron pulse.

8.1.3 Field Dynamics

Having established that the ion spectra and charge state distributions are directly linked to the ionizing and accelerating E-fields we can extract information such as field strength, which is not available from proton data. With FIBS as the dominant

ionization process the $k+$ -ionic state is created as soon as the electric field is above the threshold

$$(8.1) \quad E_k = \frac{U_k^2 \varepsilon_0 \pi}{eZ}.$$

We can use $E_{k+1} - \epsilon$ as an upper limit for the electric field strength that a $k+$ -ion has experienced. This also defines a lower limit for the acceleration time τ_k^{min} required to achieve the observed maximum ion energy for a given charge state. The acceleration length l_k^{min} is the minimal distance an ion has to travel during acceleration and is therefore a measure for the minimal spatial extension of the fields.

The maximum field a C^{2+} -ion can have experienced for any effective time $t > fs$ is therefore $E_{2+}^{max} \leq 1.3 \times 10^{11} \text{V/m}$. This field causes the maximal acceleration if it is instantaneously switched on and off. The high energy cutoff for C^{2+} is at $W_k^{max} \sim 6 \text{MeV}$ as can be seen in Fig. 7.4. The minimum acceleration time τ_{min} an ion must have spend in the influence of the field E_k^{max} is given by

$$(8.2) \quad \tau_k^{min} = \sqrt{\frac{2W_k^{max}m}{E_k^{max}q}}$$

For the C^{2+} -ions in Fig. 7.4 this results in a minimum acceleration time of 4.6 ps, considerably longer than the laser pulse and therefore the source of hot electrons. For the F^{7+} -ions (Fig. 7.6) field strengths between 0.9 and 23 TV/m would be possible. Assuming a field strength of $\sim 2.5 \text{TV/m}$ as calculated using (2.22), the minimum acceleration time is $\sim 350 \text{fs}$, i.e. the laser pulse duration. Taking this method one step further the scale length of the accelerating fields can be estimated by calculating the distance the ions move during acceleration. The distance l_{min}^k is given by

$$(8.3) \quad l_k^{min} = \frac{E_k^{max}q}{2m}(\tau_k^{min})^2.$$

The results for all carbon charge states and the helium-like fluorine are tabulated in Tab. 8.1. For the helium-like charge states the calculation is done for three different field values: the minimum and maximum fields and an intermediate value given by (2.22). The results from intermediate field values are in good agreement with other parameters, such as laser pulse duration and Debye-length.

If a more realistic field form is assumed rather than a box-like profile with infinitely steep gradients, the values in Tab. 8.1 become even larger. Fig. 8.1 shows an example for C^{4+} -ions. In this case the modelled field rises with the laser pulse and decays exponentially. The maximum field with $E_4^{max} \sim 5 \text{TV/m}$ is still too large and much

Table 8.1: Ionization potentials and corresponding field strengths according to the FIBS model and an ideal (boxlike) accelerating electric field. t_k^{min} is the minimum field duration and l_k^{min} is the minimum acceleration length.

Charge state	U_k [eV]	E_k [V/m]	$E_{k,max}$ [V/m]	$\tau_{k,min}$ [ps]	$l_{k,min}$ [μm]
C1	11.16	$2.2 \cdot 10^{10}$	$5.2 \cdot 10^{10}$	16	58
C2	24.38	$5.2 \cdot 10^{10}$	$1.3 \cdot 10^{10}$	4.6	23
C3	47.89	$1.3 \cdot 10^{11}$	$1.8 \cdot 10^{11}$	2.7	17
C4	64.5	$1.8 \cdot 10^{11}$	$1.8 \cdot 10^{11}$	2.4	17
C4	64.5	$1.8 \cdot 10^{11}$	$1.2 \cdot 10^{12}$	0.35	2.5
C4	64.5	$1.8 \cdot 10^{11}$	$5.3 \cdot 10^{12}$	0.08	0.6
C5	392.09	$5.3 \cdot 10^{12}$			
C6	490.00	$7.0 \cdot 10^{12}$			
F7	185.2	$8.5 \cdot 10^{11}$	$8.5 \cdot 10^{11}$	10	17
F7	185.2	$8.5 \cdot 10^{11}$	$2.5 \cdot 10^{12}$	0.35	5.7
F7	185.2	$8.5 \cdot 10^{11}$	$2.3 \cdot 10^{13}$	0.04	0.6

shorter than the laser pulse. A field of similar duration as the laser pulse has now a maximal value of $\sim 1.75\text{TV/m}$ instead of 1.2 in the boxlike case.

The ultrahigh-field region turns out to be short-lived and of short length (≤ 500 fs, $\leq 5\mu\text{m}$). Only the C^{4+} - and F^{7+} -ions see these highest fields, while the lower charge states are accelerated by lower fields of longer duration. The difference in spatial and temporal extension of the C^{1+} and C^{4+} accelerating fields is two orders of magnitude. The evaluation of the fluorine shot shown in Fig. 7.6 shows that $E \sim 2.5$ TV/m active over $\tau_7^{min} \sim 350$ fs is necessary to accelerate F^{7+} -ions up to 100 MeV over a scale length of $l \sim 5 \mu\text{m}$. The shot presented in Fig. 7.6 was virtually without any protons, but the modelled fields can accelerate H^+ up to ~ 25 MeV, as typically observed with unheated targets (see Fig. 8.2).

This first evaluations show that the TNSA-model explains the occurrence of high energy protons and is able to reproduce the measured spectra. It does not however, explain the spectra of other charge state and has to be considered incomplete. The estimated temporal and spatial extensions for the fields accelerating the lower charge states take place on larger timescales. A valid model for larger timescales would be the isothermal expansion model by Gurevich [97] and similar models which work well for acceleration by longpulse lasers. However, the ansatz to describe the high energetic part of the spectrum by TNSA and assume a relaxation to an isothermal regime as an explanation

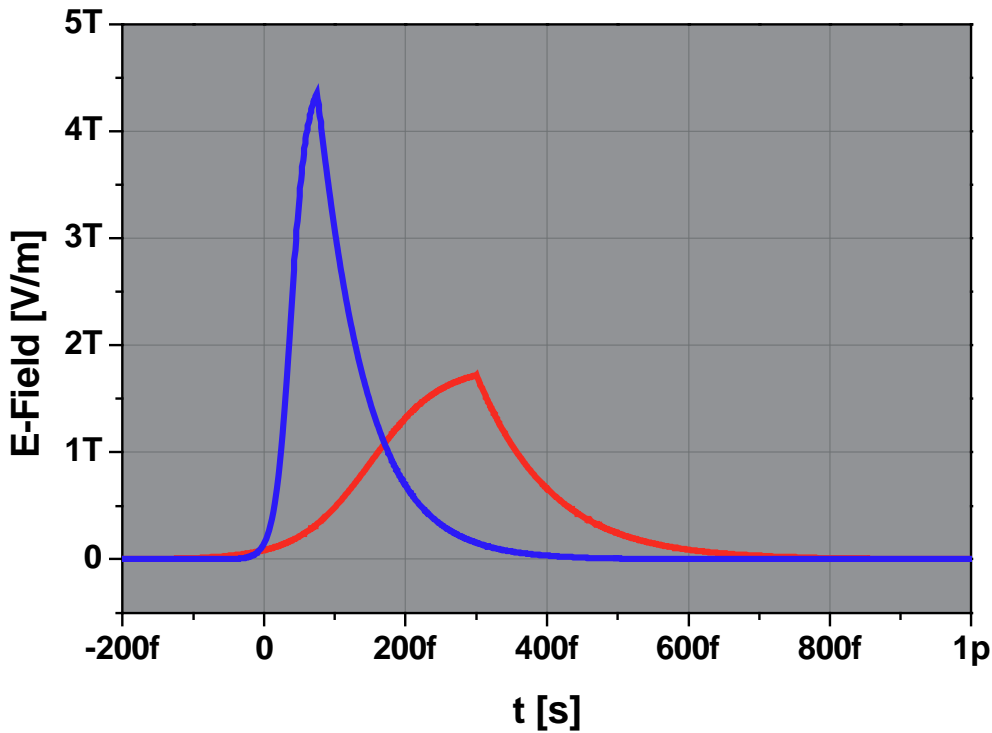


Figure 8.1: Accelerating fields for C^{4+} -ions. In order to achieve the right cutoff energy the field duration and strength are varied. The maximum field is much shorter than the laser pulse. A field of the duration of the laser pulse is in good agreement with TNSA-model predictions with respect to the field strength.

for the lower charge states does not work either. It reproduces neither the measured spectra nor the charge state balance. The most promising way to theoretically describe the physics of the acceleration process is with the use of computer simulations, which will be discussed in Sect. 8.2.

8.1.4 Front- versus Rearside mechanism

Since the first experiments on short-pulse laser ion acceleration there has been a disagreement about the origin of the observed particles. Some groups favor the rear-surface TNSA mechanism [90, 52, 50], while others suggest the acceleration of front-surface protons in the charge-separation field in the laser-plasma [39, 47, 46]. While it is now clear that both mechanisms exist, there is still discussion about the effectiveness of each mechanism and what energies can be produced. The problem in settling this dispute is that in measuring protons it is not possible to determine without doubt where the protons are coming from. Due to the vacuum conditions there is always a proton population on both surfaces and a method to reliably clean only one surface has

yet to be demonstrated. Maksimchuk [46] circumvented this problem by accelerating deuterons coated on the front of an Al-target. A nuclear reaction in a ^{10}B catcher which is sensitive to deuterons but not to protons was then used to distinguish the particles and proved the existence of a front surface mechanism. We were able to reproduce those measurements in more detail in our recent experimental campaigns at LULI and LANL (to be published). However, the deuterons out of this front layers have comparatively low energies of ~ 5 MeV and cannot explain the high energy proton signal. Furthermore when doing the reverse experiment with deuterons on the back, the proton contamination poises the acceleration process for the deuterons as was shown in Chapter 7 and Sect. 8.2.3.

By accelerating heavy ions out of prepared source layers, and removing the proton contaminants we unambiguously prove for the first time the existence of an effective rear-surface acceleration mechanism. The deduced electric field for the high energy particles is consistent with the TNSA-model and explains the proton energies observed in our experiments, as is showed in Fig. 8.2. These experiments, published in [43], together with experiments showing that the acceleration is disturbed by a plasma at the back surface (Chapter 6 and [50]), the detailed Boron measurements (to be published), and the neutron experiments published in [98] lead to the conclusion that the well-collimated high energy ions stem from the rear surface while the protons from the front surface are of much lower energy and show a larger divergence angle. This explanation is also in agreement with 3D-PIC simulations by Pukhov [48] and Ruhl [99] and finally resolves the proton-origin controversy.

8.2 Computer Simulations

Understanding ion acceleration by short pulse lasers with the help of Computer Simulations

The old self-similar solutions which can analytically describe the ion expansion in the case of a long pulse laser do not work for ultra-short pulse laser interaction. While clearly an isothermal expansion takes place on longer time-scales, after the laser-plasma interaction is finished and some degree of cooling has occurred, the main interaction is driven by other processes. The two main requirements for the self-similar ansatz as described in Chapter 2 to work are not fulfilled in the first stages of acceleration. These requirements are charge neutrality and a constant temperature during the expansion. While overall charge neutrality is of course fulfilled for the system, the acceleration by ambipolar space charge fields requires locally, i.e. at the coordinates where actual acceleration takes place, a strong negative charge distribution to create the field. The

second requirement, isothermal conditions, are not fulfilled due to the extremely short pulse duration. Especially the time scales of the laser pulse are much shorter than the time scales of the whole expansion process. Since the laser pulse creates the hot electron population their temperature starts to decrease as soon as the pulse terminates. How fast and by what mechanism the temperature decays is still a subject to discussion and further research but it is clear that the situation of the fast ions is by no means isothermal.

The analytical TNSA-model (see Sect. 2.3.3) gives a good idea on the relevant scales like the maximum accelerating field, the spatial scale and the temperatures involved but is a far to simple model to give a detailed dynamic picture of the interaction process. In order to better understand the ionization and acceleration dynamics we therefore make use of computer models simulating parts of the interaction. Two different codes are used to model different aspects of the interaction, a simple 1D-kinetic code that was developed to get a basic idea of the ionization dynamics and the first stage of the acceleration process and a more elaborate 1D-PIC code developed by Pfund [65] and expanded by A. Kemp to be able to model our experimental parameters as closely as possible. The last section of this chapter than briefly describes the struggle for full scale 3D-simulations of solid-state target ion experiments which are currently work in progress.

8.2.1 1D-code

In order to describe how the energy and charge state distributions of the individual ion species develop in space and time, we have developed a 1D-numerical model which calculates the electron dynamics behind the target, assuming a Boltzmann distribution for the electron energy spectrum and a current distribution which follows the laser pulse [43]. The code includes the ionization process (FIBS), the acceleration of different ion species as well as screening effects on the potential. In each time step, it solves Poisson's equation for the given charge distribution, calculating a self-consistent solution for the electric field behind the target. It then checks for ionization events, advances the different ion species, and solves again Poisson's equation for the new charge distribution. This operation is repeated until a stable solution for the given time step is obtained. The intermediate results are stored and the time counter is advanced until the end of the predefined computation time span is reached.

This method works well for approximately the duration of the laser pulse, i.e. the ionization phase and the first phase of acceleration. After the laser pulse no more hot electrons are supplied, while the ions move on. In the code very large decelerating fields develop due to the lack of a charge neutralization mechanism and a cooling

mechanism for the electron distribution. PIC-code simulations by Y. Sentoku [42] suggest an oscillating electron population which charge neutralizes the beam and keeps an accelerating gradient at the tip of the ion front. This however cannot be described by our simple model but needs a full PIC-code description. Therefore this kinetic code was discontinued in favor of a cooperation with the theory group at GA where much more accurate and complete PIC-codes could be used to study the acceleration physics. However to get a first idea of the physical processes involved, especially the ionization dynamics, as well as to predict the highest charge state energy spectra for given field parameters the kinetic model is still a useful tool, especially since it can be run in finite time on a normal PC and does not need large parallel cluster machines.

Exemplary results of the simulations are shown in Fig. 8.2. The spectra for the highest present charge state is reproduced within an order of magnitude (see Fig. 8.2 (a)). Fig. 8.2 (b) shows that the ion distribution starts out stratified - i.e. C^{1+} closest to the surface, followed by C^{2+} , C^{3+} and finally C^{4+} extending to the edge of the expanding ion front. This is different from the measured data, where the high energy cutoff is still increasing with charge state but the spectra overlap and e.g. the fastest C^{2+} -ions have more energy than the slowest C^{4+} -ions. This discrepancy is understandable since the simulation only runs on a time scale of the laser pulse duration. The interaction is however highly dynamic and gets increasingly complex as the system cools down after the pulse. That first period of ~ 0.5 ps is shown in Fig. 8.2 (c). When the first laser-heated electrons enter the vacuum behind the target, they create a highly dynamical situation, different from that in the simple TNSA model. When more and hotter electrons arrive at the surface, the field increases until $E_{stat} = E_1$. Now FIBS sets in and the produced ions and electrons decrease the field at the surface. An equilibrium between the growing external field and the surface ionization rate keeps the field at the surface always at E_1 . The created ions are accelerated into the vacuum whilst the freed electrons are pushed into the target. Whereas the field close to the target is shielded by the ions, the unshielded field in vacuum keeps increasing. The position of the maximum electric field moves outwards into vacuum, ionizing the outermost ions further (see Fig. 8.2 (b)).

As long as there is a source of hot electrons, nearly all ions are sequentially ionized to C^{4+} . This sequence happens extremely fast during the rising flank of the electron pulse on a temporal and spatial scales of femtoseconds and nanometers respectively. The low charge state distributions have to be created either after the pulse requiring two orders of magnitude longer time scales or in field-fringe-regions of the electric field requiring a fully three-dimensional simulation.

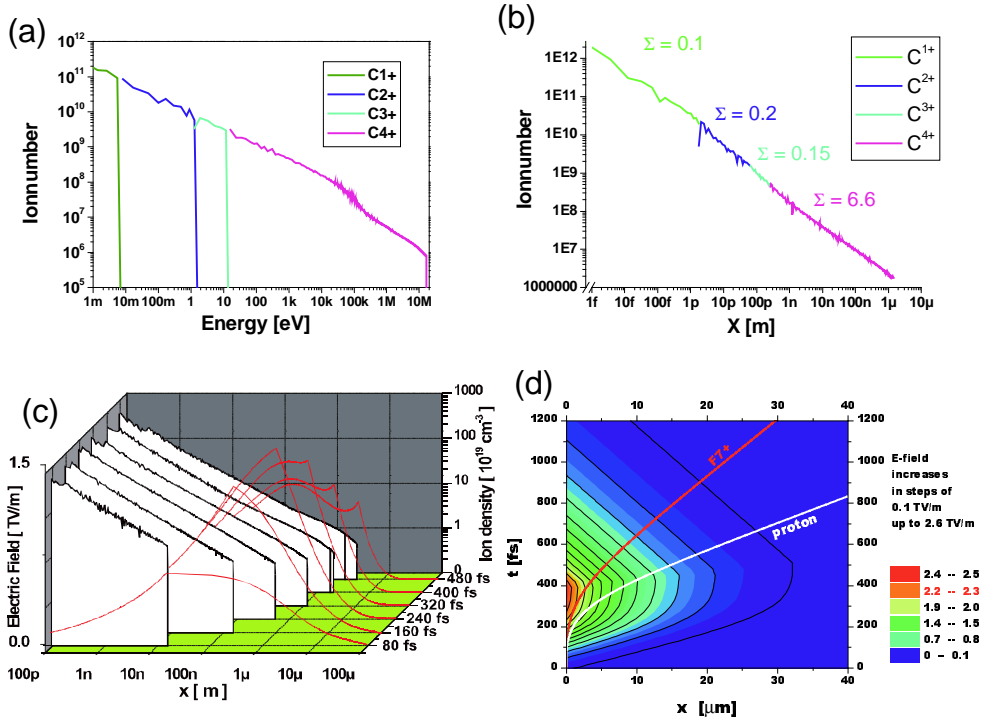


Figure 8.2: C^{4+} -spectrum calculated with 1D-kinetic model. Highest energy and absolute ion numbers are reproduced within an order of magnitude. (c) Time-space history of the accelerating electric fields (red curves) and the ion distribution (white curve): The region of maximum field moves out into the vacuum. Already during the pulse there exists an ion distribution on a μm -scale. (d) F^{7+} -trajectory and corresponding H^+ -trajectory in accelerating quasistatic field. The same field that accelerates F^{7+} to ~ 100 MeV accelerates protons to ~ 23 MeV. This result is in good agreement with the measured data.

8.2.2 1D-PIC code with ionization

A more detailed and accurate modelling of the acceleration process was possible with a one-dimensional PIC-code. This code was developed by R. Pfund in [65] and contains not only the standard PIC-physics of relativistic equations of motion for the particles and Maxwell's equations for the field but also ionization models for collisional ionization and field ionization. The code was expanded by A. Kemp to be run on massively parallel computers. This was a prerogative in order to accurately simulate the experiments which by their nature require a large computing effort. The targets have solid state densities, $n_e \sim n_i \sim 10^{23} \text{ cm}^{-3}$, which results in a very high number of particles in the simulation. As was shown before the simulations have to run on large temporal and spatial scales, ideally ~ 100 ps and several hundreds of micrometers. While this was still not possible yet due to the lack of CPU-time on sufficiently powerful parallel computers,

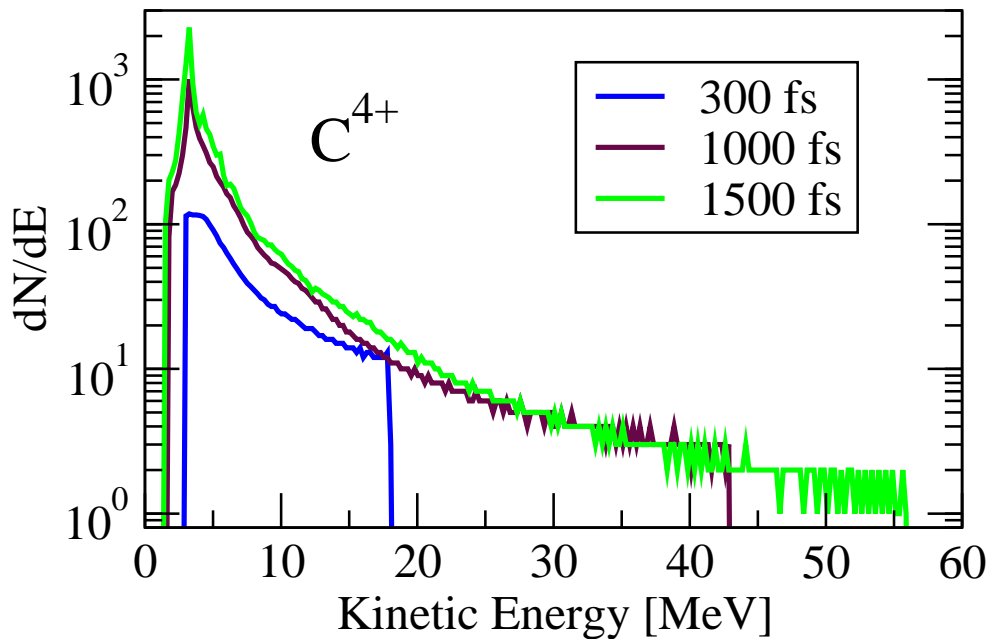


Figure 8.3: Influence of contaminating protons on the carbon spectrum: In the presence of protons the carbon spectrum has lower energies and a cutoff forms. The proton spectrum starts showing band structures.

simulation times on the order of picoseconds could be realized. This together with the simultaneous treatment of not only different charge states but also different ion species, resulted in a far more accurate simulation. While in the simple kinetic model an electron temperature and distribution has to be assumed, the PIC-code is able to model the full laser-target interaction. Fig. 8.3 shows the resulting spectra for the interaction of a 300 fs laser pulse of an Intensity $I = 5 \times 10^{19}$ W/cm² with a pure carbon target. The helium-like charge state gets accelerated to ~ 5 MeV/nucleon and the spectrum is smoothly decreasing showing a plateau-like high-energy region. In both energy and form it agrees well with the measured spectra in the absence of protons as shown in Fig. 7.6.

8.2.3 1D-PIC results: Influence of H⁺ contamination

The measured ion spectra show a distinctively different form for shots which had no protons at all and shots where still some protons were left. While in the first case the helium-like charge state shows a gentle decrease in the energy spectra ending in a plateau, in the latter a sharp cutoff is observed. The 1D-PIC-code is able to examine that situation by simulating a target with two different ion species. In the simulations a carbon target was used which contained variable degrees of hydrogen. The results

are summarized in Fig. 8.4. As the amount of hydrogen in the target is increased from 0 % to 90 % a cutoff develops and the spectra also shows fluctuations. Furthermore the cutoff energy decreases since the faster protons more and more shield the accelerating fields for the heavier. This behavior is in excellent agreement with the measured data and even allows an estimate of the proton fractions for partly heated targets. Comparing the spectra in Fig. 8.4 with the measured C^{4+} spectra in Fig. 7.5 and Fig. 7.4, proton fractions of $\sim 50\%$ and $\sim 70\%$ are obtained.

This is the first time that a multi-species PIC-calculation accurately reproduced an experimental result. Though it is only a small aspect yet, this success is encouraging further work on the computer code. Current work on 1D-simulations for thicker targets and longer timescales and 3-dimensional simulations with full ionization already looks very promising.

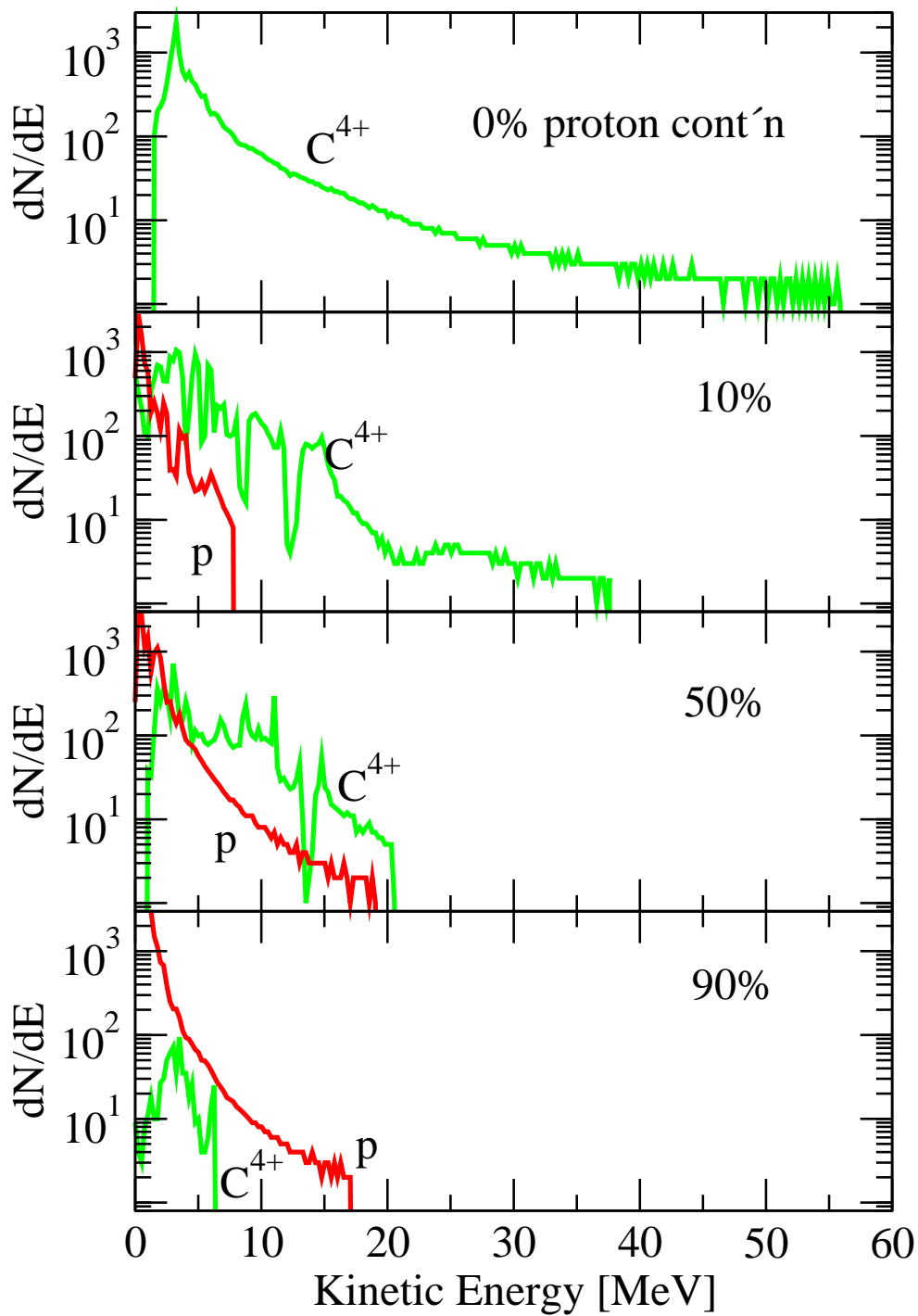


Figure 8.4: Influence of contaminating protons on the carbon spectrum: In the presence of protons the carbon spectrum has lower energies and a cutoff forms.

Chapter 9

Further Research and Potential Future Impact of Laser Accelerated Ions

Ion acceleration with short pulse lasers has only just begun. This work as well as the handful of similar experiments were all performed within the last three years and we have just started to understand the underlying physics. As explained in the preceding chapter, no complete model explaining the full spectra and charge state distribution currently exists. The electron transport through the target is still largely unclear yet and the scaling laws with respect to the laser parameters are incomplete. This leaves room for many different future experiments and simulations in order to gain a better understanding of the process. Simultaneously, however, there have been many encouraging results regarding applications. Laser accelerated ions have a number of unique characteristics: the pulse duration is at least three orders of magnitude shorter, the currents are many orders of magnitude higher and the inherent beam emittance is better than that of conventional accelerators. If one succeeds in preserving those phase space properties only partially while matching the pulse to a standard accelerator one would have a unique ion source and first accelerator stage. There are first results at the MPQ ATLAS laser, indicating that a downscaling to a table-top system and thereby an upscaling in repetition rate from once every hour to ten times a second is possible. There are also first experiments and simulations showing that focussing of the beam by shaped targets and/or shaped laser pulses is possible. This is of extreme importance for Fast Ignition with proton or ion beams in the framework of a laser-fusion scheme as simulated by Atzeni et al. [100]. It would also offer the possibility for basic astrophysics experiments in the laboratory. The next section briefly summarizes the acceleration mechanism including the adjustments and additions resulting from this

work. The other three sections then describe future perspectives within this fields, proposing near future experiments to further explore the acceleration physics and discussing further prospects of what to expect from next generation laser sources and finally giving exemplarily a number of immediate applications of laser accelerated ions.

9.1 Modified picture of the acceleration mechanism

The basis of our current picture of the acceleration physics is still rooted in the TNSA-model. However, due to the discoveries made during the course of this thesis some important modifications and limitations have to be made. The TNSA-model correctly estimates the maximum field strengths and the maximum energy for the ion species with the highest charge-to-mass ratio. Beyond that, it is far too basic to explain the underlying physics. As we see from the simulations in Sect. 8.2.1, [43], the field is not really quasistatic but shows a very dynamic behavior. It also does not reach its maximum directly at the target surface but at a short distance behind it. This is caused by the fact that at the surface there is an unlimited supply of potential positive charges (the target atoms), the ionization happens quasi-instantaneously and the freed electron is pushed away into the target. Therefore, any additional electron adding to the charge distribution and thereby building up the field, is immediately neutralized directly at the surface, once the field exceeds the first field ionization barrier. Already a few nm further out this condition does not apply anymore and the field ramps up very fast to its maximum value of several TV/m for typical laser parameters. During the course of acceleration the maximum of the electric field moves out into the vacuum with the moving ion density. If not only one charge state is accelerated, as it is always the case in an experiment, then the charge state with the highest charge-to-mass ratio outruns the others and screens and modifies the accelerating fields. By measurements and PIC-calculations we could show that the contaminating protons not only inhibit the ion acceleration and that by removing them one can effectively accelerate heavier species [43], but that they also influence the spectral shape of the other charge states (see Sect. 8.2.3, to be published). Another important result is that we were able to measure lower limits for the time-constant of the acceleration process. While the highest charge states are accelerated on a time scale equal to that of the laser pulse, the acceleration of the lower charge states takes considerably longer. A possible mechanism which could explain that phenomenon was suggested by Mackinnon and Sentoku in [42] to explain the increasing proton energy with decreasing target thickness. Their measurements and PIC-simulations indicate recirculating electron populations which retain a high temperature and density long after the laser pulse is terminated. One still missing

piece of the puzzle is the origin of the low charge states. Up to now no simulation could reproduce the measured charge state distribution correctly. Two possibilities are discussed at the moment. The first one asks whether these charge states constitute a 3-dimensional effect by originating in the spatial fringe regions of the accelerating field. In this case a 1D-simulation is fundamentally unable to reproduce the low charge states. The second notion is that the low charge states only start to accelerate when the field is cooling, requiring very long simulation runs and the correct electron transport physics, taking into account recirculation and trapping in the ion potential. Both possibilities are currently worked upon theoretically and the next section suggests an experiment to measure the effect directly.

To leave the reader with a picture of how the ion acceleration by a short pulse laser works in a very simplified but illustrative way, the current model is schematically displayed again in nine time steps in Fig. 9.1:

9.2 Future Experiments

Although the principle is simple, as discussed above there are still many open questions concerning for example the process dynamics, the cooling times, the spatial setup or the screening processes, all of which have to be understood in order to optimize the process for future applications.

9.2.1 Time-resolved measurement of the accelerating electric field

As described in Chapter 7 and [43] the dynamics of the acceleration mechanisms are far more complex than described by TNSA or any other current model. Clearly, a dedicated experiment is needed that explicitly addresses the temporal behavior of the apparently not-so "quasistatic" accelerating fields. With the new upgrades to the LULI 100TW laser facility currently under installation, which comprise a second pulse compressor, it will be possible to have two ion generating laser pulses. As was shown by Borghesi et al. in [51] the laser generated proton beam can be used for a time-dependent measurement of strong electric fields with a \sim ps time-resolution. As we were able to show in our previous experimental campaigns at the LULI-laser, this is the time frame for the acceleration of low charge state ions. We therefore plan an experiment in which one of the two pulses is used to make a high energy proton burst to generate a time-resolved radiographic image of the acceleration process at a second target. This second target is then placed at a 90° angle and a cm distance to the first

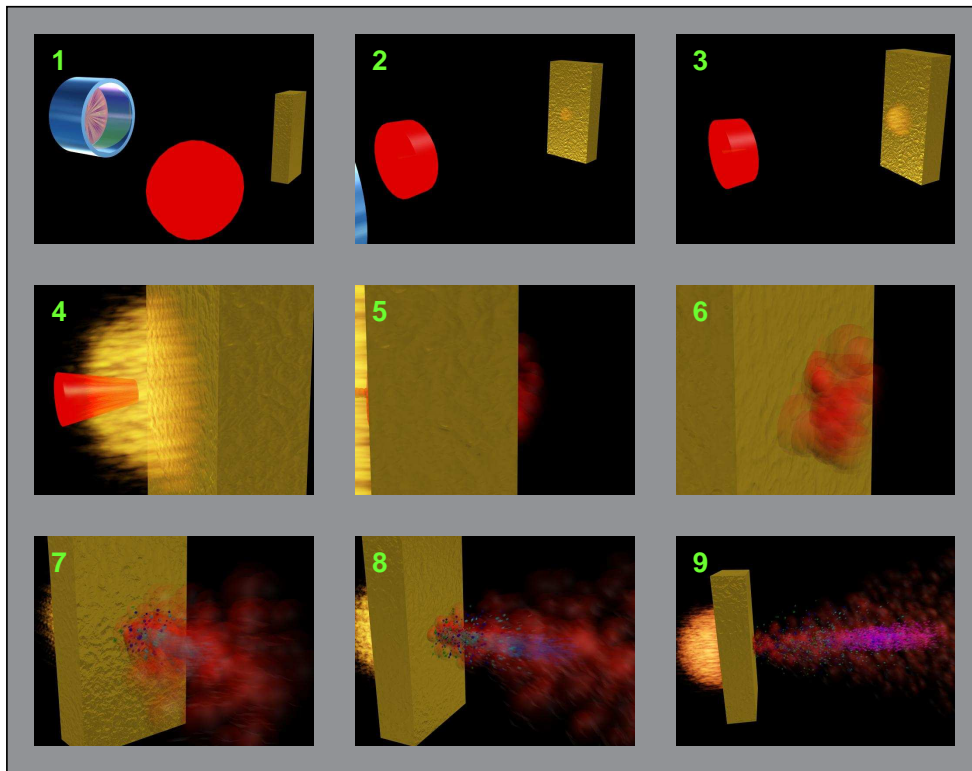


Figure 9.1: Schematics of laser induced ion acceleration: (1,2) A laser pulse is focused by an off-axis parabola on a pure carbon target. (2,3) Prepulses and ASE create a plasma density gradient at the target front side. (4) The main pulse interacts with this preplasma, (5) accelerating relativistic electrons through the target. (6) These electrons set up an ultra-strong (TV/m), quasistatic space charge field at the rear surface. (7) This electric field ionizes the rear surface atoms (C^{1+} : green). (8) The ionized atoms start moving and are further ionized (C^{2+} : blue, C^{3+} : cyan, C^{4+} : green; scales: fs, nm). (9) The ions are accelerated to MeV energies, the higher the charge state, the higher the energy and the smaller the divergence.

target. It consists of a thin W-foil coated with a light ion source layer like LiF or Be. The target has to be heated in order to remove the protons, so the light ions out of the source layer can be accelerated. The ion spectra from this target are to be recorded by Thomson parabola spectrometers as done in previous experiments. Those spectra will yield additional information on the field strength and spatial and temporal parameters as demonstrated in [43] and Chapter 7. These measurements combined with the radiographic images should yield the necessary information to form a more consistent picture of the field dynamics. The key parts of the experiments, namely the production, measurement and analysis of the ion spectra on the one hand and the time-resolved radiography on the other hand, have been demonstrated. The problems in combining these methods will be in the experimental realization, not in the physics,

while the expected gain from the experiment will yield new insights in the physics mechanism of acceleration.

9.2.2 Spatial origin of low charge state ions

Another interesting question is the origin of the lower charge state ions. So far, 1D-simulations were not able to reproduce the complete charge state distribution but only the highest charge state spectra. One possibility is that the low charge states originate in the bulk of the target and are accelerated later in time, requiring long simulation times and transport physics in the simulations. The other option is an origin in the fringe regions of the accelerating field. In that case it would require a full 3D-code to see the full low charge state spectra in a simulation. However, 3D-simulations can not yet deal with a sufficiently long timespan, a large enough simulation box and a high enough target density simultaneously, due to the limited computing power of even the biggest massively parallel machines. We therefore plan an experiment to clarify this question. The experiment will consist of two series of targets to test each hypothesis.

The first series will be tungsten targets with a few atomic layers thin coating of beryllium. This coating will be successively buried deeper and deeper in the W-substrate, the buried depth being again on the atomic layer scale. This shot series will thereby test up to which depth ions can be accelerated and contribute to the signal.

The second series will consist of tungsten targets with a Beryllium coating at the back surface in the form of a small spot of $\sim 50 \mu\text{m}$ diameter. From the source size measurements presented in Chapter 6 we know that this is roughly the source size of the high energetic part of the proton spectra, i.e. the high-field region. If the low charge states originate in the fringe region we can expect a significant drop of the low charge state ion spectra in the signal. Apart from learning more about the acceleration physics it might also be a method to obtain a single charge state ion spectrum.

9.2.3 Truly heavy ion acceleration

Last but not least we plan to try for really heavy ion acceleration by shooting a cleaned pure tungsten target, an experiment not yet done due to the lack of sufficient beamtime on big enough laser systems. Apart from the possible applications we would also get a more precise idea of the maximum field strength due to the more numerous charge states in the region of interest. To resolve this, however, the Thomson parabola spectrometer have to be improved in resolution and accuracy.

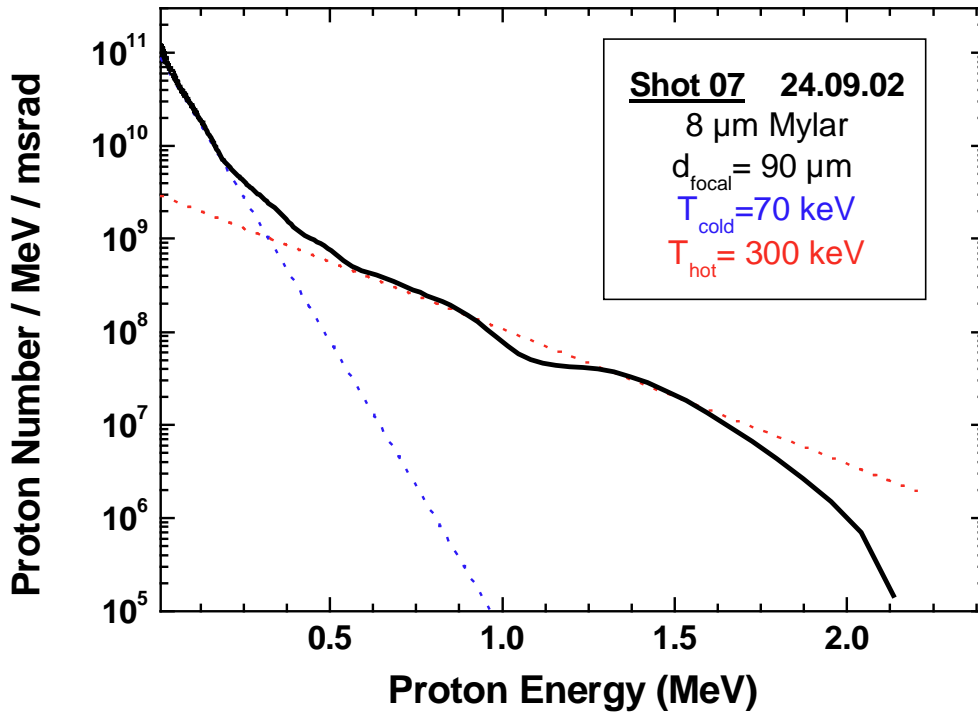


Figure 9.2: Proton spectra for a $8\ \mu\text{m}$ Mylar target irradiated by a 0.6 J pulse from the table-top, high rep-rate (10 Hz) MPQ ATLAS-10 laser.

9.2.4 MeV-Ion acceleration with table-top lasers

Another approach which will be followed at the MPQ ATLAS laser facility is the transfer of the ion acceleration scheme to a table-top laser system. In recent experiments up to 2 MeV protons were measured with a Faraday cup detector as shown in Fig. 9.2. By optimizing the parameters even 3.5 MeV protons and ~ 6 MeV carbon ions were produced by the ATLAS-10 laser, using 0.6 J pulses of 150 fs pulse duration at an intensity of $\sim 10^{19}$ W/cm². Apart from being smaller and cheaper the big advantage of this type of laser is its repetition rate of 10 Hz. For any future application such as isotope production or ion sources, a higher repetition rate is a *conditio sine qua non*. Furthermore, from the scientific point of view it enables systematic parameter studies which are difficult at high energy systems with their limited number of shots and poor reproducibility of pulse parameters. Among those parameters to be studied in future experiments at MPQ is the ion energy scaling with preplasma gradient and pulse duration.

9.3 Scaling parameters for laser accelerated ions

What ion parameters can be expected for future laser systems?

While, apart from fast ignition, all the experiments and applications described above can be conducted with existing laser systems, the question remains how the ion acceleration scales up with laser parameters and what can be realistically expected using future laser systems. Up to now no qualitative exact scaling laws could be obtained from the conducted laser ion experiments. The reasons for this lack are related to the characteristics of the high energy laser systems used in ion experiments. Due to their low repetition rate the number of shots in any experimental series is rather small. On the other hand the shot-to-shot fluctuations of the laser parameters are fairly large. When comparing experiments performed on different laser systems usually a number of parameters is different which complicates any analysis. Therefore at the moment PIC simulations have the best hope of predicting results with upscaled laser parameters, since the relevant physics problems are supposed to be inherently solved within the code. The most promising outlook for the future of laser accelerated ions is predicted by a full 3D-PIC simulation done by Pukhov. Using his VLPL code he simulated the interaction of a 15 fs, 1 kJ laser pulse at an intensity of $I = 10^{23}$ W/cm². The simulation predicts 10^{12} relativistic protons in a narrow spectral distribution between 5 and 6 GeV as is shown in Fig. 9.3.

In order to compare the simulation results to real experiments and to get an idea of the scaling behavior Fig. 9.4 summarizes the results on laser ion acceleration already done and published with respect to the scaling parameters. The experiments listed were performed on a number of different laser systems, from small 10 Hz systems like ATLAS, to high-energy systems like LULI (France), Trident (USA) or Vulcan and on to big Petawatt systems like the now decommissioned Livermore PetaWatt laser (USA) or the Gekko-Shortpulse (Japan). Also included was a 3D simulation done by Pukhov [101] to scale up to future laser parameters. Comparing those experiments is difficult though, due to the number of relevant parameters involved. Examined are the proton cutoff energy, the absolute proton number and the conversion efficiency from laser energy to ion energy. The main laser parameters are pulse energy, pulse duration and intensity on target. Unfortunately these parameters vary from system to system, and neither are they the only parameters involved, nor are they independent from each other. Especially the intensity depends on both the energy and the pulse duration, but also on the focal size. Other important characteristics which also are very different for all experiments are target material and thickness, incident laser angle, the contrast ratio of the laser pulse which is responsible for the preplasma density gradient, and last but not least detector properties. The low energy cutoff plays an important

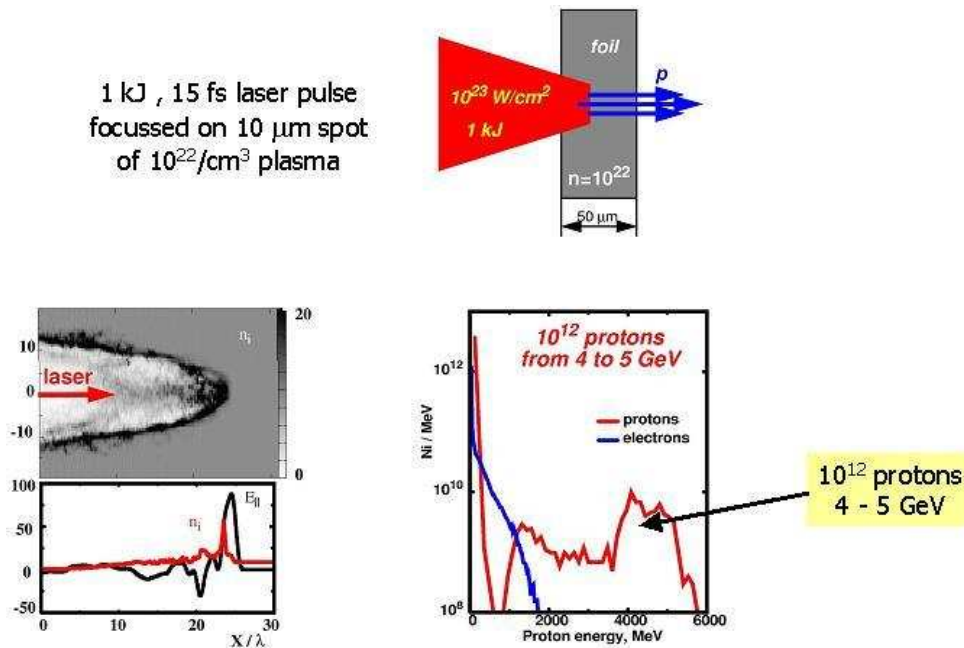
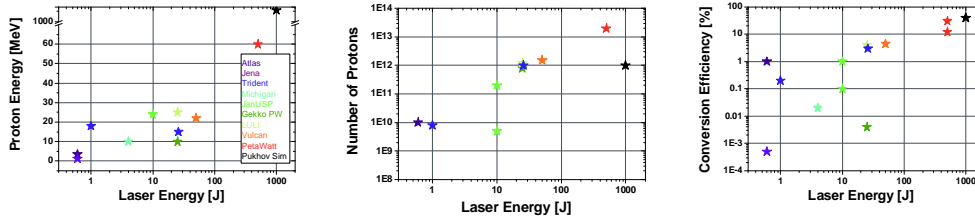


Figure 9.3: Laser-accelerated GeV protons: top: simulation setup and parameters; left: ion density (n_i) and longitudinal electric field; right: energy spectra of electrons and protons [101].

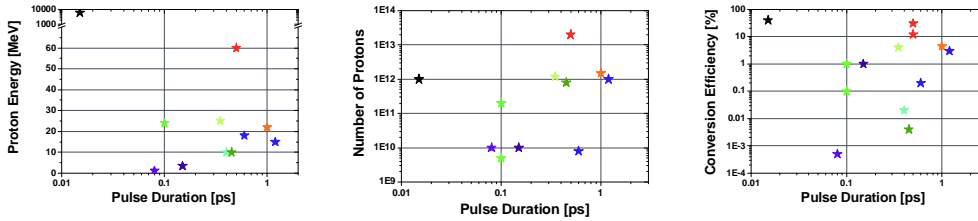
role when comparing the absolute ion yield and the energy conversion efficiency. The exact parameters of the experiments together with the references are given in Tab. 9.1. Despite those difficulties there are some trends which can be observed in Fig. 9.4.

Due to the problems discussed above it is hard to do a quantitative analysis of the scaling parameters. More experiments with carefully chosen and controlled parameters are necessary. Especially the results with high repetition-rate laser systems are very promising with regard to that purpose, due to their inherently lower shot-to-shot fluctuations. It is, however, possible to spot some qualitative trends. As one would expect especially the number of ions seems to scale with the pulse energy but the same seems true for the energy conversion efficiency. This will go into saturation at a certain level and it cannot exceed the conversion efficiency into relativistic electrons. The highest conversion factor in fast electrons reported up to date is $>40\%$ [9] at the Livermore PW laser. Anticipating some improvement and optimization one can probably expect a maximum achievable conversion efficiency from laser to ion energy on the order of 50%. The maximum energy does not only scale with laser energy, but more importantly also with laser intensity. While the laser parameters from the VLPL simulation are still far from being realized, a number of facilities with energies in the multi-kJ range and pulse durations of ~ 0.5 ps are under construction. These lasers can be expected to

Scaling with Laser Energy



Scaling with Pulse Duration



Scaling with Laser Intensity

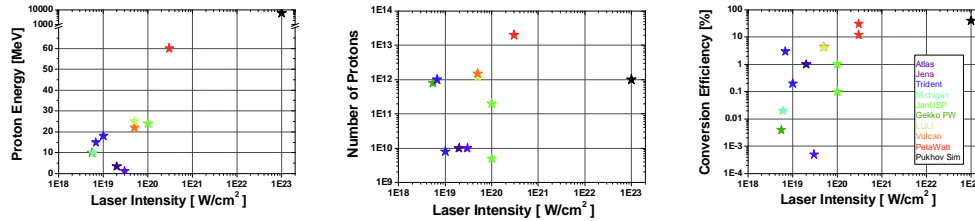


Figure 9.4: Scaling behavior of proton energy, yield and energy conversion efficiency with laser parameters. The top row shows scaling with laser energy, the middle row scaling with pulse duration and the bottom row scaling with laser intensity on target. The experiments together with the references are listed in Tab. 9.1. The colored stars are experimental data, the black star is from a 3D-simulation with VLPL.

deliver intensities exceeding 10^{22} W/cm². The Beamlet Shortpulse Upgrade at Sandia National Laboratory could deliver 5 kJ pulse at 500 fs within the next 5 years. Assuming a focal diameter of $10 \mu\text{m}$ an intensity of 1.3×10^{22} W/cm² would be achieved. Using the simple equations from Chapter 2 one would obtain an electron density of $n_e \sim 5 \times 10^{20}$ cm⁻³, a Debye length of $\sim 2 \mu\text{m}$ and an electron temperature $T_h \sim 40 - 50$ MeV. Using the 1D-kinetic code from Chapter 8 a maximum proton energy of ~ 250 MeV can be expected. The proton number can be expected to be on the order of $> 5 \times 10^{13}$ particles above 10 MeV.

Table 9.1: Listing of laser induced ion acceleration experiments.

Facility	E_{pulse} [J]	t_{pulse} [ps]	$I/10^{18}$ [W/cm^2]	contrast	E_{min} [MeV]	E_{max} [MeV]	Ionno.	Effic. [%]	ref
ATLAS	0.6	0.15	20	10^{-6}	0.2	3.5	10^{11}	2	
ATLAS	0.6	0.15	20	10^{-6}	1	3.5	10^{10}	1	
Jena	0.6	0.08	30	10^{-6}	1	1.2	10^{10}	0.0005	[98]
Trident	1	0.6	10	10^{-10}	2	18	8×10^9	0.2	[102]
CUOS	4	0.4	6	5×10^{-5}	-	10	-	0.02	[103]
JanUSP	10	0.1	100	10^{-10}	4	24	2×10^{11}	1	[42]
JanUSP	10	0.1	100	10^{-10}	7	24	$\sim 5 \times 10^9$	0.1	[42]
LULI	25	0.35	50	10^{-7}	2	25	10^{12}	4	[43]
GekkoPW	25	0.45	5.5	10^{-3}	1	10	2×10^9	0.004	[90]
Vulcan	50	1	50	10^{-7}	2	22	10^{12}	4.4	[50]
LLNL PW	500	0.5	300	10^{-7}	2	58	3.5×10^{13}	7	[9]
LLNL PW	500	0.5	300	10^{-7}	10	58	2×10^{13}	12	[9]
LLNL PW	500	0.5	300	10^{-7}	2	58	$\sim 1.5 \times 10^{14}$	~ 30	[9]
VLPL Sim	1000	0.015	10^5	-	4000	6000	10^{12}	~ 40	[101]

9.4 Applications

Laser accelerated protons are already a new tool for plasma diagnostics [51]. Also the transport of very dense charge neutralized ion beam in plasmas or isochoric heating of macroscopic volumes ($\sim 10^5 \mu\text{m}$) to hundreds of eV can now be studied. These ion beams represent a radically new tool for probing the properties of dense, strongly coupled plasmas due to their properties: very short pulse duration ($\sim\text{ps}$), unprecedented density ($\sim 10^{19} \text{cm}^{-3}$) and overall charge neutrality. With the new capability to accelerate also other ion species and indications in simulations that beam focussing, spectra- and charge state control might be feasible, applications like laser accelerators are becoming realistic.

Before we can realize the potential for this new tool, we need to understand the interaction of such neutralized, middle to high Z, high current beams ($\sim 100 \text{kA}$ for ions/electrons) with a low Z plasma or solid target. On the one hand, the neutralizing beam electrons are beneficial in allowing currents much above space-charge limits. On the other hand, they introduce the possibility of collective effects (filamentation, hoseing instabilities) in their interaction with the target plasma when its density is similar ($10^{18} - 10^{20} \text{cm}^{-3}$) to the beam density. It is not known how these instabilities would affect the range and energy deposition of such neutralized beams, particularly in realistic plasmas with a density gradient. Such understanding might enable ion-based

isochoric plasma heating, not yet conclusively demonstrated. Applications of isochoric heating include ion-driven fast ignition and spectroscopy. Heating optimization would benefit from modest focusing of the beam (factor of 4: $T_e > 300$ eV in solid Al), from improved laser/ion conversion efficiency, and from improved ion spectra.

Technologically, laser-driven ion accelerators hold the promise of supplying outstanding new ion sources as well as accelerator stages with acceleration gradients many orders of magnitude above those achievable by conventional means. If transferred to small table-top Ti:Sapphire lasers, small cheap accelerators might become available opening possibilities (e.g., isotope production for medical diagnostics) so far only accessible by large accelerators in a handful of hospitals. Laser accelerated ions also have the potential to advance the grand challenge of fusion in the laboratory and our state of knowledge in strongly coupled plasmas, another frontier area in plasma physics. The interaction of such beams with background plasmas might allow benchmarking astrophysical codes and studying problems such as radiation transport in a star in the presence of impurities like iron. Due to their inherent ion density and short duration, laser-based ion sources might prove to be the core-heating method of choice for fast ignition [100] and even the driver of choice for ion-driven fusion.

The generation and control of very low emittance ion beams, as well as plasma beams, opens the possibility of new developments and applications in basic and applied research. For example, this technique can be used to produce interestingly large microbunches of ions which could be injected into accelerators for conventional experiments. It is important to note that whereas RF technology is quite mature, laser technologies are still advancing rapidly and useful rep-rated injectors might be foreseeable and recent experimental results at MPQ's 10 Hz laser point in that direction. Other applications making use of the unique characteristics of laser accelerated ions, such as the short acceleration time and the high peak currents and current densities may be found in material studies, e.g. of fusion reactor walls. One may also be able to learn about time-resolved material damage effects, by coupling laser-accelerated ion beams with laser-based ultrafast probing techniques using optical or X-ray photons. Neutral beams are in themselves of interest as diagnostic probes for example of tokamak plasmas. One could imagine using laser accelerated protons to probe turbulent field phenomena in fusion plasmas. Finally, as we learn to produce better focused beams and high contrast, one could image using beams patterned at the source to improve the efficiency or writing speed of ion-implantation or lithographic applications. Clearly this field is only at its very start and it is difficult to predict which applications will gain enough interest and momentum to be realized, but it is clear that short-pulse laser accelerated ions hold an enormous potential in a number of fields.

Proton Imaging

One application of laser accelerated protons already realized in a number of experiments is radiographic imaging. The excellent beam quality of the ion beam is ideally matched to the requirements for these techniques. One scheme of particular interest is the use of laser accelerated protons to radiograph macroscopic samples to study their properties. Due to the different interaction mechanism protons can provide complementary information to more common techniques like X-ray backlighting. The interaction of swift protons with matter is well known and a traditional research area of accelerator laboratories over the past decades. Because of the copious amounts of protons accelerated in a very short time, laser accelerated protons provide a new diagnostic quality in research of transient phenomena. Within the scope of our campaigns at LULI and LANL a number of experiments has been performed to demonstrate the feasibility of laser accelerated proton beams for radiography applications. A compound target of different materials has been imaged by the protons. It consisted of an 1 mm thick epoxy ring structure, several copper wires of 250 μm diameter, a hollow cylinder with 300 μm walls of steel, several Ti sheets of 100 μm thickness and a glass hemisphere of 900 μm diameter and 20 μm wall thickness was used as a radiography target. The protons were recorded in multiple layers of RCF to detect the image at different proton energies. Fig. 9.5 shows the radiographic images of the target for different proton energies. The pictures basically constitute a negative image of the areal density of the target. The names of the collaborating institutes have been engraved on the epoxy ring, which results in a reduced thickness and therefore a higher energy deposition of the protons in the respective layer. The areal density variation of the hollow cylinder, including a hole in the wall on the right hand side can be seen as well as a thin metal rod placed inside the cylinder. These results show a clear dependence on the areal density rather than on a residual charging effects, which can also be diagnosed as presented in [51]. Close examination also shows the small glass hemisphere placed above the cylinder. The time of exposure in this experiment was estimated to be in the order of tens of picoseconds, based on the initial proton beam pulse duration and the energy dependent dispersion of the pulse from the source to the target.

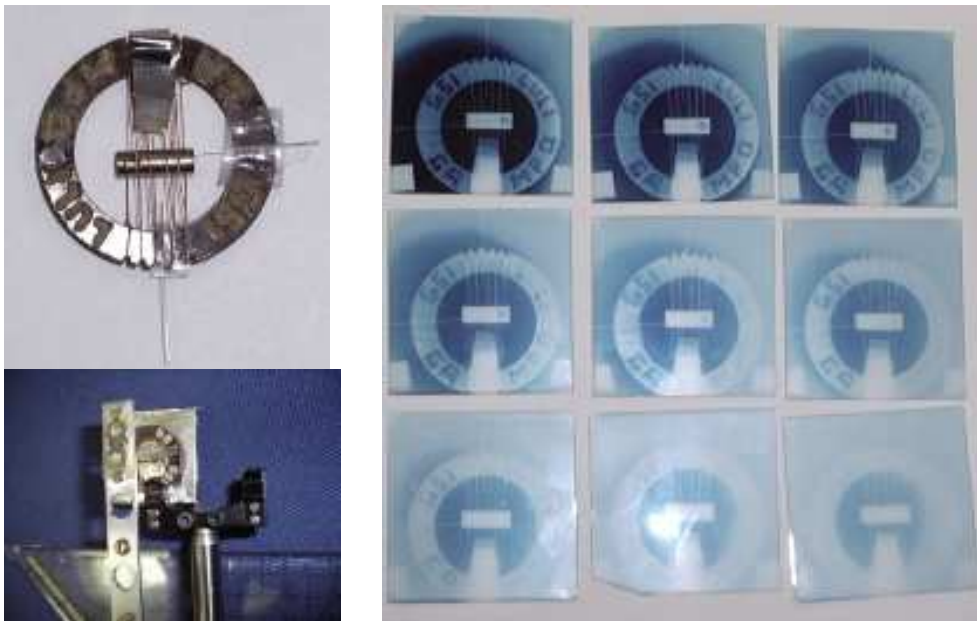


Figure 9.5: Proton radiography of a compound target. Top left: Compound target consisting of an epoxy ring, several wires of varying thicknesses, a steel hohlraum and a glass shell. Bottom left: target mounted ~ 5 cm behind the proton producing target foil. Right: Radiographic images at different proton energies.

Bibliography

- [1] D.N. Adams, *The restaurant at the end of the Universe*, Vol. 2 of *The Hitchhikers Guide to the Galaxy* (Crown Publishers, Inc., 1 Park Avenue, New York, NY 10016, 1980).
- [2] R. Decoste and B.H. Ripin, *High-Energy Ion Expansion in Laser-Plasma Interactions*, Phys. Rev. Lett. **40**, 34 (1978).
- [3] C. Joshi, M.C. Richardson and G.D. Enright, *Quantitative measurements of fast ions from CO₂ laser produced plasmas*, Appl. Phys. Lett. **34**, 625 (1979).
- [4] G.D. Tsakiris, K. Eidmann, R. Petsch and R. Sigel, *Laser induced electron acceleration in the presence of static electric and magnetic fields in a plasma*, Phys. Rev. Lett. **46**, 1202 (1981).
- [5] F. Begay and D.W. Forslund, *Acceleration of multi-species ions in CO₂ laser-produced plasmas: Experiments and Theory*, Phys. Fluids **25**, 1675 (1982).
- [6] D.W. Forslund and J.U. Brackbill, *Magnetic-field-induced surface transport on laser-irradiated foils*, Phys. Rev. Lett. **48**, 1614 (1982).
- [7] G.A. Mourou, C.P.J. Barty and M.D. Perry, *Ultra-high-intensity lasers: physics of the extreme on a tabletop*, Phys. Today **51**, 22 (1998).
- [8] V. Malka, Private Communication, 2002.
- [9] R.A. Snavely, M.H. Key, S.P. Hatchett, T.E. Cowan, M. Roth, T.W. Phillips, M.A. Stoyer, E.A. Henry, T.C. Sangster, M.S. Singh, S.C. Wilks, A. MacKinnon, A. Offenberger, D.M. Pennington, K. Yasuike, A.B. Langdon, B.F. Lasinski, J. Johnson, M.D. Perry and E.M. Campbell, *Intense high-energy proton beams from Petawatt-laser irradiation of solids*, Phys. Rev. Lett. **85**, 2945 (2000).
- [10] M. Allen, 2002, PhD-thesis, UC Berkeley, to be completed.

- [11] S. Karsch, *High-intensity laser generated neutrons: A novel neutron source and a new tool for plasma diagnostics* (PhD-thesis, LMU München, 2002).
- [12] F.V. Hartemann, S.N. Fochs, G.P. Le Sage, N.C. Luhmann Jr., J.G. Woodworth, M.D. Perry, Y.J. Chen and A.K. Kerman, *Nonlinear ponderomotive scattering of relativistic electrons by an intense laser field at focus*, Phys. Rev. E **51**, 4833 (1995).
- [13] M. Lax, W.H. Louisell and W.B. Knight, *Maxwell to paraxial wave optics*, Phys. Rev. A **11**, 1365 (1975).
- [14] L. Cicchitelli and H. Hora, *Longitudinal field components for laser beams in vacuum*, Phys. Rev. A **41**, 3727 (1990).
- [15] M. Born and E. Wolf, *Principles of optics*, sixth ed. (Pergamon Press, Oxford, 1989).
- [16] B. Quesnel and P. Mora, *Theory and simulation of the interaction of ultraintense laser pulses with electrons in vacuum*, Phys. Rev. E **58**, 3719 (1998).
- [17] P. Mora and T.M. Antonsen, *Kinetic modeling of intense, short laser pulses propagating in tenuous plasmas*, Phys. Plasmas **4**, 217 (1997).
- [18] D. Batani, C.J. Joachain, S. Martellucci and A.N. Chester, *Atoms, Solids, and Plasmas in Super-Intense Laser Fields* (Kluwer Academic/ Plenum Publishers, New York, 2001).
- [19] G.D. Tsakiris, C. Gahn and V.K. Tripathi, *Laser induced electron acceleration in the presence of static electric and magnetic fields in a plasma*, Phys. Plasmas **7**, 3017 (2000).
- [20] M.I. Santala, M. Zepf, F.N. Beg, E.L. Clark, A.E. Dangor, K. Krushelnick, M. Tatarakis, I. Watts, K.W. Ledingham, T. McCanny, I. Spencer, A.C. Machacek, R. Allott, R.J. Clarke and P.A. Norreys, *Production of radioactive nuclides by energetic protons generated from intense laser-plasma interactions*, Appl. Phys. Lett. **78**, 19 (2001).
- [21] C. Gahn, G.D. Tsakiris, A. Pukhov, J. Meyer-ter-Vehn, G. Pretzler, P. Thirolf, D. Habs and K.J. Witte, *Multi-MeV electron beam generation by direct laser acceleration in high-density plasma channels*, Phys. Rev. Lett. **83**, 4772 (1999).
- [22] T. Tajima and J.M. Dawson, *Laser electron accelerator*, Phys. Rev. Lett. **43**, 267 (1979).

- [23] A. Pukhov, Z.M. Sheng and J. Meyer-ter-Vehn, *Particle acceleration in relativistic laser channels*, Phys. Plasmas **6**, 2847 (1999).
- [24] C. Gahn, *Erzeugung relativistischer Elektronen durch Propagation hochintensiver Laserpulse in einem Plasma* (PhD-thesis (in German), LMU München, 2000).
- [25] W.L. Kruer, *The Physics of Laser Plasma Interactions* (Addison-Wesley, New York, 1988).
- [26] S.J. Gitomer, R.D. Jones, F. Begay, A.W. Ehler, J.F. Kephart and R. Kristal, *Fast ions and hot electrons in the laser plasma interaction*, Phys. Fluids **29**, 2679 (1986).
- [27] A.V. Gurevich, L.V. Pariiskaya and L.P. Pitaevskii, *Self-similar motion of rarefied plasma*, J. Exp. + Theor. Phys. **22**, 449 (1966).
- [28] E. Springate, N. Hay, J.W. Tisch, M.B. Mason, T. Ditmire, M.H. Hutchinson and J.P. Marangos, *Explosion of atomic clusters irradiated by high-intensity laser pulses: Scaling of ion energies with cluster and laser parameters*, Phys. Rev. A **61**, 063201 (2000).
- [29] T. Ditmire, J.W. Tisch, E. Springate, M.B. Mason, N. Hay, R.A. Smith, J. Marangos and M.H. Hutchinson, *High-energy ions produced in explosions of superheated atomic clusters*, Nature (London) **386**, 54 (1997).
- [30] G. Pretzler, A. Saemann, A. Pukhov, D. Rudolph, T. Schätz, U. Schramm, P. Thirolf, D. Habs, K. Eidmann, G.D. Tsakiris, J. Meyer-ter-Vehn and K.J. Witte, *Neutron production by 200 mJ ultrashort laser pulses*, Phys. Rev. E **58**, 1165 (1998).
- [31] G.S. Sarkisov, V.Y. Bychenkov, V.N. Novikov, V.T. Tikhonchuk, A. Maksimchuk, S.Y. Chen, R. Wagner, G. Mourou and D. Umstadter, *Self-focusing, channel formation, and high-energy ion generation in interaction of an intense short laser pulse with a He jet*, Phys. Rev. E **59**, 7042 (1999).
- [32] K. Krushelnick, E.L. Clark, Z. Najmudin, M. Salvati, M.I. Santala, M. Tatarakis, A.E. Dangor, V. Malka, D. Neely, R. Allott and C. Danson, *Multi-MeV ion production from high-intensity laser interactions with underdense plasmas*, Phys. Rev. Lett. **83**, 737 (1999).
- [33] E.L. Clark, K. Krushelnick, M. Zepf, F.N. Beg, M. Tatarakis, A. Machacek, M.I. Santala, I. Watts, P.A. Norreys and A.E. Dangor, *Energetic heavy-ion and*

- proton generation from ultraintense laser-plasma interactions with solids*, Phys. Rev. Lett. **85**, 1654 (2000).
- [34] M. Lezius, S. Dobosz, D. Normand and M. Schmidt, *Explosion dynamics of rare gas clusters in strong laser fields*, Phys. Rev. Lett. **80**, 261 (1998).
- [35] T. Ditmire, T. Donnelly, A.M. Rubenchik, R.W. Falcone and M.D. Perry, *Interaction of intense laser pulses with atomic clusters*, Phys. Rev. A **53**, 3379 (1996).
- [36] J. Zweiback, T. Ditmire and M.D. Perry, *Femtosecond time-resolved studies of the dynamics of noble-gas cluster explosions*, Phys. Rev. A **59**, R3166 (1999).
- [37] T. Ditmire, E. Springate, J.W. Tisch, Y.L. Shao, M.B. Mason, N. Hay, J. Marangos and M.H. Hutchinson, *Explosion of atomic clusters heated by high-intensity femtosecond laser pulses*, Phys. Rev. A **57**, 369 (1998).
- [38] A. Pukhov and J. Meyer-ter-Vehn, *Relativistic magnetic self-channeling of light in near-critical plasma: three-dimensional particle-in-cell simulation*, Phys. Rev. Lett. **76**, 3975 (1996).
- [39] E.L. Clark, K. Krushelnick, J.R. Davies, M. Zepf, M. Tatarakis, F.N. Beg, A. Machacek, P.A. Norreys, M.I. Santala, I. Watts and A.E. Dangor, *Measurements of energetic proton transport through magnetized plasma from intense laser interactions with solids*, Phys. Rev. Lett. **84**, 670 (2000).
- [40] M. Roth, T.E. Cowan, J.C. Gauthier, M. Allen, P. Audebert, A. Blazevic, J. Fuchs, M. Geissel, M. Hegelich, S. Karsch, J. Meyer ter Vehn, A. Pukhov and T. Schlegel, *The dependence of intense laser-accelerated ion beams on target properties*, Phys. Rev. Spec. Top. - AB **5**, 061301 (2002).
- [41] S.P. Hatchett, C.G. Brown, T.E. Cowan, E.A. Henry, J.S. Johnson, M.H. Key, J.A. Koch, A.B. Langdon, B.F. Lasinski, R.W. Lee, A.J. Mackinnon, D.M. Pennington, M.D. Perry, T.W. Phillips, M. Roth, T.C. Sangster, M.S. Singh, R.A. Snavely, M.A. Stoyer, S.C. Wilks and K. Yasuike, *Electron, photon, and ion beams from the relativistic interaction of Petawatt laser pulses with solid targets*, Phys. Plasmas **7**, 2076 (2000).
- [42] A.J. Mackinnon, Y. Sentoku, P.K. Patel, D.W. Price, M.H. Key, C. Andersen, R. Snavely and R.R. Freeman, *Enhancement of Proton Acceleration by Hot-Electron Recirculation in Thin Foils Irradiated by Ultraintense Laser Pulses*, Phys. Rev. Lett. **88**, 215006 (2002).

- [43] M. Hegelich, S. Karsch, G. Pretzler, D. Habs, K. Witte, W. Guenther, M. Allen, A. Blazevic, J. Fuchs, J.C. Gauthier, M. Geissel, P. Audebert, T.E. Cowan and M. Roth, *MeV Ion Jets from Shortpulse-Laser Interaction with thin foils*, Phys. Rev. Lett. **89**, 085002 (2002).
- [44] P.H. Rutherford R.J. Goldstone, *Plasmaphysik* (vieweg Lehrbuch, Braunschweig, 1998).
- [45] S.C. Wilks, A.B. Langdon, T.E. Cowan, M. Roth, M. Singh, S.P. Hatchett, M.H. Key, D. Pennington, A.J. MacKinnon and R.A. Snavely, *Energetic proton generation in ultra-intense laser solid interactions*, Phys. Plasmas **8**, 542 (2001).
- [46] A. Maksimchuk, S. Gu, K. Flippo, D. Umstadter and V.Y. Bychenkov, *Forward ion acceleration in thin films driven by a high-intensity laser*, Phys. Rev. Lett. **84**, 4108 (2000).
- [47] K. Krushelnick, E.L. Clark, M. Zepf, J.R. Davies, F.N. Beg, A. Machacek, M.I. Santala, M. Tatarakis, I. Watts, P.A. Norreys and A.E. Dangor, *Energetic proton production from relativistic laser interaction with high density plasmas*, Phys. Plasmas **7**, 2055 (2000).
- [48] A. Pukhov, *Three dimensional simulation of ion acceleration from a foil irradiated by a short pulse laser*, Phys. Rev. Lett. **86**, 3561 (2001).
- [49] A.V. Gurevich, R.Z. Sagdeev, S.I. Anisimov and Yu.V. Medvedev, *Non-linear dynamics and acceleration of ions when a plasma expands into a plasma*, Sov.Sci.Rev. A Phys. **13**, 1 (1989).
- [50] A.J. Mackinnon, M. Borghesi, S. Hatchett, M.H. Key, P.K. Patel, H. Campbell, A. Schiavi, R. Snavely, S.C. Wilks and O. Willi, *Effect of Plasma Scale Length on Multi-MeV Proton Production by Intense Laser Pulses*, Phys. Rev. Lett. **86**, 1769 (2001).
- [51] M. Borghesi, S. Bulanov, D.H. Campbell, R.J. Clarke, T.Zh. Esirkepov, M. Galimberti, L.A. Gizzi, A.J. MacKinnon, N.M. Naumova, F. Pegoraro, H. Ruhl, A. Schiavi and O. Willi, *Macroscopic Evidence of Soliton Formation in Multiterawatt Laser-Plasma Interaction*, Phys. Rev. Lett. **88**, 135002 (2002).
- [52] M. Roth, T.E. Cowan, M.H. Key, S.P. Hatchett, C. Brown, W. Fountain, J. Johnson, D.M. Pennington, R.A. Snavely, S.C. Wilks, K. Yasuike, H. Ruhl, F. Pegoraro, S.V. Bulanov, E.M. Campbell, M.D. Perry and H. Powell, *Fast ignition by intense laser-accelerated proton beams*, Phys. Rev. Lett. **86**, 436 (2001).

- [53] E.E. Fill, *Analytical theory of pulsed relativistic electron beams entering a vacuum*, Phys. Plasmas **8**, 4613 (2001).
- [54] V.T. Tikhonchuk, *Interaction of a beam of fast electrons with solids*, Phys. Plasmas **9**, 1416 (2002).
- [55] D. Bauer and P. Mulser, *Relativistic ponderomotive force, uphill acceleration, and transition to chaos*, Phys. Rev. Lett. **75**, 4622 (1995).
- [56] C.A. Ullrich, U.J. Grossmann and E.K.U. Gross, *Time-dependent optimized effective Potential*, Phys. Rev. Lett. **74**, 872 (1995).
- [57] E.K.U. Gross and W. Kohn, *Local Density-Functional Theory of Frequency Dependent Linear Response*, Phys. Rev. Lett. **55**, 2850 (1985).
- [58] K.C. Kulander, *Time-dependent Hartree-Fock theory of multiphoton ionization: Helium*, Phys. Rev. A **36**, 2726 (1987).
- [59] L.V. Keldysh, *Ionization in the field of a strong electromagnetic wave*, J. Exp. + Theor. Phys. **20**, 1307 (1965).
- [60] F.H.M. Faisal, *Multiple absorption of laser photons by atoms*, J.Phys.B **6**, L89 (1973).
- [61] H.R. Reiss, *Effect of an intense electromagnetic field on a weakly bound system*, Phys. Rev. A **22**, 1786 (1980).
- [62] D.M. Wolkow, *Über eine Klasse von Lösungen der Diracschen Gleichung*, Z. Phys. **119**, 250 (1935).
- [63] M.V. Ammosov, N.B. Delone and V.P. Krainov, *Tunnel ionization of complex atoms and of atomic ions in an alternating electromagnetic field*, Sov. Phys. JETP **64**, 1191 (1986).
- [64] J.H. Posthumus, M.R. Thompson, L.F. Frasinski and K. Codling, in *IOP Conf. Proc. No. 154: Multiphoton Processes 1996*, edited by P. Lambropoulos and H. Walther (IOP, Bristol, UK, 1997), S. 298.
- [65] R.E. Pfund, *Inelastische Prozesse in ultra-kurzer Laser-Materie-Wechselwirkung* (PhD-thesis (in German), TU München, 1999).
- [66] S. Augst, D.D. Meyerhofer, D. Strickland and S.L. Chin, *Laser-ionization of noble gases by Coulomb-barrier suppression*, J. Opt. Soc. Am. B **8**, 858 (1991).

- [67] L.D. Landau and E.M. Lifschitz, *Lehrbuch der theoretischen Physik Band III Quantenmechanik* (Akademie-Verlag, Berlin, 1976).
- [68] J.H. Posthumus, M.R. Thompson, L.F. Frasinski and K. Codling, in *IOP Conf. Proc. No. 154: Multiphoton Processes 1996*, edited by P. Lambropoulos and H. Walther (IOP, Bristol, UK, 1997), S. 98.
- [69] B.M. Penetrante and J.N. Bardsley, *Residual energy in plasmas produced by intense subpicosecond laser pulses*, Phys. Rev. A **43**, 3100 (1991).
- [70] N.F. Mott, in *Proc. R. Soc. London Ser. A 126* (R. Soc., London, UK, 1930), S. 259.
- [71] Y.-K. Kim, , Radiat. Res. **64**, 205 (1975).
- [72] H.A. Bethe, *Theory of passage of Rapid Corpuscular Rays through Matter*, Ann. Phys. **5**, 305 (1930).
- [73] Y.-K. Kim and M.E. Rudd, *Binary-encounter-dipole model for electron impact ionization*, Phys. Rev. A **50**, 3954 (1994).
- [74] L. Grémillet, F. Amiranoff, S.D. Baton, J.C. Gauthier, M. Koenig, E. Martinolli, F. Pisani, G. Bonnaud, C. Lebourg, C. Rousseaux, C. Toupin, A. Antonicci, D. Batani, A. Bernardinello, T. Hall, D. Scott, P. Norreys, H. Bandulet and H. Pépin, *Time-resolved observation of ultrahigh intensity laser-produced electron jets propagating through transparent solid targets*, Phys. Rev. Lett. **83**, 5015 (1999).
- [75] H. Ruhl, Y. Sentoku, K. Mima, K.A. Tanaka and R. Kodama, *Collimated electron jets by intense laser beam plasma surface interaction under oblique incidence*, Phys. Rev. Lett. **82**, 743 (1999).
- [76] R.W. Lee and J.T. Larson, *The ionization code FLY??*, J. Quant. Spectr. Radiat. Transf. **56**, 535 (1996).
- [77] H. Baumhacker, A. Böswald, H. Haas, M. Fischer, W. Fölsner, G. Keller, U. Andiel, X. Dong, M. Dreher, K. Eidmann, E. Fill, M. Hegelich, M. Kaluza, S. Karsch, G. Pretzler, G. Tsakiris and K.J. Witte, *Advanced Titanium Sapphire Laser ATLAS* (MPQ-Report, Max-Planck Institut für Quantenoptik, München, 2001).
- [78] J.-C. Gauthier, F. Amiranoff, C. Chenais-Popovics, G. Jamelot, M. Koenig, C. Labaune, E. Leboucher-Dalimier, C. Sauteret and A. Migus, *LULI activities in the field of high-power laser-matter interaction*, Laser Part. Beams **17**, 195 (1999).

- [79] D.E. Spence, P.N. Kean and W. Sibbett, *60-fsec pulse generation from a self-mode-locked Ti:sapphire laser*, Opt. Lett. **16**, 42 (1991).
- [80] T. Brabec, C. Spielmann, P.F. Curley and F. Krausz, *Kerr-lens mode locking*, Opt. Lett. **17**, 1292 (1992).
- [81] G. Pretzler, *Höchstleistungs-Kurzpulslaser* (lecture notes (in German), LMU München, 2000).
- [82] T.E. Cowan, A.W. Hunt, T.W. Phillips, S.C. Wilks, M.D. Perry, C. Brown, W. Fountain, S. Hatchett, J. Johnson, M.H. Key, T. Parnell, D.M. Pennington, R.A. Snavely and Y. Takahashi, *Photonuclear fission from high energy electrons from ultraintense laser-solid interactions*, Phys. Rev. Lett. **84**, 903 (2000).
- [83] G. Rusch, E. Winkel, A. Noll and W. Heinrich, *The Siegen automatic measuring system for track detectors: New developments*, Nucl. Tr. Rad. Meas. **19**, 261 (1991).
- [84] D.R. Slaughter and W.L. Pickles, *A highly sensitive silver-activation detector for pulsed neutron sources*, Nucl. Instrum. Meth. **160**, 87 (1979).
- [85] R.L. Fleischer, P.B. Price and R.M. Walker, *Nuclear Tracks in Solids: Principles and Applications* (University of California Press, Berkeley, 1975).
- [86] N. Yasuda, M. Yamamoto, K. Amemiya, H. Takahashi, A. Kyan and K. Ogura, *Track sensitivity and the surface roughness measurements of CR-39 with atomic force microscope*, Rad. Meas. **31**, 203 (1999).
- [87] S.A. Durrani and R.K. Bull, *Solid State Nuclear Track Detection* (Pergamon Press, Oxford, 1987).
- [88] C. Grupen, *Teilchendetektoren* (BI-Verlag, Berlin, 1993).
- [89] E.V. Benton, *Criteria for Track Registration No.4: Charged Particle Tracks in Polymers*, 1967.
- [90] Y. Murakami, Y. Kitagawa, Y. Sentoku, M. Mori, R. Kodama, K. Tanaka, K. Mima and T. Yamanaka, *Observation of proton rear emission and possible gigagauss scale magnetic fields from ultra-intense laser illuminated plastic targets*, Phys. Plasmas **8**, 4138 (2001).
- [91] W. Trakowski, B. Schoefer, J. Dreute, S. Sonntag, S. Beer, C. Brechtmann, H. Drechsel and W. Heinrich, *An automatic measuring system for particle tracks in plastic detectors*, Nucl. Instrum. Meth. **225**, 92 (1984).

- [92] J. Beck, *Spuren von niederenergetischen He-, C-Ionen und Cf-Spaltfragmenten im Plastikkernspurdetektor CR-39* (Diploma-thesis, Univ. Siegen, 2002).
- [93] J.J. Santos, F. Amiranoff, S.D. Baton, L. Grémillet, M. Koenig, E. Martinolli, M. Rabec Le Gloahec, C. Rousseaux, D. Batani, A. Bernardinello, G. Greison and T. Hall, *Fast Electron Transport in Ultraintense Laser Pulse Interaction with Solid Targets by Rear-Side Self-Radiation Diagnostics*, Phys. Rev. Lett. **89**, 025001 (2002).
- [94] M. Roth, M. Allen, P. Audebert, A. Blazevic, E. Brambrink, T.E. Cowan, J. Fuchs, J.C. Gauthier, M. Geissel, M. Hegelich, S. Karsch, J. Meyer ter Vehn, H. Ruhl, T. Schlegel and R. Stephens, *The generation of high quality, intense ion beams by ultra intense lasers*, Plasm. Phys. Control. Fusion **44**, 1 (2002).
- [95] H. Ruhl, S. Bulanov, T.E. Cowan, T.V. Liseikina, P. Nickles, F. Pegoraro, M. Roth and W. Sandner, *3D PIC simulation of proton acceleration from thin spherical targets*, Plasm. Phys. Rep. **27**, 363 (2001).
- [96] F. Begay, T.H. Tan, J. Hayden and J. McLeod, *Effect of target purity on laser produced plasma expansion*, J.Phys.D **13**, L29 (1980).
- [97] A.V. Gurevich and A.P. Meshcherkin, *Ion acceleration in an expanding plasma*, J. Exp. + Theor. Phys. **53**, 937 (1981).
- [98] S. Karsch, S. Düsterer, H. Schwoerer, F. Ewald, D. Habs, M. Hegelich, G. Pretzler, A. Pukhov, K. Witte and R. Sauerbrey, *Neutron TOF analysis of laser-induced ion acceleration at the target front and rear surface*, Phys. Rev. Lett. **??**, ?? (2002), submitted.
- [99] S. Bulanov, T.Zh. Esirkepov, F. Califano, Y. Kato, T.V. Liseikina, K. Mima, N.M. Naumova, K. Nishihara, F. Pegoraro, H. Ruhl and Y. Sentoku Y. Ueshima, *Generation of the Collimated Beams of Relativistic Ions in Laser-Plasma Interaction*, J. Exp. + Theor. Phys. Lett. **71**, 407 (2000).
- [100] M. Temporal, J.J. Honrubia and S. Atzeni, *Numerical study of fast ignition of ablatively imploded deuterium-tritium fusion capsules by ultr-intense proton beams*, Phys. Plasmas **9**, 3098 (2002).
- [101] A. Pukhov and J. Meyer ter Vehn, *Relativistic Optics*, Vol. x of x, 1 ed. (Springer Book, Berlin, x), to be published.

- [102] J.A. Cobble, R.P. Johnson, T.E. Cowan, N. Renard-Le Galloudec and M. Allen, *High Resolution laser-driven radiography*, J. Appl. Phys. **92**, 1775 (2002).
- [103] K. Nemoto, A. Maksimchuk, S. Banerjee, K. Flippo, G. Mourou, D. Umstadter and V.Y. Bychenkov, *Laser-triggered ion acceleration and table top isotope production*, Appl. Phys. Lett. **78**, 595 (2001).
- [104] E. Teller, *Memoirs* (Perseus Publishing, Cambridge, MA, USA, 2001), S. 63.

Publications

List of Publications

MeV Ion Jets from Shortpulse-Laser Interaction with thin foils

M. Hegelich, S. Karsch, G. Pretzler, D. Habs, K. Witte, W. Guenther, M. Allen, A. Blazevic, J. Fuchs, J.C. Gauthier, M. Geissel, P. Audebert, T.E. Cowan and M. Roth, Phys. Rev. Lett. **88**, 085002 (2002).

MeV Ion Jets from Shortpulse-Laser Interaction with thin foils

M. Hegelich, S. Karsch, G. Pretzler, D. Habs, K. Witte, W. Guenther, M. Allen, A. Blazevic, J. Fuchs, J.C. Gauthier, M. Geissel, P. Audebert, T.E. Cowan and M. Roth, Virt. J. ultraf. Sci. (2002).

Teilchenbeschleunigung mit Lasern

M. Hegelich

Physik in unserer Zeit **6**, 252 (2002).

The dependence of intense laser-accelerated ion beams on target properties

M. Roth, T.E. Cowan, J.C. Gauthier, M. Allen, P. Audebert, A. Blazevic, J. Fuchs, M. Geissel, **M. Hegelich**, S. Karsch, J. Meyer ter Vehn, A. Pukhov and T. Schlegel, Phys. Rev. Spec. Top. - AB **5**, 061301 (2002).

The generation of high quality, intense ion beams by ultra intense lasers

M. Roth, M. Allen, P. Audebert, A. Blazevic, E. Brambrink, T.E. Cowan, J. Fuchs, J.C. Gauthier, M. Geissel, **M. Hegelich**, S. Karsch, J. Meyer-ter-Vehn, H. Ruhl, T. Schlegel and R. Stephens, Plasm. Phys. Control. Fusion **44**, B99-B108 (2002).

Neutron TOF analysis of laser-induced ion acceleration at the target front and rear surface

S. Karsch, S. Düsterer, H. Schwoerer, F. Ewald, D. Habs, **M. Hegelich**, G. Pretzler, A. Pukhov, K. Witte and R. Sauerbrey, Phys. Rev. Lett., submitted (2002),

Correction of strong phase and amplitude modulations by two deformable mirrors in a multistaged Ti:sapphire laser

H. Baumhacker, G. Pretzler, K.J. Witte, **M. Hegelich**, M. Kaluza, S. Karsch, A. Kudryashov, V. Samarkin and A. Roukossouev,
Opt. Lett. **27**, 1570 (2002).

Time-resolved investigation of photoinduced birefringence in azobenzene side-chain polyesters

V. Cimrova, D. Neher, R. Hildebrandt, **M. Hegelich**, A.v.d. Lieth, G. Marowsky, R. Hagen, S. Kostromine, T. Bieringer
Appl. Phys. Lett. **81**, 1228 (2002).

Time-resolved investigation of photoinduced birefringence in azobenzene side-chain polyesters

R. Hildebrandt, **M. Hegelich**, H.-M. Keller, G. Marowsky and S. Hvilsted,
Phys. Rev. Lett. **81**, 5548 (1998).

- 1.5** M. Hegelich, S. Karsch, G. Pretzler, D. Habs, K. Witte, W. Guenther, M. Allen, A. Blazevic, J. Fuchs, J.C. Gauthier, M. Geissel, P. Audebert, T. Cowan, M. Roth,
MeV Ion Jets from Shortpulse-Laser Interaction with thin Foils,
Phys. Rev. Lett. **89**, 085002 (2002).
Copyright 2002 by the American Physical Society

MeV Ion Jets from Short-Pulse-Laser Interaction with Thin Foils

M. Hegelich,^{1,2} S. Karsch,^{1,2} G. Pretzler,^{1,2} D. Habs,² K. Witte,¹ W. Guenther,³ M. Allen,⁴ A. Blazevic,⁵ J. Fuchs,⁶ J. C. Gauthier,⁶ M. Geissel,⁵ P. Audebert,⁶ T. Cowan,⁴ and M. Roth⁵

¹MPI für Quantenoptik, 85748 Garching, Germany

²Universität München, 85748 Garching, Germany

³Universität Siegen, 57068 Siegen, Germany

⁴General Atomics, San Diego, California 92121

⁵GSI Laboratory, 64291 Darmstadt, Germany

⁶LULI, Ecole Polytechnique, 91128 Palaiseau, France

(Received 27 December 2001; published 2 August 2002)

Collimated jets of carbon and fluorine ions up to 5 MeV/nucleon (~ 100 MeV) are observed from the rear surface of thin foils irradiated with laser intensities of up to 5×10^{19} W/cm². The normally dominant proton acceleration could be suppressed by removing the hydrocarbon contaminants by resistive heating. This inhibits screening effects and permits effective energy transfer and acceleration of other ion species. The acceleration dynamics and the spatiotemporal distributions of the accelerating E fields at the rear surface of the target are inferred from the detailed spectra.

DOI: 10.1103/PhysRevLett.89.085002

PACS numbers: 52.38.Kd, 41.75.Jv

For over 25 years, energetic protons and ions have been generated by focusing \sim ns pulses from large Nd:glass and CO₂ lasers ([1] and references therein) on solid targets at intensities of 10^{14} – 10^{16} W/cm². The ions emerging from the coronal plasma are emitted into a large solid angle. They exhibit strong trajectory crossing and a broad energy spectrum with typical ion temperatures of ~ 100 keV/nucleon. These unspectacular characteristics have prevented major applications. This scenario is totally different when the ion acceleration is caused by femto-second (fs) laser pulses. When these are focused on thin foils targets (~ 50 μ m) at intensities of $> 10^{19}$ W/cm², proton beams are observed which exhibit new features [2–4]: (i) 10^{11} – 10^{13} well collimated ($< 20^\circ$) protons with 5 to 50 MeV are generated, (ii) they come from the *rear surface* and move in the laser direction, and (iii) they form a dense, charge-neutralized bunch of ~ 1 ps duration. These proton beams have already been applied for the diagnostic of high-density plasmas [5] and suggested for fast ignition [6]. Application in isotope production for positron emission tomography might follow soon.

Hatchett and Wilks [7,8] attribute the above mentioned characteristics of the proton beam to the so-called target-normal sheath acceleration mechanism (TNSA), the notion being that relativistic electrons with density, n_e , and temperature, T_e , created at the target front side penetrate the foil and by extending past the rear surface produce a strong space-charge field:

$$E \approx k_B T_e / e \lambda_D, \quad \lambda_D = (\epsilon_0 k_B T_e / e^2 n_e)^{1/2}. \quad (1)$$

Typical values of $k_B T_e \sim 2$ MeV and $n_e \sim 2.5 \times 10^{19}$ cm⁻³ yield $\lambda_D \sim 2$ μ m (distance over which the electric field E decays) and $E > 10^{12}$ V/m. A few monolayers of atoms at the rear surface experience field ionization by barrier suppression (FIBS) [9] and are accelerated normal to the sur-

face by E . The most energetic electrons always extend farther out into vacuum, maintaining the accelerating field as long as the electron temperature is high. This is fundamentally different from the long-pulse case, in which bulk effects and collisional ionization by thermal electrons in the coronal plasma are the dominant mechanisms. In the fs case, however, the ion generation and acceleration mechanisms are decoupled from the *stochastic* laser-plasma interaction, which offers many advantages for producing well-controlled ion beams. The decoupling and the rapid rear-surface acceleration are the reasons why the protons appear in a highly laminar, low emittance ps bunch inside which no trajectory crossing occurs. So far, mainly protons have been observed from the rear side. This is attributed to contaminations of hydrocarbon and H₂O layers adhered to the target. Because of its low ionization potential and high charge-to-mass ratio hydrogen is among the first ion species produced and most effectively accelerated, thereby screening the space-charge fields for all other ion species.

In this Letter, we present the first experimental study demonstrating that besides protons also high-brightness, high-energy (\sim MeV/nucleon) ion beams can be accelerated from the *rear surface* of thin foils. These ions are effectively accelerated only if the hydrogenous surface contaminants are removed. We obtain absolutely calibrated high-resolution energy spectra of different ion species and charge states. These provide additional information, not in the proton signal, about the spatiotemporal evolution of the accelerating field and the origin of the observed ions. We show for the first time that it is possible to control the accelerated ion species by choosing a target composed of a front-side interaction material and a rear-side ion source layer. The high-energy ions out of these prepared source layers unambiguously prove the existence of an effective rear-surface acceleration mechanism. For our experimental conditions, we thereby resolve the long-standing

controversy as to whether the high-energy (> 10 MeV) protons come from the rear surface and are accelerated by the TNSA mechanism [6,10–12] or stem from the front surface and are accelerated by the charge-separation field in the laser plasma [3,13]. The electric field deduced from the ion spectra can explain the high-energy protons (> 25 MeV [4]) in our experiments. This result also constitutes a major difference to long-pulse experiments, where rear-surface acceleration was a minor effect only, that vanished almost completely when either the contaminating hydrocarbons were removed [14] or foils thicker than a few μm were used [15]. With the new capability to accelerate ion species at will and indications that beam focusing [4], spectra and charge state control might be feasible, applications such as laser accelerators are becoming realistic. Also the transport of a dense charge-neutralized ion beam in plasmas and solids, enabling isochoric heating of macroscopic volumes ($\sim 10^5 \mu\text{m}^3$) to > 300 eV, could now be studied.

Our experiments were performed with the 100-TW laser at the Laboratoire pour l'Utilisation des Lasers Intenses (LULI). The laser pulses (~ 30 J, ~ 300 fs, $1.05 \mu\text{m}$) were focused at normal incidence on target to an intensity of up to 5×10^{19} W/cm². The contrast, i.e., the peak-to-pedestal intensity ratio, amounts to $\sim 10^7$ at $t = 1.5$ ns. As targets we used $50 \mu\text{m}$ thick Al and W foils coated on the rear side with $1 \mu\text{m}$ carbon or $0.3 \mu\text{m}$ CaF₂, respectively. The accelerated particles were investigated by three complementary diagnostics: (a) a stack of radiochromic films (RCF) 5 cm behind the target to record the angular distribution of the emitted proton beam [7,16], (b) a magnetic proton spectrometer [17] at 13° to the target normal with a Kodak DEF x-ray film to measure the proton energy spectra, and (c) two Thomson parabola spectrometers ($B = 0.65$ T, $E = 1.3$ MV/m) with CR-39 track detectors at 0° and 6° at a distance of about 1 m (solid angle $\sim 5 \cdot 10^{-8}$ sr) to obtain the ion energy spectra. CR-39 is sensitive to single ion events but insensitive to electromagnetic radiation and electrons. An ion striking a CR-39 plate destroys the polymer matrix along its path and causes nm-scale damage sites. These are transformed into cone- or bowl-shaped craters when the CR-39 is etched in NaOH solution. Each individual track is analyzed by optical microscopy with custom pattern recognition software [18] yielding position and track size parameters, from which the absolute ion energy spectra are then obtained. Because the optical density is not simply proportional to the number of pits, only “single-track counting” yields correct results for the areal ion density, whereas optical scanning may lead to erroneous results.

To remove the hydrogenous contaminants, we tried radiative, laser, and resistive heating and found the latter the most effective (see also [19]). We heated Al and W foils up to ~ 600 K and ~ 1200 K, respectively. Already the partial removal of hydrocarbons strongly enhanced the acceleration of carbon ions, as shown in Fig. 1. The proton spectrometer yielded typically $\sim 10^{11}$ protons of up to 25 MeV,

for unheated targets. For heated Al targets, the number of protons is reduced to $\sim 10^{10}$ with energies of up to 3 MeV. The energy of the carbon ions is increased by a factor of ~ 2.5 and the number by 2 orders of magnitude to $\sim 2 \times 10^{11}$, corresponding to a laser-to-ion energy conversion of 0.5%. Acceleration is most efficient for C⁴⁺ ions, with a cutoff energy of ~ 1 MeV/nucleon at the high-energy end. In all spectra the high-energy cutoff is dependent on the charge state, ruling out recombination as a dominant effect in our experiments. This is confirmed by the low number of neutral atoms ($\sim 1\%$) forming the pinhole image on the CR-39. This behavior is fundamentally different from that observed in the carbon spectra in long-pulse experiments [20], where all charge states had a similar cutoff and the rear-surface ion signal almost vanished for heated targets [19]. Using W targets, the higher heating temperatures resulted in a complete removal of hydrocarbons. The proton spectrometer as well as the CR-39 did not show any protons, while strong fluorine ion tracks are observed originating from the CaF₂ layer at the target rear side (Fig. 2). Since only the target rear surface is coated with either C or CaF₂, the carbon and fluorine ions originate unambiguously from the rear surface of the targets. The acceleration of heavier ions was again increased considerably: F⁷⁺ was accelerated up to 100 MeV (> 5 MeV/nucleon) at $> 5\%$ energy conversion. The RCF confirmed this by showing a narrow spot in the first layer, which, in the absence of protons, indicates fluorine ions of energies above 4 MeV/nucleon. The analysis of the lower charge states

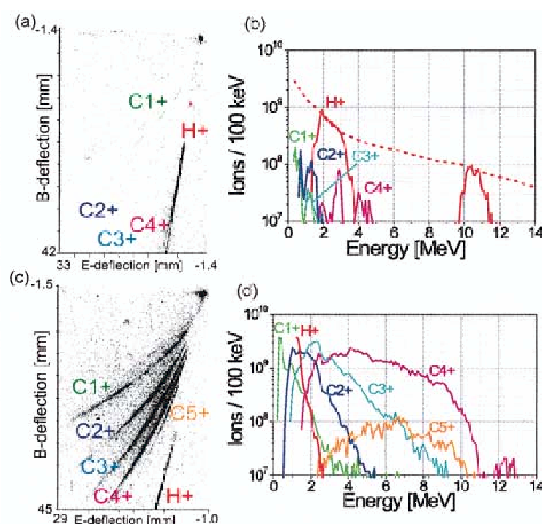


FIG. 1 (color). (a) Ion traces (on CR39) from an unheated Al|C target and (b) corresponding spectra. The gap in the proton signal is due to the CR-39 detector which is optimized for heavier particles. The dotted line illustrates the H⁺ spectra as obtained with the proton spectrometer. (c) Ion traces from a heated Al|C target and (d) corresponding spectra. The ion signals are strongly enhanced. The spot in the upper right corner of (a),(c) is the pinhole image formed by neutral atoms.

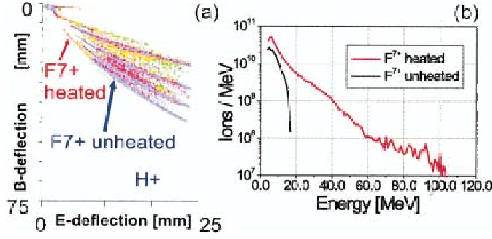


FIG. 2 (color). (a) Overlaid signals of heated (orange) and unheated (blue) W | CaF₂ targets: The proton signal vanishes for heated targets; the fluorine signals (especially F⁷⁺) go up to much higher energies. (b) Corresponding F⁷⁺ spectra: F⁷⁺ ions achieve more than 100 MeV (5 MeV/nucleon).

proves to be more difficult due to overlapping of F and Ca traces with similar charge-to-mass ratios.

Long-pulse experiments showed that ion spectra can be used to identify the ionization and acceleration mechanisms, e.g., isothermal expansion (with $T_{e,\text{hot}} \sim 10\text{--}100$ keV) and collisional ionization up to the highest

charge state (e.g., C⁶⁺), followed by recombination to the lower charge states in the drift phase ([1,20] and references therein). In short-pulse experiments, however, FIBS in the strong transient space-charge field dominates because of the fs timescale and high electron temperature (\sim MeV). We can rule out ionization by the laser pulse or by a shock front by simultaneous target interferometry. The laser pulse is completely absorbed in the preplasma and the target thickness is chosen to prevent prepulse-caused shock breakout until ~ 10 ns after the main pulse. Collisional ionization is estimated from [21]:

$$\nu_{\text{col}} \approx n_e v_e 4\pi a_b^2 (U_H^2 / U_k k_B T_e) \ln(k_B T_e / U_k), \quad (2)$$

where a_b is the Bohr radius, v_e is the electron velocity, and U_k and U_H are the ionization potentials of the ionized species and hydrogen, respectively. We also considered the influence of heating by possible return currents with a temperature $k_B T_e^{\text{ret}} \sim 50$ eV [22], which must balance the hot electron flow, i.e., $n_e^{\text{ret}} v_e^{\text{ret}} \approx n_e^{\text{hot}} v_e^{\text{hot}} \Rightarrow n_e^{\text{ret}} \sim 2.5 \times 10^{21} \text{ cm}^{-3}$. We estimated the field ionization rate from the ADK model [23]:

$$\nu_{\text{ADK}} \approx 6.6 \cdot 10^{16} (Z^2 / n_{ef}^{4.5}) \exp[-(2Z^3 / 3n_{ef}^3)(E_{\text{at}}/E)] [10.87(Z^3 / n_{ef}^4)(E_{\text{at}}/E)]^{2n_{ef}-1.5}, \quad (3)$$

where $E = 2$ TV/m [from Eq. (1)] is the ionizing field, $E_{\text{at}} = 0.51$ TV/m is the atomic electric field, Z is the charge of the created ion, and $n_{ef} = Z / \sqrt{U_k / U_H}$. The various ionization frequencies are listed in Table I. Other analytical models yield similar results and the exact numerical rates are even higher [23]. For all models field ionization dominates by orders of magnitude over the collisional processes for our set of parameters and for charge states up to He-like. For C⁵⁺, $\nu_{\text{col}}^{\text{hot}}$ is larger than ν_{ADK} , which may explain the different spectral shape and lower numbers for this charge state. Assuming detailed balancing [24], we estimate recombination rates of $\sim 1\%$ consistent with our measured data.

Having established that the ion spectra are linked to the accelerating E fields, we can now extract information such as the field strength which is not available from the proton data. With FIBS as the dominant ionization process, the

$k +$ ionic state will be created as soon as the electric field is above the threshold

$$E_k = U_k^2 \epsilon_0 \pi / eZ. \quad (4)$$

We can use E_{k+1} as an upper limit for the electric field strength that a $k +$ ion has experienced. By integrating the equations of motion for an ion in a field rising in time with the laser pulse to E_k , staying at this value for a time τ_k^{min} and then decaying exponentially, τ_k^{min} defines a lower limit for the acceleration time, required to achieve the observed maximum ion energy for a given charge state (see Table I). The acceleration length, l_k^{min} , is the distance traveled by an ion during τ_k^{min} and is therefore a measure for the minimal spatial extension of the fields. The ultra-high-field region turns out to be of the duration of the laser pulse and of short length (≤ 500 fs, $\leq 5 \mu\text{m}$). Only the C⁴⁺ ions see these

TABLE I. Calculated field and ionization parameters for carbon. U_k is the ionization potential of the k th ionic charge state and E_k is the corresponding field strength [Eq. (4)]. E_k^{max} is the maximal E field, τ_k^{min} is the minimal field duration, and l_k^{min} is the minimal acceleration length for a given k . ν are the ionization frequencies due to the hot electrons ($k_B T_e^{\text{hot}} \sim 2$ MeV, $n_e^{\text{hot}} \sim 2.5 \times 10^{19} \text{ cm}^{-3}$), the return current ($k_B T_e^{\text{ret}} \sim 50$ eV, $n_e^{\text{ret}} \sim 2.5 \times 10^{21} \text{ cm}^{-3}$), and the field ionization ($E_f = 2$ TV/m). Because $\tau_4^{\text{min}} \sim \tau_{\text{laser}}$, E_4^{max} is lower than the theoretically possible value of $5.3 \cdot 10^{12}$ V/m.

k	U_k (eV)	E_k (V/m)	E_k^{max} (V/m)	τ_k^{min} (ps)	l_k^{min} (μm)	$\nu_{\text{col}}^{\text{hot}}$ (ps^{-1})	$\nu_{\text{col}}^{\text{ret}}$ (ps^{-1})	ν_{ADK} (ps^{-1})
1	11.2	2.2×10^{10}	5.2×10^{10}	60	230	2.53×10^{-2}	2.13	5.93×10^4
2	24.4	5.2×10^{10}	1.3×10^{11}	10	48	1.1×10^{-2}	0.68	2.65×10^5
3	47.9	1.3×10^{11}	1.8×10^{11}	4.3	25	5.29×10^{-3}	0.21	1.46×10^6
4	64.5	1.8×10^{11}	1.75×10^{12}	0.35	3	3.28×10^{-3}	0.11	4.62×10^6
5	392	5.3×10^{12}				5.29×10^{-4}	...	8.5×10^{-5}
6	490	7.0×10^{12}				4.14×10^{-4}	...	7.03×10^{-9}

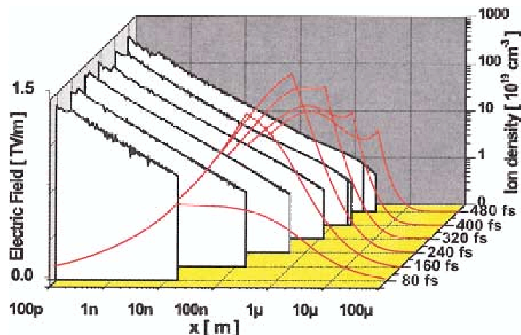


FIG. 3 (color). Space-time history of the accelerating electric fields (red curves) and the C^{4+} -dominated ion distributions (white curves) as calculated by our model: The field maximum moves out into the vacuum. Already during the pulse there exists an ion distribution on a μm scale.

highest fields, while the lower charge states are accelerated by lower fields of up to 2 orders of magnitude longer duration, which is not explainable by the static TNSA model.

In order to get a better understanding of how the ion energies and charge state distributions develop in space and time, we have developed a 1D-numerical model which calculates the electron dynamics behind the target, assuming a Boltzmann equilibrium for the electron energy spectrum and a current distribution which follows the laser pulse. We include the ionization process (FIBS), the acceleration of different ion species, and screening effects on the potential. In each time step, we solve Poisson's equation for the given charge distribution, check for ionization events, advance the different ion species, and solve again Poisson's equation for the new charge distribution. When the first laser-heated electrons enter the vacuum behind the target, they create the space-charge field E , albeit in a highly dynamic way, much more complex than in the simple TNSA model. When more and hotter electrons pass through the surface, the field increases until $E = E_1$. Now FIBS sets in and the produced ions and electrons decrease the field at the surface. An equilibrium between the growing external field and the surface ionization rate keeps the field at the surface always at E_1 . The created ions are accelerated into the vacuum while the freed electrons are pushed into the target. Whereas the field close to the target is shielded by the ions, the unshielded field in vacuum keeps increasing. The maximum of the electric field moves outwards into vacuum, ionizing the outermost ions further (see Fig. 3). The model reproduces the measurements for protons and the high charge states. As long as there is a source of hot electrons, nearly all ions are sequentially ionized to C^{4+} . As seen in the experimental data, the lower charge states require 2 orders of magnitude longer time scales and possibly a 3D treatment to allow for low fields in the fringe regions. To explain the long acceleration times the electron recirculation model of [10] may prove useful. Another approach is to envision the individ-

ual charge states in separately lined up bunches each with a charge neutralizing electron cloud lagging a bit behind, thereby setting up an effective field for the next lower charge state bunch. A model to completely explain the acceleration dynamics is currently developed. The evaluation of the fluorine shot shown in Fig. 2 shows that $E \sim 2$ TV/m active over $\tau_7^{\text{min}} \sim 350$ fs is necessary to accelerate F^{7+} ions up to 100 MeV over a scale length of $l \sim 10 \mu\text{m}$. The inferred fields would accelerate H^+ up to ~ 25 MeV, as typically observed with unheated targets.

In summary, by using high-intensity laser pulses we achieved efficient ($> 5\%$ energy conversion), directed ion acceleration to more than 5 MeV/nucleon from the rear surface of thin-foil targets. High-resolution energy spectra measured for different ionic charge states yield detailed information on the spatiotemporal behavior of the accelerating fields. They show that FIBS is the dominant ionization mechanism while recombination and collisional ionization are negligible except for C^{5+} . A 3D-TNSA model including dynamic fields and multiple ion species is needed to correctly describe the acceleration process.

We thank A. Kemp and H. Ruhl for fruitful discussions and the LULI-laser team for their support. LULI is UMR 7605, CNRS-CEA-Université Paris VI École Polytechnique. This work was supported by EU Programme No. HPRI CT 1999-0052, by Grant No. E 1127 from Région Ile-de-France, and by corporate support from GA.

- [1] S. Gitomer *et al.*, Phys Fluids **29**, 2679 (1986).
- [2] R. Snively *et al.*, Phys. Rev. Lett. **85**, 2945 (2000).
- [3] E. Clark *et al.*, Phys. Rev. Lett. **84**, 670 (2000).
- [4] M. Roth *et al.*, Phys. Rev. ST Accel. Beams **5**, 061301 (2002).
- [5] M. Borghesi *et al.*, Phys. Rev. Lett. **88**, 135002 (2002).
- [6] M. Roth *et al.*, Phys. Rev. Lett. **86**, 436 (2001).
- [7] S. Hatchett *et al.*, Phys. Plasmas **7**, 2076 (2000).
- [8] S. Wilks *et al.*, Phys. Plasmas **8**, 542 (2001).
- [9] S. Augst *et al.*, J. Opt. Soc. Am. B **8**, 858 (1991).
- [10] A. Mackinnon *et al.*, Phys. Rev. Lett. **88**, 215006 (2002).
- [11] Y. Murakami *et al.*, Phys. Plasmas **8**, 4138 (2001).
- [12] A. Mackinnon *et al.*, Phys. Rev. Lett. **86**, 1769 (2001).
- [13] A. Maksimchuk *et al.*, Phys. Rev. Lett. **84**, 4108 (2000).
- [14] F. Begay *et al.*, Phys. Fluids **25**, 1675 (1982).
- [15] G. Tsakiris *et al.*, Phys. Rev. Lett. **46**, 1202 (1981).
- [16] E. Clark *et al.*, Phys. Rev. Lett. **85**, 1654 (2000).
- [17] T. Cowan *et al.*, Phys. Rev. Lett. **84**, 903 (2000).
- [18] G. Rusch *et al.*, Nucl. Tracks Radiat. Meas. **19**, 261 (1991).
- [19] F. Begay *et al.*, J. Phys. D **13**, L29 (1980).
- [20] C. Joshi *et al.*, Appl. Phys. Lett. **34**, 625 (1979).
- [21] V. Tikhonchuk, Phys. Plasmas **9**, 1416 (2002).
- [22] L. Grémillet *et al.*, Phys. Rev. Lett. **83**, 5015 (1999).
- [23] D. Bauer *et al.*, Phys. Rev. Lett. **75**, 4622 (1995).
- [24] L. Oster, Am. J. Phys. **38**, 754 (1970).

1.6 M. Roth, T.E. Cowan, J.C. Gauthier, M. Allen, P. Audebert, A. Blazevic, J. Fuchs, M. Geissel, M. Hegelich, S. Karsch, J. Meyer ter Vehn, A. Pukhov and T. Schlegel,

The dependence of intense laser-accelerated ion beams on target properties,

Phys. Rev. Spec. Top. - AB 5, 061301 (2002).

Copyright 2002 by the American Physical Society.

Energetic ions generated by laser pulses: A detailed study on target properties

M. Roth, A. Blazevic, M. Geissel, and T. Schlegel

Gesellschaft für Schwerionenforschung mbH, Planckstrasse 1, Darmstadt 64291, Germany

T.E. Cowan and M. Allen

General Atomics, P.O. Box 85608, San Diego, California 92186-5608

J.-C. Gauthier, P. Audebert, and J. Fuchs

Laboratoire pour l'Utilisation des Lasers Intenses, Palaiseau 91128, France

J. Meyer-ter-Vehn, M. Hegelich, S. Karsch, and A. Pukhov

Max-Planck-Institut für Quantenoptik, Garching, Germany

(Received 15 November 2001; published 4 June 2002)

We present the results of a detailed study on the acceleration of intense ion beams by relativistic laser plasmas. The experiments were performed at the 100 TW laser at the Laboratoire pour l'Utilisation des Lasers Intenses. We investigated the dependence of the ion beams on the target conditions based on theoretical predictions by the target normal sheath acceleration mechanism. A strong dependence of the ion beam parameters on the conditions on the target rear surface was found. We succeeded in shaping the ion beam by the appropriate tailoring of the target geometry and we performed a characterization of the ion beam quality. The production of a heavy ion beam could be achieved by suppressing the amount of protons at the target surfaces. Finally, we demonstrated the use of short pulse laser driven ion beams for radiography of thick samples with high resolution.

DOI: 10.1103/PhysRevSTAB.5.061301

PACS numbers: 41.75.Jv, 52.59.-f, 52.38.-r, 52.70.-m

I. INTRODUCTION

Recently, the production of intense ion beams of laser irradiated targets has been observed [1–4]. Some experiments, using ultraintense short pulse lasers [5] with intensities exceeding 10^{19} W/cm², have shown collimated beams of protons that have a very low emittance, while reaching energies of up to 50 MeV [6], which is understood as rear surface emission accelerated by the target normal sheath acceleration (TNSA) mechanism [7]. This ion beam generation is attributed to electrostatic fields produced by hot electrons acting on protons from adsorbed water vapor and hydrocarbons [8,9]. Relativistic electrons generated from the laser-plasma interaction, having an average temperature of several MeV, envelope the target foil and form an electron plasma sheath on the rear, nonirradiated surface. The electric field in the sheath can reach $>10^{12}$ V/m, which field ionizes atoms on the surface and accelerates the ions very rapidly normal to the rear surface. Protons, having the largest charge-to-mass ratio, are preferentially accelerated in favor of heavier ions over a distance of a few microns, and up to tens of MeV. This forms in a collimated beam with an approximately exponential energy distribution with 5–6 MeV. This acceleration mechanism makes these intense ion beams highly interesting for many applications, especially if one can collimate or focus the beam by shaping the target, as suggested by numerical calculations [10,11]. Because of the dependence of the ion beam on the formation of the sheath, this process should reveal information about the electron transport through the

target. The transport of relativistic electrons through the target is an extensively studied area of research [12–15] because of its relevance not only for ion acceleration, but especially for the concept of fast ignition [16–18] in inertial confinement fusion. The transport of large currents through the target, the onset of beam filamentation, and the dependence on the target conductivity (with respect to the onset of return currents) are essential for a detailed understanding of the ion accelerating mechanism. We expect that details of the ion acceleration will also depend on the target material and surface conditions. Therefore we carried out experiments to investigate in detail the influence of these target parameters on the ion beam production.

II. EXPERIMENTS

The experiments presented in this paper were performed with the 100 TW laser at Laboratoire pour l'Utilisation des Lasers Intenses (LULI). Pulses of up to 30 J at 300 fs pulse duration at $\lambda = 1.05$ μ m were focused with an $f/3$ off-axis parabolic mirror onto free standing target foils at normal incidence, at intensities up to 5×10^{19} W/cm². The focal spot diameter (FWHM) measured in vacuum was about 8 μ m. Amplified spontaneous emission (ASE) occurred 2 ns before the main pulse at a level of 10^{-7} of the main pulse energy and preformed a plasma.

The diagnostic setup is depicted in Fig. 1. The free-standing target was probed by a frequency doubled laser beam parallel to the surface to determine the plasma conditions on the front and rear surfaces. A stack of

radiochromic film (RCF) was positioned a few cm behind the target to measure the spatial beam profile. Because of the pronounced energy loss of ions at the end of their range (Bragg peak), different layers of the RCF pack allow the imaging of the ion beam at different energies. The RCF changes through polymerization of a diacetylene active layer, from transparent to dark blue, in proportion to the absorbed dose (rads) of ionizing radiation (1 rad = 100 erg/g). We modeled the response of the RCF package with the SRIM [19] Monte Carlo ion transport code, assuming the beam to be protons, and obtained response functions for the layers of RCF similar to the ones presented in Ref. [2]. A slot in the center of the RCF allowed a free line of sight for the charged particle spectrometers fielded at 0° , 6° , and 13° to provide the energy distribution of the emitted electrons and ions.

Two absolutely calibrated, permanent magnetic ion spectrometers were mounted at a distance of about 1 m from the target covering a solid angle of 5×10^{-6} sr. The electrons and protons were recorded in nuclear emulsion track detectors which allow single particle detection without being overwhelmed by the blinding x-ray flash from the laser plasma. The use of an additional x-ray film layer extended the dynamic range to higher particle fluxes. A protective light tight paper in front of the emulsion and x-ray film stopped protons below 1.8 MeV. We extended the spectral range to lower proton energies using CR-39 in the low energy range of the dispersion plane. By etching the CR-39 detectors in sodium hydroxide, the material damage caused by the impacts of ions above a threshold of a few hundred keV become visible. Microscopic scanning provides position, as well as the size of the impact, which is proportional to the atomic number Z of the ion. Thus, protons produce much smaller pit sizes than heavy ions.

As a complementary measure of the total yield of protons we used a titanium catcher foil, which was placed in the path of the proton beam. The ^{48}Ti is transmuted by a (p, n) reaction by protons above a sharp reaction threshold at ~ 5 MeV to an excited state of the ^{48}V isotope. Using a low-background Ge detector we observed the gamma de-excitation lines of the $^{48}\text{Ti}(p, n)^{48}\text{V}$ reaction, which pro-

vided the total activation and therefore the yield of protons above the reaction threshold of ~ 5 MeV.

To detect heavy ions accelerated from the rear surface of the relativistic-laser illuminated targets, we substituted two high resolution Thompson parabolas in replacement of one of the charged-particle spectrometers. The parallel electric and magnetic fields in the Thompson parabolas discriminated ions with respect to their momentum and charge-to-mass ratio, at the plane of the CR-39 track detectors. Careful analysis of the scanned CR-39 detectors then provides absolute numbers of the ions with respect to their kinetic energy and charge state. In addition to the ion and laser beam detectors, a silver activation neutron detector was fielded close to the target chamber determining the neutron yield for the different experiments. The silver is activated by neutron impact capture and β^- decay with a half-life of 28 sec, which is detected in a scintillator and recorded by a photomultiplier tube (PMT).

III. RESULTS

A. Hydrodynamic target stability

For the effective acceleration of the ions, an undisturbed back surface of the target is crucial to provide a sharp ion density gradient as the accelerating field strength is proportional to T_{hot}/el_0 , where T_{hot} is the temperature of the hot electrons and l_0 is the larger of either the hot-electron Debye length or the ion scale length of the plasma on the rear surface. The preceding ASE launches a shock wave into the target which causes a destruction of the acceleration sheath. Therefore the target thickness was chosen to guarantee an undisturbed rear surface based on numerical calculations using the hydrocode MULTI [20]. The result of the simulation is shown on the left-hand side of Fig. 2. The inward propagating shock wave is clearly visible. It reached the rear surface at about 8 ns after the onset of the prepulse. Thus, the targets should maintain an undisturbed back surface for a 5 ns prepulse. When we applied a prepulse at a contrast ratio of 10^{-7} of the main pulse 10 ns before the main pulse, the maximum energy of the protons dropped to 2 MeV from the typical 10–20 MeV range typical of low-prepulse shots. This is in good agreement with the MULTI calculations, which indicate that in 10 ns a shock wave launched by the prepulse penetrates the target and causes a rarefaction wave that diminishes the density gradient on the back and therefore drastically reduces the accelerating field. The inward moving shock wave also alters the initial conditions of the target material due to shock wave heating and therefore changes, e.g., the target density and conductivity. Because of its relevance to the electron transport, we chose the target thickness such that a considerable fraction of the target was still in its unperturbed, initial condition. Figure 2 also shows interferometric measurements of the target surface with and without the additionally applied prepulse. The interferometry detects the plasma density conditions on the front and rear surfaces

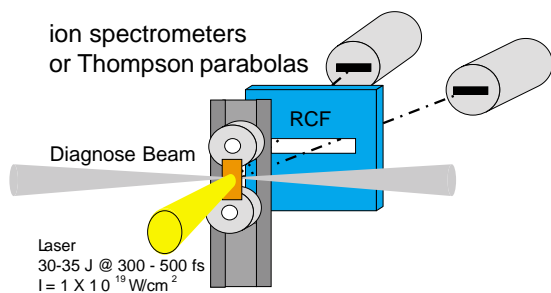


FIG. 1. (Color) Experimental setup. The freestanding target is irradiated at normal incidence. A slit in the radiochromic film (RCF) gives a line of sight for the particle spectrometer.

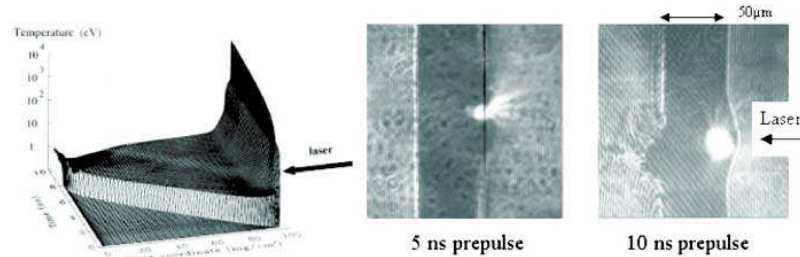


FIG. 2. Left: simulation of the shock wave launched by the prepulse. The shock wave reaches the rear surface at about 7 ns. Center: interferometric images of the plasma conditions on the front and rear target surfaces. Right: perturbation of the rear surface due to prepulse induced shock wave breakout. No protons were detected.

simultaneously. In the figure, the laser is incident from the right (note that the bright spot is 2ω emission from the laser plasma during the pulse). As shown in Fig. 2, the front surface always shows the blowoff plasma, extending up to about $200\ \mu\text{m}$, caused by the ASE. In the absence of a prepulse (left image) the rear surface is unperturbed (no plasma formation could be detected within the resolution limit of the interferometry of a few micrometers) and a strong high-energy proton signal could be detected on the RCF. In agreement with the TNSA predictions, when we observed the presence of an extended plasma (about $50\ \mu\text{m}$) at the rear surface due to the applied prepulse, no protons above the detection threshold of our RCF ($\sim 2\ \text{MeV}$) could be measured. This result is also in excellent agreement with recent experiments using a second laser to generate a plasma at the rear target surface [21].

B. Angular dependence

The angular dependence of the energy distribution of the proton beam was measured with two ion spectrometers positioned at an angle of 0° and 13° , respectively. The measured spatial distributions of protons on the dispersion plane were deconvoluted (with respect to the entrance aperture shape) [22] and corrected for the spectrometer dispersion. The energy of the protons emitted normal to the target rear surface extended up to 25 MeV. The maximum energy of the protons dropped to about 13 MeV at an angle of 13° , consistent with a 2D model of the sheath acceleration process. The spectral shape of each proton energy distribution is generally continuous up to the cutoff energy, in agreement with the electrostatic sheath acceleration mechanism, as well as previous observations in experiments with the LLNL PETAWATT laser [6]. The best fit to the spectrum obtained by the ion spectrometers, as well as to the spectral information extracted from the stacked RCF packages, was obtained by using a two component exponential distribution with 2 and 6 MeV, respectively. Details about the angular dependence of the ion beam and the origin of occasionally observed narrow features in the spectral distribution, caused by the segregation of different

ion species, are beyond the scope of this paper and will be published elsewhere.

C. Yield, surface dependence

Previous experiments using gold targets of similar size, performed at the LLNL PETAWATT laser, revealed a smooth, collimated beam of protons perpendicular to the rear surface. The origin of the protons was found to be contaminant layers of water vapor and hydrocarbons. The total yield of protons could be increased significantly using plastic targets, due to acceleration of protons from the bulk material; however, the laminarity of the beam was largely disrupted, with the spatial pattern of the accelerated protons exhibiting a large degree of filamentary-like structure. We considered several possible reasons for this behavior, including quality of the plastic versus gold material, ion-acoustic instabilities during the ion expansion, and conductivity of the bulk material or of the target rear surface. To investigate the influence of such target conditions on the creation of a collimated ion beam, we varied the target composition and structure of the rear surface.

We used thin ($48\ \mu\text{m}$) targets of gold with either a flat or structured rear surface. The proton beam ejected from the rear surface is shown in the two left-hand pictures of Fig. 3. The results showed a clear dependence of the spatial uniformity of the proton beam on the structure of the back surface. In contrast to the homogenous, collimated beam from the gold target, protons emitted from the structured gold rear surface showed filaments. To discriminate between conductivity and surface quality effects, we next used $\sim 100\ \mu\text{m}$ plastic and glass targets. The results of the glass and plastic targets were even more pronounced. While the flat surfaces of glass and plastic yielded a strong, but filamented proton beam (Fig. 3, third image), there were no protons detected above 1 MeV from the roughened targets (Fig. 3, right-hand image). The similar beam patterns obtained from plastic and glass targets exclude the origin (surface or bulk) of the protons to be the reason for the onset of the filamentary structures. In contrast, due to the strong coupling of the ion acceleration mechanism to

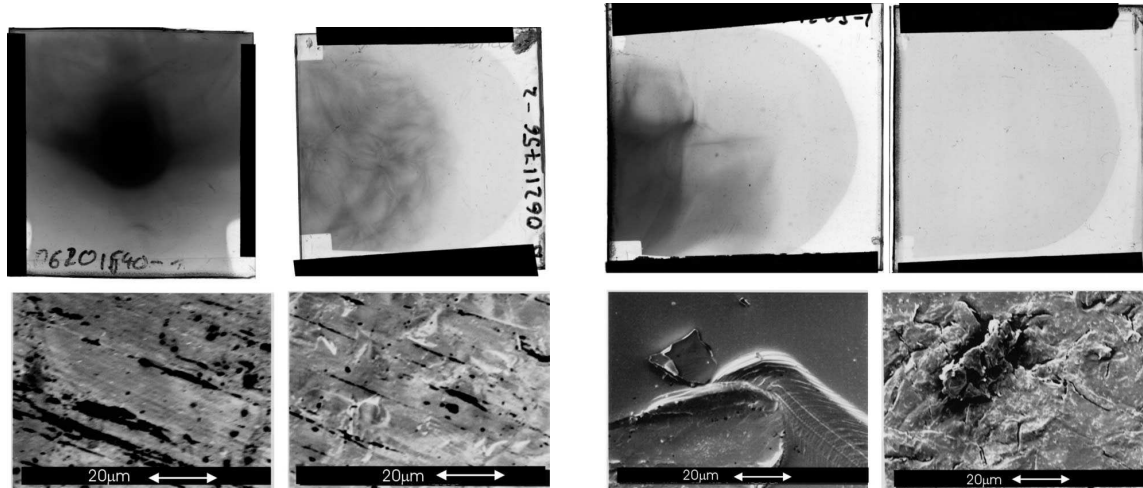


FIG. 3. Proton emission from smooth and roughened rear surfaces of gold (two left-hand columns) and plastic targets. The roughened surface in the case of gold leads to the onset of filamentation. No protons could be detected from the roughened plastic targets due to the destroyed surface. The scanning electron microscope (SEM) images show the corresponding structures of the surfaces [note that the structure visible for the smooth plastic target (third, lower inset) was an artifact to focus the SEM]. The overall surface of the target was similar to the upper right-hand part.

the electron distribution at the rear surface of the target, the smooth, laminar beam quality from metal, i.e., conductor targets, indicates a rather homogenous electron transport through the target. Insulating material seems to disrupt the electron transport, which causes filamentation of the electron distribution and therefore also a nonhomogenous ion acceleration. The dependence of the electron transport on target conductivity has been observed by other research groups as well [23]. As mentioned above, the preceding ASE leads to a shock wave that preheats the target, thereby changing the conductivity of the insulating targets. However, in our experiments the target thickness has been chosen such that a considerable fraction of the target material was still in the cold, solid state by the time of arrival of the main pulse.

Using a scanning electron microscope (SEM) we examined the structure of the target surfaces. The images are shown as the corresponding lower insets in Fig. 3. Structuring the gold surface maintained a smooth surface with hills and valleys, visible as bright shadows on the lower, second inset of Fig. 3. The surface of the plastic and glass targets was largely destroyed by numerous cracks. The different behavior of the structured gold, glass, and plastic targets can be understood within the context of the TNSA model. When the material on the rear surface is exposed to the strong electric field generated by the electron plasma sheath, it is field ionized instantaneously. As mentioned above, the accelerating electric field is characterized by $E \sim T_{\text{hot}}/el_0$, where T_{hot} is the temperature of the hot electron and l_0 is the scale length of the plasma on the rear surface, and is in the order of megavolts per micrometer. A shallow, wavelike surface, such as for the roughened gold

targets, is expected to lead to a microlensing phenomenon, consistent with the observed filamentation or spatial modulation of the accelerated protons.

Such microfocusing effects have been calculated for the case of a single concave depression of the surface [7]. In the case of a destroyed surface, the cracks and defects on the plastic and glass create many sharp excursions, very different from the rather smooth undulating surface of the gold targets. The ion plasma created by the field is therefore extended over a much larger scale length normal to the (average) surface. We expect this to partially compensate the charge separation sheath created by the hot electrons, and therefore strongly suppress the ion acceleration.

As mentioned above, it was found in recent experiments [6] that the proton yield of plastic targets was higher than the yield of hydrocarbon contaminants on gold targets, whereas the beam quality from metal targets is much better than from glass or plastic targets [24]. We attempt to increase the yield of laser-accelerated protons, while maintaining the superior beam quality, by adding hydrogen-containing layers of acrylic (CH) to the rear surface of gold targets. We varied the thickness of a CH layer between 5 and 100 nm. The results showed an increase of the proton yield according to the CH thickness while maintaining the beam quality. However, at a layer thickness of 100 nm we observed the onset of filamentlike structures in the spatial distribution of the accelerated protons.

We modeled the response of the RCF package with the SRIM [19] stopping power tables, assuming the beam to be protons, and obtained response functions for the layers of RCF similar to the ones presented in [6]. Taking into account the respective laser pulse energy in these

experiments, we obtained a conversion efficiency of laser energy into protons of 1% for the 5 nm coating and 2.5% for the 100 nm coated target.

Finally, the increase of the proton yield was limited by the laser energy available in our experiments. At a given maximum laser energy of 30 J and a conversion efficiency into hot electrons less than 35%, a layer thickness of several nanometers is sufficient to provide enough protons to be accelerated. This is quite different for petawatt laser systems operating at higher pulse length and accordingly higher total laser energy. In that case an increase in the overall proton yield by at least an order of magnitude can be expected.

A well-known technique to determine the total yield of fast protons is to use nuclear reactions in a catcher material. For our proton beam, we used the $^{48}\text{Ti}(p, n)^{48}\text{V}$ reaction that provided a sharp threshold at proton energies of ~ 5 MeV. The total yield of ^{48}V activations produced in a typical shot was 10^7 . From that we deduce a total flux of 10^{11} laser-accelerated protons, assuming a Maxwellian energy distribution with a temperature of 2 MeV. This represents a total conversion efficiency of less than 1% of the laser energy to accelerated protons.

It is interesting to note that there is an empirical indication of an efficiency scaling with respect to the laser energy. Experiments at the petawatt laser system (500 J, 10^{20} W/cm²) obtained conversion efficiencies of more than 10% [6], as mentioned in the Introduction. At the Vulcan laser at the Rutherford Appleton Laboratory (100 J, 5×10^{19} W/cm²); conversion efficiencies of a few percent have been determined, we found an efficiency less than 1% in our experiments at the LULI 100 TW laser (30 J, 3×10^{19} W/cm²), and various laser systems at lower energy obtained conversion efficiencies well below this value.

D. Proton beam shaping

An important question to be addressed for any future application of laser-accelerated protons and ions is the possibility of tailoring the proton beam, either collimating or focusing it, by changing the geometry of the target surface. Ballistic focusing of the laser-accelerated protons is expected to be rather difficult because of the inherent divergence associated with the spatial density dependence of the hot electron sheath, which drives the acceleration. Accordingly, we first attempted to defocus the beam in one dimension by using a convex target. Using a 60 μm diameter Au wire as a target basically constituted such a one-dimensional defocusing lens, and we observed a line as shown in Fig. 4. Tilting the wire also changed the orientation of the line, which results from the radial, fan-shaped expansion of the protons normal to the wire.

We then attempted to focus the protons by modifying the curvature (concave) of the target foil. Focusing laser generated protons is essential for many applications such as

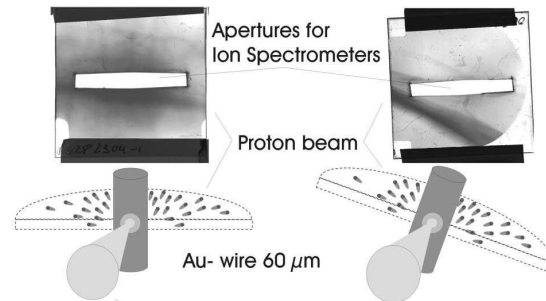


FIG. 4. Experimental setup and RCF images of experiments with 60 μm gold wires. The convex rear surface constitutes a decollimating cylinder lens. Accordingly, the proton beam was formed into a line.

ion-induced material damage research, proton driven fast ignition [25], proton radiography [26], and the use as next generation ion sources. Because of the Gaussian-like shape of the hot electron Debye sheath that causes the acceleration, there is an energy dependent angle of divergence that has to be compensated to focus the ions in the energy range of interest. Therefore the effective focal length of a curved target rear surface is longer and is dependent on the proton energy. The results, which will be published elsewhere, show a strong reduction in the divergence of the central core of the proton beam representing ballistic collimating of laser produced proton beams.

E. Heavy ion beam production

Having established that one can enhance the proton yield while maintaining the beam quality, and at least contemplate successful focusing targets, we next attempted to control the accelerated ion species and, in particular, selectively accelerate either protons or heavy ions. Because of their larger charge-to-mass ratio, which causes the protons to outrun the other ion species during the ambipolar expansion, protons are accelerated faster taking most of the energy from the electrostatic sheath. Therefore, the amount of protons had to be reduced significantly. For targets of solid metals (gold, aluminum), the majority of the protons is due to water vapor and hydrocarbons at the target surface. We reduced these impurities by resistively heating the targets. The targets consisted of thin foils of 50 μm Al coated with 1 μm of carbon. To detect the heavy ions with respect to their momentum and charge-state distribution, we substituted the ion spectrometers with two Thompson parabolas at an angle of 0° and 13° . The ions were recorded in CR-39 plastic track detectors. We compared the yield for heated and nonheated targets, as shown in Fig. 5. As expected, for the nonheated targets (left-hand side) a strong proton signal was observed together with a weak signal of carbon ions. The result changed dramatically for the heated targets, as shown in the right-hand side of Fig. 5.

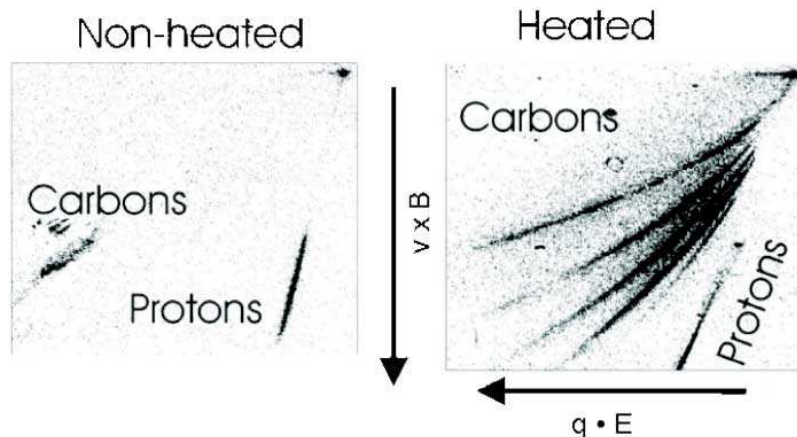


FIG. 5. Heavy ion beam production. In contrast to the strong proton signal (left), removing the hydrocarbons from the target rear surface results in a strong heavy ion (carbon) signal (right).

A sharply reduced proton signal was detected in these experiments together with a much more intense heavy ion signal (carbon and aluminum ions). We observed a higher yield, much higher ion energies and ions at higher charge states. These results are in agreement with experiments using CO_2 lasers more than 20 years ago in which removal of hydrogen contaminants by heating increased the ion yield in laser ablation plasmas. In extension to the results obtained in [8], the use of short-pulse chirped-pulse-amplification lasers allows higher focused intensities at shorter pulse length leading to electron temperatures of several MeV, and, consequently, the observed heavy ions are accelerated up to the several MeV/u range.

E. Neutron production

Complementing the laser and ion beam diagnostics we also measured the neutron emission caused by (γ, n) and (p, n) reactions from the target. We used a silver activation detector attached to a PMT. On typical shots, the neutrons are generated by (γ, n) reactions within the target (caused by the bremsstrahlung photons from the relativistic electrons) and by (p, n) reactions of our proton beam impacting on the RCF screen. We also used a target of deuterized plastic (CD_2), which was heated to produce a beam of deuterons. Fielding a CD_2 catcher foil behind the target we observed the yield of neutrons from (d, d) fusion reactions. We detected a total yield of 2.8×10^7 neutrons in this experiment, which was at least an order of magnitude above the yield on average shots.

F. Proton beam emittance

For most of the future applications of laser generated ion beams, the beam quality is the most important characteristic. Especially for the use as an ion source or the application as an inertial confinement fusion ignitor beam, the ion beam emittance is crucial with respect to the ac-

celerator structure acceptance or the achievable focus spot size. As is apparent from the radiochromic film data, the angular divergence of the proton jet is rather well defined and decreases with increasing proton energy. This suggests that protons or other light ions accelerated by this mechanism may have a usefully small emittance in the sense of an actual ion beam.

To precisely estimate our emittance, we used penumbral imaging of edges at different distances from the target with the magnetic spectrometers to directly measure the core emittance core of the proton beam. This technique is closely related to the conventional slit-emittance measurements made with apertures and screens at conventional accelerators. We determine the normalized emittance of protons from flat gold foils to be $\sim 0.2\pi$ mm mrad, and a factor of at least 2 smaller than the resolution limited measurements we performed on the LLNL PETAWATT (see Ref. [24]). Details of the present measurements, and systematics of the proton emittance versus energy, will be reported elsewhere.

The results of this analysis and subsequent modeling, developing a 2D extension of the model in [27], suggest that we observe a rather cold proton beam, which is smoothly diverging and highly laminar. The trace space of the highest energy protons exhibits a tilted ellipse, whose width ultimately is the characteristic of the ion temperature. From these data, we deduce that the proton temperature is less than ~ 1 keV. From simple electron-ion collisional heating during the expansion, one may expect the ion temperature to be even lower, of order ~ 100 eV.

G. Radiography using laser-accelerated proton beams

The excellent beam quality of the ion beam is ideally matched to the requirements for imaging techniques. One scheme of particular interest is the use of laser-accelerated protons to radiograph macroscopic samples to study their properties. Because of the different interaction

mechanism, protons can provide complementary information to more common techniques such as x-ray backlighting. The interaction of swift protons with matter is well known and has been a traditional research area of accelerator laboratories over the past decades. Because of the copious amounts of protons accelerated in a very short time, laser-accelerated protons provide a new diagnostic quality in research of transient phenomena. We performed a first set of experiments to demonstrate the feasibility of these laser-accelerated proton beams for radiography applications. Recently, there have been experiments performed to use laser-accelerated protons for object imaging [28]. In these experiments, a thin target (grid) has been placed very close to the proton source. In contrast to these experiments, where the target was exposed to the electron cloud closely behind the target, we have chosen a different geometry. We used a distance of 5 cm between the proton source and the target in order to minimize any charging of the target and placed the detector (RCF) close to the object to reduce deflection effects. In our experiments, we used a compound target of different materials to be imaged by the protons. It consisted of a 1 mm thick epoxy ring structure, several copper wires of 250 μm diameter, a hollow cylinder with 300 μm walls of steel, several Ti sheets of 100 μm thickness, and a glass hemisphere of 900 μm diameter and 20 μm wall thickness.

The protons were recorded in multiple layers of RCF to detect the image at different proton energies. Figure 6 shows the radiography of the target for final proton energies of 7.5 MeV. The image basically constitutes a negative image of the areal density of the target. The names of the collaborating institutes have been engraved on the epoxy

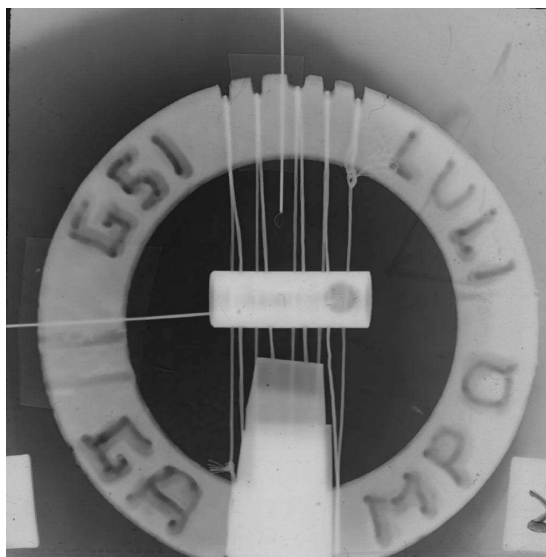


FIG. 6. Radiography of a compound target. Details of the target are given in the text.

ring, which results in a reduced thickness and therefore a higher energy deposition of the protons in the respective layer. The areal density variation of the hollow cylinder, including a hole in the wall on the right-hand side, can be seen as well as a thin metal rod placed inside the cylinder. These results show a clear dependence on the areal density rather than on residual charging effects, in contrast to the experimental technique used in [28]. Close examination also shows the small glass hemisphere placed above the cylinder. The time of exposure in this experiment was estimated to be on the order of tens of picoseconds, based on the initial proton beam pulse duration and the energy dependent dispersion of the pulse from the source to the target.

IV. CONCLUSION

We have presented a detailed investigation of the target conditions on the proton and ion beam production from intense laser solid interactions. The observed strong dependence on the rear surface conditions is in agreement with the target normal sheath acceleration mechanism. The target conductivity appears to have a major influence on the quality of the ion beam, and the quality of the surface finish of the target is very important for maintaining a high gradient sheath and a laminar beam. It has been shown that tailoring the ion beam (yield, shape, composition, homogeneity) by means of target shape and composition is possible, and we present first observations of laser-accelerated ion beam focusing. Finally, the successful generation of a heavy ion beam (carbon, aluminum) further encourages speculation that laser-accelerated ion beams may become a useful tool in a variety of future applications.

ACKNOWLEDGMENTS

This work was supported by the EU, Contract No. HPRI CT 1999-0052, and in part by Grant No. E1127 from Région Ile-de-France.

- [1] A. P. Fews, P. A. Norreys, F. N. Beg, A. R. Beg, A. E. Dangor, C. N. Danson, P. Lee, and S. J. Rose, *Phys. Rev. Lett.* **73**, 1801 (1994).
- [2] K. Krushelnick, E. L. Clark, Z. Najmudin, M. Salvati, M. I. K. Santala, M. Tatarakis, A. E. Dangor, V. Malka, D. Neely, and R. Allott, *Phys. Rev. Lett.* **83**, 737 (1999).
- [3] A. Maksimchuk, S. Gu, K. Flippo, D. Umstadter, and V. Yu. Bychenkov, *Phys. Rev. Lett.* **84**, 4108 (2000).
- [4] M. Zepf, E. L. Clark, K. Krushelnick, F. N. Beg, C. Escoda, A. E. Dangor, M. I. K. Santala, M. Tatarakis, I. F. Watts, and P. A. Norreys, *Phys. Plasmas* **8**, 2323 (2001).
- [5] M. Perry and G. Mourou, *Science* **264**, 917 (1994).
- [6] R. Snavely *et al.*, *Phys. Rev. Lett.* **85**, 2945 (2000).
- [7] S. C. Wilks *et al.*, *Phys. Plasmas* **8**, 542 (2001).
- [8] S. J. Gitomer *et al.*, *Phys. Fluids* **29**, 2679 (1986).

-
- [9] Y. Kishimoto *et al.*, *Phys. Fluids* **26**, 2308 (1983).
[10] H. Ruhl *et al.*, *Plasma Phys. Rep.* **27**, 363 (2000).
[11] A. Pukhov, *Phys. Rev. Lett.* **86**, 3562 (2001).
[12] M. G. Haines, *Phys. Rev. Lett.* **47**, 917 (1981).
[13] M. H. Key, M. D. Cable, T. E. Cowan, K. G. Estabrook, B. A. Hammel, S. P. Hatchett, E. A. Henry, D. E. Hinkel, J. D. Kilkenny, and J. A. Koch, *Phys. Plasmas* **5**, 1966 (1998).
[14] G. Malka and J. L. Miquel, *Phys. Rev. Lett.* **77**, 75 (1996).
[15] F. N. Beg, A. R. Bell, A. E. Dangor, C. N. Danson, A. P. Fews, M. E. Glinsky, B. A. Hammel, P. Lee, P. A. Norreys, and M. Tatarakis, *Phys. Plasmas* **4**, 447 (1997).
[16] M. Tabak, J. Hammer, M. E. Glinsky, W. L. Kruer, S. C. Wilks, J. Woodworth, E. M. Campbell, and M. D. Perry, *Phys. Plasmas* **1**, 1626 (1994).
[17] C. Deutsch, H. Furukawa, K. Mima, M. Murakami, and K. Nishihara, *Phys. Rev. Lett.* **77**, 2483 (1996).
[18] D. Batani, J. R. Davies, A. Bernardinello, F. Pisani, M. Koenig, T. A. Hall, S. Ellwi, P. Norreys, S. Rose, and A. Djaoui, *Phys. Rev. E* **61**, 5725 (2000).
[19] J. F. Ziegler, J. P. Biersack, and U. Littmark, *The Stopping and Range of Ions in Solids* (Pergamon, New York, 1996).
[20] R. Ramis, R. Schmalz, and J. Meyer-ter-Vehn, *Comput. Phys. Commun.* **49**, 475 (1988).
[21] A. J. MacKinnon, M. Borghesi, S. Hatchett, M. H. Key, P. K. Patel, H. Campbell, A. Shiavi, R. Snavely, S. C. Wilks, and O. Willi, *Phys. Rev. Lett.* **86**, 1769 (2001).
[22] L. B. Lucy, *Astron. J.* **79**, 745 (1974).
[23] F. Pisani, A. Bernardinello, D. Batani, A. Antonicci, E. Martinolli, M. Koenig, L. Gremillet, F. Amiranov, S. Baton, and J. Davies, *Phys. Rev. E* **62**, R5927 (2000).
[24] T. E. Cowan *et al.* (to be published).
[25] M. Roth *et al.*, *Phys. Rev. Lett.* **86** 436 (2001).
[26] A. Blazevic *et al.* (to be published).
[27] L. M. Wickens and J. E. Allen, *Phys. Fluids* **24**, 1984 (1981).
[28] M. Borghesi, A. Shiavi, D. H. Campbell, M. G. Haines, O. Willi, A. J. MacKinnon, L. A. Gizzi, M. Galimberti, R. J. Clarke, and H. Ruhl, *Plasma Phys. Controlled Fusion* **43**, A267 (2001).

- 1.7** M. Roth, M. Allen, P. Audebert, A. Blazevic, E. Brambrink, T.E. Cowan, J. Fuchs, J.C. Gauthier, M. Geissel, M. Hegelich, S. Karsch, J. Meyer-ter-Vehn, H. Ruhl, T. Schlegel and R. Stephens,
The generation of high quality, intense ion beams by ultra intense lasers,
Plasm. Phys. Control. Fusion 44, B99-B108 (2002).
Copyright 2002 by the Institute of Physics.

The generation of high-quality, intense ion beams by ultra-intense lasers

M Roth¹, M Allen², P Audebert³, A Blazevic¹, E Brambrink¹,
T E Cowan², J Fuchs³, J-C Gauthier³, M Geißel¹, M Hegelich⁴,
S Karsch⁴, J Meyer-ter-Vehn⁴, H Ruhl², T Schlegel¹ and R B Stephens²

¹ Gesellschaft für Schwerionenforschung mbH, Planckstr. 1, 64291 Darmstadt, Germany

² General Atomics, PO Box 85608, San Diego, CA 92186-5608, USA

³ Laboratoire pour l'Utilisation des Lasers Intenses, 91128 Palaiseau, France

⁴ Max-Planck-Institut für Quantenoptik, Garching, Germany

Received 12 September 2002

Published 21 November 2002

Online at stacks.iop.org/PPCF/44/B99

Abstract

Intense beams of protons and heavy ions have been observed in ultra-intense laser–solid interaction experiments. Thereby, a considerable fraction of the laser energy is transferred to collimated beams of energetic ions (e.g. up to 50 MeV protons; 100 MeV fluorine), which makes these beams highly interesting for various applications. Experimental results indicate a very short-pulse duration and an excellent beam quality, leading to beam intensities in the TW range. To characterize the beam quality and its dependence on laser parameters and target conditions we performed experiments using the 100 TW laser system at Laboratoire pour l'Utilisation des Lasers Intenses at the Ecole Polytechnique, France, with focused intensities exceeding $10^{19} \text{ W cm}^{-2}$. We found a strong dependence on the target rear surface conditions allowing to tailor the ion beam by an appropriate target design. We also succeeded in the generation of heavy ion beams by suppressing the proton amount at the target surface.

We will present recent experimental results demonstrating a transverse beam emittance far superior to the accelerator based ion beams. Finally, we will discuss the prospect of laser accelerated ion beams as new diagnostics in laser–solid interaction experiments. Special fields of interest are proton radiography, electric field imaging, and relativistic electron transport inside the target.

1. Introduction

Energetic ions have been produced by lasers focused onto solid targets for several decades. The predominant mechanism in those experiments was found to be an isothermal expansion

with ions being fed into the expanding corona by a rarefaction wave propagating at the sound speed, c_s , into the bulk plasma. In these experiments ions, mostly originating from the target front, moved against the laser direction and showed a very large dispersion. Typical energies were of the order of 100 keV/nucleon for sub-kJ lasers and up to 2 MeV for protons from kJ systems. With the advent of ultra-intense, short-pulse lasers the situation changed dramatically. Nowadays even table-top, low energy laser systems produce protons up to several MeV particle energy and collimated beams of ions have been observed [1, 2].

Ion emission has been observed originating from the front and rear surface of solid targets. In contrast to the experiments using long-pulse lasers, ions accelerated by fs-laser systems are emitted normal to the rear surface in a low divergent beam of excellent quality. The dominant mechanism of the ion acceleration is understood as rear surface emission accelerated by the target normal sheath acceleration (TNSA) mechanism [3]. Relativistic electrons generated from the laser–plasma interaction, having an average temperature of several MeV, envelope the target foil and form an electron plasma sheath on the rear, non-irradiated surface. The electric field in the sheath ($E_{\text{stat}} \sim kT_{\text{hot}}/e\lambda_D$, $\lambda_D = (\epsilon_0 kT_{\text{hot}}/e^2 n_{e,\text{hot}})^{1/2}$) can reach $>10^{12}$ V m⁻¹. A few monolayers of atoms at the rear surface are field-ionized and accelerated normal to the surface by E_{stat} , with the most energetic electrons always extending further out into vacuum, maintaining the accelerating field as long as the electron temperature is high. This is fundamentally different from the long-pulse case, in which bulk effects and collisional ionization by thermal electrons in the coronal plasma are the dominant mechanisms. So far mainly protons have been observed from the rear side, originating, as in the long-pulse experiments, from contaminating hydrocarbon layers which coat the targets. As soon as protons are present they outrun the heavier ions due to their superior charge-to-mass ratio, and screen the acceleration field. Thus protons are preferentially accelerated in favour of heavier ions over a distance of a few microns, and up to tens of MeV. This forms a collimated beam with an approximately exponential energy distribution with 5–6 MeV. The conversion efficiency from laser energy to ion beam energy can be quite high and efficiencies of order of 10% have already been measured [2]. This acceleration mechanism makes these intense ion beams highly interesting for many applications [4–6], especially if one can collimate or focus the beam by shaping the target, as suggested by numerical calculations [7, 8]. Because of the dependence of the ion beam on the formation of the electron sheath, this process should also reveal information about the electron transport through the target. We expect details of the ion acceleration will furthermore depend on the target material and surface conditions. Therefore, we carried out experiments to investigate the influence of these target parameters on the ion beam production.

2. Experiments

The experiments presented in this paper were performed with the 100 TW laser at Laboratoire pour l'Utilisation des Lasers Intenses (LULI). Pulses of up to 30 J at 300 fs pulse duration at $\lambda = 1.05 \mu\text{m}$ were focused with an $f/3$ off-axis parabolic mirror onto free standing target foils at normal incidence, at intensities up to 5×10^{19} W cm⁻². The focal spot diameter (FWHM) measured in vacuum was about 8 μm . Amplified spontaneous emission occurred 2 ns before the main pulse at a level of 10^{-7} of the main pulse energy and preformed a plasma.

The diagnostic setup is depicted in figure 1. The free standing target was probed by a frequency doubled laser beam parallel to the surface to determine the plasma conditions on the front and rear surface. A stack of radiochromic film (RCF) was positioned a few cm behind the target to measure the spatial beam profile. Due to the pronounced energy loss of ions at the end of their range (Bragg-peak) different layers of the RC film pack allow the imaging of the

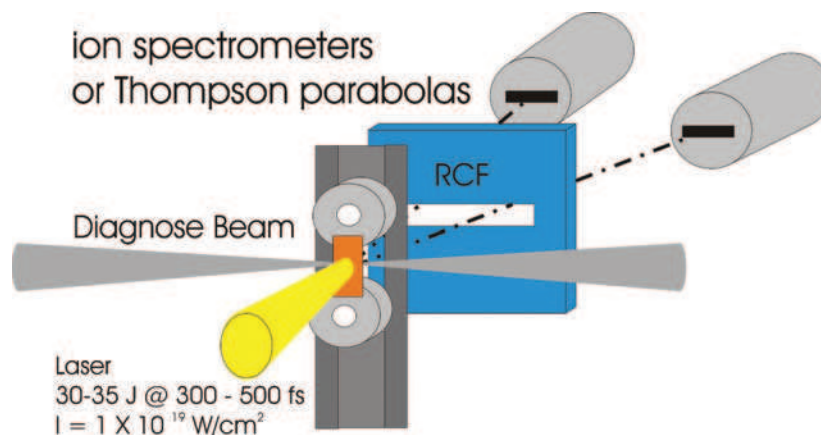


Figure 1. Experimental setup. The free standing target is irradiated at normal incidence. A slit in the RCF gives a line of sight for the particle spectrometer.

ion beam at different energies. A slot in the centre of the RCF allowed a free line of sight for the charged-particle spectrometers fielded at 0° , 6° and 13° to provide the energy distribution of the emitted electrons and ions.

Two absolutely calibrated, permanent magnetic ion spectrometers were mounted at a distance of about 1m from the target covering a solid angle of 5×10^{-6} sr.

As a complementary detector system we used titanium catcher foils, which were placed in the path of the proton beam. The ^{48}Ti is transmuted by a (p, n) reaction by protons above a sharp reaction threshold at ~ 5 MeV to an excited state of the ^{48}V isotope. Using a low-background Ge detector we observed the gamma deexcitation lines of the $^{48}\text{Ti}(p, n)^{48}\text{V}$ reaction, which provided the total activation and therefore the yield of protons above the reaction threshold of ~ 5 MeV.

To detect heavy ions accelerated from the rear surface of the relativistic-laser illuminated targets, we substituted two high resolution Thompson parabolas in replacement of one of the charged-particle spectrometers. The parallel electric and magnetic fields in the Thompson parabolas discriminated ions with respect to their momentum and charge-to-mass ratio, at the plane of the CR-39 track detectors. Careful analysis of the scanned CR-39 detectors then provides absolute numbers of the ions with respect to their kinetic energy and charge state. In addition to the ion and laser beam detectors, a silver activation neutron detector was fielded close to the target chamber determining the neutron yield for the different experiments.

Details about the experimental setup and the various detector systems were published in [5].

3. Results

3.1. Ion beam properties

We performed a series of experiments to examine the properties of the laser accelerated ion beam. Even though the majority of the beam consists of protons, as mentioned above, we have been able to efficiently accelerate heavier ions (see section 3.3).

Up to now no measurement of the initial ion beam pulse duration has been performed, but based on the finite lifetime of the hot electrons a maximum pulse duration of a few picoseconds

has been concluded. Given the absolute numbers of ions (10^{13} protons at experiments using 1 PW lasers [2], 10^{12} protons at the LULI 100 TW system) the resulting initial ion beam current ranges in the mega-ampere regime.

The angular dependence of the energy distribution of the proton beam was measured with two ion spectrometers positioned at an angle of 0° and 13° , respectively. The measured spatial distributions of protons on the dispersion plane were deconvoluted (with respect to the entrance aperture shape) [9] and corrected for the spectrometer dispersion. A typical ion spectrum is shown in figure 2.

The energy of the protons emitted normal to the target rear surface extended up to 25 MeV. The maximum energy of the protons dropped to about 13 MeV at an angle of 13° , consistent with a two-dimensional model of the sheath acceleration process. The spectral shape of each proton energy distribution is generally continuous up to the cut-off energy, in agreement with the electrostatic sheath acceleration mechanism and as well as previous observations in experiments with the LLNL PETAWATT laser [2]. The best fit to the spectrum obtained by the ion spectrometers, as well as to the spectral information extracted from the stacked RCF packages was obtained by using a two component exponential distribution with 2 MeV and 6 MeV, respectively. Details about the angular dependence of the ion beam and the origin of occasionally observed narrow features in the spectral distribution, caused by the segregation of different ion species, are beyond the scope of this paper and will be published elsewhere.

For most of the future applications of laser generated ion beams the beam quality is the most important characteristic. Especially for the use as an ion source or the application as an inertial confinement fusion (ICF) ignitor beam, the ion beam emittance is crucial with respect to the accelerator structure acceptance or the achievable focus spot size. The formation of the ion beam is highly dependent on the formation of the electron sheath at the rear surface of the target (see section 3.2). We observed highly laminar and well collimated beams of ions using metal targets. As is apparent from the RCF data (see figure 3), the angular divergence of the proton jet is rather well defined and decreases with increasing proton energy. This suggests that protons or other light ions accelerated by this mechanism may have a useful small emittance in the sense of an actual ion beam.

To precisely estimate our emittance, we used penumbral imaging of edges at different distances from the target with the magnetic spectrometers, to directly measure the core emittance of the proton beam. This technique is closely related to the conventional slit-emittance measurements made with apertures and screens at conventional accelerators. We determine the normalized emittance of protons from flat gold foils to be $\sim 0.2\pi$ mm mrad, and factor of at least two smaller than the resolution limited measurements we performed on the

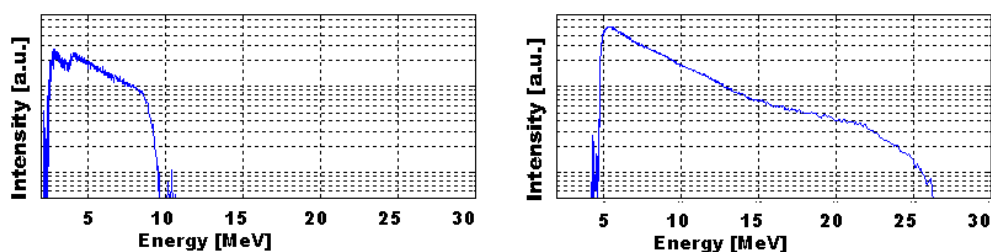


Figure 2. Typical proton spectra obtained at 20 J/350 fs pulses. Whereas the proton maximum energy extends up to 25 MeV normal to the rear surface (right), the maximum energy drops to below 10 MeV at an angle of 13° normal to the surface (left).

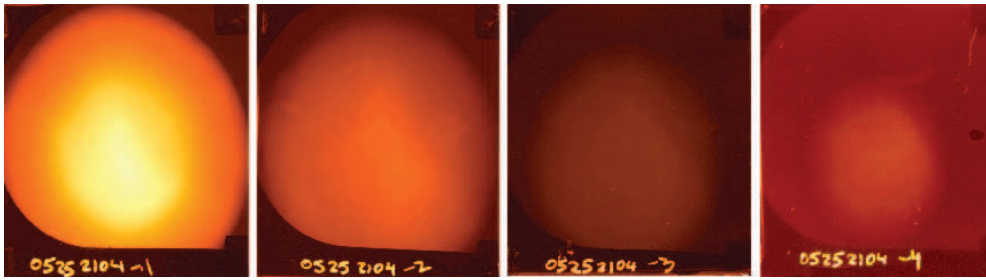


Figure 3. RCF images of the laser accelerated proton beam 5 cm behind the target. The ion energy increases from left to right. The divergence of the homogeneous beam decreases with increasing ion energy.

LLNL PETAWATT (see [2]). Details of the present measurements, and systematics of the proton emittance versus energy will be reported elsewhere.

The results of this analysis and subsequent modelling, developing a two-dimensional extension of the model in [10], suggest that we observe a rather cold proton beam, which is smoothly diverging and highly laminar. The trace space of the highest energy protons exhibits a tilted ellipse, whose width ultimately is the characteristic of the ion temperature. From these data, we deduce that the proton temperature is less than ~ 1 keV. From simple electron–ion collisional heating during the expansion, one may expect the ion temperature to be even lower, of order ~ 100 eV.

Using a newly developed technique that will be published in detail in [11] we have been able to improve the measurement of the beam core emittance by an order of magnitude. These measurements result in a transverse beam emittance of 0.06π mm mrad, which is orders of magnitude lower than achieved at any conventional accelerator.

It is interesting to note, that this measured beam emittance correspond to an effective ion temperature of less than 100 eV. This temperature is not consistent with the high temperatures present at the front surface, but likely maintained at the rear surface during the acceleration.

Moreover, one should be aware of the fact, that determining the source size by penumbral imaging techniques is misleading. The results obtained by this technique indicate spot sizes in the order of $10\text{--}20\ \mu\text{m}$. These spot sizes have been used in recent publications [12] to rule out the rear surface contaminants as the origin of the intense beams observed. However, in case of a highly laminar acceleration as expected for the TNSA mechanism the use of penumbral imaging traces back the virtual source size in the sense of a beam waist (as been reported at several conferences), which can be more than an order of magnitude smaller than the real source size at the rear surface. Recent experiments using direct surface imaging (see section 3.4) indicate the real source size to be much larger than the values obtained by penumbral imaging techniques.

Figure 4 shows the origin of the laser accelerated protons with respect to their energy. Protons up to energies of 3 MeV were emitted from an area of about $300\ \mu\text{m}$ diameter, far larger than the initial spot size at the front surface. The emission region decreases for higher energetic protons, in this case down to about $80\ \mu\text{m}$ for 10 MeV protons. The measurement is consistent with an electron sheath distribution caused by the higher electron density in the central region as predicted by numerical simulations [7, 8].

Recently, experiments at the LULI laser system using imaging techniques to determine the electron distribution at the target rear surface [13] show an excellent agreement between the electron distribution and the real proton source size at the target rear surface.

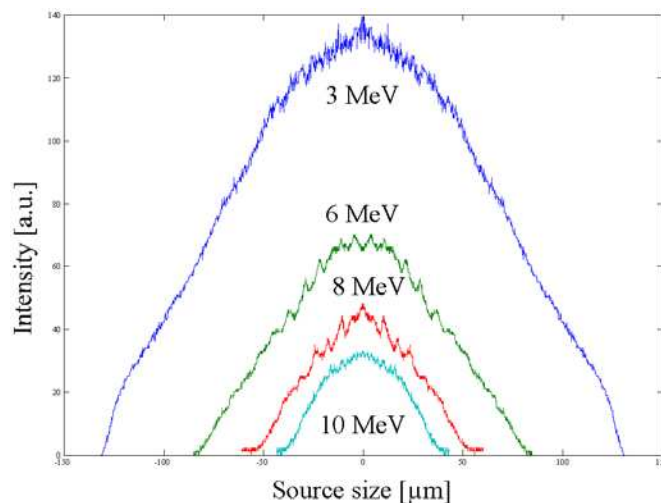


Figure 4. Real source size of the laser accelerated protons for different proton energies. The size at the rear surface decreases from $260\ \mu\text{m}$ for 3 MeV protons to $80\ \mu\text{m}$ for 10 MeV protons.

3.2. Target dependence

One of the interesting features of the laser accelerated ion beams is that their directionality is always normal to the rear surface of the irradiated target. Because of the small extension of the accelerating electron sheath and the strong dependence of their formation, target properties like the rear surface structure and target conductivity should have a major influence on the ion beam properties.

We have therefore performed detailed experiments to investigate the ion beam properties in dependence of these target parameters. In contrast to the homogeneous spatial distribution of protons originating from highly conducting (gold, aluminium) targets with a flat rear surface, ion beams emitted from targets with structured rear surfaces showed a strong filamentation. This effect could be explained by the presence of microfocusing filaments from these surface, as published in [14]. Furthermore, as expected from the TNSA mechanism, the scale length of the plasma at the rear surface is crucial for an effective ion acceleration. A large extension of a plasma at the rear surface has been shown to suppress the acceleration mechanism effectively [5, 15].

The formation of the accelerating sheath is dependent on the transport of the large electron currents through the target, thereby influenced by the onset of compensating return currents and effected by instabilities. The transport of relativistic electrons through the target is an extensively studied area of research [16–19] because of its relevance not only for ion acceleration, but especially for the concept of fast ignition [20–22] in ICF. It has been shown [2] that proton beams emitted from plastic targets always showed a filamentary structure. We used plastic and glass targets of varying thickness as well as layered targets to examine the influence of the target conductivity. Figure 5 shows a comparison of a simulation with the experiment for a $50\ \mu\text{m}$ plastic target coated with $10\ \mu\text{m}$ gold at the front surface. The left part of the figure shows the accelerating electron sheath assuming electron beam breakup into three large filaments during the propagation in the target. The central part of figure 5 presents the simulated ion beam structure at the location of our detector several cm behind the target. This is compared to the experimental data shown in the right part of figure 5. As can be seen,

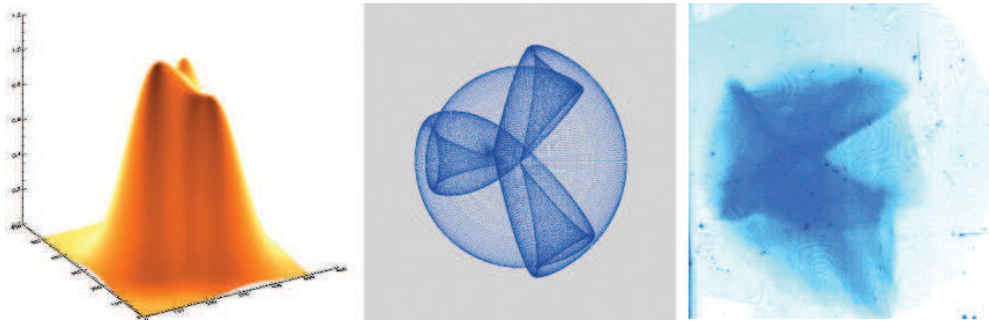


Figure 5. Proton beam filamentation due to electron transport. Simulation of a filamented electron sheath (left) in plastic causes the proton beam to show structure (central part). The experiment (right) shows an excellent agreement with the simulation.

there is an excellent agreement between the simulated beam pattern to the experiment which indicates electron beam breakup to be the origin of the beam filamentation. Similar results have been obtained using targets coated with conducting layers at the front and the rear surface.

3.3. Heavy ion acceleration

So far mainly protons have been observed from the rear side, originating, as in the long-pulse experiments, from contaminating hydrocarbon layers which coat the targets. As soon as protons are present they outrun the heavier ions and screen the acceleration field. We present the first experimental study, demonstrating that besides protons, also high-quality, high energy (\sim MeV/nucleon) heavy ion beams can be accelerated from the rear surface of (coated) thin foils. We find that heavy ions are effectively accelerated, provided the hydrogenous surface contaminants are removed. We obtained high resolution, absolutely calibrated energy spectra of different ion species, which provide additional information, not available in the proton signal, about the spatio-temporal evolution of the accelerating field and the origin of the observed ions. Details on the acceleration of heavy ions are to be published in [23]. To effectively remove the hydrogen contaminants we resistively heated tungsten targets up to temperatures of 1000 K for several minutes. The ion species of interest was coated solely on the rear surface of the target, thereby unambiguously verifying the origin of the heavy ions. The proton spectrometer as well as the CR-39 did not show any protons, while strong fluorine ion tracks are observed originating from the CaF_2 layer at the target rear side. The complete removal of contaminants increased the acceleration of heavier ions considerably. Quantitative evaluation shows that F^{7+} was accelerated up to 100 MeV, i.e. more than 5 MeV/nucleon at 4% energy conversion. The RCF diagnostic confirmed this by showing a narrow spot in the first layer, which, in the absence of protons, indicates fluorine ions of energies above 4 MeV/nucleon. The evaluation of the fluorine shot shown in figure 6 shows that E -fields $E_{\text{stat}} \sim 2 \text{ TV m}^{-1}$ on a timescale of $\tau \sim 350 \text{ fs}$ are necessary to accelerate F^{7+} -ions up to 100 MeV over a scale length of $l \sim 10 \mu\text{m}$. The shot presented in figure 6 was virtually without any protons, but the modelled fields can accelerate protons up to $\sim 25 \text{ MeV}$, as typical with unheated targets. The field distribution is in agreement with an extended TNSA model including dynamic fields and multiple ion species. We found that field ionization is the dominant mechanism while recombination and collisional ionization are by far less effective (see [23]). Since the targets were coated only at the back surface and we successfully removed contaminations and can rule out front side acceleration within the parameters of our experiment.

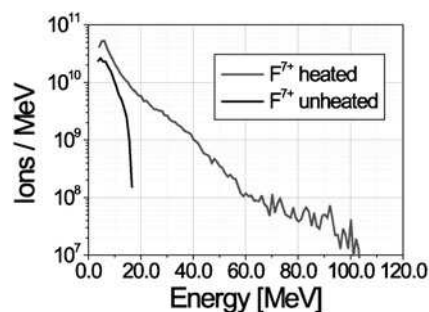


Figure 6. Heavy ion acceleration in the presence (unheated) and without (heated) proton contaminants. More than 100 MeV (5 MeV/nucleon) F^{7+} ions were measured.

3.4. Ion beam tailoring

An important question to be addressed for any future application of laser-accelerated protons and ions is the possibility of tailoring the proton beam, either collimating or focusing it, by changing the geometry of the target surface. Due to the excellent beam quality and the close correlation of the accelerating sheath to the rear surface tailoring of the ion beams should be feasible using appropriate target design. However, ballistic focusing of the laser accelerated protons is expected to be rather difficult because of the inherent divergence associated with the spatial variation of the density of the hot electron sheath, which drives the acceleration. Accordingly, we first attempted to de-focus the beam in one dimension, by using a convex target. Using a $60\ \mu\text{m}$ diameter Au wire as a target basically constituted such a one-dimensional de-focusing lens, and we observed a line image as published in [14]. Tilting the wire also changed the orientation of the line image, which results from the radial, fan-shaped expansion of the protons normal to the surface of the wire. We then attempted to focus the protons by modifying the curvature (concave) of the target foil. Due to the Gaussian-like shape of the hot electron Debye sheath that causes the acceleration, there is an energy dependent angle of divergence that has to be compensated to focus the ions in the energy range of interest. Therefore, the effective focal length of a curved target rear surface is longer and is dependent of the proton energy. The results, that will be published elsewhere show a strong reduction in the divergence of the central core of the proton beam representing ballistic collimating of laser produced proton beams.

Based on the excellent beam emittance that implies a highly laminar expansion of an initially very cold ion beam we investigated the prospect of imaging the actual target surface by means of the protons. This would further allow the precise determination of the real source size, details about the electron transport and has the prospect of many applications. Initial experiments showed substructures in the proton beam that could be related to surface structures at the μm scale. Figure 7 shows an image of a 50 mm gold target rear surface obtained by using a scanning electron microscope (SEM). Due to the fabrication process, elliptical structures (holes) at the surface remain at a diameter of a few μm . In the right part of the figure, we present typical substructures of the proton beam emitted from that surface. The shape of the structures in the beam resembles the structures at the surface. Meanwhile we have succeeded to use artificial surface structures, like lines, grids, crosses and names on a μm scale to tailor laser accelerated proton beams. The results will be published elsewhere [11], but the excellent quality of the beam allows to tailor ion beams with fiducial patterns, which is highly interesting for any imaging techniques, like proton radiography, or electrical field mapping.

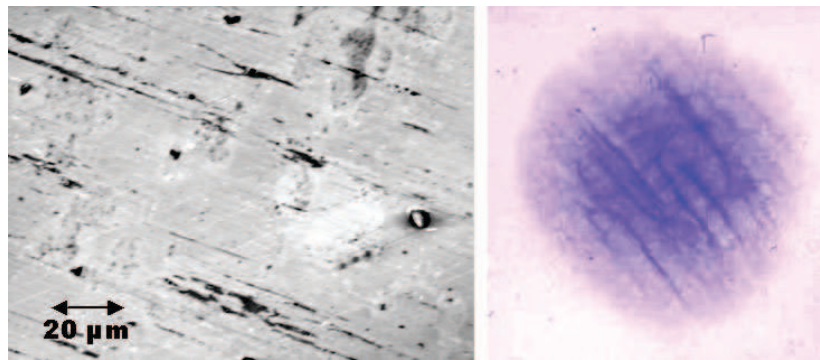


Figure 7. Surface imaging by laser accelerated protons. The structures at the target rear surface (SEM image, left) were imaged by the proton beam onto the detector (right).

4. Conclusion

Laser accelerated proton and ion beams offer new prospects for a whole variety of applications. The beam quality was found to be far superior to beams accelerated by conventional accelerators with respect to the transversal beam emittance, while the longitudinal phase space was found to be comparable. The beam intensity exceeds present accelerators by orders of magnitude. The excellent beam quality implies a highly laminar acceleration and an initially extremely cold beam and the experiments proved the beam to have optical qualities. The properties are highly interesting for applications, especially as we have shown the possibility of tailoring the beam with respect to shape, ion species, efficiency [14], and homogeneity. A wealth of applications are currently being investigated, starting from improved diagnostic capabilities [6], to industrial and medical applications, to next generation ion sources and prospects for fast ignition in inertial ICF [4, 24]. Still the underlying physics is subject to further investigation and, with respect to the extensive interest, future improvements are likely to be developed in the next years.

Acknowledgments

This work was supported by the EU Contract No. HPRI CT 1999-0052, and in part by grant E1127 from Region Ile-de-France.

References

- [1] Clark *et al* 2000 *Phys. Rev. Lett.* **84** 670
- [2] Snavely R *et al* 2000 *Phys. Rev. Lett.* **85** 2945
- [3] Wilks S C *et al* 2001 *Phys. Plasmas* **8** 542
- [4] Roth M *et al* 2001 *Phys. Rev. Lett.* **86** 436
- [5] Roth M *et al* 2002 *PRST-AB* **5** 061301
- [6] Borghesi M *et al* 2001 *Plasma Phys. Control. Fusion* **43** A267
- [7] Ruhl H *et al* 2000 *Plasma Phys. Rep.* **27** 363
- [8] Pukhov A 2001 *Phys. Rev. Lett.* **86** 3561
- [9] Lucy L B 1974 *Astron. J.* **79** 745
- [10] Wickens L M and Allen J E 1981 *Phys. Fluids* **24** 1984
- [11] Cowan T E *et al* *Nature* submitted
- [12] Zepf M *et al* 2001 *Phys. Plasmas* **8** 2323

-
- [13] Santos J J *et al* 2000 Rapport LULI 2000, p 19
 - [14] Roth M *et al* 2002 *AIP Conf. Proc.* vol 611, ISBN 0-7354-0057-1, p 199
 - [15] MacKinnon A J *et al* 2001 *Phys. Rev. Lett.* **86** 1769
 - [16] Haines M G 1981 *Phys. Rev. Lett.* **47** 917
 - [17] Key M H *et al* 1998 *Phys. Plasmas* **5** 1966
 - [18] Malka G and Miquel J L 1996 *Phys. Rev. Lett.* **77** 75
 - [19] Beg F N *et al* 1997 *Phys. Plasmas* **4** 447
 - [20] Tabak M *et al* 1994 *Phys. Plasmas* **1** 1626
 - [21] Deutsch C *et al* 1996 *Phys. Rev. Lett.* **77** 2483
 - [22] Batani D *et al* 2000 *Phys. Rev. E* **61** 5725
 - [23] Hegelich M *et al* 2002 *Phys. Rev. Lett.* **89** 085002
 - [24] Atzeni S *et al* 2001 *Proc. 28th EPS Conf. on Contr. Fusion and Plasma Physics (Madeira, 2001)*

- 1.8** H. Baumhacker, G. Pretzler, K.J. Witte, M. Hegelich, M. Kaluza, S. Karsch, A. Kudryashov, V. Samarkin and A. Roukossouev, *Correction of strong phase and amplitude modulations by two deformable mirrors in a multistaged Ti:sapphire laser*, *Opt. Lett.* **27**, 1570 (2002).

Copyright 2002 by the Optical Society of America

1570 OPTICS LETTERS / Vol. 27, No. 17 / September 1, 2002

Correction of strong phase and amplitude modulations by two deformable mirrors in a multistaged Ti:sapphire laser

H. Baumhacker, G. Pretzler, K. J. Witte, M. Hegelich, M. Kaluza, and S. Karsch

Max-Planck-Institut für Quantenoptik, Hans-Kopfermann-Strasse 1, D-85748 Garching, Germany

A. Kudryashov, V. Samarkin, and A. Roukossouev

Adaptive Optics for Industrial and Medical Applications Group, Institute on Laser and Information Technology of the Russian Academy of Science (ILIT RAS), Svyatoozerskaya Street 1, Shatura, Moscow Region, 140700 Russia

Received May 23, 2002

We describe a novel scheme consisting of two deformable bimorph mirrors that can free ultrashort laser pulses from simultaneously present strong wave-front distortions and intensity-profile modulations. This scheme is applied to the Max-Planck-Institut für Quantenoptik 10-TW Advanced Titanium-Sapphire Laser (ATLAS) facility. We demonstrate that with this scheme the focusability of the ATLAS pulses can be improved from 10^{18} to 2×10^{19} W/cm² without any penalty in recompression fidelity. © 2002 Optical Society of America
OCIS codes: 010.1080, 140.3590, 220.1000.

In high-power multistage Nd:glass and Ti:sapphire (TiS) laser systems, wave-front aberrations (WFAs) that result in deterioration of beam quality are common. These WFAs originate from imperfections in the many optical components that are present in the beamline as a result of optical figure errors, pump-induced thermal distortions in the amplifiers, and the third-order nonlinear n_2 effect. In TiS lasers, cooling the crystals to the temperature of liquid nitrogen can essentially eliminate pump-induced distortions.^{1–3} A more versatile approach, however, is to use adaptive optics, which can counteract each of the three WFA sources, regardless of whether they occur individually, in pairs, or all together simultaneously. This was demonstrated in Refs. 4–7 by use of just a single deformable mirror (SDM).

In the SDM concept, only the WF of the pulse is corrected, not the intensity profile. This scheme works well as long as the WF perturbing action of each individual optical element is so weak that the shortest local radius of curvature, R , of the WF of the exiting pulse is many times the distance to the adaptive mirror. In addition, the pulse should not pick up strong intensity modulations, e.g., by nonuniform amplification. However, when an optical element such as a multipass amplifier causes a single-pass WFA with an associated R value of the order of the pass-to-pass propagation distance, the pulse intensity profile becomes increasingly modulated from pass to pass. On further propagation, these modulations may get even worse. If one stays with the SDM concept, the beam loading would then have to be reduced so that the optical components placed downstream from the amplifier are not damaged. In chirped-pulse amplification laser systems, the compressor gratings are then particularly endangered because of their low damage threshold. The system efficiency is thereby decreased considerably, too.

In this Letter we study this heavy-perturbation case, which to our knowledge has not been investigated experimentally before and is characterized here by the simultaneous presence of strong phase and amplitude modulations. We show that by invoking two DMs one can cancel the modulations without any sacrifice

in beam loading. In our concept, the compressor is placed between two DMs and thus has to be operated with a distorted WF. For this situation, we present conditions that, when met, maintain the pulse recompressibility and focusability within reasonable limits.

The two-DM concept has also been investigated for applications in areas others than the one studied here, so far only theoretically. These other applications include beam shaping for high-power laser beams in laser photochemistry and material processing⁸ as well as delivering a high-quality pulse on a remote target after propagation through turbulent atmosphere.⁹ In astronomy, the use of two DMs may enable one to overcome turbulence-induced phase and amplitude modulations for widely enlarged fields of view (Refs. 10 and 11, and references therein). The algorithms developed in Refs. 8–11 for control of the DM surfaces are not applicable to our situation because of the presence of the gratings between the two DMs, which limits beam loading.

The heavy-perturbation case that we are confronted with arises in the final disk amplifier of our Advanced Titanium:Sapphire Laser (ATLAS) facility (Fig. 1). The front end of the laser¹² delivers a 300-mJ pulse that is centered at 790 nm and stretched from 100 fs to 200 ps with a smooth intensity profile and a well-behaved WF. After four passes, the fluence pattern of the pulse inside the compressor is heavily modulated (Fig. 2, left) due to crystal-growth defects (Fig. 3) and pump-induced aberrations. At a pulse energy of 1.3 J at the compressor entrance, the peak fluence reaches 0.3 J/cm² on the first grating, far beyond its damage threshold of 0.15 J/cm². Under these loading conditions, the energy that is transmittable through the compressor is limited to only 0.5 J. Because of the simultaneous presence of WFAs and intensity modulations, the SDM concept is no longer applicable. To increase the amount of energy that is transportable through the compressor, we must first smooth the fluence profile. This is achieved with deformable mirror DM1 (17 electrodes, 30-mm diameter, bimorph),¹³ which replaces the plane mirror in the beamline before the pulse makes its final transit through the amplifier

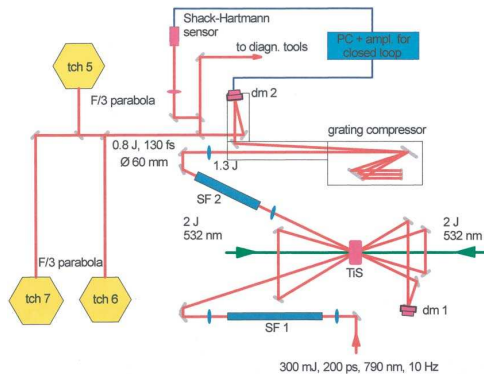


Fig. 1. Setup of the final amplifier in the ATLAS facility with two deformable mirrors, DM1 and DM2, closed loop, and three target chambers (TCH5–TCH7). The TiS crystal of 40-mm outer diameter is pumped from two sides. The TiS pulse provided by the front end passes through the crystal four times and is thereby amplified from 0.3 to 1.5 J. The pulse then runs through spatial filter SF2, and the pulse diameter increases from 18 to 63 mm. The pulse is then recompressed to 130 fs in an evacuated compressor chamber that houses two holographic gold gratings and is connected to the target chambers by evacuated tubes.

(Fig. 1). The best electrode voltage settings for DM1 can be found manually with a few iterations by use of a real-time beam-profile analyzer. For the same energy of 1.3 J as before, the peak fluence of the smoothed profile is then reduced to 90 mJ/cm^2 so that the 1.3-J energy can be safely transmitted through the compressor. At constant voltage settings, the smoothed beam profile remains stable over weeks and changes little on propagation inside the compressor and a few meters downstream.

The action of DM1 modifies the WFAs originating in the amplifying crystal but does not generate a plane WF. A plane WF is generated with a second deformable mirror, DM2 (33 electrodes, 80-mm diameter, bimorph).¹³ DM2 is placed behind the compressor so that it is able to compensate for the optical figure errors of the gratings and to ensure that highly peaked intensity patterns that might occur when DM2 is optimized cannot damage the gratings. The compressor is thus fed with a chirped pulse whose WF is distorted. In this situation, which was investigated theoretically in Ref. 14, the following three effects are of major importance: loss of compression fidelity, astigmatism, and chromatic aberration. For an estimate of the level of WFAs that are tolerable without too high a loss in beam quality, the rigorous theory¹⁴ is not needed. It is sufficient to replace the real pulse with a spherical WF whose curvature is chosen to be equal to the maximum local curvature in the real distorted WF. The focus of the model WF is downstream DM2.

From measurements, we find that the recompression fidelity in terms of pulse duration and contrast is hardly affected as long as any local radius of curvature of the WF exceeds 15 m. The condition is met in the ATLAS for pulse energies of up to 1 J after compression.

The originally spherically convergent beam turns astigmatic when it leaves the compressor, leading to the occurrence of two focal lines instead of a single point focus because the beam behaves differently in the dispersion and nondispersion planes of the compressor. With $R \geq m$, the compressor-induced astigmatism turns out to be weak and is hence easily correctable with DM2, since the necessary displacement is $\leq 1 \mu\text{m}$. The compensation of the original beam convergence is not a problem, either.

The chromatic aberration originates from the different path lengths of the individual spectral components on their way through the compressor. When they are exiting, the individual spectral components still have the same cone angle, but at a fixed position in space the radii of curvature are different. This effect cannot be compensated for with DM2. The beam emerging from DM2 will hence be parallel for the spectral component near λ_0 but divergent for the components with $\lambda < \lambda_0$ and convergent for those with $\lambda > \lambda_0$. The focus of such a beam is hence no longer pointlike but exhibits longitudinal spreading, with each spectral component having its own focus located at a different position. This spreading is tolerable when the foci of all colors inside the spectral range $4\Delta\lambda_{\text{FWHM}}$ lie within the Rayleigh length of the spectral beam component at λ_0 . For the ATLAS, this criterion requires $R > 15 \text{ m}$, which is met. The theoretical analysis reveals that $R \propto \Delta\lambda_{\text{FWHM}}$. Very short pulses with $\Delta\lambda_{\text{FWHM}} \geq 50 \text{ nm}$ thus need to be rather well collimated if one wishes to avoid intensity degradation in the focus. This conclusion is in fair agreement with the results of the rigorous theory.¹⁴

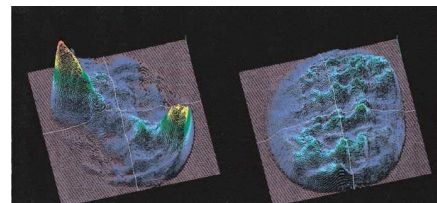


Fig. 2. Fluence patterns in the plane of the first compressor grating. Left, DM1 is replaced with a plane mirror; peak fluence, 300 mJ/cm^2 . The double-peak pattern is due to the coarse two-half structure of the WFAs shown in Fig. 3. Right, DM1 is optimized; peak fluence reduced to 90 mJ/cm^2 . The remaining fluence modulation arises from the fine structure of the WFAs (Fig. 3). The very high spatial frequencies, which carry little energy, are lost on propagation through the spatial filter SF2 (Fig. 1).

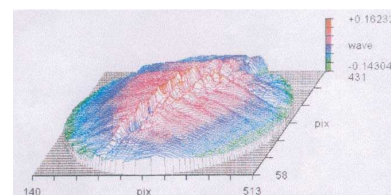


Fig. 3. WFAs that are due to growth defects in the final disk amplifier of 40-mm diameter, 17-mm thickness, and $\alpha l = 2.3$ at 532 nm.

1572 OPTICS LETTERS / Vol. 27, No. 17 / September 1, 2002

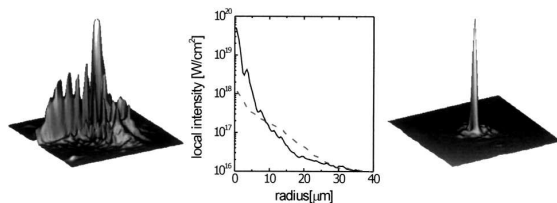


Fig. 4. Fluence profile in the focus of the $F/3$ off-axis parabola. Left, DM1 and DM2 are on, but DM2 acts as a plane mirror. Middle; local intensity as a function of radius for the fluence profiles shown to the left (---) and right (—). Right, DM1 and DM2 are on, but DM2 is locked to operation for minimal WFAs.

We generate a parallel beam with DM2 by comparing the actual WF as measured with a Shack–Hartmann sensor that has a 12×12 lenslet array with a reference WF obtained from a diode laser running at 790 nm and expanded to a parallel beam of 63-mm diameter. Edge points with an intensity of less than 10% of the maximal intensity are disregarded. The reference WF is stored in the computer for subsequent use. The voltage settings to be assigned to the electrodes of DM2 then have to be found so that the WF of the ATLAS pulse matches the reference WF as closely as possible. This is achieved by application of a closed loop. The algorithm employed for this purpose is the same as that developed in Ref. 5. The deviations between the actual and the reference WFs are minimized by use of the peak-to-valley optical-path difference as a criterion. Usually, approximately five iterations are needed to decrease the peak-to-valley value from the original 10λ to $\lambda/4$. The voltage settings corresponding to minimal WF distortion are stored. They can be used for hours because of the high thermomechanical stability of the ATLAS and the correspondingly low shot-to-shot fluctuations of the WF. For routine operation of the ATLAS, the closed loop is no longer needed once the WF correction is complete. We can then remove the beam splitter feeding the Shack–Hartmann sensor from the beam line to keep the B integral low. In case of performance deterioration, e.g., because of thermal drift, the whole WF correction procedure, which takes ~ 15 s, has to be redone.

We check the quality of the corrected WF in each target chamber by measuring the fluence patterns in the foci of the $F/3$ off-axis parabolas, using an 8-bit CCD camera and a set of calibrated filters. This combination provides an effective dynamic range of $>10^4$. The focus is viewed at $50\times$ magnification. Because of the 1-mm-diameter pinhole SF2, there can be no energy outside the sensor chip ($6\text{ mm} \times 4\text{ mm}$). Hence, the amount of energy that can possibly be hidden in the pixels showing no direct response is at most 10% of the total pulse energy. In each chamber, we obtain the same result for thousands of shots. With DM1 on and DM2 acting as a plane mirror, we find the multiple-peak fluence pattern depicted in the left-hand part of Fig. 4. The Strehl ratio (for its definition, see Ref. 15) is only ~ 0.04 . However, when DM2 is locked to operation for minimal WFA, we find

a dramatic improvement (Fig. 4, right). A single peak appears that contains 65% of the pulse energy within the diffraction-limited diameter. The mean intensity inside the diffraction-limited diameter is raised by a factor of ~ 20 from $\sim 10^{18}$ to 2×10^{19} W/cm². The Strehl ratio increases to 0.7. The Strehl ratio estimated from the corrected WF with a peak-to-valley optical path difference of $\lambda/4$ is 0.8. The difference in the two ratios is attributed to the fact that the real WF has higher-order aberrations that are not measurable with our Shack–Hartmann sensor and are not correctable with our adaptive optics.

We have shown that a combination of two DMs can free ultrashort laser pulses from simultaneously present heavy phase and amplitude modulations without any penalty in recompression fidelity and focusability.

This work was supported by the Commission of the European Union (EU) within the framework of the Association Euratom–Max-Planck-Institut für Plasmaphysik and the EU project ADAPTOOL (contract HPRI-CT-1999-50012). K. Witte's e-mail address is klaus.witte@mpq.mpg.de.

References

1. G. Erbert, L. Bass, R. Hackel, S. Jenkins, K. Kanz, and J. Paisner, in *Conference on Lasers and Electro-Optics*, Vol. 10 of 1991 OSA Technical Digest Series (Optical Society of America, Washington, D.C., 1991), pp. 390–391.
2. M. Pittmann, J. Rousseau, L. Notebaert, S. Ferré, J. Chambaret, and G. Cheriaux, in *Conference on Lasers and Electro-Optics*, Vol. 56 of OSA Trends in Optics and Photonics Series (Optical Society of America, Washington, D.C., 2001), p. 83.
3. S. Backus, R. Bartels, S. Thompson, R. Dollinger, H. Kapteyn, and M. Murnane, *Opt. Lett.* **26**, 465 (2001).
4. B. Van Woutherghem, J. Murray, J. Campbell, D. Speck, C. Barker, I. Smith, D. Browning, and W. Behrend, *Appl. Opt.* **36**, 4932 (1977).
5. K. Akaoka, S. Harayama, K. Tei, Y. Marayuma, and T. Arisawa, *Proc. SPIE* **3265**, 219 (1997).
6. F. Druon, G. Cheriaux, J. Faure, J. Nees, M. Nantel, A. Maksimchuk, J. Chanteloup, and G. Vodvin, *Opt. Lett.* **23**, 1043 (1998).
7. J. Chanteloup, H. Baldis, A. Migus, G. Mourou, B. Loiseaux, and J. Huignard, *Opt. Lett.* **23**, 475 (1998).
8. K. Nemoto, T. Fujiti, and N. Goto, *Proc. SPIE* **2119**, 155 (1994).
9. G. Roger, *J. Phys. Colloq.* **41**, 399 (1980).
10. K. Li You, Q. C. Dong, and W. D. Xiang, *High-Power Laser Particle Beams* **12**, 665 (2000).
11. A. Tokovinin, M. Le Louarn, E. Viard, N. Hubin, and R. Conan, *Astron. Astrophys.* **378**, 710 (2001).
12. K. Yamakawa, P. Chin, A. Magano, and J. Kmetec, *IEEE J. Quantum Electron.* **37**, 2698 (1994).
13. DM1 and DM2 were produced in the mainframe of Max-Planck-Institut–ILIT RAS collaboration. See also J. Dainty, A. Koryabin, and A. Kudryashov, *Appl. Opt.* **37**, 4663 (1998).
14. Z. Wang, Z. Xu, and Z.-Q. Zhang, *IEEE J. Quantum Electron.* **37**, 1 (2001).
15. W. J. Smith, *Modern Optical Engineering*, 2nd ed. (McGraw-Hill, New York, 1990), p. 337.

- 1.9** M. Hegelich,
Teilchenbeschleunigung mit Lasern,
Physik in unserer Zeit **6**, 252 (2002).

TREFFPUNKT FORSCHUNG

PLASMAPHYSIK

Teilchenbeschleunigung mit Lasern

Einer internationalen Gruppe von Forschern aus Deutschland (MPI für Quantenoptik, LMU München, GSI Darmstadt) sowie Frankreich (LULI) und den USA (General Atomic) ist es gelungen, Fluor- und Kohlenstoffionen mittels eines Hochleistungslasers auf Energien von über 100 MeV zu beschleunigen. Diese Methode eröffnet Anwendungsmöglichkeiten in Bereichen wie Laserfusion, Medizin oder Laborastrophysik.

Hochenergie-Kurzpuls-Laser erzeugen für die Dauer des Laserpulses im Fokus Intensitäten von 10^{19} - 10^{21} W/cm² und ionisieren die Materie. Die im Plasma auftretenden elektrischen und magnetischen Felder übertreffen alle jemals zuvor im Labor erzeugten Feldstärken um viele Größenordnungen und sind vergleichbar mit Verhältnissen, wie sie sonst nur in Pulsaren, Supernovae und anderen astrophysikalischen Objekten auftreten. Erzeugt man solche Bedingungen neu kontrolliert im Labor, lassen sich neuartige Materiezustände und Phänomene beobachten.

In unseren Experimenten fokussieren wir den 100-TW-Laser des Laboratoire pour l'Utilisation des Lasers Intenses (LULI) in Palaiseau, Frankreich, auf eine wenige Mikrometer dünne Folie aus Aluminium oder Wolfram, die auf der Rückseite mit Kohlenstoff bzw. CaF₂ beschichtet ist (Abbildung 1). Die 300 fs kurzen Laserpulse erzeugen im Fokus eine Leistungsdichte von $5 \cdot 10^{19}$ Watt/cm².

Dadurch werden die Elektronen der Folienatome von den Laserfeldern innerhalb von ca. 2 fs nahezu auf Lichtgeschwindigkeit (Energie: 2 MeV) beschleunigt. Die Atomrümpfe verbleiben zunächst im Laserfokus. Sie werden auf Grund ihrer größeren Trägheit nicht so schnell beschleunigt. Noch bevor sie einen nennenswerten Impuls aufnehmen können, wechselt das Laserfeld sein Vorzeichen und wirkt nun bremsend.

Die Elektronen haben jedoch die Region bereits verlassen und behalten deshalb ihre Geschwindigkeit bei. Aufgrund von relativistischen Effekten wirkt auf die Elektronen trotz der transversalen Natur der Laserfelder eine Beschleunigung in Laserrichtung. Dies führt zu einem starken Elektronenstrom durch die Folie, der bei seinem Austritt auf der Rückseite dort ein sehr starkes quasistatisches, das heißt nicht oszillierendes, elektrisches Feld erzeugt. Dieses Feld erreicht eine Stärke von mehr als 10^{12} Volt pro Meter und ist damit

rund zehnmal größer als das Feld, das ein Elektron im Wasserstoffatom hält. Dadurch werden die Atome an der Folienoberfläche ionisiert und beschleunigt, wobei die höchste Energie mit F⁷⁺-Ionen erzielt wurde. Ein Laserpuls erzeugt etwa 10^{12} Ionen und beschleunigt sie auf einer Distanz von nur 10 µm auf Energien von über 100 MeV [1]. Konventionelle Beschleuniger benötigen dazu Strecken von ca. 100 Metern.

Die Ionen werden in einem kurzen Puls aus einem sehr kleinen Raumvolumen emittiert und ihre Trajektorien überschneiden sich nicht. Die daraus resultierende hohe Strahlqualität ist eine wichtige Voraussetzung für weitere Anwendungen und eine bessere Kontrolle des Ionenstrahls. Die Ionenpulse haben ungefähr die Dauer des Laserpulses und sind damit mehr als tausendmal kürzer als jeder herkömmlich erzeugte Puls. Da die positive Ionenladung im laserbeschleunigten Puls durch begleitende Elektronen kompensiert wird, können außerdem Teilchenströme von einigen MA realisiert werden und liegen damit um viele Größenordnungen über denen konventioneller Beschleuniger. Aufgrund dieser einzigartigen Eigenschaften konnten laserbeschleunigte Protonen bereits erfolgreich in der Diagnostik von hochdichten, kurzlebigen Plasmen und elektrischen Felder eingesetzt werden.

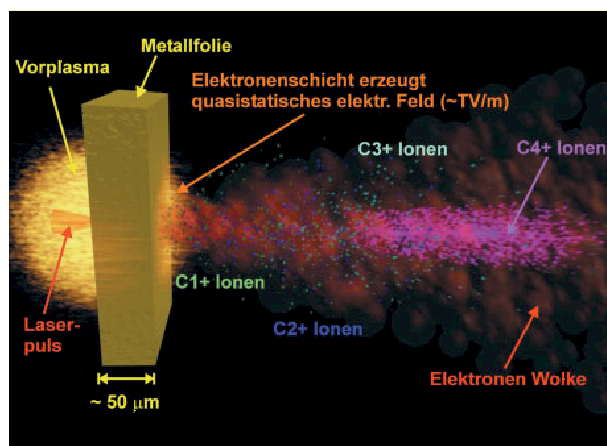
Aus den Energiespektren der Ladungszustände lassen sich wichtige Informationen über die Dynamik der Felder und den Beschleunigungsmechanismus gewinnen, die in Zukunft eine bessere Kontrolle des Prozesses und der Pulseigenschaften ermöglichen. Die Methode eröffnet eine Vielzahl von Anwendungen. Im medizinischen Bereich zur Produktion von kurzlebigen Isotopen für die Positronen-Emissions-Tomographie (PET), in der Grundlagenforschung als Diagnostikverfahren oder Zündfunke in Fusionsexperimenten, für neuartige Teilchenbeschleuniger und sogar für astrophysikalische Experimente im Labor. So kann man mit den Ionenpulsen makroskopische Proben in wenigen Pikosekunden auf über 100 000 Grad erhitzen, bevor diese sich ausdehnen.

Die Arbeit wurde unterstützt im Rahmen des EU-Programmes Nr. HPRI CT 1999-0052, Grant-Nr. E1127.

[1] M. Hegelich et al., Phys.Rev.Lett. **2002**, 89, 085002

Manuel Hegelich,
MPI für Quantenoptik, Garching

Abb. 1 Beschleunigungsmechanismus: Der Laserpuls beschleunigt in einer Folie Elektronen (rot-orange), die auf der Rückseite eine Ladungsschicht und damit ein elektrisches Feld erzeugen. Diese ionisiert und beschleunigt die Atome (in diesem Fall Kohlenstoff) aus der Folienrückseite.



Danksagung

Zu guter Letzt möchte ich mich bei allen bedanken, die zum Gelingen dieser Arbeit beigetragen haben. Die Arbeit entstand am Max-Planck-Institut für Quantenoptik und am Lehrstuhl für Kernphysik der Ludwig-Maximilian Universität München. Im Rahmen der Arbeit wurden ausserdem Experimente am Laboratoire pour l'Utilisation des Lasers Intenses der École Polytechnique in Palaiseau, Paris, sowie dem Los Alamos National Laboratory in New Mexico, USA, durchgeführt. Das System zur Auswertung der Kernspurdetektoren wurde von der AG Heinrich der Universität Siegen bereitgestellt. Den Mitarbeitern dieser Institute gilt mein herzlichster Dank für die hervorragende Unterstützung. Mein besonderer Dank gilt ausserdem:

- ... Herrn Prof. Dr. Dieter Habs, meinem Doktorvater, für die Betreuung und für die grosszügige Unterstützung mit Rat, Tat, Reise- und Sachmitteln während der gesamten Arbeit. Während der letzten vier Jahre habe ich viel gelernt, sowohl über Physik, als auch darüber, wie man sie organisiert. In diesem Sinne vertraue ich weiterhin auf eine gute Zusammenarbeit und Unterstützung in der Zukunft, wenn auch vorerst transatlantisch.
- ... Herrn Prof. Dr. Klaus Witte, in dessen Gruppe am MPQ ich diese Arbeit anfertigen konnte. Besonders seine bedingungslose Unterstützung, seine grundsätzlich positive Haltung zu allen von einem kleinen Doktoranden vorgebrachten Ideen und Vorschlägen, selbst als es darum ging die Experimente zum Grossteil an ein anderes Institut auszulagern und Reisephysik zu betreiben, seine immer wertvollen Ratschläge sowohl fachlicher als auch organisatorischer und karrierebezogener Natur (und natürlich wo man welchen Wein kaufen sollte), haben mich viel gelehrt und die 4 Jahre am MPQ für mich zur denkbar angenehmsten Doktorandenzeit gemacht.
- ... Herrn Prof. Dr. T.W. Hänsch für die extrem kurzfristige und unbürokratische Übernahme der Zweitkorrektur, ohne die ich in ernstliche terminliche Schwierigkeiten mit meinem zukünftigen Arbeitgeber gekommen wäre.
- ... Herrn Prof. Dr. Jürgen Meyer-ter-Vehn, der mich für die Hochintensitätslaserei begeistert hat und mir diese Doktorandenstelle vermittelt, selbst als sich herausstellte, das ich keine Theorie- sondern eine Experimentalstelle wollte. Auf seinen Rat in Theoriefragen konnte ich mich dennoch immer voll und ganz verlassen.

- ... Prof. Dr. Georg Pretzler, als ich begann noch Habilitant, für die fundierte Einführung in mein Arbeitsgebiet und die Unterstützung bei den Rechnungen zu Felddynamik. Von hier aus nochmal herzlichen Glückwunsch zu deiner Professur und das deine neue Arbeitsgruppe so erfolgreich werden möge wie die alte.
- ... Prof. Dr. Markus Roth, Dr. Thomas Cowan, Dr. Jean Claude Gauthier und Dr. Patrick Audebert, dafür das sie mich and den Experimenten in LULI teilnehmen liessen, obwohl die Gruppe schon so gross war. Der Erfolg gibt der Entscheidung Recht. Auch für die grosse fachliche Unterstützung und die vielen Diskussionen, ohne die meine Arbeit nicht geworden wäre was sie ist, möchte ich mich bei euch bedanken und hoffe, dass wir unsere erfolgreiche (berühmt-berüchtigte) und nicht zuletzt vor allem viel Spass machende GSI-LULI-GA-MPQ-Kollaboration auch in Zukunft aufrechterhalten werden. (Auch wenn noch ein oder zwei Institutslogos hinzukommen).
- ... M. Allen, Abel Blazevic (diesmal richtig geschrieben), Erik Brambrink und Matthias Geissel für die tatkräftige Unterstützung bei den Experimenten am LULI
- ... Jim Cobble, Randy Johnson, Sam Letzring and Juan Fernandez für selbige in Los Alamos
- ... und ganz besonders Julien Fuchs, ohne dessen nimmermüden Einsatz am LULI Laser bis in die frühen Morgenstunden den Strahlzeiten nicht der Erfolg beschieden gewesen wäre, den sie hatten. Selbst Gerüchte über angebliche Verwandte konnten Ihn nicht davon abhalten auch in Los Alamos kräftig mitzumischen.
- ... meinem Bürogenossen Stefan Karsch für seine gute Zusammenarbeit in wirklich allen Bereichen. Du warst eine grosse Hilfe und ein noch grösserer Ansporn. Und wenn ich denn eine neue Walspezies entdecken soll, wird es bei dir ein inerstellarer Nebel, viel Glück mit der neuen Teleskopmontierungist. Und immer dran denken: Alles wird gut!
- ... den Kollegen Michael Jost, Malte Kaluza, Matthias Dreher, Ulrich Andiel, Christoph Gahn, Jürgen Fließer, Jürgen Stein, Marko Santala, der sehr kompetenten Francesca Pisani (die sich immer darüber ärgert, zuerst mit dem Adjektiv "hübsch" in Verbindung gebracht zu werden, deshalb hier mal andersherum), sowie Klaus Eidmann und George Tsakiris, für die gute Arbeitsatmosphäre in der Gruppe und die zahlreichen fachlichen und weniger fachlichen Gespräche.
- ... Alois Böswald und Harald Haas, die für einen allzeit zuverlässigen ATLAS-Laserbetrieb Sorge trugen. Weiterhin gebührt Josef Bayerl, Manfred Fischer, Walter Fölsner (nochmal Danke für die Kiste), Günter Keller mein Dank für ihre kompetente Unterstützung bei technischen Problemen.
- ... der MPQ-Werkstatt

... den Mitarbeitern des Lehrstuhls Habs

... meinen Eltern, die mir mein Studium ermöglicht und mich immer unterstützt haben. Es ist vollbracht, hiermit ist meine Ausbildung, wenn auch nicht mein Studium, abgeschlossen.

... meinen Geschwistern, insbesondere meinem Bruder Kolja, der eine unschätzbare Hilfe in allen Computer- und Programmierfragen ist.

... und natürlich Quynh Anh.

...

Science is unforgettable - but only if you work on it out of interest and not for some other purpose, such as getting a degree.

E. Teller [104]

...

Lebenslauf

Persönliche Daten

Name Manuel Hegelich
Geburtstag/-ort 05.02.73 in Herdecke
Familienstand verheiratet
Staatsangehörigkeit deutsch

Schulbildung

7/79 - 7/83 Grundschule in Sinn und Burbach
7/83 - 5/92 Gymnasium auf der Morgenröthe, Eiserfeld, Abitur

Hochschulausbildung

10/92 - 7/95 Physik an der Universität Siegen
Abschluss: Vordiplom

8/95 - 7/96 Angewandte Physik und Informatik an der Napier University Edinburgh
Abschluss: Bachelor of Science with first Class Honours
Thesis bei Prof. Leifer: *Single Beam Reflection Holographic Interferometry - A Study of the Deformation of Bolted Timber Joints.*

10/96 - 10/98 Physikstudium an der Georg August Universität Göttingen
Abschluss: Diplom
Diplomarbeit am Laser Laboratorium Göttingen bei Prof. Marowsky: Zeitaufgelöste Untersuchung der photoinduzierten Doppelbrechung in Azobenzenseitenketten Polyestern.

Promotion

11/1998 bis 12/2002 Universität München, Lehrstuhl Prof. Habs und Max-Planck-Institut für Quantenoptik, Laser-Plasma-Gruppe, in Garching bei München
Titel: Acceleration of heavy Ions to MeV/nucleon Energies by Ultrahigh-Intensity Lasers

Auslandsaufenthalte

8/95 - 7/96 Napier University Edinburgh, Scotland
10/2000 - 12/2002 mehrere Aufenthalte am Laboratoire pour l'Utilisation des Lasers Intenses, École Polytechnique, Palaiseau, Frankreich, sowie Los Alamos National Laboratory, New Mexico, USA